The Pennsylvania State University

The Graduate School

College of Earth and Mineral Sciences

DIMENSIONAL SCALING OF PEROVSKITE FERROELECTRIC THIN FILMS

A Dissertation in

Materials Science and Engineering

by

Ryan R. Keech

Submitted in Partial Fulfillment

of the Requirements for the Degree of

Doctor of Philosophy

December 2016

The dissertation of Ryan Keech was reviewed and approved* by the following:

Susan Trolier-McKinstry
Professor of Ceramic Science and Engineering and Electrical Engineering
Dissertation Adviser
Chair of Committee

Clive A. Randall
Professor of Materials Science and Engineering

Thomas R. Shrout
Senior Scientist and Professor of Materials Science and Engineering

Mehdi Kiani
Professor of Electrical Engineering

Glenn Martyna
Honorary Professor of Physics
School of Physics and Astronomy
The University of Edinburgh, Edinburgh, UK
Special Member

Suzanne Mohney
Professor of Materials Science and Engineering and Electrical Engineering
Chair, Intercollege Graduate Degree Program in Materials Science and Engineering

*Signatures are on file in the Graduate School

Abstract

Dimensional size reduction has been the cornerstone of the exponential improvement in silicon based logic devices for decades. However, fundamental limits in the device physics were reached ~2003, halting further reductions in clock speed without significant penalties in power consumption. This has motivated the research into next generation transistors and switching devices to reinstate the scaling laws for clock speed. This dissertation aims to support the scaling of devices that are based on ferroelectricity and piezoelectricity and to provide a roadmap for the corresponding materials performance.

First, a scalable growth process to obtain highly {001}-oriented lead magnesium niobate – lead titanate (PMN-PT) thin films was developed, motivated by the high piezoelectric responses observed in bulk single crystals. It was found that deposition of a 2-3 nm thick PbO buffer layer on {111} Pt thin film bottom electrodes, prior to chemical solution deposition of PMN-PT reduces the driving force for Pb diffusion from the PMN-PT to the bottom electrode, and facilitates nucleation of {001}-oriented perovskite grains. Energy dispersive spectroscopy demonstrated that up to 10% of the Pb from a PMN-PT precursor solution may diffuse into the bottom electrode. PMN-PT grains with a mixed {101}/{111} orientation in a matrix of Pb-deficient pyrochlore phase were then promoted near the interface. When this is prevented, phase pure films with {001} orientation with Lotgering factors of 0.98-1.0, can be achieved. The resulting films of only 300 nm in thickness exhibit longitudinal effective $d_{33,f}$ coefficients of ~90 pm/V and strain values of ~1% prior to breakdown.

300 nm thick epitaxial and polycrystalline lead magnesium niobate – lead titanate (70PMN-30PT) blanket thin films were studied for the relative contributions to property thickness dependence from interfacial and grain boundary low permittivity layers. Epitaxial PMN-PT films were grown on $SrRuO_3$ /(001)$SrTiO_3$, while polycrystalline films with {001}-Lotgering factors >0.96 were grown on $Pt/TiO_2/SiO_2/Si$ substrates via chemical solution deposition. It was found that both film types exhibited similar, thickness-independent high-field ε_r of ~300 with highly crystalline electrode/dielectric interfaces. The dielectric data suggest that irreversible domain wall motion is the major contributor to the overall dielectric response and its thickness dependence. In epitaxial films the irreversible Rayleigh coefficients reduced 85% upon decreasing thickness from 350 to 100 nm. T_{max} was the only measured small signal quantity which was more thickness dependent in polycrystalline than epitaxial films. This was attributed to the relaxor nature present in the films, potentially stabilized by defect concentrations, and/or chemical inhomogeneity. The effective interfacial layers are found to contribute to the measured thickness dependence in $d_{33,f}$ measured by X-ray diffraction. Finally, high field piezoelectric characterization revealed a field-induced rhombohedral to tetragonal phase transition in epitaxial films.

While the mechanisms causing thickness dependence are mostly understood, the functional properties of blanket PMN-PT films remain about an order of magnitude lower than what is achieved in constraint-free bulk single crystals. These property reductions are attributed to substrate clamping, and the process of declamping via lateral subdivision was studied in 300-350 nm thick, {001} oriented 70PMN-30PT films on Si substrates. In the clamped state, the films exhibit relative permittivity near 1500 and loss tangents of approximately 0.01. The films showed slim hysteresis loops with remanent polarizations of about 8 μC/cm^2 and breakdown fields over 1500 kV/cm. Using optical and electron beam lithography combined with reactive ion etching, the PMN-PT films were systematically patterned down to lateral feature sizes of 200 nm in spatial scale with nearly vertical sidewalls. Upon lateral scaling, which produced partially declamped films, there was an increase in both small and large signal dielectric properties, including a doubling of the relative permittivity in structures with width-to-thickness aspect ratios of 0.7. In addition, declamping resulted in a counterclockwise rotation of the hysteresis loops, increasing the remanent polarization to 13.5 μC/cm^2. Rayleigh analysis, Preisach modeling, and the relative permittivity as a function of temperature also indicated changes in the domain wall motion and intrinsic response of the laterally scaled PMN-PT.

The longitudinal piezoelectric coefficient, $d_{33,f}$, was interrogated as a function of position across the patterned structures by finite element modeling, piezoresponse force microscopy, and nanoprobe synchrotron X-ray diffraction. It was found that $d_{33,f}$ increased from the clamped value of 40-50 pm/V to ~160 pm/V at the free sidewall under 200 kV/cm excitation. The sidewalls partially declamped the piezoelectric response 500-600 nm into the patterned structure, raising the piezoelectric response at the center of features with lateral dimensions less than 1 μm (3:1 width to thickness aspect ratio). The normalized data from all three characterization techniques are in excellent agreement, with quantitative differences providing insight to the field dependence of the piezoelectric coefficient and its declamping behavior.

Table of Contents

List of Figures

List of Tables

Acknowledgments

With outcomes defined by calculations, chemical reactions, and data, science is sometimes considered to be an impersonal field. My experience and outcomes at Penn State, however, have been defined and enriched by the people I have met here and to whom I am sincerely grateful.

Professor Susan Trolier-McKinstry, I cannot thank you enough for the mentorship and generosity in time you have given to me in reviewing my writing, discussing scientific matters, and providing constructive criticism to help me grow. You provide an exemplary model of work ethic and professionalism and I truly appreciate the way you challenge your students to exceed their own expectations. I also want to sincerely thank you for the support and compassion you showed me during times of personal difficulty outside the laboratory. Thank you for believing in me and doing everything you could to help me reach my goals and more.

Thank you to my thesis committee members who supported, motivated, and challenged me to produce this thesis, which I am very proud of. Thank you, Professor Clive Randall, Professor Thomas Shrout, Professor Mehdi Kiani, Dr. Glenn Martyna, and Professor Suman Datta, for your invaluable insights, perspective, and investment in me as a student.

It has been a pleasure to work with the caring and hardworking people of the Materials Research Institute. In the Materials Characterization Laboratory (MCL), I'd like to thank Trevor Clark, Maria DiCola, Raegan Johnson-Wilke, Tim Klinger, Jeff Long, Steve Perini, Gino Tambourine, Tim Tighe, Ke Wang, Derek Wilke, and Nichole Wonderling for their support in collecting the data presented in this dissertation and time in teaching me how to properly, carefully, and accurately characterize materials. Also, my sincere thanks to the staff of the Nanofabrication Facility: Bill Drawl, Chad Eichfeld, Andy Fitzgerald, Kathy Gehoski, Beth Jones, Mike Labella, Guy Lavallee, Bangzhi Liu, and Shane Miller. Thank you for your expertise and for the patience you showed me as I learned the finesse needed to perform good experimental science.

The majority of this dissertation was done in a collaborative program with IBM TJ Watson Research Center in an effort to support the development of a next generation transistor device. It was incredibly exciting and insightful for me to participate in conference calls and meetings with our colleagues at IBM and to hear their perspectives on some of the challenges faced in materials synthesis, device fabrication, and characterization. Thank you, Brian Bryce, Marcelo Kuroda, Josei Chang, Paul Solomon, Tom Shaw, Matt Copel, Glenn Martyna, and Dennis Newns for helping me grow technically and encouraging me throughout my Ph.D.

The Penn State side of the next generation transistor project included my group members Smitha Shetty and Carl Morandi. Thank you both for the many troubleshooting conversations and support you have offered in meeting deadlines and solving problems. I similarly leaned on the rest of the STM group members, past and present, throughout my Ph.D. for mentorship, feedback on presentations and papers, examples of excellent scholarship, discussions on topics I didn’t understand, and most of all, friendship. Jon, Margeaux, Aaron, Charley, Lizz, Raegan, Derek, Beth, Hong Goo, Dan, Jung In, Song Won, Jason, Adarsh, Wanlin, Lauren, Betul, Trent, Lyndsey, Dixiong, Tianning, Julian, and my Penn State friends from outside the group, Arnab and Max, thank you all for being there for me! Special thanks to Amanda and Susie for all of their work and the support that kept things moving smoothly for us all.

I've had the privilege of collaborating with several first-class professors and students from other universities as well. Thank you Prof. Jacob Jones, Chris Fancher, Gio Esteves, and Jonathan Guerrier for your tutelage and for keeping things fun at the Advanced Photon Source (APS). Also from the APS, I'd like to thank Rick Spence and Yang Ren at beamline 11-ID-C and Zhonghou Cai at beamline 2-ID-D for their technical expertise in performing advance XRD experiments. From my alma mater, the University of Connecticut, thank you Professor Bryan Huey, Jim Bosse, and Linghan Ye for your help in performing the piezoresponse force microscopy experiments presented in this dissertation. I would also like to thank Professor Huey for encouraging me to pursue a graduate degree in Materials Science and Engineering. The belief you had in me from my days as an undergraduate often gave me the extra boost of confidence to see a problem though and not give up when it seemed too difficult.

To my family, you are the reason I have done this. Mom, you often say that you stopped being able to help me with my math homework once high school started. But the love you have given me and sacrifices you have made for us helped me more than any math tutor ever could. Dad, your excitement and interest in my work has been contagious. When I have called you feeling stumped or tired, you would tell me how proud you are of me and how cool it was that I had gotten to the point to recognize such a formidable challenge. Thank you for always reminding me I could do anything if I put my mind to it. I think that my brother Adam complements every side of my personality. When I am unsure, you are confident. When I am overly serious about something, you bring levity and remind me what life is all about. Thank you for rooting for me and keeping me going. In my second year at Penn State, my sister, Emily, started as an undergraduate freshman. I am beyond thankful for you, Emily, and for having the opportunity to go to Penn State together. I will never forget the comfort I found while working late nights in the Millennium Science Complex and shining a light from my office window across the fields and Pollock quad to your dorm room window. Seeing your light flash back reminded me I was never alone and filled my heart with love. You may never know how much it meant to me when you brought snacks and motivational cards to the study-fortress that Arnab and I built in the MSC while preparing for candidacy. Thank you for always encouraging and supporting me and for being the funniest person I know. Also, thank you to a Dr. Keech that came before me, my Papa, Ray- you instilled in me a great sense of optimism and a can-do attitude that was my crutch many times throughout the pursuit of my doctorate.

I would also like to thank my family which I came to know more recently, the Villegas-Ospina family. I remember being surprised at your home with a congratulatory dinner shortly after I found out that I was accepted to Penn State University. That moment, and the love that would follow throughout my graduate work, has meant so much to me. You gave me a place to relax, recharge, and be at home. Gracias Ana, Carlos, y Simon!

Words cannot fully express the gratitude I have for my partner in life, Sara. You have selflessly encouraged me to reach further, do more, and grow as a scientist and person because you believed in me. Thank you for the countless reminders, spoken and unspoken, that even if I never obtained highly oriented PMN-PT films, or never avoided film/substrate delamination, you would always love me. I will never forget your patient sacrifice in time together for me to achieve this degree. You have been my biggest support over the last five years and I am extremely lucky to have you in my life. Thank you for everything.

This work in this thesis was funded by a National Security Science and Engineering Faculty Fellowship (NSSEFF), the DARPA Meso program (N66001-11-C-4109), and the U.S. National Science Foundation through DMR-1410907, Penn State MRSEC (DMR-1420620), and the Cooperative Agreement with the Pennsylvania State University Materials Research Institute Nanofabrication Lab (No. ECS-0335765) Use of the Advanced Photon Source, an Office of Science User Facility operated for the U.S. Department of Energy (DOE) Office of Science by Argonne National Laboratory, was supported by the U.S. DOE under Contract No. DE-AC02-06CH11357.

Chapter 1

Introduction and Thesis Organization

The development of piezoelectric and ferroelectric materials has enabled and transformed numerous technologies. Spurred on by the need for high permittivity capacitors during World War II, discoveries in ferroelectricity boomed in the mid 1900's with key advances in barium titanate ($BaTiO_3$) and lead zirconate titanate ($Pb(Zr_{1-x}Ti_x)O_3$, or PZT).[1] Ferroelectrics with large piezoelectric constants were employed in medical ultrasound, sonar, and numerous other devices including sensors, actuators, rf filters, valves, switches, and other electromechanical systems.[1–7]

During the Digital Age, revolutions in computing were made possible by the scaling down in size and increases in performance of first bipolar transistors and then the present technology, the complementary metal-oxide semiconductor (CMOS) transistor.[8] The transistor is employed to execute logic operations with additional applications in data storage and voltage amplification. The semiconductor industry was advanced in part based on meeting Gordon E. Moore's prediction of scaling, which stated in 1975 that the transistor density on integrated circuit chips would double every two years.[9] With the dimensional scaling of transistors came a logarithmic increase of clock speed as well due to Dennard scaling.[10] Moore's law of scaling, as it came to be known, was followed for several decades but Dennard scaling has stalled since ~2003,[11] as is shown in Figure 1-1.

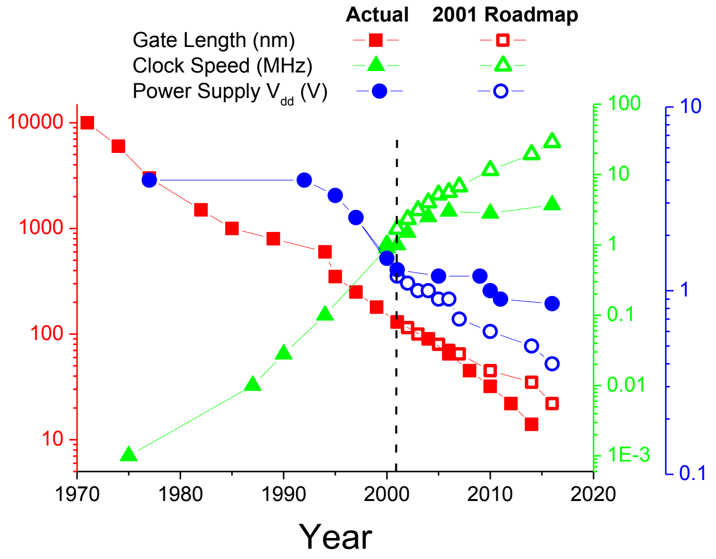

Figure 1-1: The scaling of CMOS transistor gate size (red), clock speed (green), and drive voltage (blue) as a function of time since ~1970 to 2016. The filled in data points are the actual achieved scaling, while the open data points are the predictions from the International Technology Roadmap for Semiconductors 2001 report, published just two years prior to the stall in Dennard Scaling, responsible for the differences in achieved and predicted clock speed and power scaling.

In 2015, after a decade of clock speeds saturated at ~ 2 GHz, Moore stated that he expected his namesake "law" to end within a decade or so.[9] Recently, Intel Corporation reported that the major chip producer would be slowing the pace of scaling.[12] The saturated clock speed is a result of the inability to further reduce drive voltage in the device without incurring significant penalties in Joule heating, stemming from a fundamental limit in the device architecture that marks the end of classic Dennard scaling.[11] The end of Moore's law itself, which generates fewer rewards in performance than in the past, has been predicted numerous times , but the roadblocks were circumvented through innovative engineering.[8] The challenges facing the CMOS industry in the coming decade of dimensional scaling, however, are approaching the physical limits of electronic tunneling.[13] Thus, industry is exploring a range of potential alternative transistor technologies to enable for a more dramatic change than size reduction of the planar CMOS transistor- and piezoelectric materials are a part of a proposed solution.[14]

Numerous approaches to circumventing the CMOS voltage scaling bottleneck have been proposed, including tunnel transistors,[15–18] FinFETs,[19–21] and carbon nanotube transistors.[22–24] Among these is the piezoelectronic transistor (PET)- a fast, low power, transistor-type switching device in which piezoelectric and piezoresistive materials are employed in a stacked sandwich structure within a stiff shell, such as Si_xN_y, depicted schematically in Figure 1-2.[25] With voltage applied across the common and gate electrodes, piezoelectric actuation leads to pressure on the piezoresistor, inducing a continuous insulator-to-metal transition in the electrical conductivity of the piezoresistive. With this transition, current can flow from the common to the sense electrode, turning the switch on from the normally off state. The result is an electrical switch that can be combined to produce all of the major logic functions implemented in CMOS.[26–28]

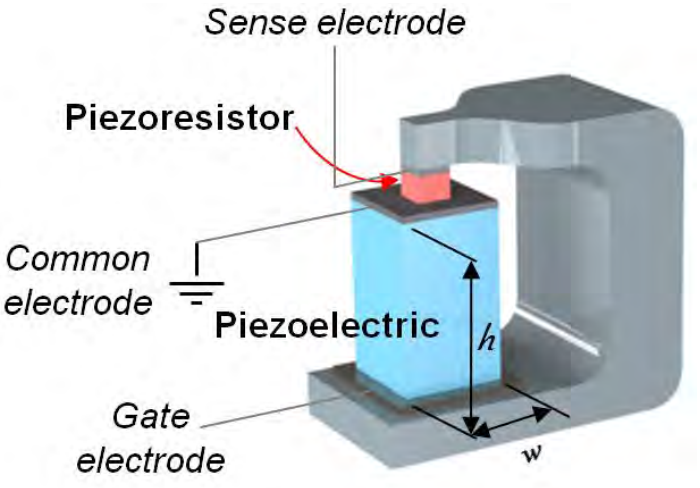

Figure 1-2: Schematic of the piezoelectronic transistor with piezoelectric component of height h and width w. Adapted from Copel *et al.*[29]

There are several materials considerations required of the PET to enable switching speeds and power levels that compete with those of modern CMOS electronics. The piezoresistive component, for example should exhibit a change in resistivity of several orders of magnitude to yield high I_{on}/I_{off} ratios at low pressure.[29] For the piezoelectric, a high d_{33} piezoelectric coefficient, that is stable at high strain, is required to provide the maximum stress to the piezoresistor for a given applied electric field. The difference in contact surface area of the piezoelectric and piezoresistor assist in this matter, via the so-called hammer and nail effect, to step up the pressure applied to the piezoresistor from a given force stemming from the piezoelectric strain (as pressure is equal to force/area). Large strain in the piezoresistor (6%) is accommodated by fabricating the piezoelectric (straining ~0.6%) to be ~10x thicker than the piezoresistor. In order to achieve power savings with respect to CMOS, the bulk, unclamped piezoelectric properties are needed.[26] The challenge is that the materials properties of continuous blanket thin films are often significantly reduced by phenomenon known as substrate clamping.

The suppressed piezoelectric response measured in thin films is referred to as $d_{33,f}$., where the "f" signifies the biaxial constraints present in thin films. Approaches to *declamp* the piezoelectric response have been implemented to increase the thin film piezoelectric coefficient. In these cases, the effective, partially declamped response is referred to as $d_{33,\,eff}$. For a completely released film, $d_{33,\,eff}$ approaches d_{33}, while a fully clamped film has $d_{33,\,eff} = d_{33,\,f}$. Declamping can be achieved via substrate undercut,[30–32] thin film transfer to more compliant substrates,[33,34] and microfabrication of island structures with free sidewalls.[35–37] Chapter 5 discusses the evolution of dielectric, ferroelectric, and piezoelectric behavior of $Pb(Mg_{1/3}Nb_{2/3})O_3$-$PbTiO_3$ (PMN-PT) near the morphotropic phase boundary composition, at 70PMN-30PT, upon declamping via lateral scaling of the blanket film. PMN-PT responds strongly to declamping due to its elastic moduli; effective declamping should allow films to achieve large piezoelectric coefficients comparable to those of bulk single crystals. The developed synthesis and orientation control for maximized piezoelectric response in 70PMN-30PT thin films is discussed in Chapter 3.

The clock speed of the PET, or any piezoelectric switching device, is determined by the time required for acoustic transduction through the thickness of piezoelectric. Therefore, the thinner the piezoelectric, the higher the clock speeds. The thickness dependence of the functional properties in ferroelectrics and piezoelectric systems such as $BaTiO_3$ and PZT has been studied for several decades. Ultimately, this thesis extends these studies to PMN-PT.

Thickness scaling research of ferroelectrics has been largely motivated by the development of ferroelectric random access memory, or FeRAM, which employs ferroelectrics in information storage applications.[38] PZT and strontium barium titanate ($Sr_xBa_{1-x}TiO_3$) thin films have been the main materials of interest for FeRAM applications, due to the high remanent polarizations that differentiate the "0" and "1" memory states.[39,40] Improvement in FeRAM technology from a materials perspective has mainly come from reduced switching voltages, increased die density, and improved fatigue characteristics with better control of stoichiometry in thin films.[38,41–43]

The thickness dependence of functional properties like the piezoelectric response in relaxor-based ferroelectrics is less well studied, especially in the sub-400 nm regime. These materials exhibit higher relative permittivity at a given thickness than PZT films, for example, but use of relaxor-ferroelectrics in many applications is waiting for strongly understood thickness dependence. Additional factors such as changes in the Curie temperature, relaxor characteristics, and phase stability as a function of thickness must be explored. Chapter 4 of this thesis presents the thickness dependence of the dielectric, ferroelectric, and piezoelectric properties of 70PMN-30PT thin films from 100 to 350 nm in thickness.

Realizing the promises of reduced operating voltages and increasing clock speed in logic operations from the piezoelectronic transistor requires a deeper understanding of the controlling mechanisms of declamping and thickness dependence in high strain piezoelectric films. This would enable scaling laws to be developed for this post-CMOS switch (the piezoelectronic transistor). This thesis aims to support that pursuit and advance the current understanding of PMN-PT thin film processing and behavior. Recommendations for future work in the dimensional scaling and declamping of ferroelectric thin films are made in Chapter 6.

The background section discusses PMN-PT as a material of choice in detail, along with the details of the considerations taken in materials processing and characterization in this work.

Chapter 2

Background

2.1 Lead magnesium niobate-lead titanate

Lead magnesium niobate ($Pb(Mg_{1/3}Nb_{2/3})O_3$), or PMN, is a relaxor ferroelectric with a macroscopic cubic structure for the perovskite phase at room temperature.[44] As a result, PMN is symmetry forbidden to exhibit any macroscopic polarization. However, it has been demonstrated via transmission electron diffraction,[45] neutron diffraction,[46] and optic index of refraction[47] experiments that the chemical ordering of Mg^{2+} and Nb^{5+} in PMN supports the formation of polar regions within the lattice. These regions are of nanometer dimension[45] and are therefore called polar nanoregions (PNRs). PNRs develop below the Burns temperature, T_d (~350 °C in pure PMN).[47,48] The large difference in valence of the B-site cations and high polarizability of the PMN lattice contributes to the anomalously high dielectric permittivity >12,000 at room temperature and 100 Hz in bulk ceramic form, as shown in Figure 2-1[49]. Relaxor ferroelectric systems show broad frequency dispersion in the dielectric permittivity, as is seen in Figure 2-1. The dielectric response of relaxors deviates from the Curie–Weiss law (which states that $\varepsilon' = C/(T - \Theta)$, where C is the Curie–Weiss constant and Θ is the Curie constant).[50] Rather, the dielectric constant of PMN follows a modified Curie-Weiss law approximated by $1/(T-T_{max})^2$ in the vicinity of T_{max}, the temperature at which ε_r is at its maximum.[51] The dielectric dispersion is lost above T_{max}.

The cause of the dielectric dispersion is still not fully understood. However, one potential explanation for the frequency dependence is from the size variation in polar regions. At low frequencies, the boundaries of most polar regions can respond to an applied AC-field. As frequency is increased, however, the larger domains with lower resonant frequencies cannot keep up with the applied field, and as a result, this contribution is lost.[52,53]

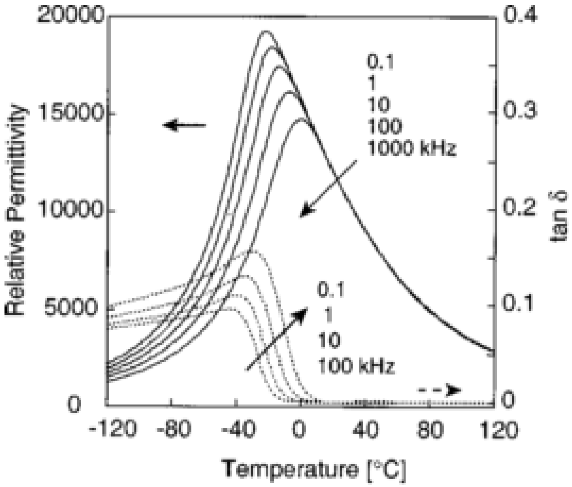

Figure 2-1: Temperature dependence of the relative permittivity and loss tangent of ~0.5 mm thick PMN bulk ceramic.[49]

In normal ferroelectrics, T_{max} occurs at the Curie temperature, below which the material exhibits a stable, spontaneous polarization that is reorientable between crystallographically equivalent states with applied electric field. In PMN relaxors, however, the material maintains an average cubic structure down to 5 K in zero field in PMN, to temperatures well below T_{max}.[54–56]

A proper ferroelectric transition temperature can be introduced to the PMN system with addition of some B-site substitutional elements. Addition of ~10 vol. % Ti to PMN, for example, raises T_{max} to room temperature and stabilizes the rhombohedral phase with polarization along <111> upon cooling.[57] Further addition of Ti yields a narrow monoclinic phase (M_A type), serving as a "structural bridge"[58] from the rhombohedral to tetragonal phase. Some authors report a second, M_C, monoclinic phase which exists in the Ti composition range of ~37-47% prior to stabilization of the tetragonal phase.[59] From the monoclinic phase, additional Ti content stabilizes the tetragonal P4mm perovskite structure (analogous to that of $PbTiO_3$) below T_C.[59,60] Furthermore, the rhombohedral to tetragonal phase transition on increasing Ti content is nearly temperature independent, making it a morphotropic phase boundary (MPB), as seen in the PMN-PT phase diagram in Figure 2-2.[61]

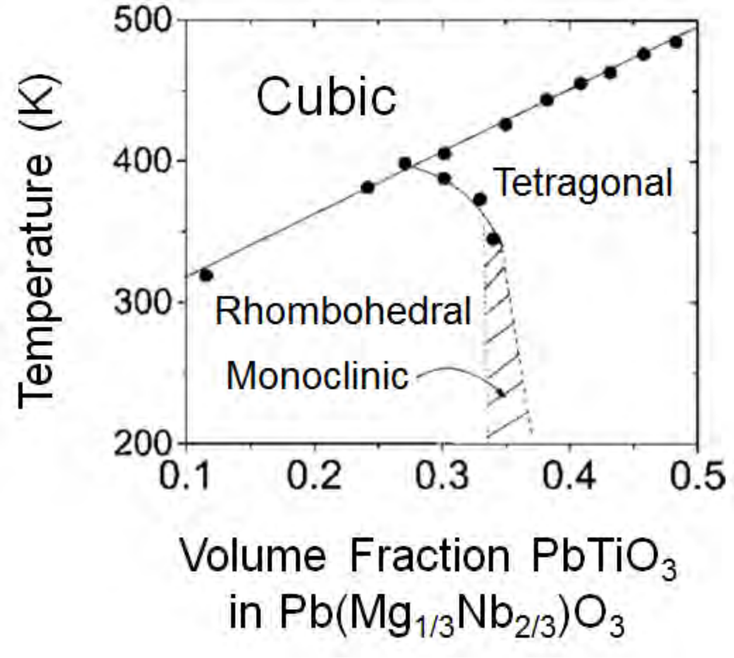

Figure 2-2: (1-x)$Pb(Mg_{1/3}Nb_{2/3})O_3$-x$PbTiO_3$ phase diagram, adapted from Shrout *et al.,*[62] Ye *et al.,*[61] and Choi *et al.*[63]

Ferroelectric compositions near a MPB offer considerably enhanced functional properties, as the relative energy barriers separating allowed polarization states are lowered, allowing for improved dipole alignment to a given applied field.[64] Typically, the polarizability rises as well.[64,65] The most widely utilized MPB composition for commercial piezoelectric applications is $Pb(Zr_{0.52}Ti_{0.48})O_3$ (or 52/48 PZT). Figure 2-3 depicts the enhancement of d_{33} as a function of $PbTiO_3$ composition for end members of $PbZrO_3$ and the relaxor PMN.[64,66] The piezoelectric coefficient d_{33} as a function of $PbTiO_3$ in PMN exhibits two local maxima near the MPB composition from the R → M and M → T transitions. Further $PbTiO_3$ addition yields the M→T transition and a second (lesser) d_{33} maximum[66].

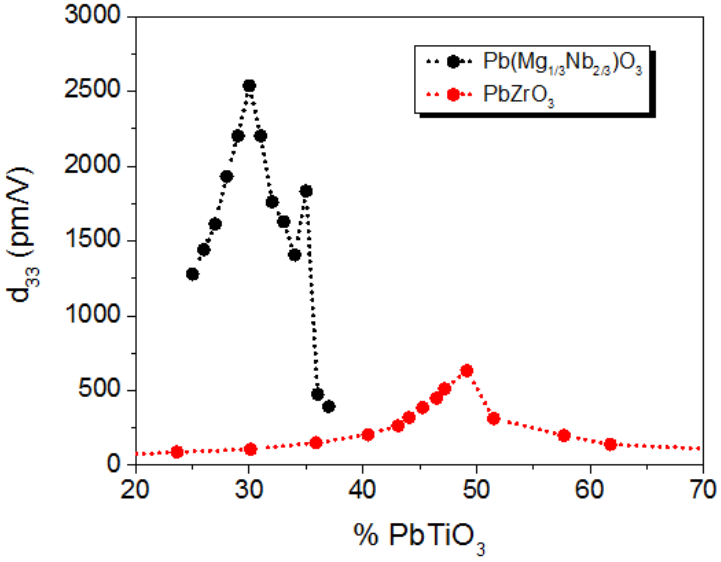

Figure 2-3: The piezoelectric coefficient, d_{33}, as a function of $PbTiO_3$ content in $PbZrO_3$ (from Jaffe *et al.*[64]) and $Pb(Mg_{1/3}Nb_{2/3})O_3$ (from Li *et al.*[66]).

Domain engineering and crystal orientation can further enhance functional properties in 70PMN-30PT. For example, the dipole in a rhombohedral 70PMN-30PT unit cell lies along the <111> direction. An ideal single crystal oriented with [001] out-of-plane has four energetically degenerate polarization states with “up” component, and four degenerate polarization states with a “down” component. Application of an electric field along the [001] poling direction can switch downward pointing polarizations upward to align to the field and increase the magnitude of the polarization in already aligned domains. The resulting domain structure is referred to as a 4R engineered domain configuration and gives rise to property enhancement related to the collective rotation of the four polar states. This behavior is called “polarization rotation” and is postulated as one of the main mechanisms contributing to the anomalously large piezoelectric response of PMN-PT and similar relaxor-ferroelectrics.[60,67] The "rotation" mechanism itself is interpreted in a number of ways in the literature, involving stable intermediate,[61,68] metastable,[69–72] or "adaptive"[73,74] monoclinic phase formation as a pathway for <111>$_{PC}$ → <001> aligned polarization. Due to the low energy barriers separating polar phases near the MPB, first principle calculations predict,[32] and experiment shows,[29] that the <111> polarization can transition fully to align along the <001> direction with adequate field along that direction with the lowest energy pathway of rotation being within the {110} planes.[67] A schematic representation of the polarization rotation mechanism is presented with the experimentally obtained strain vs. field data for a 0.92Pb($Zn_{1/3}Nb_{2/3}$)O_3-0.08PbTiO_3, by Park *et al.*[60] are shown in Figure 2-4.

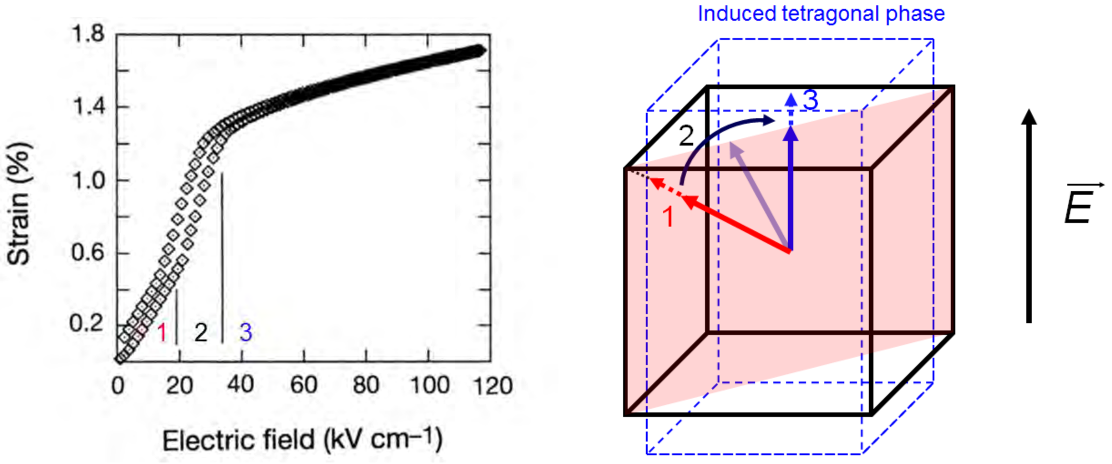

Figure 2-4: The electric field induced strain of a 0.92Pb($Zn_{1/3}Nb_{2/3}$)O_3-0.08PbTiO_3 crystal, reported by Park *et al.*[60] The regions marked 1 through 3 are correlated with the schematic of the polarization direction as a function of field in an {001} oriented unit cell. In region 1, the rhombohedral exhibits increased displacement along <111>. In region 2, due to the relatively flat nature of the free energy profile separating rhombohedral and tetragonal phases,[75] the <111> polarization rotates along the (110) plane towards the [001] direction, giving the largest slope in strain vs. field, or d_{33}. Finally, in region 3, the tetragonal phase is induced.

2.2 Substrate clamping

The anomalously high piezoelectric coefficient and dielectric permittivity offered by relaxor-ferroelectric crystals and textured ceramics are appealing to applications requiring thin film geometries as well as those bulk devices discussed above. Numerous processing techniques have been developed to grow such complex oxides in film form with crystallinity varying from epitaxial to polycrystalline, in tensile and compressive stress states, and with random or crystallographically aligned orientation.[76,77] In all cases, the magnitudes of the functional properties reduce about an order of magnitude as compared to bulk single crystal values. This reduction is due to a phenomenon known as substrate clamping.[78] Consider the simple case of a thin piezoelectric film grown on a Si substrate with a bottom Pt electrode with top electrodes sputtered onto the top film surface of the film (Figure 2-5: Schematic piezoelectric actuation of material beneath an isolated top Pt electrode. The frustrated lateral contration due to bonds with the substrate and unactuated material limits the out-of-plane response.Figure 2-5). For a voltage applied across the film thickness, the piezoelectrically-induced strain scales with the material's d_{33} coefficient. In perovskite materials such as PMN-PT, as the film expands out-of-plane, it contracts in-plane due to the d_{31} coefficient. Because the blanket film is bonded to the underlying substrate, the lateral contraction is frustrated, thereby reducing the out-of-plane strain and the effective d_{33} coefficient, or $d_{33,\ eff.}$ Additionally, the actuated material under the top electrode (typically deposited as an isolated array) is bonded to non-actuated material, further restricting its lateral contraction.

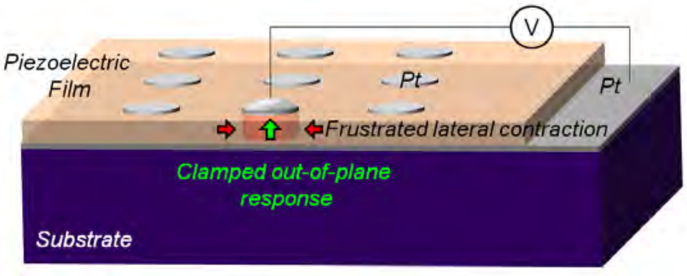

Figure 2-5: Schematic piezoelectric actuation of material beneath an isolated top Pt electrode. The frustrated lateral contration due to bonds with the substrate and unactuated material limits the out-of-plane response.

The “substrate clamping” nomenclature was carried over from bulk studies on the piezoelectric coefficients of materials in zero-strain, or clamped, systems to describe the reduction in properties observed in thin films.[79,80] In 1994, Lefki and Dormans published a method to predict the effective clamped piezoelectric coefficient ($d_{33,f}$) of thin films from the unclamped d_{33} value, the mechanical compliances of the piezoelectric films (s_{13}, s_{12}, and s_{11}), the transverse piezoelectric coefficient (d_{31}), as shown in Equation 2-1, under the assumption of zero in-plane strain.[79]

$$d_{33,f} = d_{33} - \frac{2d_{31}s_{13}^{E}}{s_{11}^{E}+s_{12}^{E}} \qquad \text{Equation 2-1}$$

In addition to substrate clamping, other mechanisms can also reduce the functional properties of thin films. For example, in 52/48 PZT ceramics about 70%[81–83] of the relative permittivity comes from extrinsic contributions (primarily domain wall motion). Domain wall motion, especially of non-180° domain walls[84,85] is often strongly clamped in thin films. Furthermore, given the ferroelastic nature of many ferroelectrics, Theis and Schlom demonstrated that bonding of the film and substrate may elastically reduce domain wall motion in highly crystalline, epitaxial films as well.[86] They showed that if the piezoelectric film is sufficiently thin and of high crystalline quality, well-defined strain values can be imposed on the film with magnitudes and sign determined by the difference in lattice parameter of the film and substrate. The difference in lattice parameter is an important factor in determining the maximum critical thickness to which the film may be grown before stress relieving dislocations form through the thickness of the lattice.[77] Such films are typically grown via techniques such as molecular beam epitaxy and pulsed laser deposition.[76]

Highly scalable growth techniques, such as sputtering and chemical solution deposition, are likely to have a higher concentration of defects such as dislocations which relieve lattice stress. Moreover, they are often used to grow thicker relaxed films. In relaxed films, the stresses that develop from thermal expansion mismatch with the underlying substrate are more important than growth stresses. As materials cool, they strain a given amount determined by the coefficient of thermal expansion (CTE), or α. If the CTE of the substrate is difference from the film, as is seen in Figure 2-6, stress accumulates in the film until the Curie temperature is reached, where domain formation partially alleviates further stress development.[87,88] Thermal strain, ξ, in the film is given by Equation 2-2, where α is the thermal expansion coefficient, $T_{crystallization}$ is the highest temperature reached in the RTA during crystallization, and T_C is the Curie temperature. From this, Figure 2-7 depicts the calculated strain incurred in a (1-x)PMN-xPT film as a function of PT content, changing T_C. From the modulus of PMN-PT[89] it can be expected that a film on Si would be under ~500 MPa tensile stress. Tensile stress reduces the out-of-plane polarizability, resulting in a higher population of *a*-domains in tetragonal materials and reduced polarization in rhombohedral perovskites.[90] Compressive stresses, on the other hand, can yield more square polarization-electric field hysteresis loops with increased spontaneous out-of-plane polarization[90] which may be expected for a PMN-PT film grown on $SrTiO_3$.

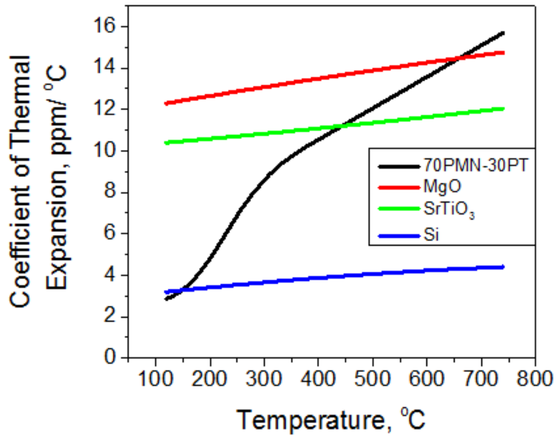

Figure 2-6: Thermal expansion coefficient for PMN-PT films and MgO, SrTiO$_3$, and Si substrates as a function of temperature.[91,92]

$$\xi = \int_{T_C}^{T_{crystallization}} [\alpha_{\text{sub}}(T) - \alpha_{film}(T)]\ dT \qquad \text{Equation 2-2}$$

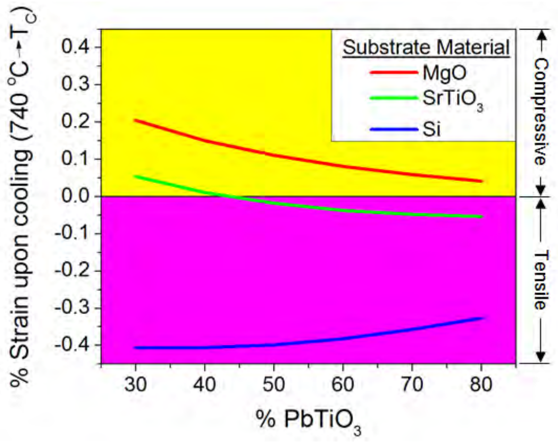

Figure 2-7: Calculated in-plane strain values due to thermal expansion mismatch for PMN-PT grown on various substrates as a function of PbTiO$_3$ content, which vary in T$_C$ and therefore the temperature range over which strain is accumulated.

2.3 Declamping

From Equation 2-1 it can be seen that a material that has high piezoelectric responses and is highly compliant is more sensitive to clamping, and hence more responsive when *declamped*. Several methodologies have been developed to declamp thin films, serving to increase both intrinsic and extrinsic contributions to the functional properties. Undercutting the substrate to form cantilevers or diaphragms is one means of reducing the constraints imposed by the substrate and partially declamping the film. The material property enhancements are dependent on the volume of substrate which is removed and whether the continuous diaphragm structure is broken to remove the global stress state of a film.[30,32] While substrate undercut can yield structure geometries well suited for some applications, the rigidity of the active part of the device is mostly lost. For applications where out-of-plane stiffness is necessary, a separate method of in-plane patterning can be utilized. This process yields isolated features with free sidewalls which both reduces the stress imposed by the substrate and partially relieves clamping effects.[36,93,94]

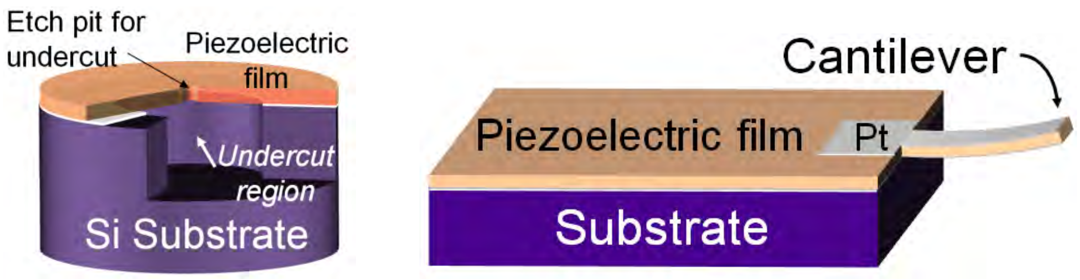

Figure 2-8: Schematics of partially declamped structures via substrate removal. On the left, a microfabricated diaphragm structure with substrate undercut in an isolated region beneath the film. On the right, a cantilever structure exhibiting bending from global stresses within film.

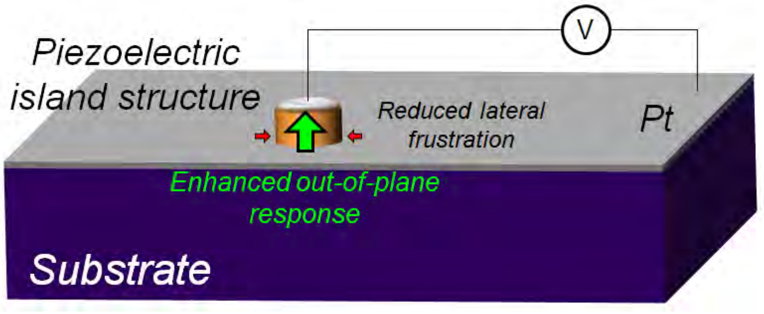

Figure 2-9: Schematic depicting a patterned island structure from a continuous piezoelectric film. With free sidewalls, the material is partially declamped, yielding enhanced properties while maintaining structural rigidity. In the limit of the thickness to width ratio going to zero, the material will attain single crystal responses.

2.4 Thin film patterning

Selective subtractive lateral subdivision of blanket films can be carried out via etching processes. Patterning to define the etching pattern is often done via lithography. In this process, a blanket film is spin coated with a photoresist layer. Depending on the polarity of the photoresist, high energy photons or electrons can either initiate crosslinking of the polymer chains (negative photoresist) or break the bonds that originally crosslinked the polymer chains (positive photoresist).[95] The light exposure can be done using a mask which covers desired areas of the photoresist during exposure. For lithography at feature resolution less than approximately 500 nm, an electron beam can be used to expose specific areas of the photoresist in a process called e-beam lithography. Following exposure, the photoresist-coated sample is submerged in a developing bath, typically a base or solvent, in which the non-crosslinked areas of the photoresist are soluble and wash off of the sample surface. The result is a film surface with selectively defined regions of polymer coating.

With the desired feature shapes covered with a lithographically defined mask, the film/substrate sample can be etched by either wet or dry processes. Wet chemical etch processes are isotopic in nature, etching any exposed material equally in all directions.[95] Similarly, there are numerous dry etching techniques to control etching directionality, repeatability, and pattern fidelity. [95–97]

It is instructive to consider a simple chamber setup, like the capacitively coupled plasma (CCP) system shown schematically in Figure 2-10. The CCP geometry is commonly used for plasma processing of thin films and was one of the geometries employed in this thesis. It is comprised of a gas inlet, a gas/byproduct outlet, a substrate holder, and electrodes to apply a bias at a desired frequency. The position and size of the electrodes is the key differentiating factor of the various etch chambers.[98] As seen in Figure 2-10, for a CCP system the substrate is placed on the drive electrode, with the ground positioned above it. To begin the etch process, gas is introduced into the chamber and an RF field is applied to the electrodes. In most etch systems the frequency is regulated to be 13.56 MHz.[99] In this frequency range, free electrons respond to the oscillating field, leading to collisions with gaseous species and ionization events. The heavier ions and molecules, however, are influenced very little by the AC field.[100] The applied bias to strike a plasma from a given gas chemistry should be greater than the breakdown potential of that gas, noting that $V_{\text{RF-breakdown}} < V_{\text{DC-breakdown}}$.[101] In ionization processes, more electrons are generated, creating an electron cascade to sustain the plasma at lower energy levels than are needed to initially form it.[101,102] To ensure maximum power transfer from the generator to the plasma, an external variable capacitor matches the input plasma impedance to the generator output impedance.[98,102] This impedance matching sets the net charge flow to both electrodes to zero per RF cycle. Because the drive electrode is much smaller in physical dimension, this zero current condition requires a negative charge be built up at the drive electrode.[98] This results in the DC offset of the drive electrode, which holds the target sample, from the potential of the plasma (V_P) which accelerates the positively charged ions from the plasma towards the sample surface to increase the etch rate and sidewall angle.[95,98,102,103]

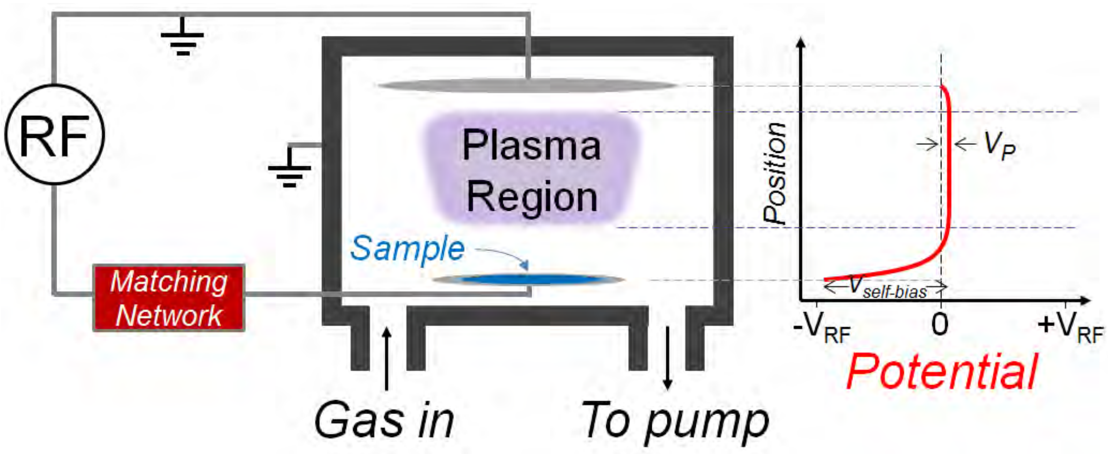

Figure 2-10: Schematic of a CCP system with time averaged and potential values for an RF reactor with different electrode sizes. Adapted from figures in Ref [[102]] and [[98]].

The chamber parameters dictate the way in which the reactive species interact with the sample surface. These interactions can be chemical or physical in nature, and are often a combination of both.[101] Physical etch processes remove matter from the sample via bombardment from the ions and radicals with high kinetic energy, ejecting atoms from the target. These processes are sensitive to the bond strengths and atomic structure in the sample rather than the enthalpy of formation of a given volatile sample/ion byproduct.[95,101] In contrast, chemical etching, which is based on the reactivity of the constituent atoms and radicals within the sample and the plasma, is highly selective.[96] If regions exposed to the plasma differ in composition they will etch at very different rates. This is desirable for stopping an etch process at a given layer in a stack, for example. One drawback of chemical etching, however, is that it occurs isotropically, limiting pattern fidelity. For this reason, ions and radicals are often accelerated towards the target, imparting a physical bombardment component to their interactions with the sample surface.

Limitations of CCP systems are linked to the relatively low particle density within their plasmas and high operating pressures.[99] The particle density is directly related to the ion energy through the RF power, making it difficult to decouple the chemical and physical components of the etch. Additionally, the chamber pressure must be above ~5 mTorr to sustain a plasma. Operation at higher operating pressures reduces the energy of incoming ions and broadens the impingement angle on the film surface due to increased occurrence of collisions, making vertical sidewalls very difficult to obtain.

Inductively coupled plasma (ICP) systems offer a different method of plasma processing which enables lower operating pressures, increased particle density and uniformity, and additional means of controlling ion bombardment with a substrate bias in kHz regime operating separate from the plasma bias. In an ICP system, gas is flowed into the chamber and an RF voltage is applied to a coil electrode above the substrate in either a cylindrical or planar geometry, as shown in Figure 2-11. The plasma is initiated and the ion-producing electrons are coupled with the induced magnetic field, improving plasma density and uniformity.[95]

Improved control over plasma density, uniformity, and ion energy has facilitated the development of more advanced RIE patterning techniques, such as sidewall passivation, to further improve sidewall angles and selectivity. Sidewall passivation entails use of specific gas chemistries that will form a protective polymer-type coating to protect against isotropic etching via chemical processes. The passivation chemistry is typically fed intermittently to the chamber between etching steps and is removed by ion bombardment and oxygen ashing at the bottom of the etch trench.[104]

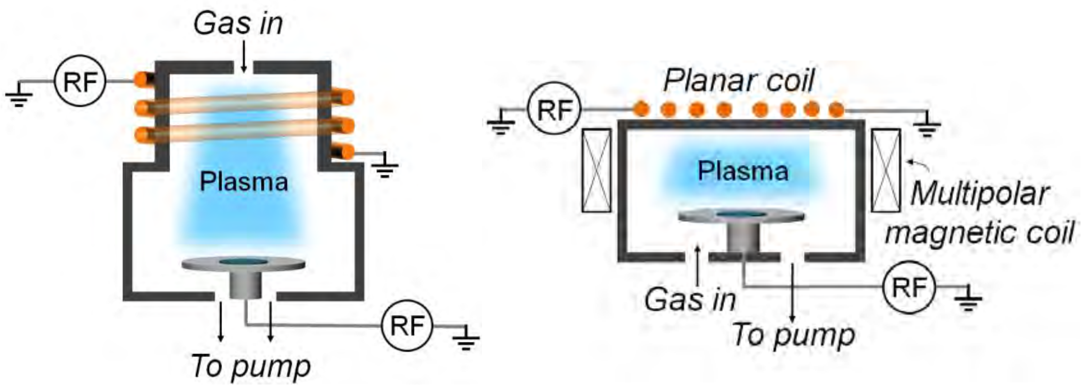

Figure 2-11: Schematic cross-sections of a cylindrical coil (left) and planar coil (right) ICP systems. Adapted from Ref. [102].

ICP systems and modern CCP systems also enable the tuning of the relative physical and chemical components of an etch process. The increased vertical directionality of the reactive species increases the sidewall angles in the patterned features.[96,102] This is important for several technologies including FeRAM, which requires more vertical sidewalls to reduce pitch from one capacitor to another, hence increasing storage density. Additionally, etch rate is increased while maintaining selectivity. The trade-offs of sidewall angle, selectivity, etch rate, and sidewall damage are determined by the chamber configuration and process parameters.

The above discussion of etching processes describes the ideal case of removing material from a target in a stoichiometric and controllable fashion. Furthermore, many of the conclusions about ion energy, plasma characteristics, reactions and selectivity stem from microfabrication literature focusing on Si and Si related materials.[95,105] There are well known chemistries and processes which yield vertical sidewalls with exceptionally high aspect ratios for Si.

Complications develop, however, for the patterning of complex oxides, for which degradation in crystallinity or stoichiometry affects the functional responses of the material.[105,106] The implications of the point defects and amorphous material which can be generated via patterning processes are discussed in detail in Chapter 5 of this thesis. The domain wall motion through a ferroelectric lattice can be reversible or irreversible in nature.[64] The nature and extent of the domain wall motion is heavily influenced by the crystallographic terrain through which the domain wall traverses. Defects in the lattice can pin a domain wall, thereby limiting the field induced polarization or strain.[107] If significant populations of defects form during patterning, the functional properties would be expected to degrade, rather than improve due to declamping, on lateral scaling.[108]

2.5 Size effects

(Parts of this section appear in J. F. Ihlefeld, D. T. Harris, R. Keech, J. L. Jones, J.-P. Maria, S. Trolier-McKinstry, "Scaling Effects in Perovskite Ferroelectrics: Fundamental Limits and Process-Structure-Property Relations," Journal of the American Ceramic Society, 2016)

The dimensionality of ferroelectrics is relevant in a much broader scope than solely the transition from bulk ceramic to thin film and the accompanying reduction in properties known as substrate clamping. For any given material geometry, from free bulk materials to dimensionally confined films, wires, and nanodots, size effects can be observed. Indeed, ferroelectricity is a collective phonon mediated phenomenon, requiring at least 3 unit cells of thickness for stability.[109,110] From this fundamental size limit, reductions in ferroelectric distortions are observed in materials with dimensions in the tens of nanometers length scale.[111] In addition to these intrinsic size effects, however, is the size dependence of properties observed at the tens of nanometers through tens of microns length scales. These effects are not inherent to the ferroelectric stability, but are rather induced by changes in factors such as domain wall configuration, domain wall mobility, and defects as a function of sample thickness or grain size.

For example, Figure 2-12 depicts changes in d_{33} of MPB composition PZT ceramics and thin films as a function of grain size. In addition to the large change in d_{33} due to substrate clamping, both the film and bulk ceramic exhibit grain size dependence in d_{33}. Grain size has similarly been reported to influence the properties in relaxor-based ferroelectrics including pure and La-modified PMN-PT.[112–114]

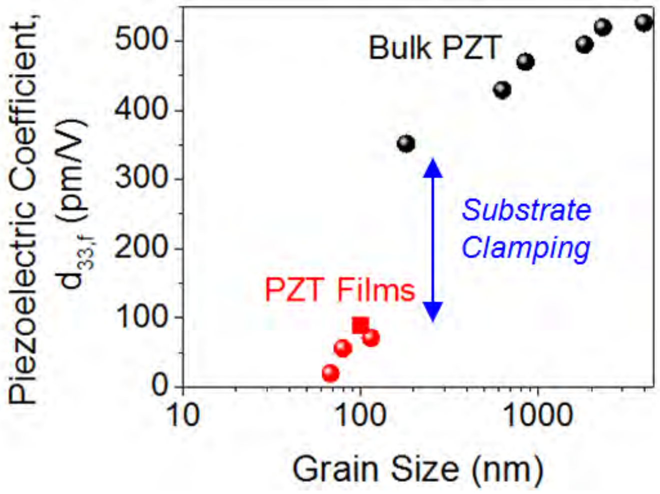

Figure 2-12: Grain size dependence of the d_{33} piezoelectric coefficient of bulk and thin film PZT at the MPB composition of 52/48. Both material geometries exhibit grain size dependence in addition to a factor of ~4x factor change upon confining PZT in thin film form. Bulk Nb-doped PZT data are from Randall *et al.*,[115] while the thin film data come from Bastani *et al.* (spheres)[116] and Xu *et al.* (square).[84]

The grain size dependence observed in various ferroelectric materials, such as PZT[115] and $BaTiO_3$,[117,118] has been found to induce changes in domain configuration.[119–121] Many studies on the grain size dependence of $BaTiO_3$ ceramics, for example, elucidate the mechanisms at play upon grain size scaling.[117,119–122] Typically, for dense $BaTiO_3$, the room temperature relative permittivity essentially saturates at ~1700 with grain sizes > 10 µm.[117] The relative permittivity increases with decreasing grain size until a peak is observed for a grain size of about 1 µm, as seen in Figure 2-13. As the grain size changes, so does the domain size, as noted by Kinoshita[122] and Arlt.[117] In particular, Arlt reported that the domain size $\propto$ (grain size)$^{1/2}$.[117] Cao and Randall *et al.* found the same dependence in PZT ceramics.[115,123] With that, it follows that reduced grain sizes yield increased potential for extrinsic contributions to functional properties.[117,124] Wada *et al.* further supported that domain size is the controlling mechanism of the property enhancement by measuring increased permittivity and piezoelectric coefficients in poled $BaTiO_3$ single crystals with decreasing domain size.[125]

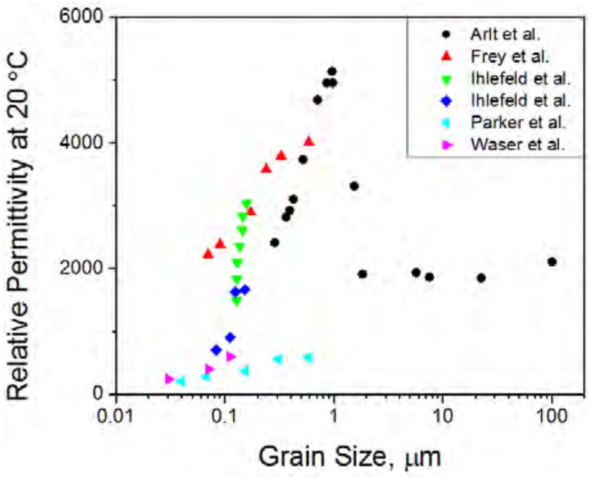

Reference	$BaTiO_3$ Morphology
Arlt *et al.* [117]	Ceramic
Frey *et al.*[126]	Ceramic
Ihlefeld *et al.* [127] ($BaTiO_3$ with barium borate)	Thin film
Ihlefeld *et al.*[128]	Thin Film
Parker *et al.*[129]	Thin film
Waser [130]	Ceramic

Figure 2-13: Relative permittivity as a function of average grain size at room temperature for various reported $BaTiO_3$ ceramics and thin films (Adapted from Ihlefeld *et al.*[127] with additional data from Arlt *et al.*[117], Frey *et al.*[126], Ihlefeld *et al.*[128], Parker *et al.*[129], and Waser[130].)

For the reasons given above, it may seem surprising that the relative permittivity then reduces with grain size reduction below 1 µm. There are several explanations for this, however. It was recently shown by in-situ, high-energy x-ray diffraction that reduction of the grain size below 1 µm actually lowers the mobility and/or the density of 90° domain walls, and hence extrinsic contributions to the functional properties.[131,132] Moreover, submicron grains in $BaTiO_3$ ceramics exhibit reduced unit cell tetragonality[117] as well as decreased complexity of domain structures and their stable variants.[123,133,134] In this case, because domain walls move collectively, limited twin configurations in a given grain could clamp the movement of domain walls in adjacent grains. Domain wall displacement and nucleation of new domains become more difficult under application of electric fields as grain size is reduced towards the dimension of a single domain.[131,135–137]

These results point to the significance grain boundaries can have in pinning domain walls from moving through a crystal lattice in response to an electric field or mechanical force. Grain boundaries, by definition, are regions which separate two distinctly different crystal orientations or structures. There is a finite width, therefore, of material which may not be ferroelectric or crystalline at all. The role of grain boundaries can be described, at least in part, by a “brick-wall” model. For a diphasic microstructure of high permittivity ($\varepsilon_r \approx 4600$) grains with thin low permittivity ($\varepsilon_r \approx 130$) grain boundaries, the grain boundaries account for reduced permittivity via a dilution effect in ceramics with grains sizes down to 40 nm in bulk $BaTiO_3$.[126]

Figure 2-12 shows that grain size dependence persists in thin films as well. This grain size dependence has been coupled to film thickness in numerous materials, with thinner films having smaller grains. The discussion of grain size dependence in films follows that of bulk ceramics in that the domain configuration is strongly dependent on grain size. In films however, the grain size tends to be only in the 50-250 nm length scale. In this regime, the domain wall pinning characteristics of the grain boundary have significant influence over the global response. Several groups have employed piezoresponse force microscopy (PFM) to quantify changes in piezoelectric coefficients near grain boundaries with controlled misorientation to one another. PFM data recorded across a 24° crystallographic tilt about [001] in bismuth ferrite demonstrated that grain boundaries can attract nearby domain walls and restrict the growth of the energetically preferred polarization direction.[138] Local electric and strain fields at grain boundaries were also reported to control the local domain structure and domain wall mobility in PZT thin films. In this case, it was demonstrated that the magnitude of the domain wall contributions to the piezoelectric properties is a function of the tilt and twist angles between the adjacent grains. Small angle grain boundaries (~10° for $PbZr_{0.52}Ti_{0.48}O_3$) provide local fields which can be significantly smaller than the drive field. As a result, the domain structure can readily be changed, and local *enhancement* of irreversible motion of domain walls can be observed. In contrast, larger grain boundary angles act as stronger pinning sites.[139] The spatial extent of a grain boundary on the pinning of domain walls is a complex function of the ferroelectric distortion, domain variants and the strain energy in a given material. Reduction in the piezoelectric activity with respect to the grain average from 24° tilt grain boundary in PZT, for example, was observed ~800 ±70 nm away from the boundary itself in tetragonal 45/55 PZT and only half that distance (450 ± 30 nm) for MPB composition 52/48 PZT.[140] This is likely to be due to the fact that the more complex domain structure possible at the morphotropic phase boundary means that local stresses and fields can be accommodated in a smaller volume.[141,142] The large length scale associated with the grain boundary influence explains why size effects are frequently observed at length scales that are orders of magnitude larger than those associated with loss of ferroelectricity. The discussion of size effects in thin films requires the added consideration of film thickness. Indeed, the grain size typically reduces with decreasing thickness in films, making this aspect of the pinning density a function of thickness. Reductions in the dimensionality of grain size or thickness have shown to reduce peak properties near transition temperatures in ferroelectric materials and broaden the shape of the peak as well.[115,143–146]

Additionally, as thickness decreases, there is change in the ratio of atoms at/near interfaces as compared to bulk ceramics. Part of the property suppression at these thicknesses comes from surface layers of finite thickness which exhibit different responses from the bulk of the film. To show that it's not the absolute surface/bulk ratio dominating the property suppression in films of hundreds of nanometers in thickness, Chang *et al.* thinned $SrTiO_3$ and $BaTiO_3$ single crystals to 300 nm and deposited Pt electrodes. The thinned $BaTiO_3$ crystals exhibited relative permittivity behavior as a function of temperature which matched the bulk crystal.[147] Similar results were observed in thinned $BaTiO_3$ crystals of only 75 nm thickness.[148] The thinned $SrTiO_3$ crystals of Chang's work, however, did show suppressed ε_r from what is observed in thicker crystals. The difference between the two cases is attributed to the specific nature of the electrode/ferroelectric bonding and electronic properties which have increased significance at reduced thicknesses.[147,149] These results demonstrate that bulk like responses can be engineered through careful sample preparation. Films grown from more scalable techniques often possess interface layers of higher defect densities. The result is a series capacitor structure of dead layers and crystalline layers of high response which decreases the global response.

To facilitate strongly scaled devices, the significance of thickness dependent properties should be well understood, predictable, repeatable, and minimized. PZT films have been utilized in piezoelectric MEMS systems for decades and their thickness dependence is fairly predictable,[116,150–153] although the underlying mechanisms are debated in the literature. The functionality of some piezoelectric MEMS systems and FeRAM applications would benefit from reduced operating voltages, increased device capacitance, and decreased switching speeds all while maintaining high relative permittivity, remanent polarization, or piezoelectric coefficients. Thickness scaling of the ferroelectric or substitution of the more commonly used PZT for PMN-PT could enable these design goals. Such a transition, however, requires the thickness scaling mechanisms of the relaxor-ferroelectric system be well understood.

Chapter 3

Synthesis and Characterization of {001}-Oriented 70/30 Lead Magnesium Niobate-Lead Titanate Thin Films

3.1 Introduction

Domain engineered {001} oriented lead magnesium niobate – lead titanate, or PMN-PT, single crystals[154] and textured ceramics[155–159] near the morphotropic phase boundary (MPB) composition are of interest for high-strain actuators.[60,160,161] {001} oriented materials on the rhombohedral side of the MPB exhibit anomalously high piezoelectric coefficients and provide high coupling coefficients due to a polarization rotation mechanism.[60,67] In the same way, there is a growing need for high strain piezoelectrics for microelectromechanical systems (MEMS) in highly scaled thin film and nanowire devices.[25,162] Growth of perovskite phase-pure, {001} oriented PMN-PT on silicon substrates, however, can be challenging due to the nucleation and growth on dissimilar bottom electrodes.[25,163] Additionally, the widely observed parasitic pyrochlore phases drastically reduce the functionality of PMN-PT films.[164,165] Therefore, a repeatable and highly scalable processing procedure is needed for phase-pure perovskite, {001}-oriented PMN-PT thin films. In this work, chemical solution deposition (CSD) was employed as a growth technique for PMN-PT films on platinized Si wafers and the role of Pb content in orientation control was studied.

During the crystallization of Pb-based ferroelectric films, it is important to maintain high crystallinity without inducing excessive tensile stresses which degrade the switchable polarization, piezoelectric, and pyroelectric responses,[78,166] as well as potentially causing cracks.[165,167] The local physical and chemical environment present during the nucleation of perovskite nuclei is a key to the determination of the crystallographic orientation of the lattice. For example, Muralt *et al.* showed that increased bottom electrode surface roughness results in the formation of randomly oriented grains from a process that would otherwise produce strongly {111} textured lead zirconate titanate (PZT) films.[168] Textured films, such as those shown in Muralt's work, are typically grown on a seed layer which lowers the nucleation energy associated with a given crystallographic orientation. For example, {111} oriented $PbTiO_3$ seed layers template the growth of {111} oriented PZT films. Such template layers enable reduced perovskite PZT nucleation temperature and thereby reduce tensile stresses associated with thermal expansion coefficient mismatch between the film and the substrate and increase the polarization response.[169,170] Additionally, rutile TiO_2 seed layers can also yield strongly {111} textured $PbTiO_3$ and PZT.[168,171]

There are numerous previous reports on approaches to grow {001}-oriented perovskite ferroelectric films, with varying ability to avoid off-textured material.[165,172–177] Lead-based perovskite thin films with strong {001} orientation have been grown on {001}-oriented $PbTiO_3$ seed layers batched with significant levels of excess Pb.[168,178–180] Bi-layer {001} seeds of $PbTiO_3$/PbO[165] and PZT/PbO[181] have also produced strongly {001}-oriented PMN-PT thin films with Lotgering factors of 0.94-0.97. However, buffer layers can be detrimental in some technologies. The relatively lower permittivity of $PbTiO_3$ or PZT seed layers electrically in series with PMN-PT causes a voltage drop across the seed layer, reducing the net piezoelectric coefficient. Such seed layers are particularly problematic in applications where sub-100 nm thick ferroelectric layers are required for reduced coercive voltages (piezoelectric transistor[25] and ferroelectric memory[38]).

It is clear that local Pb stoichiometry is a significant factor in determining the most favorable nuclei orientation in Pb based thin film ferroelectrics. The common technique of batching precursor chemical solutions with excess Pb can be effective for accommodating Pb loss to the atmosphere during high temperature crystallization. However, it is hypothesized that a key role of seed layers is associated with reducing the driving force for Pb diffusion out of the ferroelectric film and into the bottom electrode, as is commonly reported to occur.[182,183] The aim of this work is to demonstrate the growth of highly {001}-oriented PMN-PT films by management of Pb content, circumventing the need for a seed layer of another perovskite material.

3.2 Experimental procedure

To study the role of Pb content on orientation and microstructure of 70PMN-30PT films, separate solutions of 10 mol%, 15 mol%, and a 20mol% excess Pb were prepared. The solution preparation process began by dissolving magnesium ethoxide (98% pure) powder into a volume of 2-MOE that was ½ the volume of the target final solution. The mixture was stirred at 125 °C for 12 hours in a dry Ar atmosphere in a rotary evaporator system. Then, the remaining B-site cations of niobium ethoxide (99.95% pure) and titanium isopropoxide (97% pure) were added to the magnesium mixture with the addition of 2-MOE so that the volume of the B-site mixture was that of the final solution. The mixture was stirred for 6 hours at 120 °C in dry Ar. Lead acetate trihydrate (99.99% pure) was dissolved separately in 2-MOE at 120 °C for 30 minutes and subsequently vacuum distilled to a powder. The B-site cation solution was then added to the Pb powder with a volume of 2-MOE equal to the final solution volume. The mixture was stirred at 120 °C for 3 hours in Ar atmosphere before partial vacuum distillation to reduce the total volume to 87.5% of the total target volume. 22.5 vol. % of the stabilizing chelating agent acetylacetone was then added to the solution; this was subsequently mixed for 30 minutes at 100 °C under an Ar atmosphere. The resulting solution was 0.2 M $70Pb_{1+x}(Mg_{1/3}Nb_{2/3})O_3-30PbTiO_3$. Figure 3-1 and Table 3-1 depict the chemical solution preparation process and amounts of precursor material necessary for a 120 mL bath of 0.2 M 70PMN-30PT solution with 10% excess Pb.

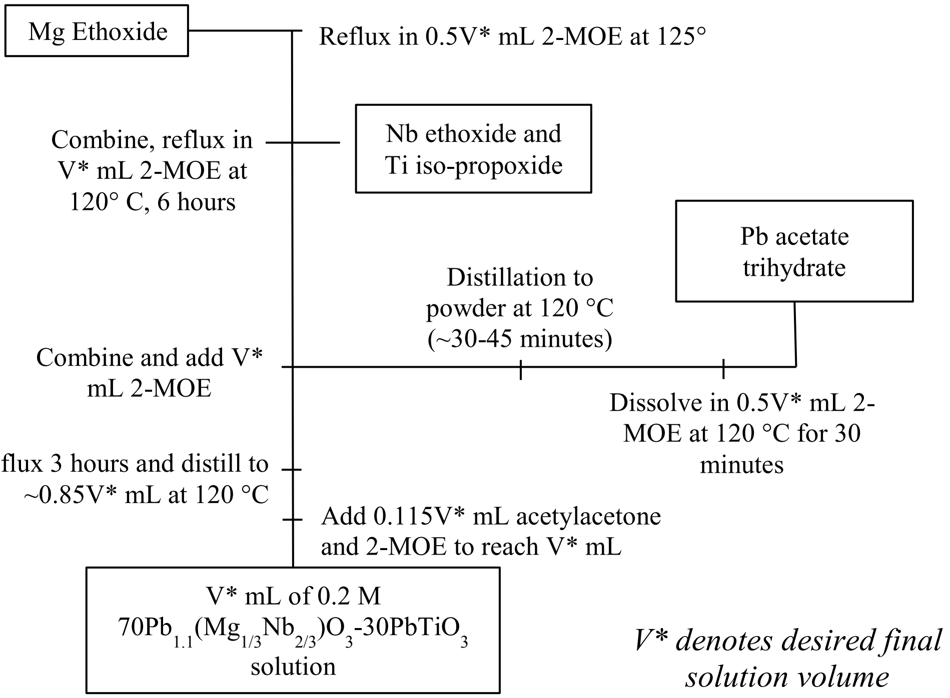

Figure 3-1: Chemical solution processing route for 0.4M 70PMN-30PT with 10% excess Pb.

Table 3-1: Precursor chemicals and their respective weights used to prepare 120 mL of 0.2 M 70PMN-30PT solution with 10% excess Pb with respect to stoichiometry

	Pb II Acetate Trihydrate	**Mg Ethoxide**	**Nb Ethoxide**	**Ti Isopropoxide**
Molecular Wt. (g/mole)	379.34	114.43	318.21	293.05
Molar Factor	1.1	$0.7 * \frac{1}{3}$	$0.7 * \frac{2}{3}$	0.3
Moles	0.0264	0.0056	0.0112	0.0072
Grams	**10.015**	**0.64081**	**3.5640**	**2.1100**

The 70PMN-30PT solutions, varying in excess Pb content, were loaded into separate syringes equipped with a 0.1 μm Whatman filter (GE Healthcare Life Sciences, Pittsburgh, PA).

A 150 nm Pt/30 nm Ti/1 μm SiO_2/550 μm Si substrate, from Nova Electronic Materials (Flower Mound, TX), was centered on a vacuum spin chuck. The platinum on these substrates was {111} oriented. The solution was dispensed onto the substrate and spun at 3000 rpm for 45 seconds. During the spin process, the wafer is evenly coated (within 1-2%), excess solution is cast-off, and some of the solvent evaporates from the cast layer.[184] Following spin casting, the films were dried at 250 °C for 1 minute and pyrolyzed at 425 °C for 5 minutes on hot plates in air. These pyrolysis conditions were determined to yield the most structurally collapsed amorphous layer prior to crystallization by contact profilometry, as seen in Figure 3-2, a prerequisite to achieve dense crystalline films.[185] For second-step pyrolysis temperatures less than 425 °C, Figure 3-2 also shows that the first pyrolysis, or drying step, has significant influence on the final amorphous film thickness. The first pyrolysis step should be at temperatures greater than 250 °C in these cases. As the second pyrolysis temperature is increased above 425 °C, the final collapsed film thickness converges to 1500-1750 Å for films with a first pyrolysis temperature of 225 °C or greater. In these PMN-PT films, it was found that using a pyrolysis temperature above 450 °C, although yielding the most dense films prior to crystallization, can also cause nucleation of low temperature or Ti-rich pyrochlore grains which disrupt orientation upon crystallization of the film.

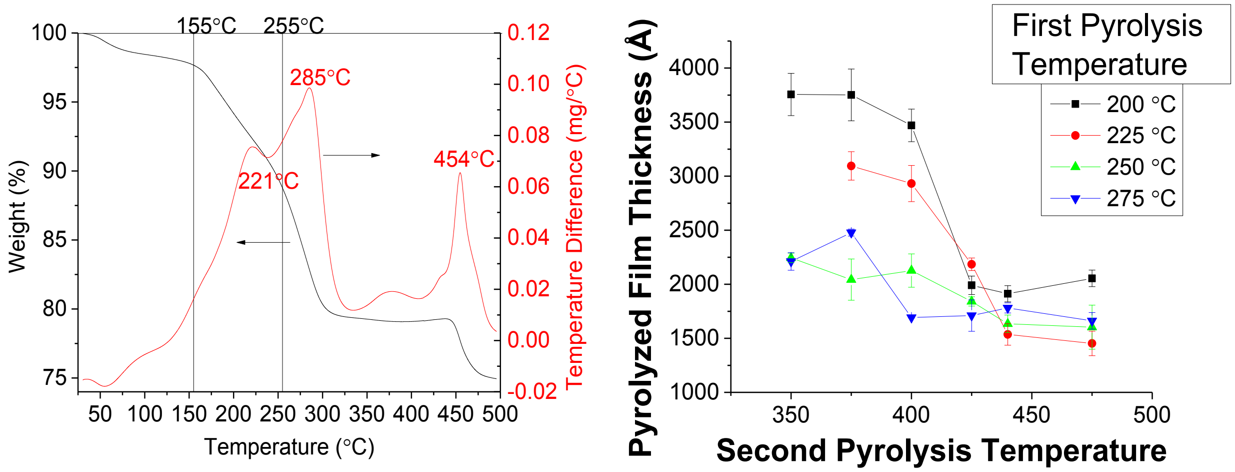

Figure 3-2: Left: Thermogravimetric analysis of a PMN-PT powder derived from a drying a PMN-PT precursor solution at room temperature. Right: Film thickness following the second pyrolysis step as a function of the second pyrolysis temperature for films with varying initial pyrolysis temperatures.[185]

In addition to the solutions of varying Pb content deposited directly onto the Pt substrate, a film batched with 10mol% excess Pb was prepared on a PbO buffer layer. The buffer layer was 2-3 nm thick PbO buffer layer, measured by contact profilometry (KLA-Tencor P16+, Milpitas, California) following a 250 °C/2 min. and 400 °C/10 min. pyrolysis sequence. Following the PbO pyrolysis, the 10 mol% excess Pb was deposited under the conditions described above.

Crystallization of the PMN-PT was done layer-by-layer with the first layer crystallized at 740 °C for 1 minute to nucleate the perovskite structure. Subsequent layers were crystallized at 720 °C to minimize thermally induced stresses. Crystallization was performed in a rapid thermal annealing furnace with ramp rates of +50 °C/sec and -5 °C/s. The deposition, pyrolysis, and crystallization procedure was repeated to build up the desired thickness of 300 nm, and is summarized in Figure 3-3.

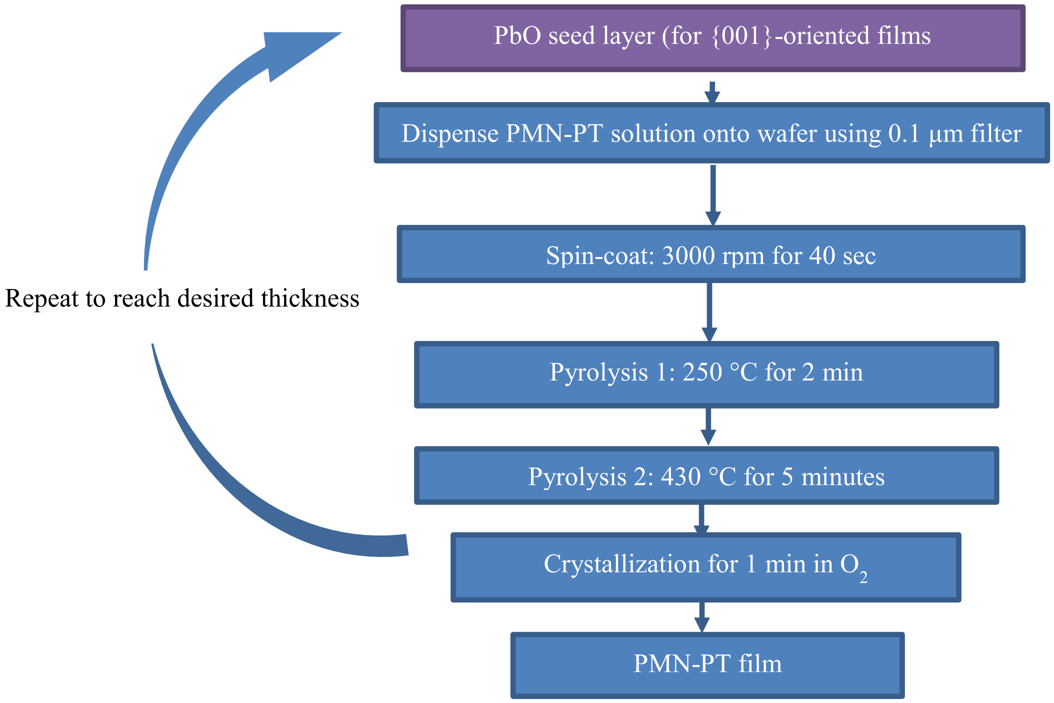

Figure 3-4: Process flow for PMN-PT thin film grown via chemical solution deposition.

Following the growth of the PMN-PT films, the crystalline structure and volume fractions of relevant phases (accurate to a few volume percent) was investigated by X-ray diffraction (XRD) in a θ-2θ arrangement using a PANalytical Empyrean x-ray diffractometer (PANalytical B.V., Almelo, The Netherlands). Lotgering factors were used to approximate the degree of orientation of the films.[186] An in-lens secondary electron detector in a field emission scanning electron microscope (Leo 1530 FESEM, Carl Zeiss Microscopy GmbH, Jena, Germany) was employed to compare the resulting microstructures. 100 nm thick platinum top electrodes were sputter deposited via a lift-off procedure for dielectric property characterization. The measurements were made at room temperature on 200 µm diameter Pt electrodes with a small 30 mV_{ac} signal at 1 kHz with an HP 4248A precision LCR meter (Agilent Technology, Palo Alto, CA).

The relative atomic composition of the films at the interfaces, which plays an important role in the texture development of nuclei, was investigated using a FEI Titan3 dual aberration corrected scanning/TEM (S/TEM) instrument operated at 200 kV. The TEM specimens were prepared by *in situ* milling and coupon lift-out procedure in a FEI Helios NanoLab DualBeam 660 focused ion beam (FIB). Prior to milling, a thick protective amorphous carbon layer was deposited over the region of interest by electron beam deposition. The FIB-TEM membrane was fabricated with a starting milling voltage of 30 kV and then stepped down to 2 kV to minimize sidewall damage and thin the specimen to electron transparency. A SuperX Energy Dispersive Spectrometry (EDS) system, integrated with the TEM instrument, was employed for elemental mapping with EDS in STEM mode. This transmission electron microscopy work was performed in the Materials Characterization Laboratory at the Pennsylvania State University by Ke Wang.

Top Pt electrodes were patterned for electrical characterization via a lift-off procedure. The lift-off procedure began with dynamic spin casting of SPR LOR5A photoresist with a final spin speed of 4000 rpm for 40 seconds and a bake time of 1 minute at 180 °C. On this layer, the positive photoresist SPR 3012 was spin deposited under the same conditions and baked for 1 minute at 95 °C. A Karl Suss MABA6 contact aligner (SUSS MicroTec Inc. Sunnyvale, CA) was used to expose the photoresist coated wafer to a 365 nm Hg I-line lamp with an exposure power density of 8 mW/cm^2 for 10 seconds. The resists were developed in CD-26 (Rohm and Haas Electronic Materials LLC, Marlborough, MA) for 1 minute, then the samples were DI water rinsed and blown dry with nitrogen. Platinum top electrodes were deposited via RF magnetron sputtering in a Kurt Lesker CMS-18 deposition system (Kurt J. Lesker Co., Clairton, PA) at room temperature to 100 nm in thickness.

Characterization of the ac-field and frequency dependence of the relative dielectric permittivity and loss tangent was performed using an HP 4248A precision LCR meter (Agilent Technology, Palo Alto, CA) at 1 kHz. The relative permittivity was calculated using Equation 3-1:

$$\varepsilon_r = \frac{Ct}{\varepsilon_0 A} \qquad \text{Equation 3-1}$$

C is the measured capacitance from the LCR meter (recorded with 30 mV ac signal at 1 kHz, unless otherwise noted), t is the PMN-PT film thickness, ε_0 is the permittivity of free space, and A is the area of the top electrode. Contact to the bottom and top electrodes was achieved though point probes on a Cascade Microtech probe station (Cascade Microtech Inc., Beaverton, Oregon 97008, USA) equipped with Penn State developed data acquisition software (GADD and Vision) to control temperature set points, ramp rate, and rest time. The stage area, contact probes, and microscope objective (for viewing contacts) were enclosed in an aluminum case which enabled the flow of nitrogen gas through the system to prevent H_2O condensation at temperatures < 0 °C. Prior to a temperature dependent experiment, the stage, sample, and probes were heated to 150 °C for 2 minutes to evaporate H_2O and hydroxyl groups from the sample and tip surfaces to avoid data artifacts associated with H_2O freezing, melting, and evaporation. The stage was then cooled and data were recorded upon heating.

Polarization-electric field (P-E) hysteresis loops were measured using a multiferroic tester (Radiant Technology, Inc. Albuquerque, NM) with point probe contacts as described above. Minor and major loops were recorded in the frequency range of 20 Hz – 100 kHz. To ensure de-aging effects were not included in the reported data, five P-E loops were recorded in sequence for a given set of measurement parameters with the 5th loop being reported (unless otherwise noted).

Characterization of the direct piezoelectric coefficient, $d_{33,\,eff}$, of the PMN-PT blanket films was performed using an aixACCT double-beam leaser interferometer (DBLI) (aixACCT Systems, Aachen, Germany). If the substrate of the film being measured was not double-side polished as received from the vendor (Nova Electronics Materials, Flower Mound, TX), the substrate backside was polished prior to DBLI measurement. In this procedure, the PMN-PT film surface was first coated in a photoresist and dried for protection during polishing. The photoresist-coated side of the sample (the top surface) was adhered to an aluminum block using Crystalbond (SPI Supplies / Structure Probe, Inc., West Chester, PA, USA). The backside of the Si substrate was then polished using Al_2O_3 slurry in steps of 30 µm, 15 µm, and 9 µm particle size on a glass plate and then diamond polished with 9 µm, 6 µm, 3 µm, 2 µm, 1 µm, and 0.5 µm slurry.

Samples were loaded onto the piece part stage of the DBLI and the brought into the pathway of the laser and the system was calibrated using aixACCT software. Large signal piezoelectric strain measurements were made at 100-1000 Hz on electrodes with diameters approximately equal to the thickness of the substrate (550 µm), to avoid inflation of $d_{33,f}$ in accordance with the findings of Sivaramakrishnan *et al.*[187] Small signal $d_{33,f}$measurements were performed using an AC signal amplitude of 0.5-1 V at 1 kHz over a triangular voltage sweep at 5 Hz to a maximum voltage amplitude of 5-15 V.

3.3 Results and discussion

3.3.1 Effects of Pb content

Figure 3-5 shows the x-ray diffraction patterns for PMN-PT films grown on Pt bottom electrodes from precursor solutions with 20%, 15%, and 10% excess Pb content as well as a 10% excess Pb solution deposited on a PbO buffer layer on Pt. Firstly, the perovskite volumes of the films are rhombohedral, with no visible peak splitting and d-spacing corresponding to the R3c space group of PMN-PT. This is in agreement with the structure predicted from the composition of the films. Several differences in phase and orientation are apparent as a function of Pb content in the grown films. Table 3-2 summarizes the phases detected by XRD, the Lotgering factors, and the dielectric properties of various films. The pyrochlore {202} peak at 29.2° 2θ is sharpest and of greatest relative intensity for the PMN-PT film grown directly on Pt from a 10% excess solution. Increasing the excess Pb content to 15% still yields pyrochlore peaks, although it is smaller in intensity relative to that of the film grown from the 10% excess solution. When grown directly on Pt films, phase-pure perovskite was obtained only from a 20% excess Pb solution. However, implementation of the thin PbO buffer layer reduced the driving force for Pb diffusion from the PMN-PT into the bottom electrode and provided enough Pb to the lattice to yield perovskite pure films from only a 10% excess Pb solution. It should also be noted that no PbO peaks were detected, suggesting the PbO buffer layer was incorporated into the PMN-PT lattice and Pt bottom electrode. The correlation between lead excess and pyrochlore content demonstrate that the pyrochlore phase is favored by lead deficiency.[188]

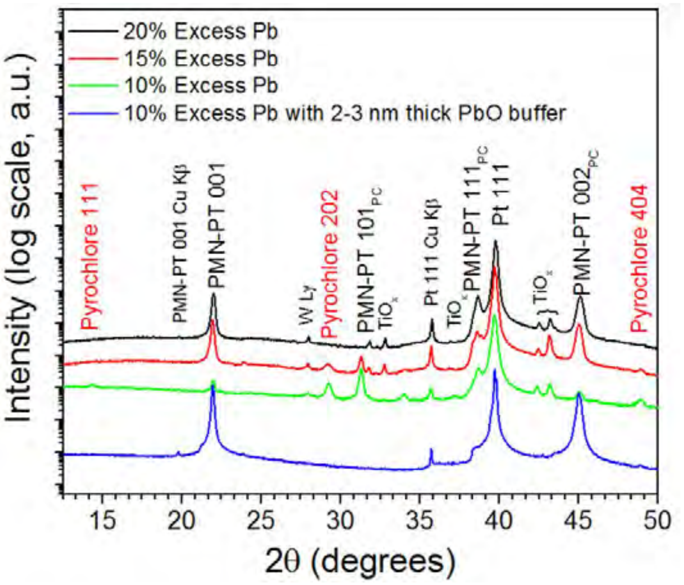

Figure 3-5: X-ray diffraction patterns of ~300 nm thick PMN-PT thin films grown from precursor solutions varying in excess Pb content from 10-20%. Additionally, the pattern for a film grown from a 10% excess Pb solution on a PbO buffer layer is shown.

Table 3-2: Summary of phases and crystalline orientations present in the chemical solution deposited PMN-PT thin films grown from varying excess Pb content solutions.

Percent Excess Pb	**20 mol%**	**15 mol%**	**10 mol%**	**10mol% + PbO buffer**
Pyrochlore detectable by XRD?	No	Yes	Yes	No
{001} Perovskite Lotgering Factor	0.56	0.65	-0.04	1
Relative Permittivity	1510 ±30	1420 ±40	1360 ±30	1710 ±15
Loss Tangent	0.013 ±0.002	0.022 ±0.003	0.028 ±0.003	0.008 ±0.001

Films grown from solutions with 15 mol% and 20 mol% excess Pb exhibit positive {001} Lotgering factors with some misoriented material. The film grown from a 10 mol% excess Pb solution showed preferential {101} and {111} texture, at the expense of the {001} orientation, yielding a negative {001} Lotgering factor. In contrast, a PbO buffer layer with a PMN-PT solution of 10 mol% excess Pb yielded phase-pure perovskite films, {001} Lotgering factors of 0.97-1.0, higher relative permittivity, and lower loss tangents. The significance of Pb stoichiometry to the dielectric properties is further noted in the reduced magnitude of ε_r in films with Pb-deficient pyrochlore phase. Films with such secondary phases exhibit lower ε_r than those observed in perovskite phase pure films of lesser {001}-orientation.

FESEM micrographs in Figure 3-6 show the microstructures of PMN-PT films grown from various precursor solutions. The film grown from a 10% excess Pb solution on a PbO buffer is dense and is comprised of grains that are 280 ± 20 nm in diameter. There is a small amount of surface pyrochlore visible on the film surface, likely caused by a slight Pb deficiency at the film surface upon reaching 300 nm in thickness via 12 crystallization steps, lessening the influence of the PbO buffer layer. Without the PbO buffer layer, the film grown from the 10% excess Pb solution developed a large volume fraction of pyrochlore grains between perovskite grains; the perovskite grain diameter increased to 440 ± 70 nm. Increased grain size with decreasing Pb content in the precursor solution implies that higher Pb content at a nucleation surface yields higher nucleation densities. Many pyrochlore grains are observed along perovskite grain boundaries and the Pb deficient phase occupies most of the triple point areas between perovskite grains in films grown directly on Pt from 10 mol% and 15 mol% excess Pb solutions. The 20 mol% excess Pb films exhibit high pore densities, rather than pyrochlore at the triple points. It is hypothesized that increased Pb volatilization from these regions of high surface area result in pore formation between the grains.

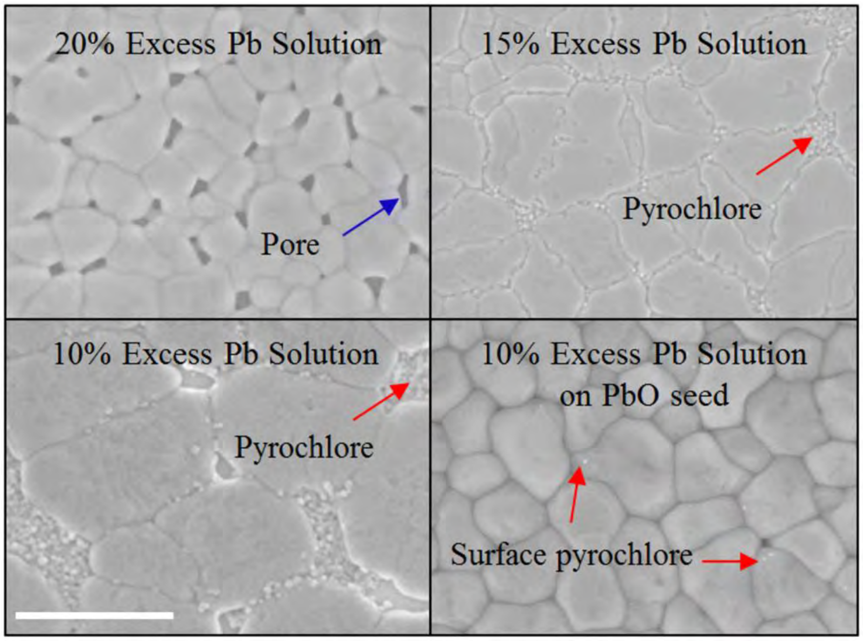

Figure 3-6: FESEM micrographs of ~300 nm thick PMN-PT film surfaces grown from precursor solutions with varying excess Pb content. Scale bar is 500 nm.

From the XRD patterns and FESEM micrographs, it is evident that Pb rich nucleation layers result in both improved perovskite phase purity and {001} textured growth of PMN-PT films. This point is corroborated and further quantified via energy dispersive spectroscopy (EDS) measurements performed across the film/electrode interface. The EDS plots shown in Figure 3-7 correspond to two films grown under the same processing conditions from a 10% excess Pb solution with and without a PbO buffer layer. The Ti content in the films is constant over the measured area, up to 12 nm away from the interface. Thus, differences in Pb content can be attributed to the presence of the PbO buffer, rather than error in EDS calibration.

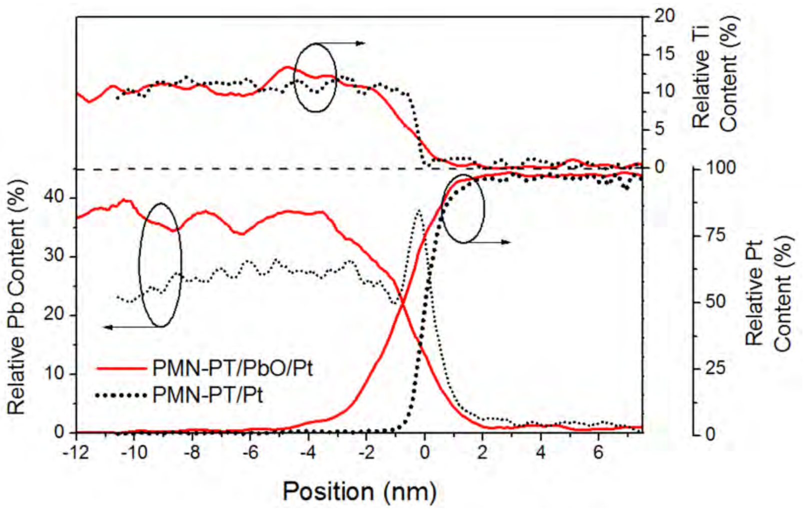

Figure 3-7: The relative Pb (left axis), Pt (lower right axis), and Ti (upper right axis) concentration measured across the bottom electrode interface for PMN-PT films grown directly on Pt (dotted black curves) and with a PbO buffer layer (solid red curves) as measured by energy dispersive spectroscopy.

From the EDS spectra, it is shown that the PbO buffer layer increases the local Pb content by 10%, providing a similar nucleation environment as is achieved with a 20% excess Pb solution without the buffer layer. This result suggests that as much as 10% of the local Pb content diffuses into the bottom electrode during crystallization. Additional features of interest in the EDS spectra are the shapes of the Pb profiles. The Pb content in the film without a buffer layer drops 5% within 1 nm of the interface with Pt, and rises 15% very near the interfacial region. This peak in Pb content at the interface further demonstrates the strong driving force for Pb diffusion into the Pt electrode, leaving behind a Pb deficient nucleation layer. This process likely also occurs in the films with a PbO buffer layer but the Pb diffusion is compensated by the excess Pb. As a result, the compositional gradients are broader in films with a PbO buffer, increasing the thickness of the interface, from ~3 to ~4.5 ±0.5 nm in this case. The precise thickness and properties of an interfacial layer is significant in determining the properties of the total capacitor,[153] but could potentially be tuned by adjusting the buffer layer deposition conditions.

3.3.2 Functional properties of {001}-oriented PMN-PT thin films on Si substrates

In the rhombohedral structure, which 70PMN-30PT assumes at room temperature, there are 8 degenerate domain variants with dipoles aligned along the <111> of a unit cell. Upon increasing temperature, the tetragonal phase is stabilized prior to the transition into the paraelectric phase at the Curie temperature (T_C). At T_C, the relative permittivity peaks sharply and there is little frequency dispersion in the dielectric.[189] Well poled 70PMN-30PT single crystals[62,190] and oriented ceramics[156] with {001} parallel to the electric field exhibit a second, lesser peak in relative permittivity at the rhombohedral to tetragonal (R-T) transition temperature, $T_{R\text{-}T}$, as well. However, structural imperfections including point defects, dislocations, grain boundaries, surface layers, and chemical heterogeneity can suppress the maximum relative permittivity, increase diffusivity of the ε_r peak, and yield a single maximum in relative permittivity.[156,159,191–193,114,194] In these cases, $T_{R\text{-}T}$ is often not resolvable due to the transition occurring at slightly different temperatures throughout the material.[159] Hence, T_{max} develops as a convolution of both $T_{R\text{-}T}$ and T_C.[167,192,195] This is widely observed in thin films which often have higher relative densities of the defect-related factors listed above than bulk ceramics do.[153,192,196]

Figure 3-8 shows the relative permittivity of unpoled 76PMN-26PT and 66PMN-34PT single crystals,[189] and a 350 nm thick {001}-oriented 70PMN-30PT film as a function of frequency over the temperature range of -55 °C to 200 °C. T_{max} of the film occurs near 70 °C, which is slightly below the bulk $T_{R\text{-}T}$.[197] In addition to the convolution of $T_{R\text{-}T}$ and T_C shifting T_{max}, it's possible that in-plane strain and chemical inhomogeneities within the PMN-PT film shifted the transition temperatures.[192] T_C has been reported to be modulated by lattice strain in numerous materials[77] and Yokoyama *et al.* reported shifts in the PT composition of the MPB in tensile stressed PMN-PT thin films grown on Si, which could, in principle, also lead to shifted transition temperatures.[198] In that work, the mixed phase region around the MPB also broadened in PT composition for thin films.[198] With potential shifts in phase stability as a function of composition in thin films, it follows that there may also be changes in the relaxor character of films from bulk ceramics. To this point, Zhang *et al.* demonstrated that the degree of relaxor character reduced sharply within a few weight percent of $PbTiO_3$ near the MPB[197] Therefore, in addition to the above mentioned defect-related factors which may increase diffusivity in thin films, there are also stress-related mechanisms that could produce increased relaxor character in thin films compared to bulk ceramics of similar composition.

While the films do exhibit relaxor character in the dielectric behavior, ferroelectric switching and saturation is observed in the polarization-electric field lops exhibit (below). The frequency dispersion in relative permittivity is likely an indicator of relatively small domain sizes in the film with some size variation, and not a net paraelectric stat. Finally, the strong convergence of the permittivity data above T_{max} is indicative of the low space charge and high crystal quality of the films.

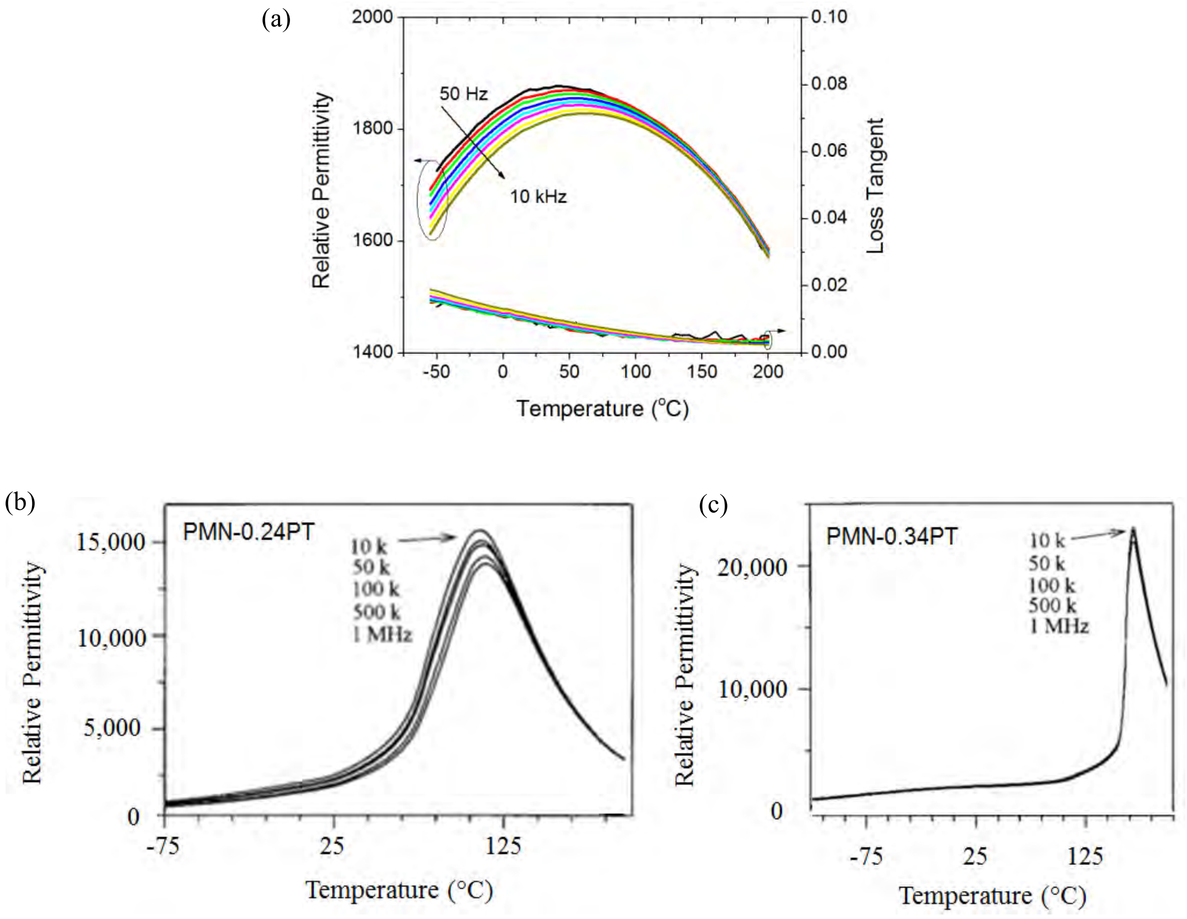

Figure 3-8: Relative permittivity of a (a) blanket 350 nm thick 70PMN-30PT film on a platinized Si substrate, (b) unpoled 76PMN-24PT single crystal,[189] and unpoled 66PMN-34PT single crystal[189] as a function of temperature and frequency.

Nested polarization-electric field (P-E) hysteresis loops measured on a 400 µm diameter top Pt electrode are shown in Figure 3-9 for fields up to 700 kV/cm. The slim and clockwise rotated nature of the P-E loops can be attributed to instability of the out-of-plane polarization due to the tensile stress imposed by the Si substrate. This P-E behavior is in agreement with data measured on similar films grown by various techniques.[165,192,199] The remanent polarization and coercive fields are low, relative to PZT films of similar thickness and orientation,[116] while the maximum polarization and maximum field excursion prior to breakdown (see also Figure 3-10) remain high. These characteristics make such PMN-PT blanket films attractive for low field switching applications and high field unipolar applications requiring large differences in on/off polarization states. Additionally, the slim nature of the P-E loop and high breakdown strength may be of interest for some energy storage applications. [200,201]

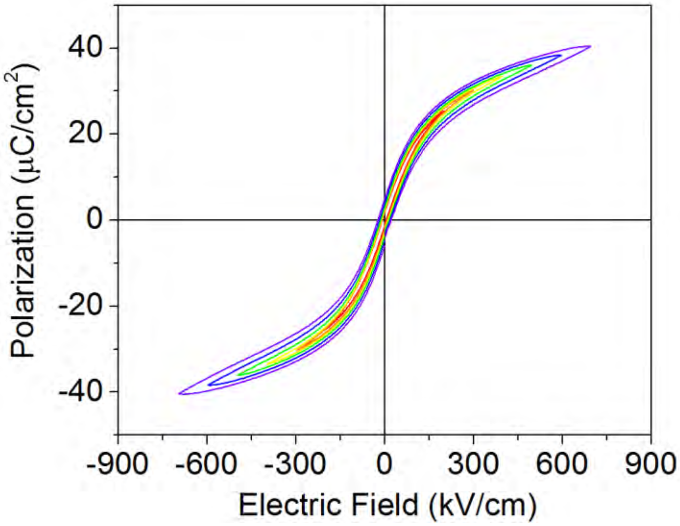

Figure 3-9: Polarization-electric field hysteresis loops with increasing field excursions recorded on a 300 nm thick 70PMN-30PT film at room temperature on a 400 μm top Pt electrode at 1 kHz.

The electric field induced strain is shown in Figure 3-10 along with a high field P-E loop. The data were recorded at 1 kHz on an aixACCT double beam laser interferometer (AixACCT Systems, Aachen, Germany) on 600 μm top Pt electrodes to minimize measurement artifacts due to substrate strains.[187] The 70PMN-30PT films breakdown at fields nearing 1500 kV/cm and exhibit high strains nearing 1% in 300 nm thick films prior to breakdown. By fitting the strain response to a linear slope, the clamped $d_{33,f}$ is determined to be ~90 ±15 pm/V. This linear fit method is in good agreement with the maximum $d_{33,f}$ reported from small signal strain measurements, shown in Figure 3-14. The strain loop exhibits little hysteresis out to fields nearing 1.5 MV/cm, making these films of interest especially for unipolar applications such as the piezoelectronic transistor.[25,202]

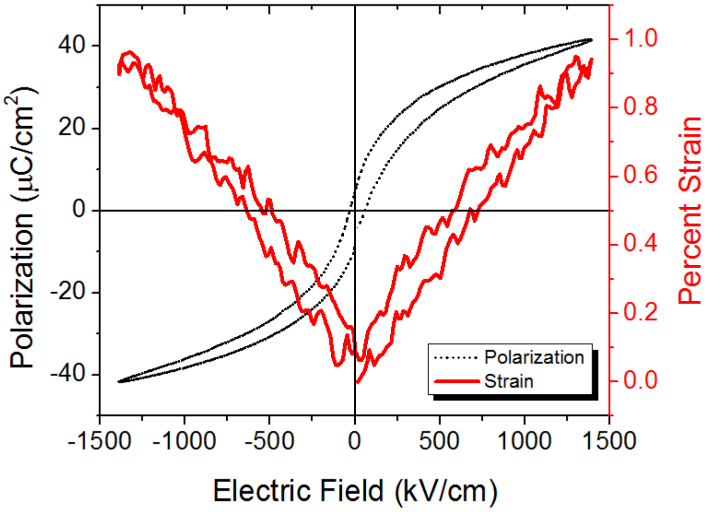

Figure 3-10: Large field polarization and strain hysteresis as a function of electric field in 300 nm thick 70PMN-30PT film, measured at 1 kHz on a 600 µm top Pt electrode.

The P-E and strain loops are very slim, and appear similar in shape to those of some electrostrictive ceramics.[60,203] Electrostriction relates strain to the square of applied electric field or polarization and can be expressed mathematically as shown in Equation 3-2:[204]

$$x_{ij} = Q_{ijkl}P_kP_l \qquad \text{Equation 3-2}$$

$$x_{ij} = M_{ijkl}E_kE_l \qquad \text{Equation 3-3}$$

where the strain (x) is related to the field induced polarization (P) by the electrostrictive coefficient, Q, or to the electric field (E) by the M coefficient. In the 33-mode, the effective film electrostrictive coefficient $Q_{33,f}$ can be taken as the slope of strain vs. P^2,[205] depicted in Figure 3-11. Using this approach, it is found that $Q_{33,f} \approx 5.2\text{x}10^{-2}$ m^4/C^2 for the blanket 300 nm thick 70PMN-30PT films on platinized Si substrates, which is quite high for a clamped film and nearly matching the bulk Q_{33} of $5.5\text{x}10^{-2}$ m^4/C^2 measured along <001> in 72PMN-28PT crystals.[206] Interestingly, this electrostrictive response is much higher than one may expect based on relative permittivity in these films and the trend reported by Kholkin *et al.* in various thin film ferroelectrics, summarized in Figure 3-12.[205]

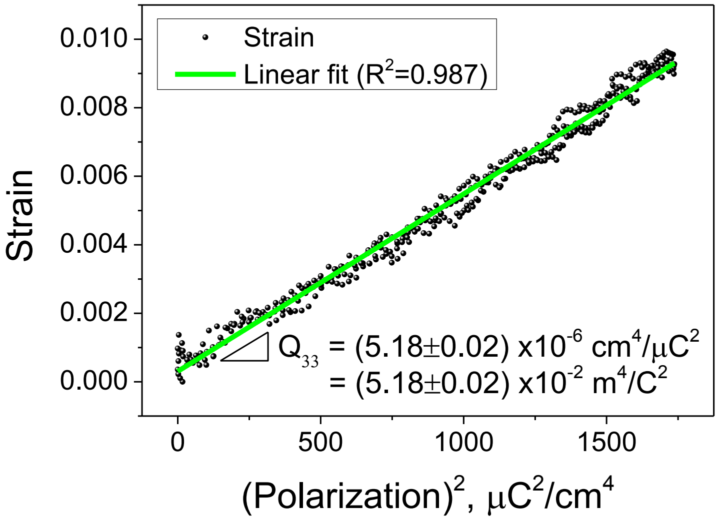

Figure 3-11: The field-induced strain vs. square of the polarization for 300 nm thick blanket 70PMN-30PT films on platinized Si substrates. The slope of the strain dependence on P^2 gives the film electrostrictive coefficient, Q_f, as ~$5.2x10^{-2}$ m^4/C^2.

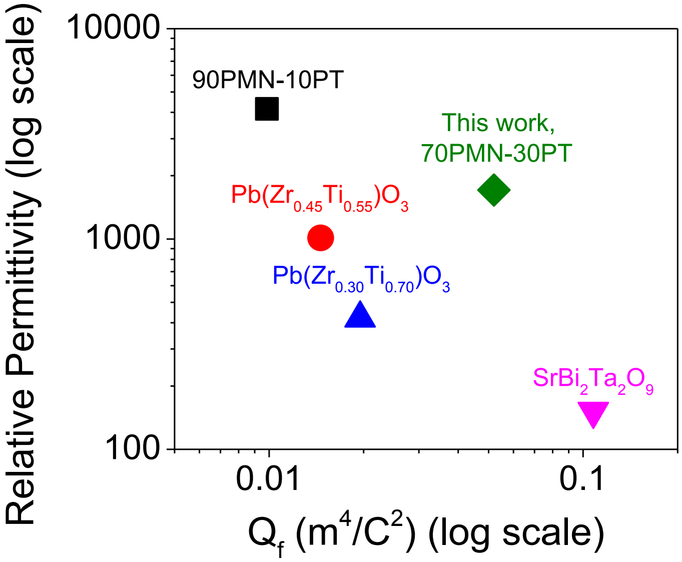

Figure 3-12: The relative permittivity plotted as a function of electrostrictive coefficient, $Q_{33,f}$, for the 70PMN-30PT films grown in this dissertation compared to other thin film compositions characterized by Kholkin *et al.*[205]

While Q_{eff} is high in these films, the overall strain is not solely attributed to electrostriction. It was found that the strain was more linear when plotted as a function of field, rather than E^2, as shown in Figure 3-13. The ferroelectric nature of these films leads to the strain being dominated by the effective film piezoelectric coefficient. Figure 3-14 shows further characterization of the low field $d_{33,f}$ response in the 300 nm thick, 001-oriented 70PMN-30PT films.

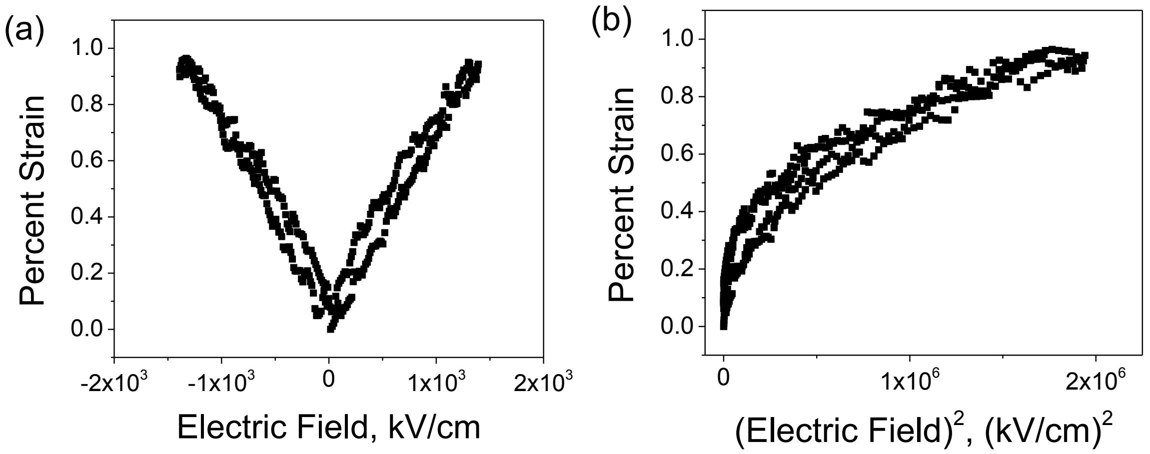

Figure 3-13: Percent strain measured via double beam laser interferometry as a function of (a) the applied electric field and (b) the squared applied electric field to compare the linearity in the piezoelectric and electrostrictive behavior, respectively.

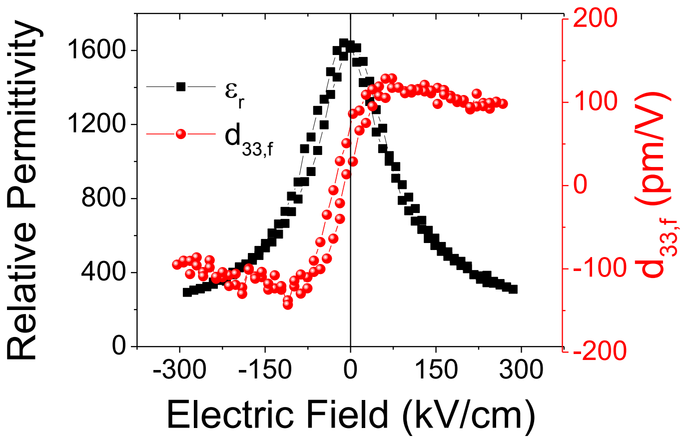

Figure 3-14: Electric field dependent relative permittivity and piezoelectric coefficient of 300 nm thick {001}-oriented 70PMN-30PT, measured with 1 V_{ac} at 1 kHz on a 600 μm top Pt electrode.

3.3.3 PMN-PT film deposition on large area substrates

The process for growth of {001}-oriented films on platinized substrates was ramped up for deposition on 8” substrates to demonstrate utility and scalability for device production applications. Since niobium and titanium precursors used in the solutions are especially moisture sensitive, care must be taken to ensure deposition over the large area substrate is done efficiently to prevent hydrolysis and precipitation from solution. To assist in this goal, spin casting was performed in a humidity controlled cleanroom (relative humidity maintained < 20%). For deposition onto substrates with a diameter of 4” or less, solution would be dispensed to wet and coat the stationary substrate surface. The substrate was then ramped up to a spin speed of 3000 rpm at a rate of 500 rpm/sec. The long time required for solution deposition and wetting of the solution on substrates larger than 4” in diameter, however, often resulted in solution hydrolysis and precipitation formation prior to the spinning procedure. The small precipitates that result cause comets to form in a spin-cast layer, reducing crystal orientation and yield in subsequently deposited top electrodes. In the cases of 6” and 8” substrates, the solution was dynamically dispensed onto a spinning wafer at 500 rpm for 10 seconds before ramping to the final spin casting speed.

Following the spin process, the wafer was placed on a hot plate at 250 °C for 2 minutes as a drying step before being transferred to a hot plate set at 430 °C for 5 minutes for pyrolysis. With wafer sizes exceeding 4” in diameter, the thermal expansion coefficient of the wafer induced wafer flexure, causing the edges of the wafer to lose contact with the hotplate. In these cases, the pyrolysis time was extended to 8 minutes and light pressure was applied to a wafer edge with tweezers around the circumference of the wafer to ensure even heating and complete pyrolysis. Films of similar crystal quality and functionality were prepared in this manner on 8" wafers from several vendors with varying Pt crystallinity and density.

3.4 Conclusions

It was found that Pb stoichiometry and diffusion at the Pt interfaces in chemical solution deposited PMN-PT films is critical to orientation and phase purity. 70PMN-30PT films were grown with excellent {001} texture without a crystalline seed layer of another material with a PbO buffer to account for Pb loss to the atmosphere and bottom electrode. At least 10% of the local Pb content can diffuse to the bottom electrode, changing the grain morphology and crystallinity of the film significantly. This approach minimizes formation of a series-capacitor structure that a second perovskite seed layer would introduce.

The properties of the 300 nm {001}-oriented blanket films included dielectric permittivities of ~1650 with loss tangent < 1%, and high breakdown strengths enabling ~1% strain from the ~90 pm/V piezoelectric coefficient in clamped films. The P-E characteristics were heavily influenced by the tensile stress imposed by the Si substrate, as expected from elastic constants, and were rotated clockwise and slim in nature. These results may be helpful in furthering the development of high strain piezoelectric films for highly scaled device applications and other unipolar or high permittivity based devices.

Chapter 4

Thickness Dependent Domain Wall Reorientation in 70/30 Lead Magnesium Niobate-Lead Titanate Thin Films

4.1 Introduction

The anomalously high piezoelectric coefficients ($d_{33} > 2000$ pm/V),[60,207] relative permittivity ($\varepsilon_r > 8000$ at room temperature),[189,195] and electromechanical coupling factors ($k_{33} >$ 90%)[60,208,209] observed in single crystal[60] and textured ceramic[155,157] relaxor-based ferroelectrics have afforded improvement in the functionality of sonar, ultrasound,[210] and various other transduction devices.[210–212] The high response in {001} oriented rhombohedral relaxor-based ferroelectric crystals has been attributed in part to the substantial polarizability of the lattice and polarization rotation.[60,67] Implementation of relaxor-based ferroelectrics can yield similar improvement in functionality in thin film ferroelectrics,[213] such as ferroelectric random access memories (FeRAM),[41,214–216] ferroelectric field effect transistors (FeFET),[217] dynamic random access memories (DRAM),[39] and the piezoelectronic transistor (PET).[27,163] These devices require reduced operating voltages, increased device capacitance, and decreased switching speeds all while maintaining high relative permittivity, remanent polarization, or piezoelectric coefficients. These design goals are, in principle, achievable via thickness reduction of the ferroelectric. However, it is widely reported that the functional properties of ferroelectric films are strongly thickness dependent, reducing concomitantly with film thickness.[84,116,129,150,151,153,218–225]

Functional properties in ferroelectric materials are the sum of intrinsic and extrinsic contributions. Intrinsic contributions to ferroelectricity in perovskites originate from distortions of the unit cell by cation displacement or oxygen octahedral rotation in response to an applied electric field or stress. *Ab initio* calculations predict some thickness dependence in the intrinsic contributions related to suppressed spontaneous polarization and broadened temperature dependence of functional properties with changes in the polarization order parameter developing near surfaces and interfaces.[109,149,153,226–228] Although ferroelectricity has been observed in films with thicknesses of only 3 unit cells,[109,110] partial suppression of ferroelectric displacements is experimentally observed to begin in $PbTiO_3$ films below ~20 nm.[111] Thus, the observed thickness dependence of the dielectric and piezoelectric properties of films at thicknesses in the hundreds of nanometers to several microns regime has been attributed largely to extrinsic effects – predominantly size-induced suppression in domain wall motion through the crystal lattice. Several studies have found such domain wall motion, along with potential variation in domain wall density as a function of film thickness, to be responsible for most of the property degradation in thinner films.[116,150,223,224]

A third mechanism by which thickness dependence can be introduced to a system is through processing-related effects. Many growth techniques introduce defect densities much greater than would be thermodynamically predicted; these can play a major role in the formation of so-called “dead” layers.[149] Dead layers are often visualized as a thin layer of non-ferroelectric material near electrode interfaces formed by degraded stoichiometry or crystallinity at interfaces due to diffusion, atomic mixing, and/or poor nucleation of the ferroelectric. The result is a series capacitor structure comprised of material with “bulk-like” response electrically in series with a layer of decreased polarizability (a dead layer). The dead layer ultimately reduces the magnitude of the response with film thickness. Moreover, grain boundaries with significantly reduced properties from the bulk[229] and domain pinning capability[230] may cause thickness dependence in films with either spherical[117,128] or columnar[231] grains.

In addition to physical defects which can form during processing, several groups have shown that the electronic interactions of a ferroelectric with a given electrode material can also contribute to measurable size effects.[221,232,233] For example, while $BaTiO_3$ lamella thinned from bulk single crystals with Pt electrodes exhibit very little deviation from the bulk permittivity as a function of temperature with respect to both magnitude and peak shape, significant property degradation is observed in $SrTiO_3$ lamella.[147,234] Han and coworkers identified non-switchable lead zirconate titanate (PZT) domains near a Nb-doped $SrTiO_3$ (STO) electrode interface attributed to built-in electric fields associated with electronic band bending across the heterojunction, while material near the Au top electrode could be completely switched.[235] Varying the bottom electrode chemistry or structure may also influence the nucleation energy for given phases or compositions of a growing film. In principle, most processing-related thickness dependencies could be engineered out of the system with careful film growth and choice of electrode material.

The substrate on which a ferroelectric film is grown can also have a significant effect on the polarizability. Differences in thermal expansion mismatch between the film and substrate place the ferroelectric in a non-zero stress state upon cooling from the crystallization temperature. Si substrates, for example, put PZT and PMN-PT thin films under tens to hundreds of MPa of tensile stress, stabilizing in-plane polarization directions. For a relaxor ferroelectric - based composition, this stress could hinder polarization rotation.

Clearly, numerous factors contribute to the size effects of ferroelectric films. To support the integration of high strain relaxor-ferroelectrics in the aforementioned devices, this work aims to identify the dominant mechanisms of thickness dependence in 70PMN-30PT, especially at thicknesses below 400 nm where PMN-PT can be grown crack-free on Si.[236–238] 70PMN-30PT films were grown by chemical solution deposition (CSD) in a thickness series from 100-350 nm on two different substrates. Strongly {001} oriented polycrystalline films were grown on platinized Si substrates, while $SrTiO_3$ single crystals with $SrRuO_3$ bottom electrodes were employed for growth of epitaxial {001} PMN-PT. Functional properties and structure were then studied as a function of thickness, interface crystallinity, and electrode type.

4.2 Experimental procedure

Substrates of 150 nm Pt/30 nm Ti/1 μm SiO_2/550 μm Si and {001}-oriented $SrTiO_3$ single crystals were obtained from Nova Electronic Materials (Flower Mound, TX) and Crystec (GmbH, Berlin, Germany), respectively. $SrRuO_3$ bottom electrodes were grown on the $SrTiO_3$ to 100 nm in thickness via pulsed laser deposition with a KrF excimer 248 nm laser (Lambda Physik Compex Pro) at a laser energy density of 1.1 +/- 0.1 J/cm^2, a laser frequency of 10 Hz, a target to substrate distance of 8 cm, and a substrate temperature of 680 °C.[239] A rocking curve x-ray diffraction scan of the $SrRuO_3$ films exhibited a 002 peak full width at half maximum (FWHM) of ~0.1°, while the Pt electrode was {111} oriented with a FWHM of ~11°.

The $0.70Pb_{1.1}(Mg_{1/3}Nb_{2/3})O_{3.1}$-$0.30Pb_{1.1}TiO_{3.1}$ precursor solutions were prepared with a 2-methoxyethanol (2-MOE) solvent in a dry Ar atmosphere with precursor chemicals from Sigma Aldrich, Inc. (St. Louis, MO) in a process described in detail elsewhere.[167] The solution was distilled to 0.2 M and modified with 11 vol. % acetylacetone as a chelating agent. The final solution was batched for 10% excess Pb to account for Pb loss to the atmosphere during crystallization. A 0.04 M PbO buffer solution for {001} texture on Pt electrodes was prepared separately under similar conditions.

The solutions were dispensed through a 0.1 μm Whatman filter (GE Healthcare Life Sciences, Pittsburgh, PA) onto the substrate and spun at 3000 rpm for 45 seconds. The films were pyrolyzed in two steps on hot plates in air to remove organics; first at 300 °C for 2 minutes and second at 410 °C for 5 minutes. The resulting amorphous layer was crystallized in a rapid thermal annealing furnace (Allwin21 Co. Morgan Hill, CA) under 10 sccm flowing O_2 at 740 °C for 1 minute. Each layer was 25±1 nm thick and the deposition process was repeated to grow PMN-PT films from 100 nm to 350 nm in thickness in 50 nm increments. To obtain {001} orientation in the polycrystalline PMN-PT films on Pt, a 0.04 M solution of PbO was spun onto the substrate at 4000 rpm for 45 seconds, and pyrolyzed at 400 °C for 10 minutes prior to PMN-PT deposition.[202] The as-deposited PbO buffer layer was 2-3 nm thick; ultimately the layer was incorporated into the PMN-PT lattice or bottom electrode.

For electrical measurements, 50 nm thick top Pt electrodes were sputtered onto the PMN-PT film surface and patterned by a lift-off technique. The bottom electrode was accessed with alternating exposure to a buffered HF etchant and hydrochloric acid. Film thickness was verified by contact profilometry (KLA-Tencor P16+, Milpitas, CA).

A Leo 1530 Field Emission Scanning Electron Microscope (Carl Zeiss Microscopy GmbH, Jena, Germany) was employed to observe grain morphology. Film texture and quality were characterized by a PANalytical Empyrean x-ray diffractometer (PANalytical B.V., Almelo, The Netherlands) in the Bragg-Brentano θ-2θ arrangement. A Philips X'Pert Pro MRD high resolution 4-circle diffractometer (PANalytical Inc., Tempe, AZ) was used to measure the full width at half maximum (FHWM) of epitaxial 002 peaks and to verify epitaxy by examining off-axis peaks. The diffractometer was equipped with a graphite hybrid monochromator which selectively collimated Cu Kα1 radiation. A schematic depicting the axes of rotation in a 4-circle diffractometer is shown in Figure 4-1.[240] The X-ray source and detector rotate along the 2θ axis. The sample is attached to a stage which can be rotated about φ and χ and rocked along the ω axis.

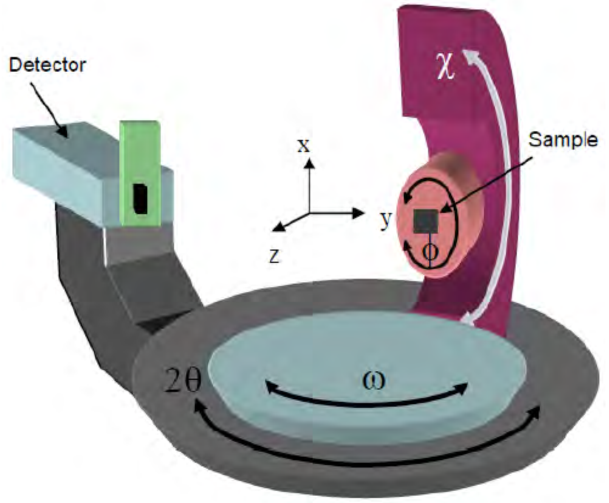

Figure 4-1: Schematic depiction of a 4-circle diffractometer similar to the Philips X'Pert Pro MRD used in this work. Figure from [240]

After determining source and detector position by aligning for maximum intensity along 2θ, the sample was brought forward to cut the beam intensity in half. The sample surface was then aligned parallel to the beam path by rocking ω and finding maximum intensity. With the sample surface aligned, the detector and sample stage were repositioned to locate a substrate peak, typically the Si 400 at 69.132° 2θ, or $SrTiO_3$ 002 at 46.7° 2θ. Alignment scans were performed by rotating the sample about the ω, 2θ, and χ, axes and along the *x*, and *y* directions in an iterative fashion to hone in on the highest peak intensity. Once the intense substrate peaks were located and aligned with the stage and detector axes, the tool was driven to the film peak locations in a similar manner.

The degree of crystallinity was quantified with the FWHM of 002 peak rocking curves. Rocking about ω brought the sample in and out of the conditions for Bragg diffraction for the PMN-PT {002} peak. A broad peak in ω is indicative of misaligned {002} planes with respect to the sample surface, so that the diffraction condition was met at a wider range of ω values. A perfect single crystal material would ideally diffract the incident X-ray beam at one ω position. Therefore, the FWHM of this peak is an indication of the crystal quality. Rocking curves were typically acquired over a 4° range in ω with a 0.005° step size and count time of 0.5 sec. Verifying film epitaxy with an underlying bottom electrode and substrate was done via 360° φ scans after aligning θ to the off-axis 101 peak and χ to 45°.

Site specific cross sectional transmission electron microscope (TEM) samples including both top and bottom electrode interfaces with PMN-PT were prepared by focused ion beam (FIB) milling (*FEI Helios NanoLab DualBeam 660)*. FIB-TEM samples were prepared via an *in situ* lift-out technique. Prior to cross-sectional milling, a protective carbon layer was deposited over the region of interest by electron-beam deposition. The starting FIB milling voltage was 30 kV to create a membrane of the cross sectional sample and thin the sample to electron transparency. The final milling voltage was stepped down to 2 kV to further thin the samples and minimize sidewall damage. Electron energy loss spectroscopy (EELS) measurement in TEM showed that the sample thickness was < 50nm.

The interface structure and quality were investigated using a FEI Titan3 dual aberration corrected scanning/TEM (S/TEM) instrument (FEI, Hillsboro, OR) operated at 200 kV. The microscope conditions for STEM imaging were 70 pA for beam current with a C2 aperture of 70 μm. A high angle annular dark field, or HAADF, detector (E.A. Fischione Instruments, Inc., Export, PA) with a collection angle of 51-300 mrad for Z-contrast imaging was used for STEM. Elemental mapping across each interface was performed in STEM mode by a SuperX Energy Dispersive Spectroscopy (EDS) system with four Bruker Silicon Drift Detectors, which enabled rapid collection rates of characteristic X-rays. EDS mapping was performed with acquisition times of up to 5 minutes.

Polarization-electric field (P-E) hysteresis loops were measured at 1 kHz using a multiferroic tester (Radiant Technology, Inc. Albuquerque, NM). Characterization of the ac-field and frequency dependence of the relative dielectric permittivity was performed using an HP 4248A precision LCR meter (Agilent Technology, Palo Alto, CA) at 1 kHz. In temperature dependent measurements, custom data acquisition software (GADD and Vision) was used to control a thin film temperature stage equipped with a calibrated thermocouple adhered to the stage surface. An enclosure was built over the sample, enabling the flow of dry nitrogen gas through the system to reduce H_2O condensation below 0 °C.

The longitudinal effective piezoelectric coefficient, $d_{33,f}$, was characterized by electric field induced shifts in the {002} d-spacing, measured at beamline 11-ID-C the Advanced Photon Source. The experimental setup was described by Johnson-Wilke *et al.*[241] and included an area detector placed ~2250 cm from the sample. The position of the detector was calibrated using a National Institute of Standards and Technology standard cerium dioxide powder. The 70PMN-30PT films were placed on a stage with translational motion in x, y, and z, as well as rotational motion about the stage normal (ζ) and beam path (ψ). The diffraction experiments were performed in reflection and transmission with the sample tilted 1° or 1.7° for the polycrystalline and epitaxial films, respectively, with respect to the beam path. This geometry increased the irradiated area. Care was taken to ensure that the beam was confined to the electrically actuated material.

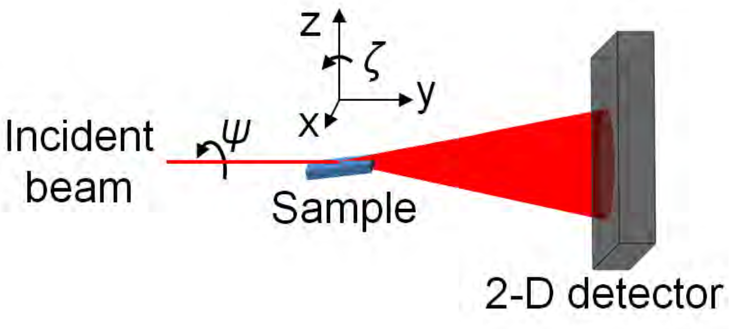

Figure 4-2: Schematic depiction of piezoelectric characterization by X-ray diffraction

The electrodes were contacted with probes connected to an HP 4194 (Hewlett-Packard, Palo Alto, CA) LCR meter to verify electrical contact and check dielectric permittivity and loss before and after a given voltage excursion. Electric field was supplied to the films by a Keithley 2410c 1100 V source meter (Keithley Instruments, Cleveland, OH) connected to the contact probes. An X-ray pattern was recorded at 0 V, 0.25 V_C, 0.5 V_C, 0.75 V_C, and then integer multiples of V_C (the coercive voltage) in a stepwise manner until breakdown was reached. The leakage current remained below 10 μA/cm^2 for the duration of the experiments. The films were probed with an X-ray energy of 115 keV.

Fit2D software (European Radiation Synchrotron Facility, Grenoble, France) was employed to integrate the intensity of the polycrystalline Debye-Scherrer rings over a sector corresponding to the direction of the applied electric field and convert the data to a 1-D intensity vs. 2θ plot. The integration sector over the azimuthal angle was 20° wide. The 2θ data, collected as a function of electric field, were then converted to d-spacing. Table 4-1 summarized the χ^2 (the quantity which is minimized for fitting, equal to the residual sum of squares/degrees of freedom) and R^2 values for four peak fitting functions and the 350 nm thick 002 peak at 0 kV/cm. The Pseudo-Voigt function achieves the lowest χ^2 with R^2 closest to 1, indicating good fitting of the experimental data. Since the relevant rhombohedral 002 peaks exhibit no peak splitting, the fits were performed in OriginLab software. The fitting procedure for the epitaxial films was slightly different due to peak splitting that was observed at high fields. The data were integrated in Fit2D over 8° due to the smaller FWHM of the relevant peaks and the intensity vs. d-spacing data fit with Mathematica code, given in Appendix C.

Table 4-1: Example fitting parameters of Lorentzian, Gaussian, Pearson VII, and Pseudo-Voigt fits to the 002 diffraction peaks of 350 nm thick 70PMN-30PT film at 0 kV/cm; data recorded at the APS.

	Lorentz	Gauss	Pearson VII	Pseudo-Voigt
Reduced χ^2 (x10^5)	5.53	1.62	0.618	0.265
Adjusted R^2	0.98839	0.99658	0.9987	0.99944

4.3 Results and discussion

4.3.1 Film characterization

Figure 4-3 and Figure 4-4 show the X-ray diffraction patterns of the polycrystalline and epitaxial films respectively. It is apparent that the {001} Lotgering factor remains above 0.96 for the polycrystalline samples, while the {002} ω-rocking curve FWHM remains below 0.24°, indicating little to no thickness dependence in preferred orientation for a given film set. It is also noted that the FWHM of the {002} PMN-PT peak in the polycrystalline films on Pt was between 4 and 7°, significantly narrower than the Pt FWHM.

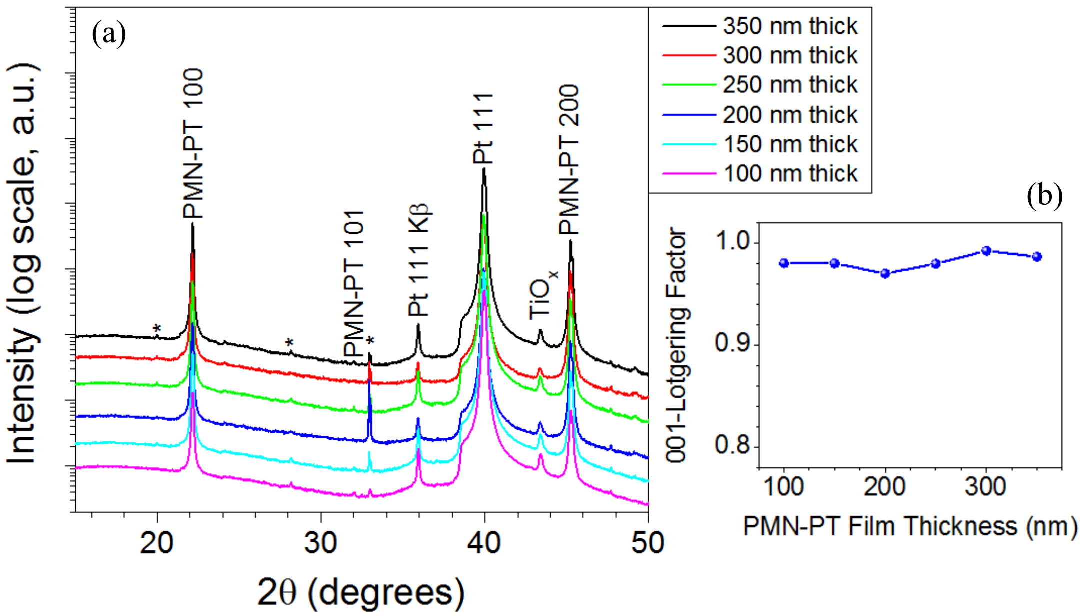

Figure 4-3: (a) θ-2θ diffraction pattern for {001} oriented 70PMN-30PT films grown on Pt for a thickness range of 100-350 nm thick. The FWHM of the {002} peaks ranged from 4-6° in this film series. An * denotes peaks from the substrate or k_β radiation. (b) The {00*ℓ*} Lotgering factors of the polycrystalline 70PMN-30PT films on Pt-coated Si substrates as a function of thickness.

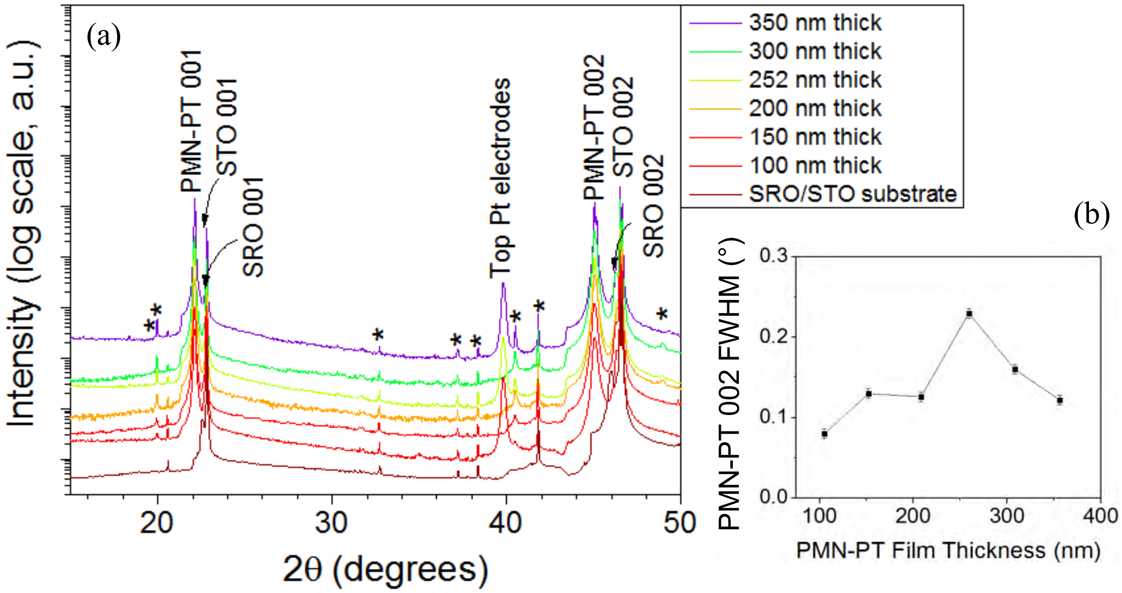

Figure 4-4: (a) θ-2θ diffraction patterns for {001} oriented 70PMN-30PT films grown on Pt from ~100-350 nm thickness. (b) {002} FWHM taken from ω-rocking curves as a function of film thickness. An * denotes peaks from the substrate or K_β radiation.

The grain morphology of the polycrystalline films is shown in Figure 4-5 as a function of thickness. The diameter of the columnar grains increases with film thickness, rising from ~90 nm in the 100 nm thick films and saturating at ~175 nm when film thickness reaches 300 nm. Scanning probe microscopy has demonstrated the strong domain wall pinning potential for grain boundaries in PZT[139,140,142] and BiFeO$_3$.[138] Therefore, the observed thickness dependence in the grain boundary density may play a role in the global ferroelectric behavior of the polycrystalline films.

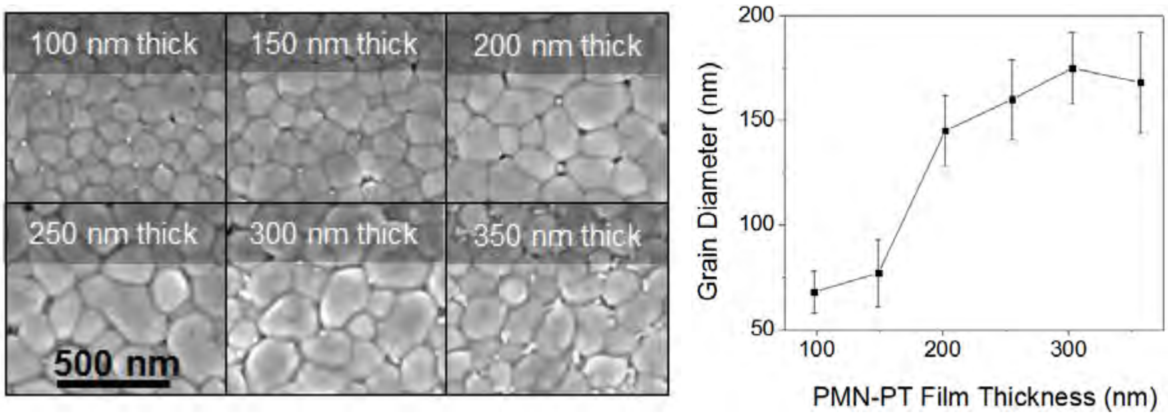

Figure 4-5: Top surface grain morphology and grain diameter as determined by the linear intercept method for oriented PMN-PT films on Si.

Figure 4-6 shows the high resolution scanning transmission electron microscopy images of the PMN-PT/SRO and PMN-PT/PbO/Pt interfaces. The epitaxial films exhibit cube-on-cube epitaxy. Likewise, PMN-PT films on Pt appear crystalline up to the Pt surface. Small isolated regions of amorphous material were observed near grain boundaries of the Pt electrode. These volumes were typically less than 2 nm thick and were within 4 nm of the Pt grain boundary. Both the surface pyrochlore seen in Figure 4-5 and the amorphous PMN-PT pockets at Pt grain boundaries constitute less than a percent of the top and bottom surfaces of the film, respectively, and are expected to have only a modest effect on the measured properties. Additionally, the films exhibit no evidence of a continuous amorphous dead layer, however, energy dispersive spectroscopy shows a region of graded composition of ~3-6 nm in thickness near the dielectric-electrode interface. This region of increased defect density will influence the free energy landscape of pinning sites in these films, introducing a means of thickness dependence.

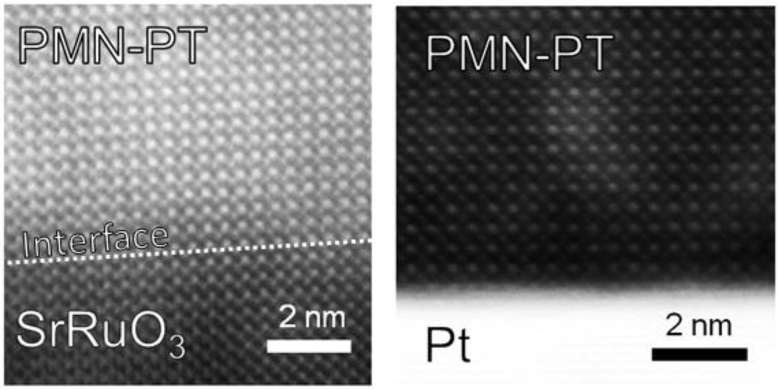

Figure 4-6: High resolution scanning transmission electron microscope images of the {001} epitaxial 70PMN-30PT/$SrRuO_3$ interface (left) and the {001} oriented 70PMN-30PT/Pt interface (right).

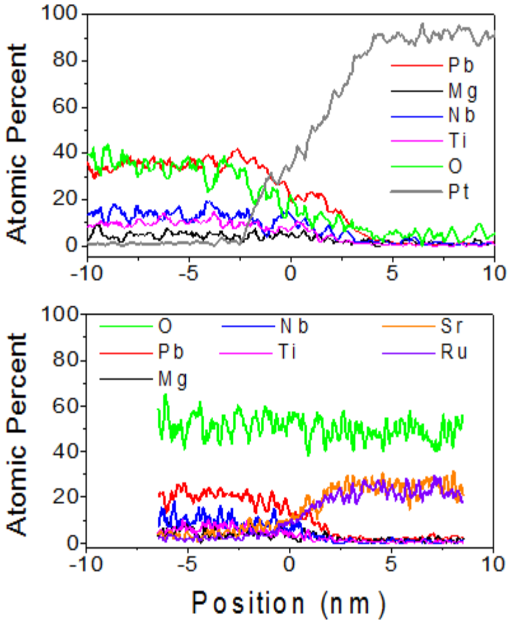

Figure 4-7: Energy dispersive spectroscopy data showing the relative atomic composition as a function of position across the interfaces of {001} oriented 70PMN-30PT films on Pt (top) and epitaxial {001} 70PMN-30PT films on $SrRuO_3$ (bottom).

At the thicknesses studied in this work, the PMN-PT films are structurally relaxed, as can be seen by the misalignment of the film and substrate 113 peaks in the reciprocal space map in Figure 4-8. Therefore, the in-plane stress state of both the epitaxial and polycrystalline films is dominated by mismatch in the thermal expansion coefficient of the films and substrates.[242] From the thermal expansion coefficients of PMN-PT,[92] $SrTiO_3$,[91] and Si,[91] along with the modulus of PMN-PT[89] and the respective crystallization temperatures, it was determined that films on Si are under ~500 MPa tensile stress while films on $SrTiO_3$ are under ~60 MPa compressive stress. The tensile stress of the polycrystalline films may slightly reduce the magnitude of remanent polarization, while compressively stressed epitaxial films are expected to have increased out-of-plane polarization.

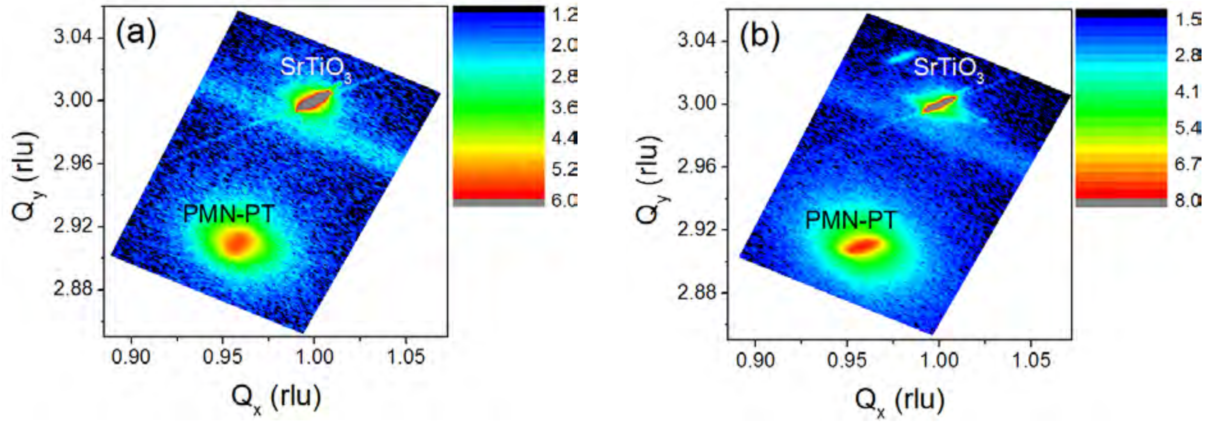

Figure 4-8: Reciprocal space map of the {113} peaks in (a) 100 nm thick and (b) 350 nm thick PMN-PT films on $SrRuO_3/SrTiO_3$ substrates.

4.3.2 Electrical characterization

The difference in stress state of the films grown on $SrTiO_3$ and Si is apparent in the shape of the polarization-electric field (P-E) hysteresis loops, shown in Figure 4-9. The changes in loop width and maximum (P_{max}) and remanent (P_r) polarization as functions of thickness are summarized in Figure 4-10. Polycrystalline films exhibit clockwise rotation in P-E loops as thickness is reduced, which decreases both the maximum and remanent polarization. Such rotation has been observed as a function of PZT film thickness, and is attributed to residual stress levels or strain gradients through the thickness of the films.[90,178] Epitaxial films, on the other hand, are more square in shape and exhibit no significant trend in P_r or P_{max}, but do show increased E_C upon thickness reduction, as is commonly reported in the literature.[116,165,243,244] The increase in coercive field with decreasing film thickness has previously been attributed to a higher density of strong domain pinning sites at the film-electrode interfaces.[116,165] The loop width in polycrystalline films slightly decreases with film thickness, however. This result, combined with the thickness dependent grain size shown in Figure 4-5, suggests the possibility that the grain boundaries acting as nucleation sites for polarization reversal, as has been shown in $Pb(Zr_{0.2}Ti_{0.8})O_3$.[245]

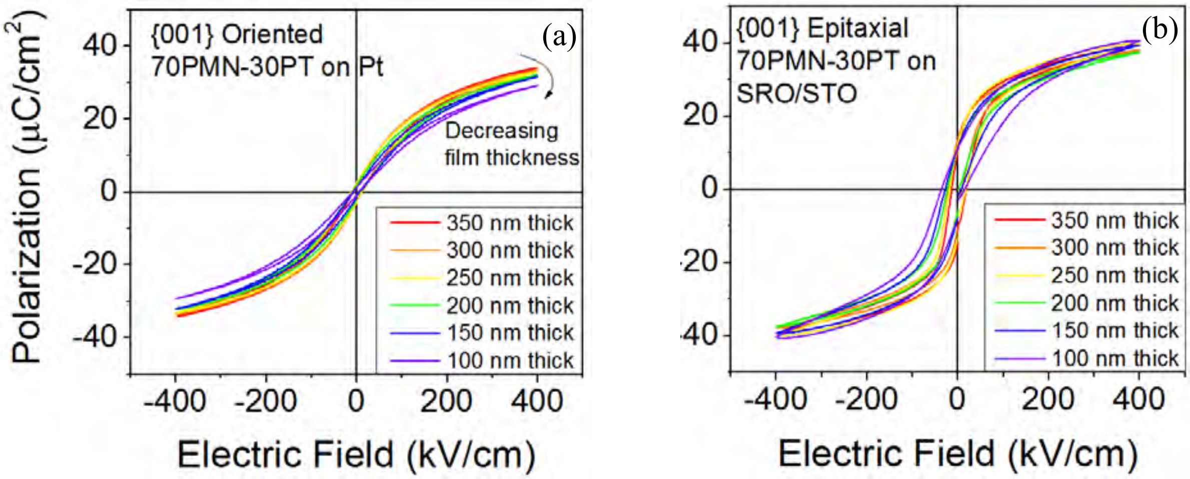

Figure 4-9: Polarization vs. electric field loops for (a) {001}-oriented polycrystalline and (b) epitaxial 70PMN-30PT films as a function of thickness.

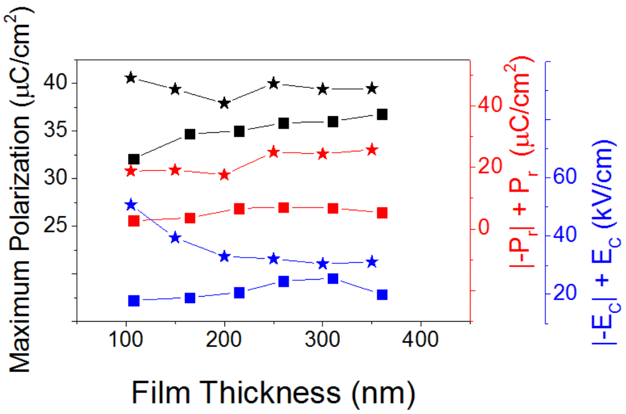

Figure 4-10: Maximum polarization, remanent polarization, and P-E loop width as a function of film thickness for epitaxial and polycrystalline {001} 70PMN-30PT films. Stars and squares are for the epitaxial and polycrystalline films, respectively.

The potential that dead layers along columnar grain boundaries contributed to the thickness dependence in polycrystalline films was investigated. The thickness dependence of grain size (Figure 4-5) was fit with the model proposed by Sinnamon *et al.*[231] assuming that the grain boundaries (GB) were amorphous with ε_r^{GB} ≈ 30-50 and ~10 nm thickness with the bulk of the grain having $\varepsilon_r \approx 2200$. The latter assumption is reasonable for fully clamped PMN-PT on Si substrates.[108] However, TEM analysis of the polycrystalline film GBs (Figure 4-11) does not support the assumption of thick amorphous layers at the grain boundaries. Thus, the primary role of the grain boundaries is expected to be strong pinning sites for domain wall motion.

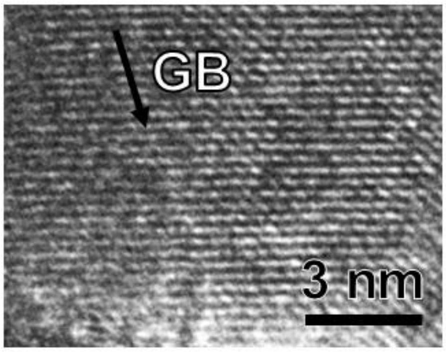

Figure 4-11: Transmission electron micrograph of a polycrystalline, {001}-oriented PMN-PT grain boundary (GB) grown on a platinized Si substrate.

Figure 4-12 shows the frequency dispersion in relative permittivity and loss tangent for the thickest films studied in this work as a function of temperature. The overall film quality is reflected in the convergence of the relative permittivity above T_{max}, indicating very little space charge. Below T_{max}, the films do exhibit relaxor character in their frequency dispersion, as has also been reported elsewhere.[192] Bulk PMN-PT of compositions near the MPB, however, exhibit very little frequency dispersion, and that near T_{C}.[189] These differences could be associated with increased defect concentrations,[192] smaller coherent diffraction region sizes,[192] and/or shifts in the MPB[198] in PMN-PT films. Despite the relaxor characteristics in the dielectric constant, the P-E loops, and piezoelectric characteristics (to follow) demonstrate that for at least part of the film, ferroelectricity is retained and stable.

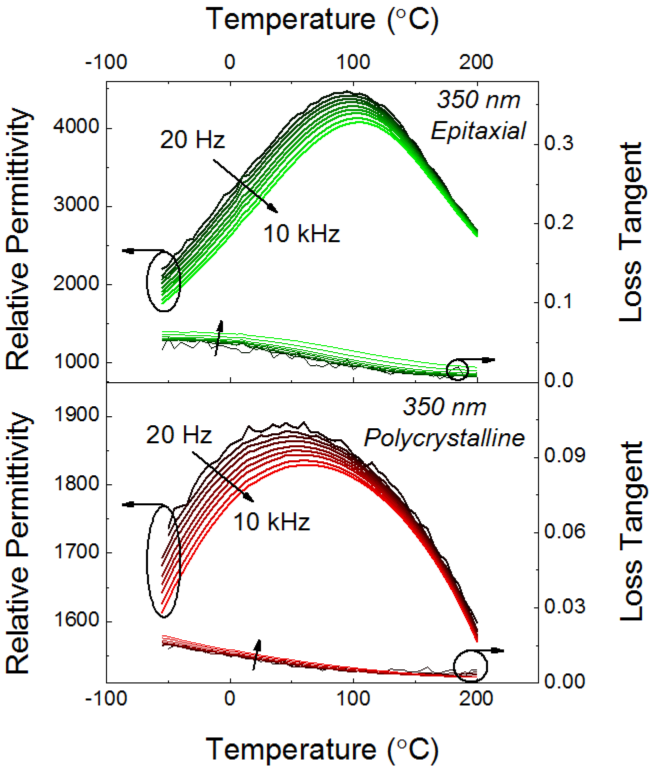

Figure 4-12: The frequency dispersion in the relative permittivity and loss tangent for the 350 nm thick epitaxial and polycrystalline films as a function of temperature.

The degree of relaxor character, γ, in ferroelectric materials can be characterized with a modified Curie law expressed in terms of the relative permittivity, the maximum relative permittivity ($\varepsilon_{r,\ max}$) observed at T_{max}, the Curie constant (C) as written in Equation 4-1:[197]

$$\frac{1}{\varepsilon_r} - \frac{1}{\varepsilon_{r,max}} = \frac{(T - T_{max})^\gamma}{C} \qquad \text{Equation 4-1.}$$

γ for free, normal ferroelectrics is about one and reaches about two for relaxors. Figure 4-13: Analysis of the modified Curie law to find γ in the 350 nm thick epitaxial PMN-PT film.Figure 4-13 shows that the γ for the 350 nm thick, epitaxial 70PMN-30PT film is about two. While this suggests that the relaxor character of PMN is largely maintained in the films, even with 30% $PbTiO_3$, and is in agreement with the observed dielectric dispersion, it must be noted that even proper ferroelectric films exhibit broadened peaks in permittivity and tend to deviate from the bulk-observed Curie-Weiss behavior due to the strain state and significance of defects and interfaces.[153,192,196] For this reason, observation of a γ of two cannot alone indicate the length scale of polar regions or the nature of the ferroelectric behavior in thin films.

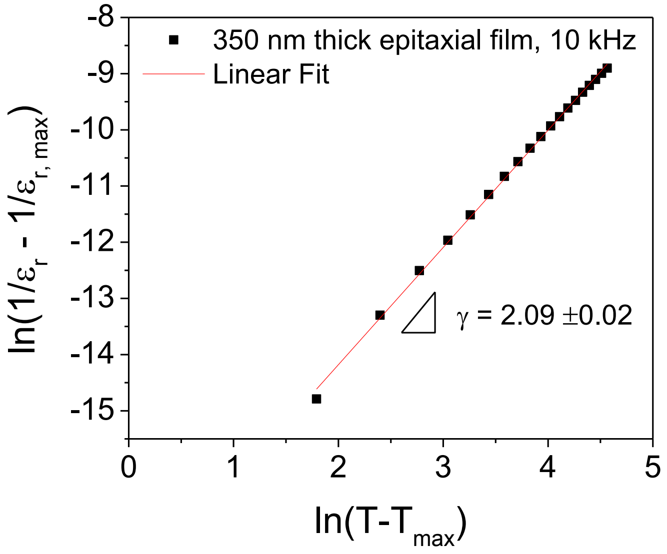

Figure 4-13: Analysis of the modified Curie law to find γ in the 350 nm thick epitaxial PMN-PT film.

Application of a DC bias across a thin film minimizes extrinsic domain wall contributions to the relative permittivity and decreases polarizability of the lattice displacements comprising the intrinsic response. Figure 4-14 shows ε_r converging for both epitaxial and polycrystalline films as a function of thickness under DC bias. This suggests that the intrinsic polarizability of the films is not a strong function of thickness. Furthermore, since the high field value of the relative permittivity converges to ~300 ±30 for all thicknesses in both film types, the intrinsic contributions show a weaker dependence on crystallinity or grain boundary density than the extrinsic part of the response. Therefore, differences in the dielectric behavior as a function of thickness for the films can be largely attributed to the extrinsic domain wall contributions. These data also demonstrate the difference in tunability of the two film types due to the large difference in domain contributions to the dielectric response.

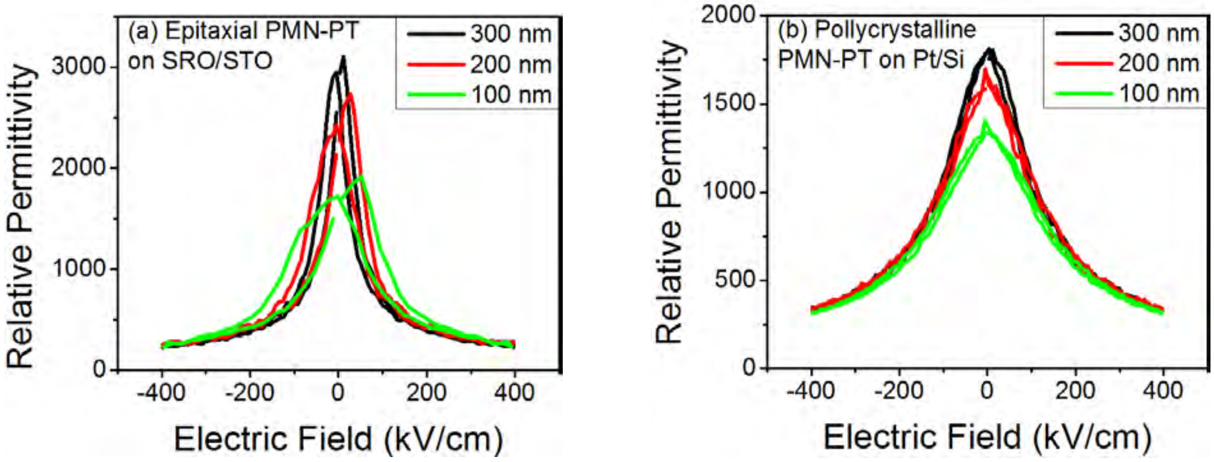

Figure 4-14: DC-electric field dependent relative permittivity for select thicknesses of (a) epitaxial and (b) polycrystalline 70PMN-30PT thin films, recorded at room temperature with an AC-signal of 30 mV at 1 kHz.

Fitting the high field dielectric data (dc bias = 400 kV/cm) to the series capacitance model used to assess dead layers (described in detail elsewhere)[147,227,246] would suggest no interfacial layer is present and all of the prepared films, epitaxial and polycrystalline, have a relative permittivity of 300. Because this is not the case observed under zero field bias, the thickness dependence observed in the low field dielectric data can be largely associated with domain wall motion.

To gain further insight into the controlling mechanisms of the observed thickness dependence, and to decouple reversible and irreversible domain wall contributions, the dielectric response was measured as a function of temperature and ac-field amplitude. The temperature dependence of permittivity and loss for the epitaxial and polycrystalline films as a function of thickness are shown in Figure 4-15. There is a single maximum in ε_r at T_{max} which occurs at temperatures less than the bulk Curie temperature, or T_C, of 120 °C. This is probably due to the combined effect of an increased defect density and stress in the films, and a convolution of T_C with the rhombohedral to tetragonal transition temperature T_{R-T}.[192] For a given temperature, the relative permittivity of the PMN-PT films increases with film thickness and the permittivity of the epitaxial films are higher than those of the polycrystalline films for a given thickness.

The slope of the dielectric response as a function of temperature $\left(\frac{\partial \varepsilon_r}{\partial T}\right)$ in polycrystalline films does not vary significantly as a function of thickness; rather, the $\varepsilon_r(T)$ curve measured in 100 nm thin films essentially shifts to higher values as thickness increases. 55-75 °C below their respective T_{max}, $\frac{\partial \varepsilon_r}{\partial T}$ decreases only ~20% in scaling from 350 to nm thick polycrystalline films and ~85% for epitaxial films.

Figure 4-16 summarizes the relative changes in both T_{max} and maximum ε_r as a function of thickness. Polycrystalline films exhibit ~60% reduction in T_{max} upon scaling thickness from 350 nm to 100 nm, ~3.3x more relative reduction than epitaxial films exhibit. The polycrystalline films likely show a stronger decrease in T_{max} due to the grain size reduction with film thickness (known to suppress T_C),[143–145] a change in dimensionality the epitaxial films are not subjected to. For the maximum ε_r, however, epitaxial films reduce 53 ±3% as compared to 32 ±3% in polycrystalline films.

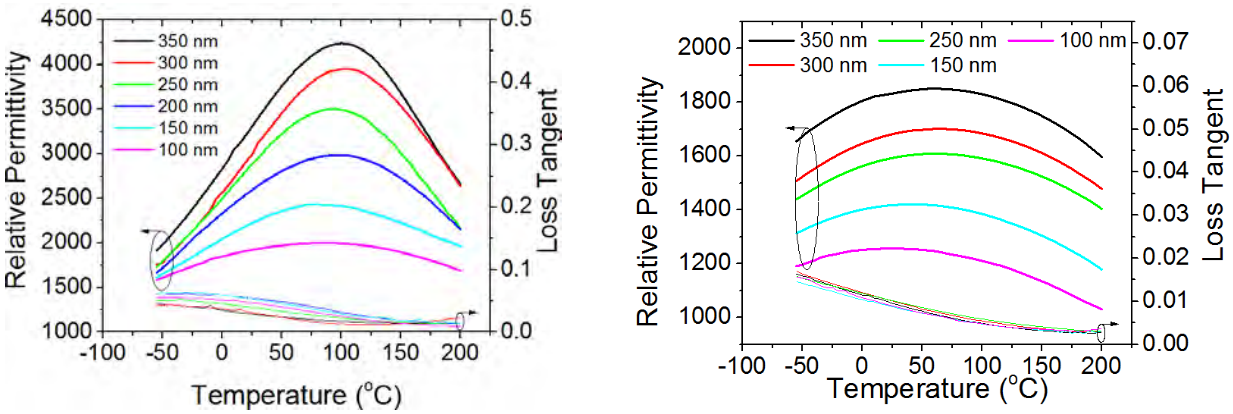

Figure 4-15: Temperature dependence of the relative permittivity and loss tangent for (a) epitaxial and (b) polycrystalline PMN-PT films of varying thickness, recorded with 30 mV$_{ac}$ at 1 kHz.

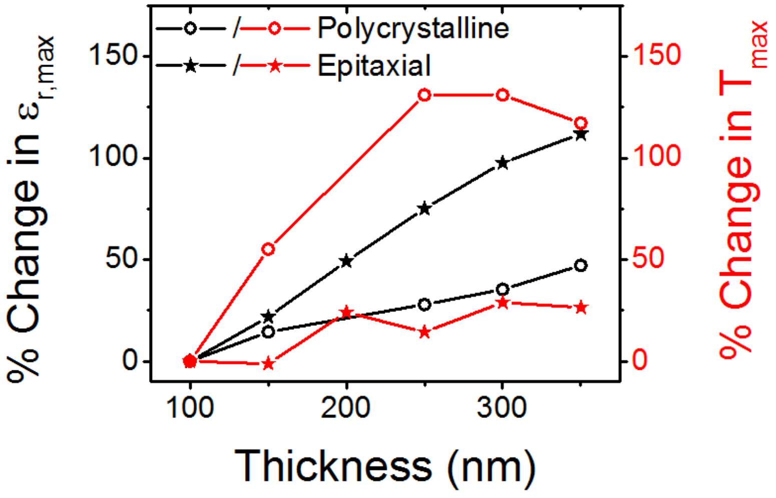

Figure 4-16: Percent change in the maximum relative permittivity and T$_{max}$ as a function of thickness for polycrystalline, {001}-oriented 70PMN-30PT films on Si and epitaxial {001} 70PMN-30PT films on SrTiO$_3$ substrates.

The Rayleigh law pertains in cases where the ac field dependence of the permittivity is linear, typically below ~1/3 – 1/2 E$_C$, with the intercept value representing the reversible contributions (ε_{init}) to permittivity and slope representing the irreversible contributions (α’). α’ also describes the hysteresis in minor polarization – electric field loops. Reversible contributions include both the intrinsic response as well as reversible domain wall motion while irreversible domain wall motion or phase boundary motion contributes to the irreversible Rayleigh coefficient.[132,247,248] As aforementioned, it is believed that the thickness dependence of the intrinsic contributions to relative permittivity is weaker than the thickness dependence of the extrinsic contributions. Hence, differences in the reversible Rayleigh behavior among the measured films were attributed predominantly to reversible domain wall contributions.

Figure 4-17a depicts ε_{init} and α′ for the epitaxial and polycrystalline films from 100 nm-350 nm in thickness. It was found that the epitaxial films have higher Rayleigh coefficients for a given thickness, which is consistent with their higher permittivities. The Rayleigh data were then normalized to values measured in the thickest films of each type in Figure 4-17b. It was found that most of the Rayleigh coefficients reduce ~40% upon thickness reduction from 350 nm to 100 nm; the exception is that α′ for the epitaxial films reduces ~85% over the same thickness range.

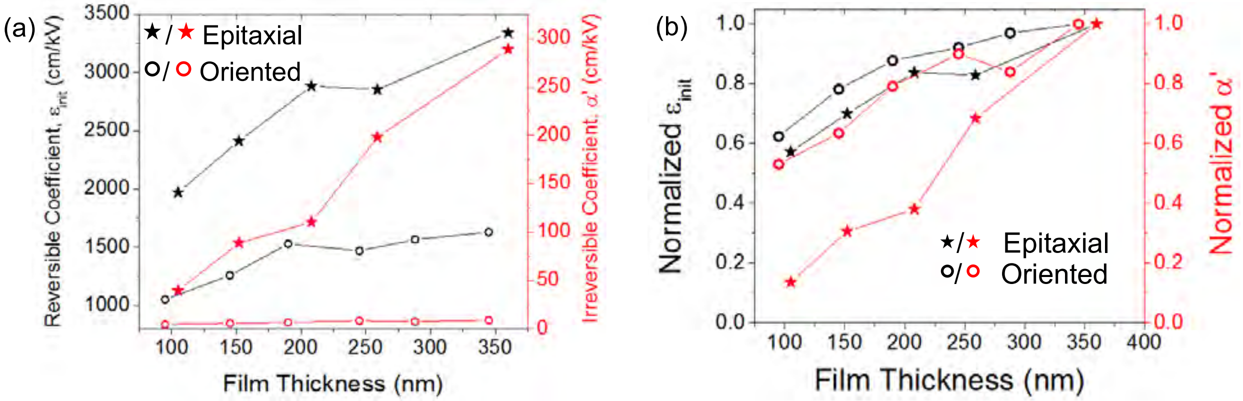

Figure 4-17: Reversible and irreversible Rayleigh coefficients of the relative permittivity of epitaxial and polycrystalline PMN-PT films of varying thickness (a). The Rayleigh coefficients normallized to the value observed in the thicknest film are shown in plot (b).

Table 4-2 summarizes the relative changes in the dielectric behavior upon scaling thickness of epitaxial and polycrystalline films from 350 nm down to 100 nm. The thickness dependencies of the intrinsic and reversible domain wall contributions among the film types are modest and within 10% of one another. The irreversible Rayleigh coefficient, is much more thickness dependent in epitaxial films than in polycrystalline films. This result, combined with the temperature dependence of ε_r, demonstrates that the majority of enhancement in the dielectric properties of the epitaxial films with increasing thickness is associated with increased irreversible domain wall motion.

Table 4-2: Summary of differences in the percent changes in various dielectric properties upon thickness scaling from 350 to 100 nm thick epitaxial and polycrystalline 70PMN-30PT films.

	Intrinsic contributions	$\frac{\partial \varepsilon_r}{\partial T}$ (°C^{-1})	Max. ε_r	T_{max} (°C)	ε_{init}	α' (cm/kV)
$\frac{\%\boldsymbol{reduction}\text{ in }\boldsymbol{epi.\ films}}{\%\boldsymbol{reduction}\text{ in }\boldsymbol{poly.\ films}}$ upon thickness reduction	*Modest difference*	4.3±0.5	1.6±0.05	0.63±0.05	1.1±0.1	2±0.2

Quantities associated with domain wall motion are more thickness dependent in epitaxial films, a result that would be consistent with a model in which interfacial domain pinning dominates. Lacking any large angle grain boundaries, the volumes of material within the epitaxial films with high defect concentrations are likely confined near the interface, where PMN-PT exhibits intermixing with the $SrRuO_3$ bottom electrode (as seen in Figure 4-7). Supporting the high crystallinity away from the interface are the high dielectric permittivities for PMN-PT films in this thickness range.[192,236] Given the Rayleigh data, it is believed that a classic dead layer model is too simplistic to describe a case where strong thickness dependence is exhibited only in extrinsic contributions.

In addition to interfacial layers, polycrystalline films have large angle grain boundaries which have been observed to be strong pinning sites in PZT[139,140,142] and $BiFeO_3$.[138] The thickness-dependent grain size in the oriented films may thus introduce thickness dependence in the functional properties.[231] Coupled with the finite degree of misoriented material present in polycrystalline films, the relatively high density of domain wall pinning sites is maintained through the film thickness, effectively reducing the small signal response and the corresponding thickness dependence.

It is notable that the difference in T_{max} and the bulk T_C is higher in the polycrystalline films. These results are consistent with the polycrystalline films having higher defect concentrations.[192] Another factor which could influence T_{max} is chemical inhomogeneity which has been observed in several chemical solution deposited ferroelectrics.[174,196,249,250] The smaller grain sizes in PMN rich films (shown in Figure 4-18) imply that unit cells with Mg and Nb at the B-site nucleate more readily on Pt than those with Ti. Development of such regions of PMN rich phases in deposited 70PMN-30PT is a potential factor in the lowered T_{max}, as pure PMN exhibits a T_{max} of ~0°. [49] It is noted, however, that the EDS data of Figure 4-7 does not resolve a strict layer-by-layer segregation of the PMN and PT phases. Therefore, if phase separation does occur, it likely develops on a local lateral length scale in the first deposited layer on Pt.

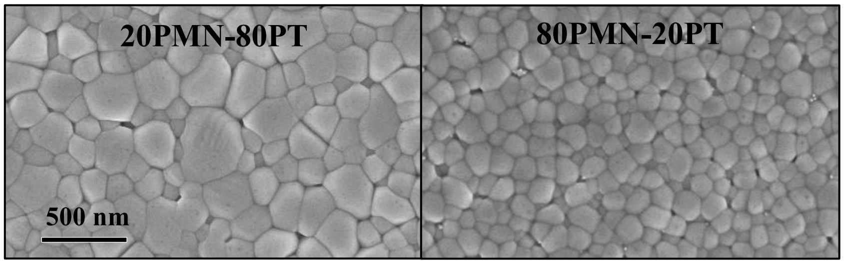

Figure 4-18: Top-down SEM micrographs depicting grain sizes of 20PMN-80PT and 80PMN-20PT thin films grown on Pt to a thickness of 200 nm grown simultaneously under identical processing conditions.

A final note on the thickness dependence of ε_r is regarding the dielectric behavior above the bulk Curie temperature, where the material should be paraelectric with no domain contributions. Differences in ε_r as a function of thickness are maintained above T_C is both films series, where domain contributions should be extinguished, despite the weaker thickness dependence of the intrinsic component. These differences as a function of thickness above T_C could be related to residual ferroelectricity, as observed in $Ba_{1-x}Sr_xTiO_3$.[251] Given the finite degree of relaxor character of the films, this would suggest that the properties should converge closer to the Burns temperature (T_d), which is which is ~347 °C in bulk PMN ceramics.[47,48] The temperature dependent data from the epitaxial films project convergence about 100 °C below the Burns temperature of PMN. The polycrystalline films, however, maintain differences in ε_r up to a projected temperature of ~550 °C. This may suggest a higher Burn's temperature, the origin of which is unknown at present time.

4.3.3 Piezoelectric characterization

Examples of the Pseudo-Voigt fits to the X-ray data as a function of field are shown in Figure 4-19 for a 350 nm thick polycrystalline film. As summarized in Table 4-1, the residual between the fits and experimental data is very low and concentrated at the highest intensity of the peak. Also shown in Figure 4-19 are the shifts in peak position as a function of electric field for the 350 nm thick polycrystalline film. A significant difference was observed in comparing polycrystalline and epitaxial films. For the oriented films, the 002 peak remained largely symmetric in shape as the field increased; the peaks shift to larger d spacing and decrease in intensity with electric field. Comparable behavior was observed at lower fields for the epitaxial films. However, at higher fields, the X-ray patterns of the epitaxial films showed clear evidence for peak splitting.

The recorded 002 peaks and the corresponding Pseudo-Voigt fits are presented as a function of electric field for all polycrystalline (up to breakdown) and epitaxial (up to fields where peak splitting was observed) film thicknesses in Figure 4-20 and Figure 4-21, respectively, as a function of d-spacing.

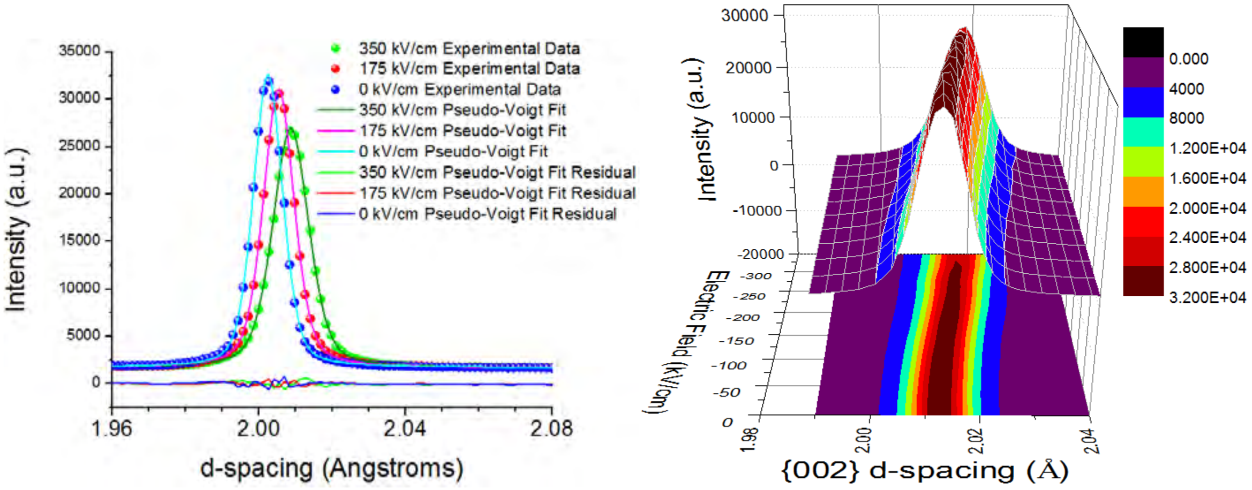

Figure 4-19: (Left) Example of 002-peak fitting for a 350 nm thick polycrystalline film under 0, 175, and 350 kV/cm DC excitation. The data were fit with Pseudo-Voigt functions with the difference between the experimental data and fit shown at the bottom of the figure. On the right is the visualization of the peak intensity for the strain in 002 d-spacing of the 350 nm thick PMN-PT as a function of electric field from 0 kV/cm to 350 kV/cm.

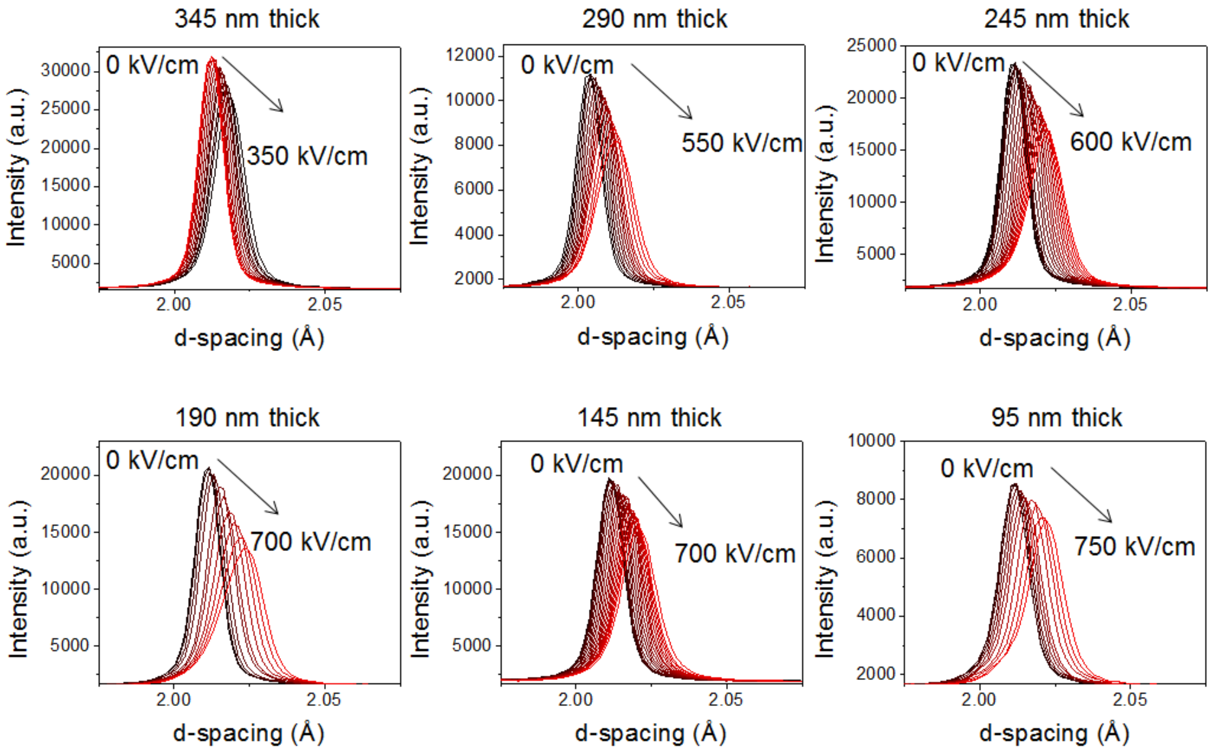

Figure 4-20: Experimental diffraction data taken from beamline 11-ID-C and Pseudo-Voigt fits for the 002 peaks of the polycrystalline 70PMN-30PT thickness series on platinized Si substrates plotted as a function of d-spacing.

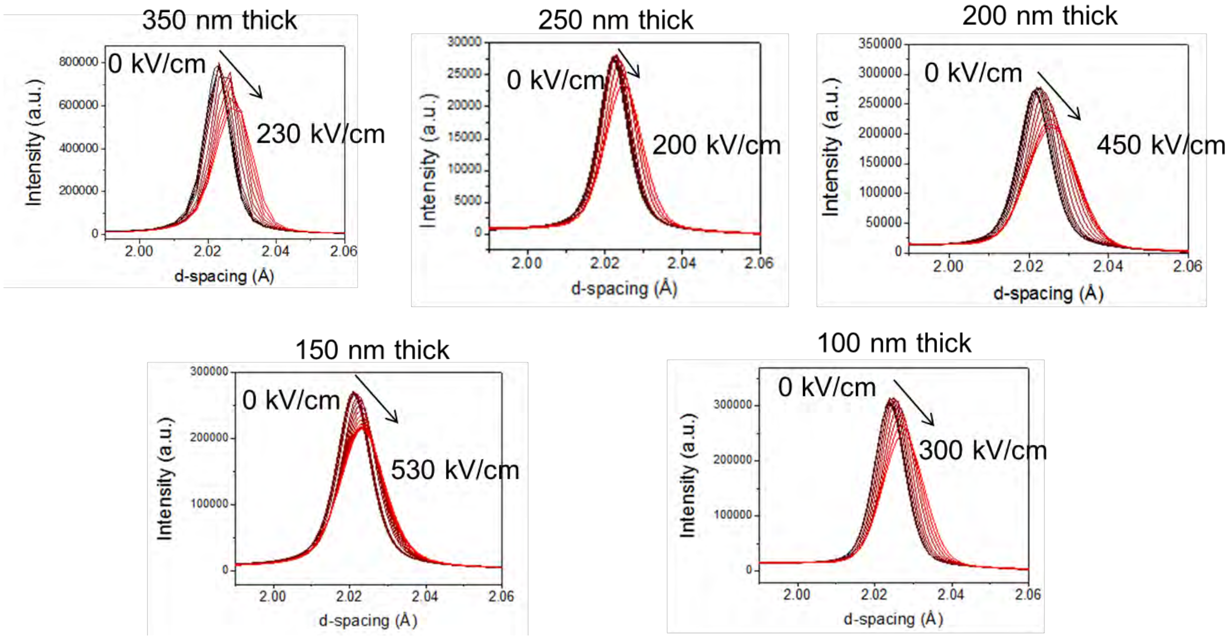

Figure 4-21: Experimental diffraction data taken from beamline 11-ID-C and Pseudo-Voigt fits for the 002 peaks of the epitaxial 70PMN-30PT thickness series on $SrRuO_3/SrTiO_3$ substrates plotted as a function of d-spacing.

Figure 4-22 presents the change in 002 peak FWHM and the integrated intensity of the 002 peaks normalized to the area of the peak under 0 kV/cm for the polycrystalline and epitaxial films. The integrated intensity remains constant over the measured field range, indicating that the broadening in FWHM is correlated to the reduction of peak intensity that is observed in Figure 4-20 and Figure 4-21. Below ~60 kV/cm there is no significant change in the peak shape in either film type, with FWHM and the intensity remaining constant. As seen in Figure 4-23 for the epitaxial films as an example, the sub-60 kV/cm region where no significant changes in FWHM are observed corresponds to the areas where both polarization and the instantaneous $d_{33,f}$ coefficient exhibit the steepest dependence on electric field.

The origin of the observed behavior in the 002 peak as a function of field is believed to be a function of both polarization switching and the intrinsic piezoelectric response. In the absence of an external electric field, a rhombohedral perovskite unit cell has 8 degenerate polarization directions. An external field applied along the c-axis of the unit cell, for example, induced domain wall motion which grows the up-pointing domains at the expense of down-pointing domains. While such domain switching does not result in a change in the c-lattice parameter, it does increase the volume fraction of aligned domains which do increase in (002) d-spacing. Therefore, the out-of-plane strain in (002) d-spacing can be mostly attributed to intrinsic effects, including polarization rotation, at sufficiently high fields. Above 60 kV/cm, the slope in P-E hysteresis loop flattens and the 002 peak FWHM broadens suggesting that the strain in the films during this process in inhomogeneous, potentially related to thickness effects.

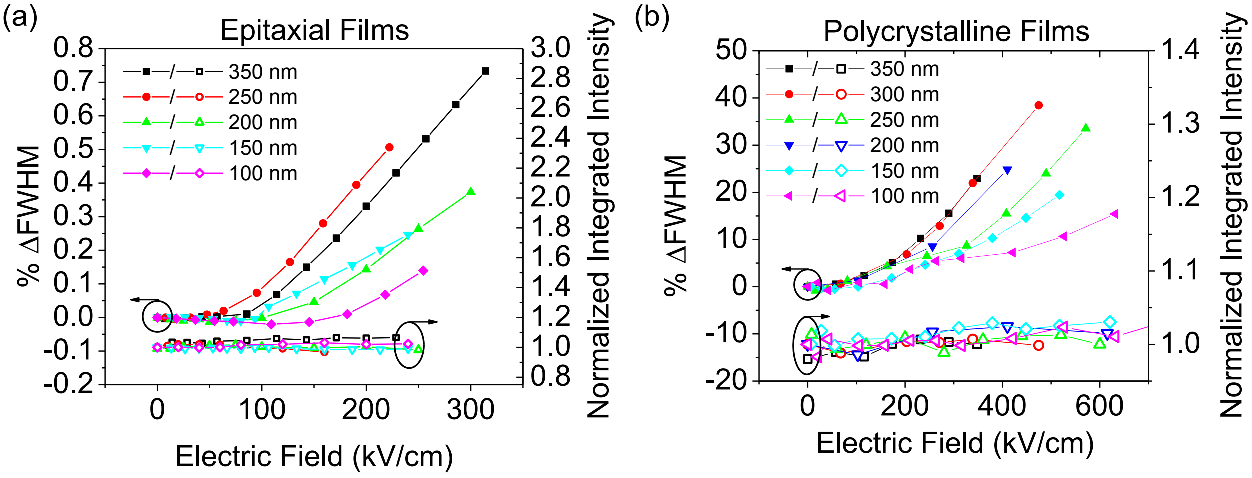

Figure 4-22: Summary of the changes in 002 peak shape as a function of electric field for the epitaxial (a) and polycrystalline (b) 70PMN-30 PT thickness series.

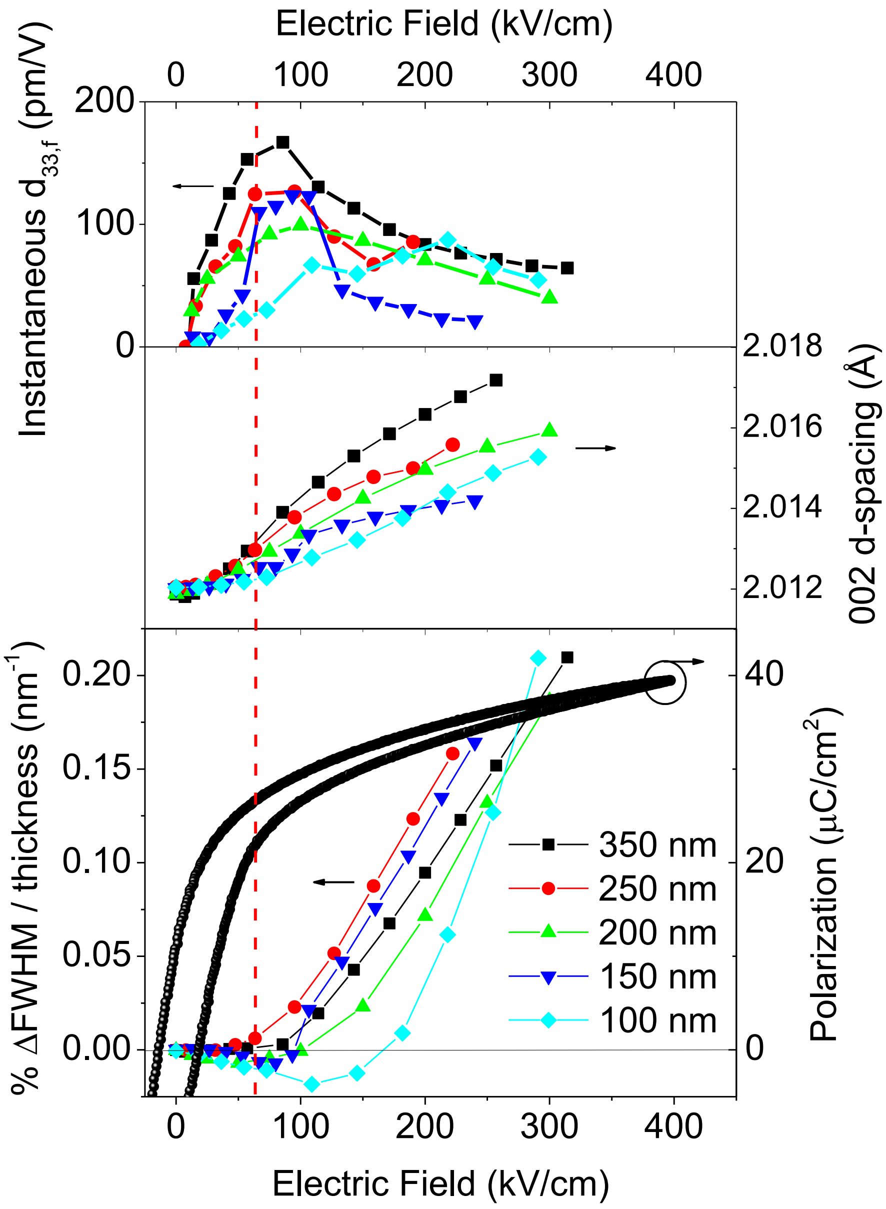

Figure 4-23: The relative changes in the FWHM of the epitaxial 70PMN-30PT 002 peaks from films 100-350 nm in thickness along with their changes in d-spacing, instantaneous $d_{33,f}$, and the polarization hysteresis loop of the 350 nm thick film as functions of electric field. The P-E loop was recorded at 1 kHz while the changes in 002 peak shape were recorded under DC bias.

The thickness dependence of the clamped piezoelectric coefficient, $d_{33,f}$, as determined by DC electric field induced shifts in the {002} d-spacing during XRD at fields below 300 kV/cm, is shown in Figure 4-24. The stronger thickness dependence of the epitaxial films, which was also evident in the dielectric properties, results in a ~40% reduction in the $d_{33,f}$ of the 350 nm thick film upon scaling to 100 nm. At thicknesses of 200 nm and below, the epitaxial and polycrystalline films exhibit very similar $d_{33,f}$ values of 70 – 90 pm/V. This reduction in the epitaxial film response mimics the thickness dependence of the reversible contributions to relative permittivity. As was also seen in the dielectric characterization, the polycrystalline films exhibit a smaller thickness dependence, with only ~25% reduction in the $d_{33,f}$ coefficient. It will be shown below that the observed thickness dependence in $d_{33,f}$ is not related to the ferroelectric portion of the film, but can be attributed to interfacial layers which drop the electric field which is applied to the ferroelectric layer.

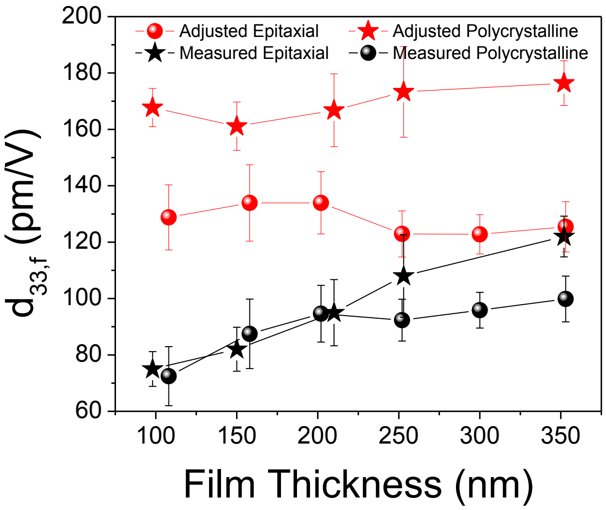

Figure 4-24: Measured piezoelectric coefficient, $d_{33,f}$, of epitaxial and polycrystalline PMN-PT films as a function of thickness as measured by shifts in {002} d-spacing under applied electric field (black symbols, solid lines) and the adjusted $d_{33,f}$ for the same films from accounting for the voltage drop across an interface layer of lower permittivity (fit by the series capacitor model) with thickness corresponding to the intermixed layer observed via EDS (red symbols, dotted lines). It should be noted that the Lefki-Dormans approximation of the $d_{33,f}$ a fully clamped film determined from the electromechanical and elastic constants of the free single crystal and Equation 2-1 is ~250 pm/V.

The thickness dependence of $d_{33,f}$ was modeled to test the validity of the series-capacitor model in these films. A linear fit of the 0 V_{DC} dielectric data was plotted as film thickness/ε_r vs. film thickness, shown in Figure 4-25. The linearity of this data supports the presence of a series capacitor structure in the film, stemming from the interfacial layer of intermixed composition observed in the EDS spectra shown in Figure 4-7. The total effective capacitance of the film is therefore given by $\frac{\mathbf{1}}{\boldsymbol{C_{total}}} = \frac{\mathbf{1}}{\boldsymbol{C_1}} + \frac{\mathbf{1}}{\boldsymbol{C_2}}$, which can be rearranged to be $\frac{t_{total}}{\varepsilon_{eff}} = \frac{1}{\varepsilon_{bulk}} t_{total} + t_{int}\left(\frac{1}{\varepsilon_{int}} - \frac{1}{\varepsilon_{bulk}}\right)$. The measured thicknesses of the respective interfacial layers observed in EDS, along with the slopes and intercepts of the data in Figure 4-25, were used to extract the $thickness/\varepsilon_r^{int}$ ratios for the two film sets which are ~0.033 nm and ~0.039 nm for the epitaxial and polycrystalline films, respectively. From this, the fraction of the applied voltage (V_{app}) which drops across the interfacial layer of the film is given by:

$$V_{drop} = V_{app}\left(\frac{\varepsilon_r^{eff}}{t_{eff}} * \frac{t_{int}}{\varepsilon_r^{int}}\right) \qquad \text{Equation 4-2}$$

where ε_r^{eff} is the effective measured permittivity of the capacitor stack of thickness t_{eff}, and ε_r^{int} is the relative permittivity of the interface of thickness t_{int}. From

$$V_{drop} = V_{app}\left(\frac{\varepsilon_r^{eff}}{t_{eff}} * \frac{t_{int}}{\varepsilon_r^{int}}\right)$$

Equation 4-2Equation 4-2 and Figure 4-26, it is seen that V_{drop} is thickness dependent.

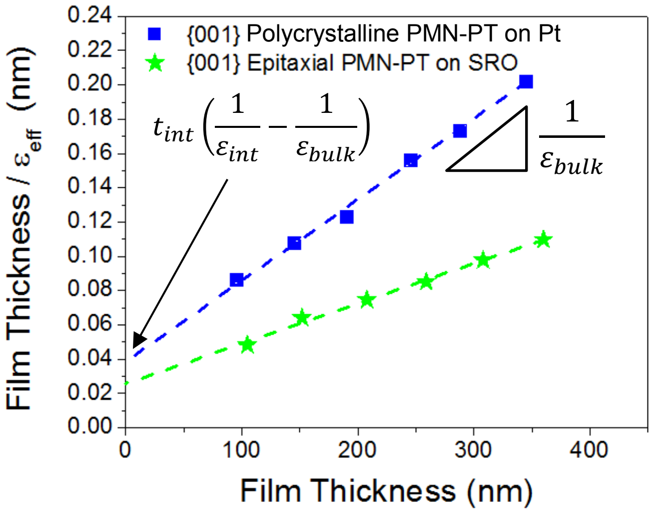

Figure 4-25: PMN-PT film thickness divided by the effective permittivity of the series capacitor structure vs. film thickness. Linearity of the data supports the series capacitor model where the total effective capacitance is given by $\frac{1}{C_{total}}=\frac{1}{C_1}+\frac{1}{C_2}$ which can be rearranged to yield $\frac{t_{total}}{\varepsilon_{eff}}=\frac{1}{\varepsilon_{bulk}}t_{total}+t_{int}\left(\frac{1}{\varepsilon_{int}}-\frac{1}{\varepsilon_{bulk}}\right)$.

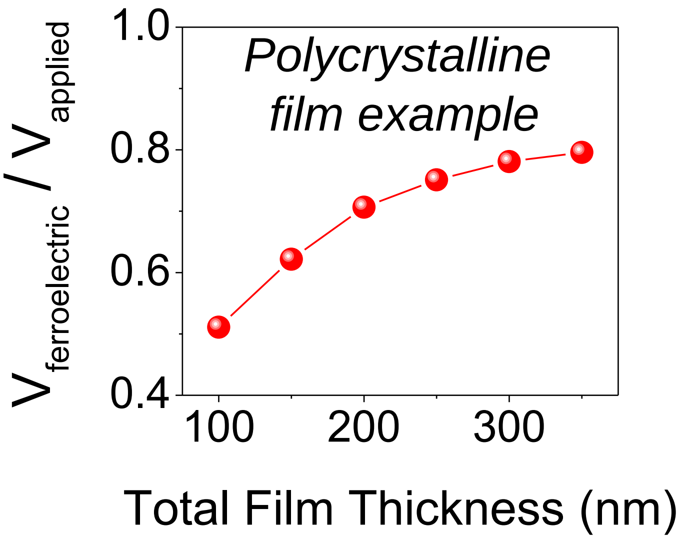

Figure 4-26: Fraction of externally applied voltage which drops across the ferroelectric portion of the film. The fraction departs from unity due to interfacial capacitance that is detected through relative permittivity measurements as a function of thickness.

The measured $d_{33,f}$ coefficients shown in Figure 4-24 were re-calculated based on the voltage applied to the piezoelectric layer, inducing the measured d-spacing shifts, after the voltage drop across the low permittivity interface layer. The adjusted data are shown as red symbols and dotted lines in Figure 4-24. The adjusted piezoelectric responses are thickness independent, supporting the model of the interface having a significantly reduced ε_r owing to strongly pinned domain walls and reduced intrinsic response due to intermixing. Furthermore, the adjusted $d_{33,f}$ value for the epitaxial films approaches the predicted fully clamped piezoelectric value of 250 derived from the Lefki-Dormans model[79] with single crystal 70PMN-30PT materials constants.[89] The polycrystalline films exhibit lower $d_{33,f}$ values which may be attributed to the high tensile stress state in the films on Si and presence of domain wall pinning grain boundaries.

4.3.4 Field-induced phase transitions

MPBs serve to reduce the energy barrier separating two or more polar phases, thereby making domain reorientation under a stimulus easier. In addition to these decreased energy barriers, MPB compositions of relaxor-based ferroelectric crystals exhibit anomalously high piezoelectric properties due in part to the polarization rotation mechanism. Furthermore, sufficiently high stress or electric fields can induce full phase transitions in relaxor-based crystals.[60,67] With the addition of a mechanical bias to bring rhombohedral $Pb(In_{1/2}Nb_{1/2})O_3$-$Pb(Mg_{1/3}Nb_{2/3})O_3$-$PbTiO_3$ (PIN-PMN-PT) crystals to the brink of an orthorhombic phase stability, these large strain-producing phase transitions have been leveraged for magnetoelectric energy harvesters which exhibit 0.5% strain under only 1 kV/cm.[252,253]

Microelectromechanical systems employing ferroelectric thin films would similarly benefit from such high strain under low field, yet additional challenges are incurred. First, tensile stresses imposed by the commonly used Si substrate favor the in-plane components of a polarization vector, reducing the stability of domain with out-of-plane polarization (e.g tetragonal *c*-domains in {001} oriented films). Additionally, increased defect densities stemming from large angle grain boundaries, misoriented material, and the relatively low thermal budget used for crystallization of polycrystalline films could strongly pin any phase boundary from traveling through the lattice. The *in situ* synchrotron diffraction experiments on the polycrystalline thickness series exhibit no such phase transition under fields exceeding 700 kV/cm. The high film crystallinity of the epitaxial films, however, coupled with the reduced tensile stress from being grown on $SrTiO_3$ rather than Si, did enable such field induced phase transitions, as is presented below.

First, Figure 4-27 demonstrates the change in the Bayesian Information Criterion (BIC)[254] for 002 peak fitting as a function of applied voltage for the 350 nm thick epitaxial film. With DC fields greater than ~315 kV/cm (11 V), the BIC is significantly reduced when two peaks are used to fit the 002 peak. The reason for this change is attributed to a partial R→T transition occurring near 300 kV/cm for 350 nm, 250 nm, and 100 nm thick films. The reason why these films exhibit the phase transition, while the 150 and 200 nm films do not, is believed to be related to film quality. Figure 4-28 depicts the FWHM (in d-spacing, Å) of all epitaxial films as recorded by the integrated 2-D diffraction patterns. The films which exhibit peak splitting are those with FWHM below 0.0097 Å; the most pronounced R→T transition is observed in the 350 nm thick film which also shows the lowest FWHM in the epitaxial film set. As shown in Figure 4-29, the phase transition begins with the development of a shoulder on the 002 rhombohedral peak at higher d-spacing. The integrated peak intensity increases and further peak splitting develops with increasing electric field, as shown in Figure 4-30. The summation of the integrated intensities from all of the apparent {002}-type peaks at a given electric field is essentially constant, as expected.

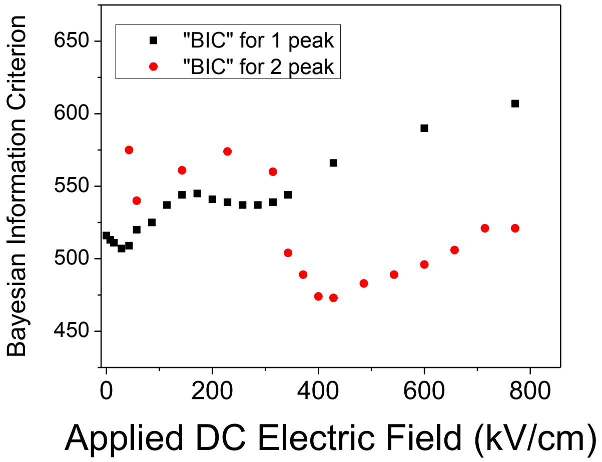

Figure 4-27: Bayesian Information Criterion, used as a model selection tool, describing the quality of fit from a one or two peak Pseudo-Voigt function with the experimental X-ray diffraction data.

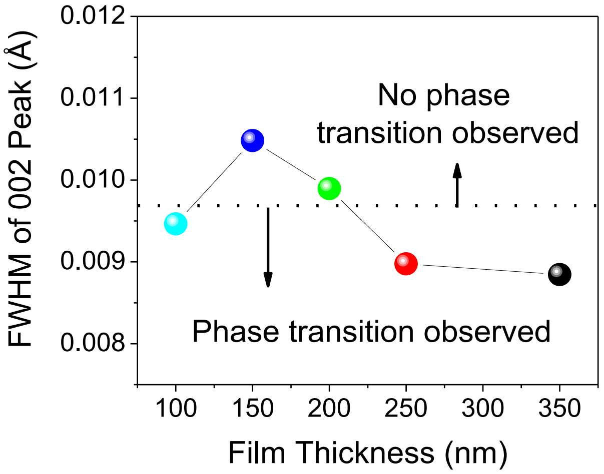

Figure 4-28: 002 peak FWHM of the epitaxial 70PMN-30PT films. The FWHM of each film was taken from the Pseudo-Voigt fits of the 0 kV/cm data which was recorded and integrated over the 8° wide azimuthal sector from the 2-D area detector.

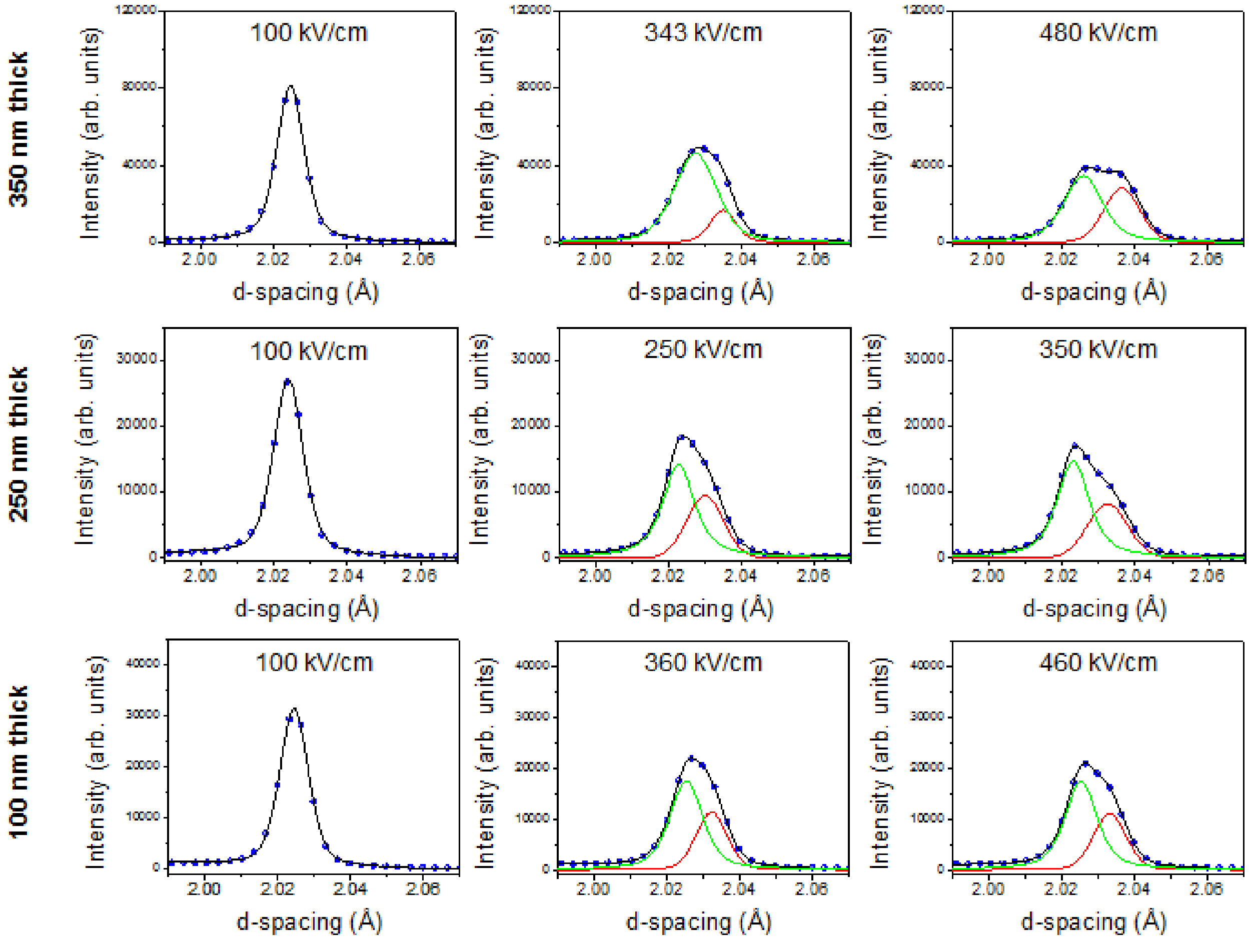

Figure 4-29: Pseudo-Voigt peak fits for the in-situ diffraction experiments. Shown are the fit data for the zero field, rhombohedral crystal case, through the R→T phase transition occurring near 300 kV/cm for 350 nm, 250 nm, and 100 nm thick epitaxial films.

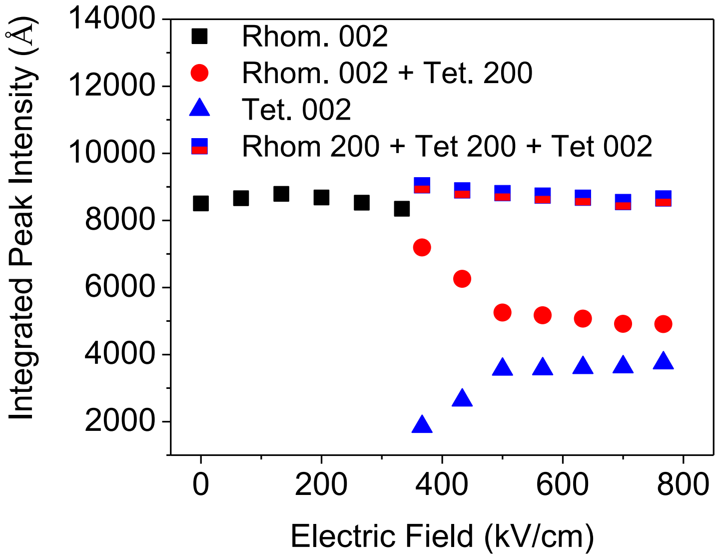

Figure 4-30: Integrated peak intensity as a function of applied DC field for the rhombohedral 002 peak (for fields below 300 kV/cm), the tetragonal 002 domain peak, and the 200 tetragonal/002 rhombohedral convoluted peak at fields above the phase transition. The sum of integrated intensities is approximately field independent.

In the 350 nm thick film, the second peak develops with d-spacing that matches well with the expected d-spacing of a tetragonal c-domain under 0 kV/cm, as shown in Figure 4-31. The (002) d-spacing of the field-induced phase continues to increase under field with an effective piezoelectric coefficient of ~100 pm/V. It should be noted that as the tetragonal c-domain develops, the original rhombohedral peak position shifts to smaller d-spacing. This is because the film develops *a*-domains to reduce the spontaneous stain in the film upon an R→T transition. Therefore, the "rhombohedral" peak above 300 kV/cm is actually a convolution of rhombohedral {002} domains and tetragonal (200) domains. Similar conclusions were made by Kovacova *et al.* in PZT which developed a tetragonal phase from a monoclinic matrix.[255] Figure 4-32 depicts the 002 d-spacing as a function of electric field for all epitaxial film thicknesses studied.

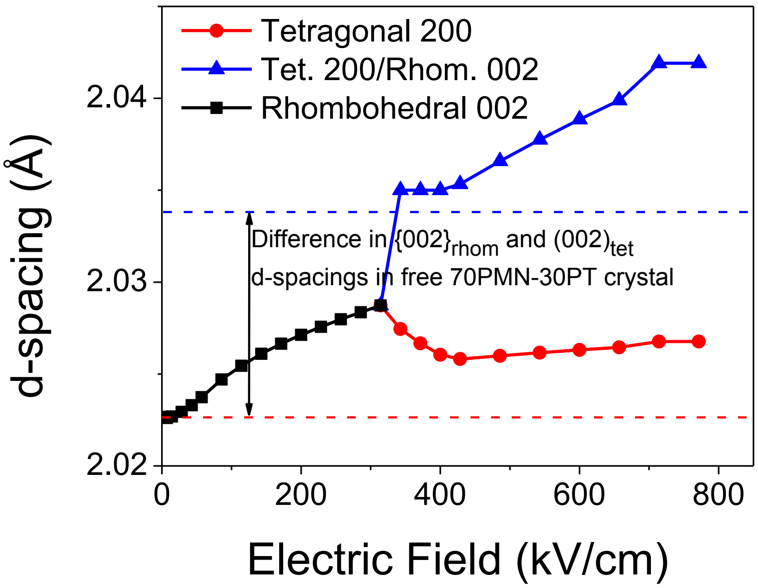

Figure 4-31: d-spacing for the {002} family of planes for the three observed phase variants in 70PMN-30PT thin films under DC electric fields.

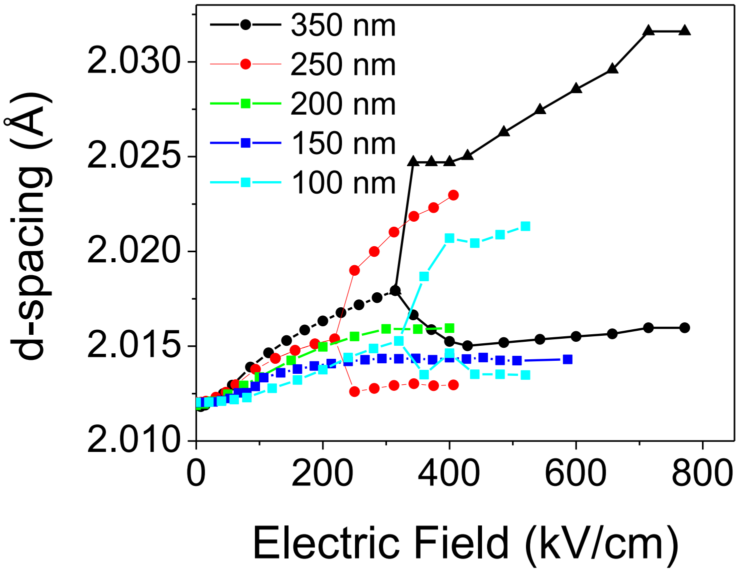

Figure 4-32: The high field diffraction data of all epitaxial films measured at beamline 11-ID-C. Near 300 kV/cm, the three studied films with the lowest 002 FWHM (350, 250, and 100 nm thick films) exhibit splitting of the 002 peak as seen in Figure 4-29.

A signature of a phase transition was sought in the dielectric behavior of the 350 nm thick epitaxial film as a function of DC bias. Figure 4-33 shows the relative permittivity and loss tangent recorded from 0-525 kV/cm DC bias with a 30 mV AC-signal at 1 kHz. The data were also recorded with increasing temperature, up to 120 °C, to provide thermal energy to facilitate the phase transition. However, no anomaly in the dielectric data is observed. This suggests that the global response remains dominated by the rhombohedral phase. To verify this, the volume fraction of rhombohedral PMN-PT that switched to the tetragonal phase was estimated using Equation 4-3 where I_{Thkl} and I_{Rhkl} are the integrated intensities of the given hkl reflection of the tetragonal and rhombohedral phases, respectively, and the I'quantities in the denominators are the corresponding reference intensities from the powder diffraction files. These normalizations and leading factors of three and two for the R002 and T200 peaks, respectively, account for differences in the structure factors and multiplicity of the symmetry related orientations among the relevant phases.

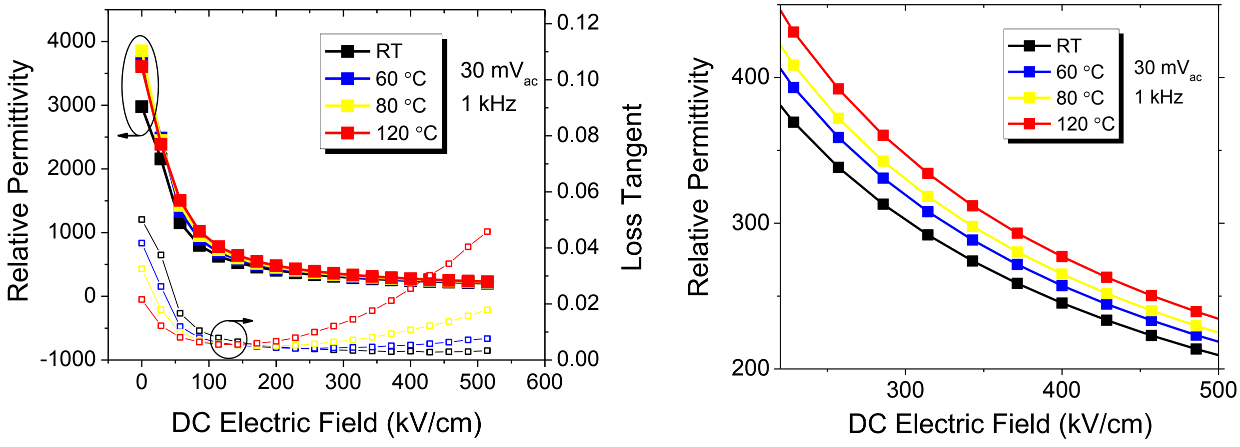

Figure 4-33: Relative permittivity and loss tangent as a function of DC bias for a 300 nm thick epitaxial 70PMN-30PT film from 0-550 kV/cm (left) and from 225-500 kV/cm (right) where the phase transition is expected to occur. The data were taken as a function of temperature as a means to increase the energy in the system.

$$\nu_{T002} = \frac{\frac{I_{T002}}{I'_{T002}}}{\frac{I_{T002}}{I'_{T002}} + \frac{3I_{R002}}{I'_{R002}} + \frac{2I_{T200}}{I'_{T200}}} \qquad \text{Equation 4-3}$$

Consider the data at 343 kV/cm, where the transition occurs in the 350 nm thick film and the newly developed tetragonal c-domains exhibit d-spacings that agree with the free, zero field (002) d-spacing of the c-domain. Using Equation 4-3 it is estimated that the volume fraction of R→T switching is ~13 vol. %. As the peak splitting develops, the rhombohedral 002 peak shifts to lower d-spacing. Because tetragonal a-domains have a lower 200 d-spacing than rhombohedral 002 d-spacing, it is possible that the reduction in R002 d-spacing that develops with the peak splitting is due to some of the material which did not switch to tetragonal *c*-domains in fact switched to tetragonal *a*-domains perhaps to relieve stresses incurred by the transition. A modified Equation 4-3 can be used to estimate the volume fraction of material which switch to *a*-domains. Linearly extrapolating the pure R002 peak from the 315 kV/cm data point yields an expected R 002 d-spacing of 2.0291 Å at 343 kV/cm. From the d-spacings listed in the relevant PDF cards, it follows that ~8% of the material that did not transition to the tetragonal c-domain switched to tetragonal a-domain, yielding the observed 2.0274 Å d-spacing. With over 85% of the material remaining rhombohedral, it is reasonable that there is not a strong signature of the phase transition in the dielectric data at different dc biases.

4.4 Conclusions

Thin films of 70PMN-30PT ranging in thickness from 100-350 nm were grown via chemical solution deposition in polycrystalline, {001}-oriented and {001}-epitaxial form on platinized Si substrates $SrRuO_3/SrTiO_3$ substrates, respectively. Both film types exhibited similar intrinsic dielectric responses. EDS measurement across the interface revealed, however, ~3-6 nm thick regions of graded composition. The functional properties of the epitaxial films suggest that pinning of domain wall motion at the interface is a significant factor in the observed thickness dependence. The Rayleigh behavior demonstrated that irreversible domain wall motion is strongly thickness dependent in the epitaxial films. It is believed that large angle grain boundaries may be responsible for a higher density of pinning sites though the thickness of the polycrystalline films, reducing the thickness dependence.

The thickness dependence of the piezoelectric coefficient mimicked that of the dielectric behavior. Correcting for the presence of interfacial layers largely eliminates the thickness dependence of the piezoelectric properties. High field piezoelectric characterization revealed a field-induced rhombohedral to tetragonal phase transition in epitaxial films with FWHM below 0.0097 Å. With further work to determine a means of switching a larger volume fraction of the material, a highly scaled device may leverage the phase transition for increased functionality.

Chapter 5

Lateral Scaling of 70/30 Lead Magnesium Niobate-Lead Titanate Thin Films

Portions of this chapter are reproduced from: R. Keech, S. Shetty, M.A. Kuroda, X. Hu Liu, G.J. Martyna, D.M. Newns, and S. Trolier-McKinstry, "Lateral scaling of $Pb(Mg_{1/3}Nb_{2/3})TiO_3$-$PbTiO_3$ thin films for piezoelectric logic applications," J. Appl. Phys., ***115****, [23], 234106, (2014).*

5.1 Introduction

The high piezoelectric coefficients of {001}-oriented relaxor-based ferroelectric materials near a morphotropic phase boundary composition have been shown to improve the functionality of sonar systems and medical ultrasound transducers.[2,155,211,256] These properties are also attractive for applications requiring thin film piezoelectrics. However, clamping effects imposed on the film by the substrate reduce the functional properties by about an order of magnitude relative to single crystals ($d_{33} > 2000$ pm/V and $\varepsilon_r > 8000$).[78,108,165,192,257,258] The property reductions in continuous thin films are associated with a number of factors. Stress in thin films grown on a substrate of a dissimilar thermal expansion coefficient, for example, can destabilize specific polarization directions.[87,166,237,259] Additionally, piezoelectric material beneath an island top electrode is bonded to non-actuated material, thereby elastically constraining the ideal piezoelectric deformation. Finally, any out-of-plane displacement is limited by the coupled and frustrated lateral contraction, proportional to the d_{31} coefficient, due to attachment to the thick, passive substrate. For example, Zhang *et al.* demonstrated that the relative dielectric permittivity in {001} poled 67PMN-33PT single crystals dropped to 680 from 8200 upon imposing a strain-free boundary condition.[260] Circumventing these property-reducing mechanisms is the focus of this chapter.

Several studies have shown that the functional response in ferroelectric thin films can be at least partially declamped from the substrate so that a larger fraction of the bulk properties can be recovered. Removal or thinning of a Si substrate in the microfabrication of cantilevers and diaphragms, for example, can increase the functionality and figures of merit for numerous MEMS devices including vibrational energy harvesting,[261,262] biological sensors,[263,264] and transducers.[265,266] Rayleigh measurement of the relative permittivity[32] and X-ray diffraction experiments[30] demonstrate that the property enhancement is linked to increases in both intrinsic and extrinsic contributions to the ferroelectric behavior upon substrate undercut.

Other MEMS devices, such as ferroelectric random access memory (FeRAM) and the piezoelectronic transistor[25,163] would similarly benefit from declamping, but require the structural integrity offered by continuous thin films on rigid substrates. In these cases, lateral subdivision of a blanket film, generating free sidewalls, can also declamp the dielectric, piezoelectric, and ferroelectric response of thin films.[94,108]

Experimental results on declamping through lateral subdivision of blanket piezoelectric thin films have been reported for films patterned via reactive ion etching or focused ion beam milling.[35,36,93,108,267–270] In both cases, care must be taken to limit patterning damage which can reduce piezoelectric response through domain wall pinning defects and redeposition of sputtered material.[106,267,271–275] It has been widely reported that plasma-based etching processes can induce significant damage in ferroelectric thin films.[40,105,274] Especially in PMN-PT films, the complex chemistry, with four cations, all of which have different bond strengths with oxygen, can cause difficulty in stoichiometric removal of the material.[106] Property degradation in etched ferroelectric and piezoelectric films stems from the fact that piezoelectric properties depend critically on stoichiometry, grain morphology, impurities and defect concentrations, all of which are altered in a finite volume near etched sidewalls.[25, 27] These defects, as well as any formation of reactant residue, can increase the number of domain wall pinning sites and increase the energy barriers for domain wall motion.[32,84,277] Finely patterned features, in particular, are more susceptible to property degradation from a given process since the proportion of etch-damaged material to the undamaged volume increases.[276] The degradation of properties can be observed in pinching of the polarization-electric field hysteresis loops,[274,278] clockwise rotation of P-E loops,[40,273,279,280] reduction in crystallinity,[40] and reduced lifetime, reliability,[281,282] and dielectric and piezoelectric constants.[84,275,283]

Once patterning damage is reduced, it was shown that stresses imposed on a thin film from the mismatch in thermal expansion coefficient with the substrate can be partially relieved by lateral patterning.[36,108] Bühlmann *et al.* proposed that the relaxed stress state in 70-100 nm wide features dry etched in 200 nm thick tetragonal PZT films grown on $SrTiO_3$ increased the achievable *c*-domain density, as tensile stresses which stabilized *a*-domain formation was removed.[36] In addition to changes in the stress state with lateral scaling, Nagarajan *et al.* report a significant increase in 90° domain wall motion in 1 μm thick 20/80 PZT island-capacitors with a 1:1 aspect ratio fabricated by ion beam milling. The patterned films exhibited a doubling in the remanent polarization and tripling of the $d_{33,\,\mathrm{eff}}$.[94] A 120 nm thick PZT film of the same composition exhibited a 2-fold increase in $d_{33,f}$ upon scaling to a 0.25 μm x 0.25 μm island structure. [268] Similar observation of increased domain wall motion were made from the Rayleigh response of the dielectric permittivity in systematically scaled PMN-PT films; a tripling of the irreversible domain wall motion was reported on scaling to aspect ratios approaching 1:1.[108] Missing from the literature are data on the local declamping of patterned structures as a function of position. This is partially due to the difficulty in reporting quantitative piezoelectric response with submicron lateral resolution. A detailed description of local $d_{33,eff}$ characterization techniques can be found in the article by Shetty *et al.*[284]

The excellent lateral resolution of PFM stems from the fine tip radius, making it well suited for local declamping characterization. However, the cantilever tip geometry may also introduce error in $d_{33,eff}$ characterization associated with inhomogeneous and often poorly quantified electric fields[285,286] stemming from tip-film contact mechanics.[287–289] This limits the vertical resolution of PFM to ~1pm, generating upwards of 40% error in detecting displacements from piezoelectric strains in thin films.[284,285,290] Vertical resolution can be improved two orders of magnitude by employing laser interferometery.[291] Until recently,[284] however, the lateral resolution of laser interferometry was typically greater than 50 μm due to laser spot sizes and difficulty in aligning the two incident lasers needed for double beam interferometry. Imperfect alignment can produce large error associated with actuation-induced substrate bending.[269,291,292]

X-ray diffraction is another technique by which strain may be determined with excellent resolution. Depending on crystal quality, high resolution synchrotron diffraction experiments, for example, can determine field induced changes in d-spacing with precision to 10^{-5}Å.[293] For local characterization of lattice plane spacing, focused X-ray beams, such as those available at the nanoprobe beamline (2-ID-D) at the Advanced Photon Source (APS) at Argonne National Laboratory, can be employed. This beamline can achieve a focused X-ray spot size of 240 nm (as defined as the FWHM of the beam intensity). Furthermore, the beam can be translated across a patterned structure in sub-micron steps with excellent control and repeatability.[293]

In an effort to further develop the roadmap for ferroelectric thin film scaling, this chapter presents the systematic characterization of the low and high field dielectric properties (polarization-electric field loops, Rayleigh analysis, and Preisach models). Additionally, the local mapping of the partially declamped $d_{33,\,eff}$ along patterned {001}-oriented 70PMN-30PT “arm” structures by two experimental characterization techniques (piezoresponse force microscroscopy and synchrotron X-ray diffraction experiments) is presented and compared to predictions made by finite element modeling.

5.2 Experimental procedure

5.2.1 Finite element modeling

As can be gleaned from experiments reported throughout the literature, the degree of declamping which a patterned piezoelectric capacitor exhibits is related to the structure’s width:thickness aspect ratio (AR), with lower aspect ratios yielding higher functional properties. This outcome is predicted by finite element models based on the description of clamping of piezoelectric films by Lefki and Dormans[79] using the materials properties of {001}-oriented single crystals and ceramics.[89,294] In these models, prepared by Marcelo Kuroda of Auburn University in work performed in collaboration with Xiao-Hu Liu, Glenn Martyna and Dennis Newns, the piezoelectric features were placed on top of a thick Si substrate (thickness of Si >> thickness of the piezoelectric). Local modeling of the $d_{33,\,eff}$ coefficient (Figure 5-2 b-d) shows that the material near the sidewalls is more declamped than material towards the feature center. In aspect ratio’s greater than 1, the peak $d_{33,\,eff}$ is effectively constant, along with the rate of decay in $d_{33,eff}$ upon moving towards the feature center from the sidewall. This demonstrates that the mechanism of property enhancement with reducing aspect ratio of Figure 5-2a is an increase in volume fraction of material within ~500 nm of the free sidewall (in 300 nm thick films) where the majority of declamping occurs.

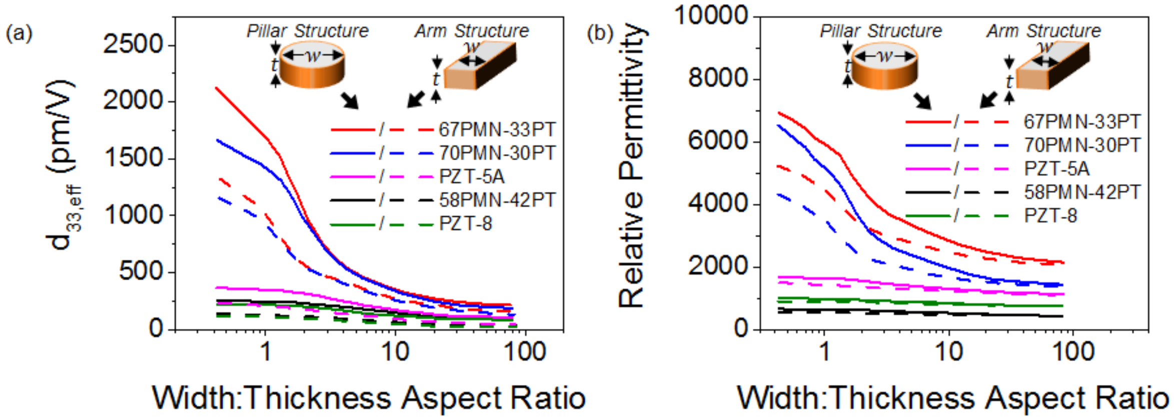

Figure 5-1: The finite element modeled longitudinal effective piezoelectric coefficient, $d_{33,\,eff}$, (a) and the relative permittivity (b) in laterally scaled 300 nm thick PMN-PT and PZT films of various compositions on platinized 550 µm thick Si for pillar and arm structures. Note single crystal $d_{33} \approx 2800$ pm/V and $d_{33,f}$ from Lefki-Dormans is ~250 pm/V.

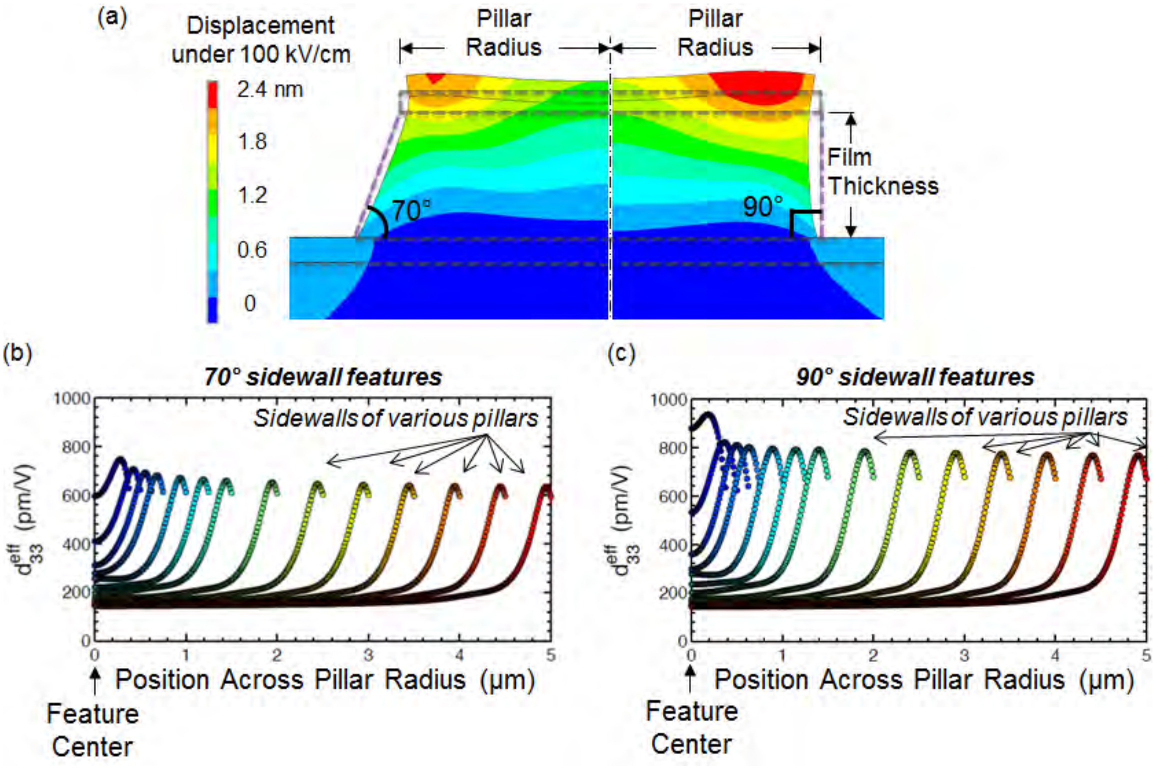

Figure 5-2: (a) The finite element modeled vertical displacement profile for pillar structures with under 100 kV/cm for the cases of 70° (left) and 90° (right) sidewall angles of 70PMN-30PT pillar structures on 550 μm Si. Parts (b) and (c) depict the $d_{33,f}$ coefficient as a function of position across pillar structures of various radii with 70° and 90° sidewalls, respectively.

There are several other noteworthy features of the modeled local declamping behavior. First, features with 70° sidewalls exhibit a maximum $d_{33,eff}$ about 15% lower than that of features with 90° sidewalls due to the lower effective electric field experienced in the sidewall regime. Additionally, pillar structures declamp more efficiently, producing larger piezoelectric responses than arm structures which are continuous in one dimension (and presumably partially clamped in this dimension). Finally, the maximum declamped $d_{33,eff}$ coefficient occurs ~100 nm from the sidewall; this is believed to be related to both the bending rigidity of the top metal layer (100 nm of Pt in these models) limiting strain at the free edge and inward curvature of the sidewall, visible in Figure 5-2: (a) The finite element modeled vertical displacement profile for pillar structures with under 100 kV/cm for the cases of 70° (left) and 90° (right) sidewall angles of

70PMN-30PT pillar structures on 550 µm Si. Parts (b) and (c) depict the $d_{33,f}$ coefficient as a function of position across pillar structures of various radii with 70° and 90° sidewalls, respectively. attributed to Poisson's ratio. Further experiments are necessary to determine relative significance of these hypothesized mechanisms.

5.2.2 Microstructural characterization

To realize the enhancements explained in the finite element models in a real material system, 300 and 350 nm thick {001} oriented 70PMN-30PT films (Lotgering factor > 0.99, see section 3.3 were grown via chemical solution deposition on commercial Pt/Ti/SiO_2/Si substrates (Nova Electronic Materials, Flower Mound, TX) by methods described in Chapter 3.[295] The microstructure of the 300 nm thick {001}-oriented polycrystalline 70PMN-30PT thin film was observed using a Field Emission Scanning Electron Microscope (Leo 1530 or Merlin, Carl Zeiss Microscopy GmbH, Jena, Germany). Both film surface and cross-sectional images were recorded. The crystal structure and orientation of the PMN-PT films was characterized using a PANalytical Empyrean x-ray diffractometer (PANalytical B.V., Almelo, The Netherlands) in the Bragg-Brentano θ-2θ arrangement with Cu Kα radiation. Lotgering factors were used to approximate the degree of orientation of the grown films.[186]

The local crystallinity following the patterning process was characterized by site specific cross sectional transmission electron microscopy (TEM). Samples were prepared by Ke Wang (Materials Characterization Laboratory, Materials Research Institute, The Pennsylvania State University) via focused ion beam (FIB) milling (*FEI Helios NanoLab DualBeam 660*. FIB-TEM samples were prepared using via an *in situ* lift-out technique. Prior to cross-sectional milling, a protective carbon layer was deposited over the region of interest by electron-beam deposition.

The starting FIB milling voltage was 30 kV to create a membrane of the cross sectional sample and thin the sample to electron transparency. The final milling voltage was stepped down to 2 kV to further thin the samples and minimize sidewall damage. EELS measurement in TEM showed the sample thickness was < 50nm.

The patterned sidewall structure and crystal quality were investigated using a FEI Titan3 dual aberration corrected scanning/TEM (S/TEM) instrument (FEI, Hillsboro, OR) operated at 200 kV. The microscope conditions for STEM imaging were 70 pA for beam current with a C2 aperture of 70 μm. A high angle annular dark field (HAADF, Fischione) detector with a collection angle of 51-300 mrad for Z-contrast imaging was used for STEM. The elemental mapping across each interface was performed in STEM mode by a SuperX Energy Dispersive Spectroscopy (EDS) system with four Bruker Silicon Drift Detectors (SDD), which enabled rapid collection rates of characteristic X-rays. EDS mapping was performed with acquisition times of up to 5 minutes. This work was also performed by Ke Wang in the Materials Characterization Laboratory, Materials Research Institute, The Pennsylvania State University.

5.2.3 Film patterning

In order to assess the relative importance of declamping and etch damage on the evolution of the film properties with lateral scaling, a series of features with equal surface areas but varying perimeter were patterned in 320-370 nm thick 70PMN-30PT films. The feature geometries were either relatively large clamped circular shapes or antennae-like shapes. The antennae structures were comprised of a small contact pad (50x70 μm^2), and a bus bar with many thin “arms” jutting out from it. For a given structure, these arms varied in width from 10 μm down to 200 nm, for aspect ratios from approximately 33:1 to 2:3, respectively, to offer a variation in the degree of declamping. The most finely patterned structures, with the smallest width/thickness aspect ratio, have the highest degree of declamping as well as the most sidewall surface area exposed to etching damage.

Prior to the etching step, a 50 nm thick blanket Pt layer was sputtered onto the PMN-PT using a CMS-18 deposition system (Kurt J. Lesker Co., Clairton, PA) at room temperature with a chamber pressure of 2.5 mTorr. Antennae structures with arm widths ≥1 μm were lithographically defined by SPR 3012 photoresist (Dow Electronic Materials, Malborough, MA) using a GCA 8500 i-line Stepper. The patterned resist was developed in MF-CD-26 (Rohm and Haas Electronic Materials LLC, Marlborough, MA) for 1 minute to expose the underlying Pt top electrode layer. Antennae structures with arm widths <1 μm were patterned into ZEP 520A (Zeon Chemical Corporation, Louisville, KY) resist using a Vistec EBPG5200 electron beam lithography system (Vistec Electron Beam GmbH, Jena, Germany) with a dose of 200 $\mu C/cm^2$. These features were developed by submersion in N-amyl acetate (Sigma Aldrich, St. Louis, MO) for 3 minutes, a 1:3 methyl isobutyl ketone (MIBK) to isopropyl alcohol (IPA) (Sigma Aldrich, St. Louis, MO) solution for 30 seconds and finally in an IPA (Sigma Aldrich, St. Louis, MO) bath for 30 seconds.

A Ni hard mask was then electroplated onto the exposed Pt areas defined by the photoresist mold using a Dynatronix MicroStart Pulse Precise programmable power supply (Dynatronix, Amery, WI) and Ni sulfamate plating solution (Transene CO Inc. Danvers, MA). The sample was submereged in the plating solution and electrically contacted with an alligator clip connected to the power supply. An aluminum plate, 4" x 4" in size, was positioned across the bath and contacted in a similar manner, as depicted in Figure 5-3. The growth parameters required for Ni electroplating are very sensitive to sample size, feature density, the pH of the Ni sulfamate solution, and the voltage supply parameters. It was found that the Transene Ni sulfamate solution should be maintained at $3.7 < pH < 4.2$ to ensure low stress Ni layers. Additionally, a low plating rate reduced the stress of the electroplated Ni, with <20 nm Ni/min being the target for Ni growth in this work. It should be noted that the stress within the Ni was not measured quantitatively. Rather, it was categorized by a "low" or "high" stress state. The threshold for a plating process to be categorized as high stress was if the plated Ni buckled or peeled off during growth, which often resulted in delamination of the top Pt and/or PMN-PT layers from the substrate as well.

The Dynatronix power supply can be set to maintain a steady voltage or current during a given plating step. This work employed the constant current configuration, which allowed the system to vary voltage as necessary to maintain the programmed forward and reverse current setpoints, as shown in Figure 5-4. Higher feature density enabled lower voltages to be used to achieve a given current setting, which was found to be necessary to avoid high stresses in the grown Ni. The forward current was set to 0.04 A, while the reverse current was set to 0.015 A, which combined with the pulse timing parameters (listed in Table 5-1) yielded an effective current within the system of 0.012 A. These parameters plated Ni at rate of 15 nm/min for part pieces with an exposed plating area of ~2.4 cm^2, correlating to an effective current density of ~5 mA/cm^2. The Ni mask was grown to be 150-200 nm thick (verified via contact profilometry from photoresist surface to Ni surface) before the photoresist mold was removed with Remover PG solvent (Microchem Corp, Newton, MA) and O_2 plasma ashing.

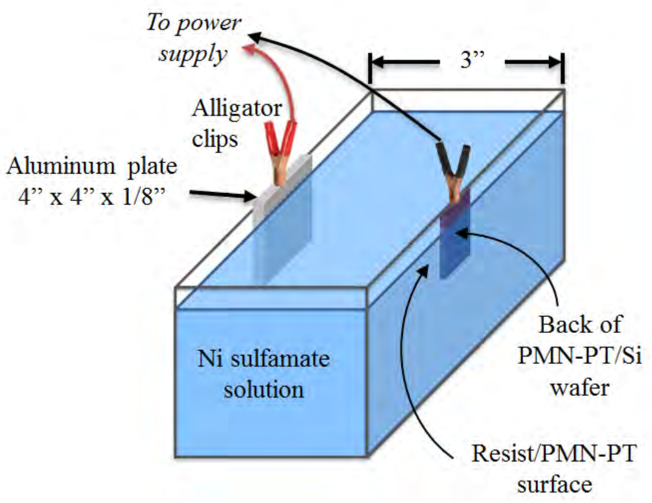

Figure 5-3: Schematic of electroplating experimental set up.

Table 5-1: Nickel plating parameters used with the Dynatronix power supply and a 3” separation distance between sample and Al plate. Colors are correlated to Figure 5-4 labels.

Forward bias on time (ms)	Forward bias off time (ms)	Forward bias duration (ms)	Reverse bias duration (ms)	Reverse bias on time (ms)	Reverse bias off time (ms)
1.14	2.76	17.62	0.85	0.35	0.4

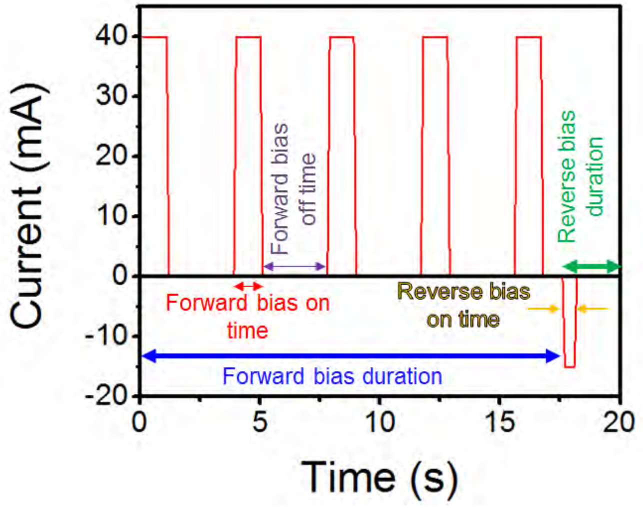

Figure 5-4: Electroplating current waveform used for Ni electroplating.

The Pt/PMN-PT/Pt structures were patterned in either a capacitively coupled plasma (CCP) reactive ion etching tool, the Tegal 6572 (Tegal Corporation, Petaluma, CA), or an inductively coupled plasma RIE tool, the Ulvac NE-550 (Ulvac Technologies, Inc., Methuen, MA), using the Ni hard mask to define features. The choice of etch tool was based on availability; etch recipes were developed and calibrated to yield similar results. The RIE plasma gas in both cases was composed of a 50/50 mixture of Cl_2 and CF_4. In the CCP tool, that plasma was excited using 700 W bias power at 13.56 MHz with 100 W applied in the kHz frequency and the chamber pressure was maintained at 2 mTorr. The ICP tool used 600 W bias at 13.56 MHz. Etching steps of 60 s in duration were repeated cyclically with off-times between 1 and 3 minutes until the bottom electrode Pt was reached. These etching conditions were found to yield sidewall angles as high as 70-80° with a ~1.7-2.5 nm/s etch rate of the PMN-PT and a selectivity to the Ni mask of ~3:1.

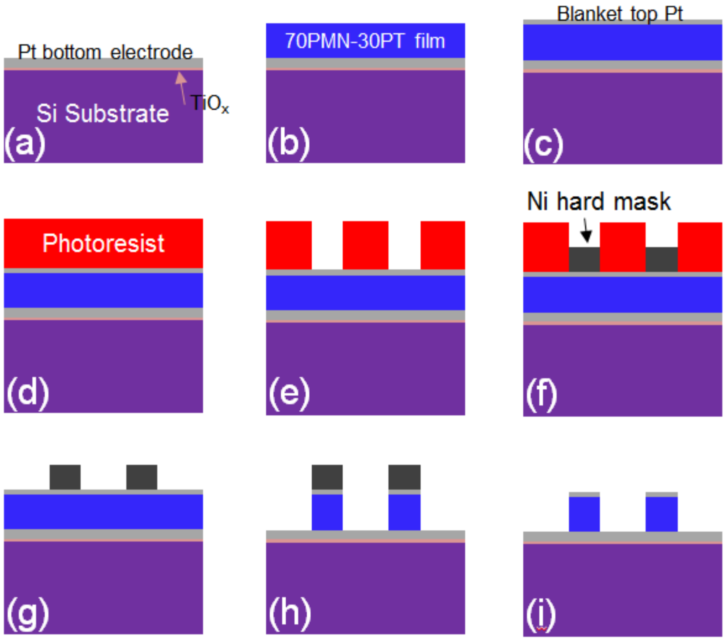

Figure 5-5: PMN-PT film patterning process flow from film deposition to removal of Ni hard mask after reactive ion etching. Steps (a) to (b) represents the PMN-PT film deposition with step (c) showing the deposition of a blanket Pt layer. Steps (d) and (e) show the lithographically defined photoresist mold for the Ni hard mask plating done in step (f). The sample is prepared for reactive ion etching by removal of the photoresist, as shown in step (g). Step (h) schematically shows the end result of reactive ion etching and step (i) is the sample structure following Ni mask removal.

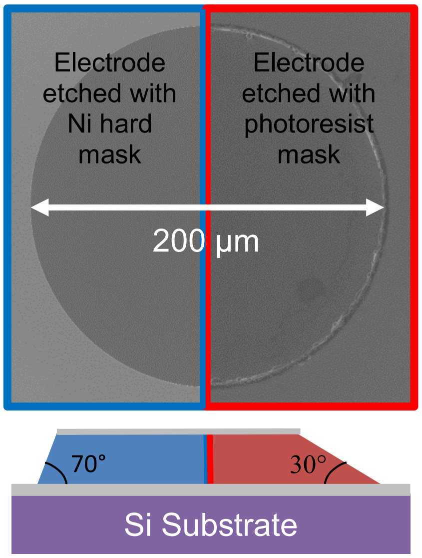

Figure 5-6: Scanning electron micrographs of an electrode surface after etching and mask removal for a film etched with a Ni hard mask (left) and a photoresist hardmask (right) which exhibited residue and fencing at sidewalls. The bottom schematic depicts the difference in sidewall angle achieved in both cases.

Following the patterning process, the Ni hard mask was removed via submersion in Ni etchant TFB (Transene CO Inc. Danvers, MA) at 40 °C for ~2 min. Electrical measurements at this phase of the processing typically showed degraded dielectric responses with high loss tangents and high frequency of electrical shorting through the films. To recover the structures, the patterned films were placed on a hot plate at 420 °C in air for 1 hr to anneal etch-induced damage. Following the heat treatment, large area patterned structures (dominated by the clamped response) exhibited dielectric properties matching those of the unpatterned films (within measurement error) and loss returned to <2%. In some cases, features comprised of highly scaled structures exhibited maintained unphysical loss tangents >1 and resistance through the capacitor in the tens of Ohms signifying an electrical short after annealing. To recover these features, the structures were electrically connected to two D batteries in series using point probes, vaporizing conductive pathways and returning the features to an insulating state with low loss tangents matching the larger area structures. Figure 5-7 depicts schematics of the patterned structure for dielectric, ferroelectric, and piezoelectric characterization. Figure 5-8 shows the FESEM micrographs of patterned antennae structures in the 300 nm thick PMN-PT films before and after the Ni hardmask was removed.

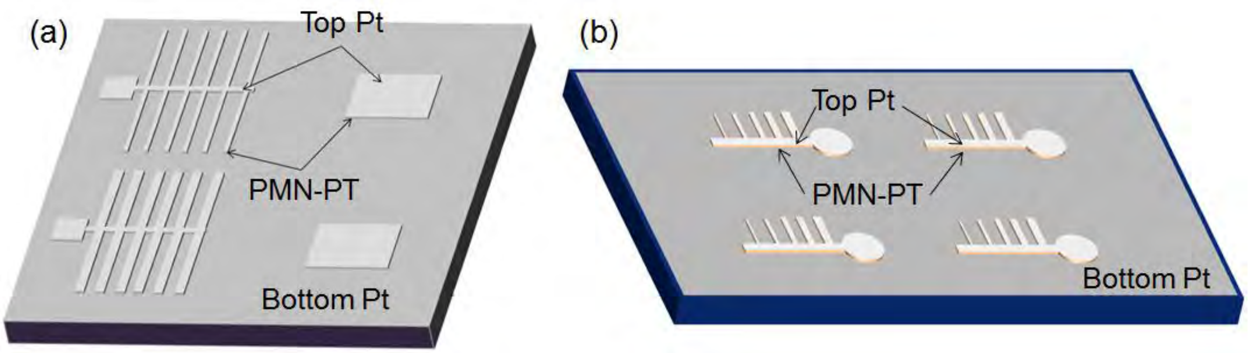

Figure 5-7: Schematic of antennae structures for (a) dielectric and ferroelectric and piezoelectric (b) characterization as a function of lateral scaling. A given antennae structure was comprised of a contact pad, a bus bar, and "arms" jutting out from the contact pad. The width of the arm structures was varied to vary the degree of declamping from one antenna to another.

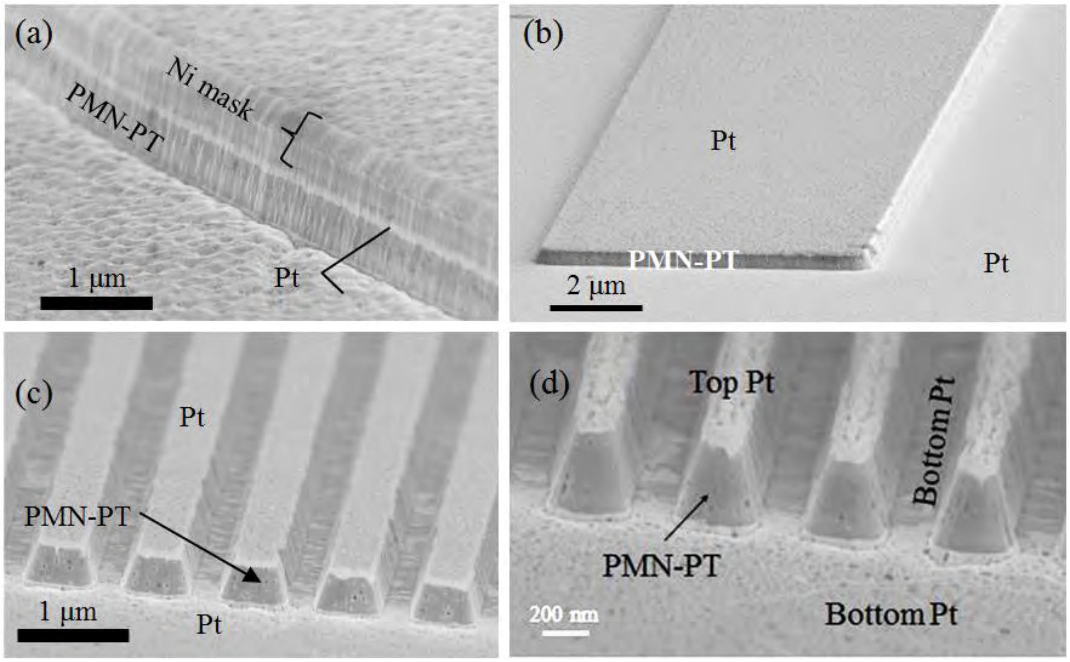

Figure 5-8: (a) FESEM micrograph of a patterned PMN-PT sidewall with the Ni hard mask. Patterned 7 µm (b), 750 nm (c), and 300 nm (d) wide "arms" of the antennae structures in 350 nm thick PMN-PT.

Because electrode area is an important parameter in these data sets (appearing in the calculation of relative permittivity and polarization), the final arm widths were measured via top down FESEM and used to calculate the final achieved electrode dimension. Additionally, all data were corrected to subtract out the contribution from the contact pad and the central electrical connection.

5.2.4 Electrical characterization

Dielectric characterization of structures with varying degrees of declamping was completed by measuring polarization-electric field (P-E) hysteresis loops, the Rayleigh behavior of the relative permittivity, and first order reversal curves (FORC) coupled with a Preisach analysis. P-E hysteresis loops and the dielectric behavior were measured using the experimental procedures described in Chapter 3 using a multiferroic tester (Radiant Technology, Inc. Albuquerque, NM) and a HP 4248A precision LCR meter (Agilent Technology, Palo Alto, CA), respectively.

The Rayleigh law was used to decouple patterning-induced changes in the reversible and irreversible contributions to the relative permittivity.[247,296] Within the Rayleigh regime, typically limited below 1/3-1/2 the coercive field, the relative permittivity exhibits a linear dependence on the amplitude of the AC-signal. Expressed mathematically, the Rayleigh law for relative permittivity is,[132,247,248]

$$\varepsilon' = \varepsilon'_{init} + \alpha' E_{ac} \qquad \text{Equation 5-1}$$

where ε' is relative permittivity ε'_{init} represents reversible contributions to relative permittivity including reversible domain wall motion and the intrinsic response, α' is the irreversible domain wall contribution to permittivity, and E_{AC} is the applied AC field. Therefore, the equation for the linear fit of the relative permittivity vs. E_{AC} amplitude contains the y-axis intercept, or ε'_{init}, and the slope, α', parameters.

In order to study changes in dielectric behavior of the patterned structures above the coercive field, first-order reversal curves (FORCs) and the Preisach model were employed.[297] The Preisach model assumes that a P-E loop can be described using a distribution of rectangular hysteresis loops, referred to as hysterons. The hysterons have up and down switching coercive fields of α and β, respectively, and can be reversible ($\alpha = \beta$) or irreversible ($\alpha \neq \beta$) in nature. FORC measurements were done by sweeping from a negative electric field, $-E_{initial}$, to $-E_{initial}+\Delta E$, where $\Delta E = E_{initial}/40$. By performing 40 consecutive cycles of this nature, the switching characteristics of the hysterons comprising the total P-E loop were recorded from $-E_{initial}$ to $+E_{initial}$.[298] The FORC loops were used to calculate the Preisach distribution describing the concentration of reversible and irreversible hysterons, as is discussed in more detail elsewhere.[150,297,299,300]

5.2.5 Piezoelectric characterization

The piezoelectric response of the blanket PMN-PT films was measured using an aixACCT double-beam leaser interferometer (AixACCT Systems, Aachen, Germany). Large signal piezoelectric strain measurements were made at 1 kHz on unpoled 600 μm wide circular electrodes with diameters, close to 1.2 times the substrate thickness to minimize measurement artifacts in accordance with the findings of Sivaramakrishnan *et al.*[187] The relatively large electrode area implies that the patterned structures measured for piezoelectric response remain in the clamped state.

For characterization of the partially declamped $d_{33,\mathrm{eff}}$ behavior, the patterned PMN-PT structures were wire bonded to a Si carrier wafer with isolated electrodes for a given patterned feature, depicted schematically in Figure 5-9. Additionally, the patterned antennae structures were slightly modified to include various arm widths, from 0.75 µm to 9 µm all share a common bus bar. This simplified the measurement procedure and ensured the arm structures being compared had the same field exposure.

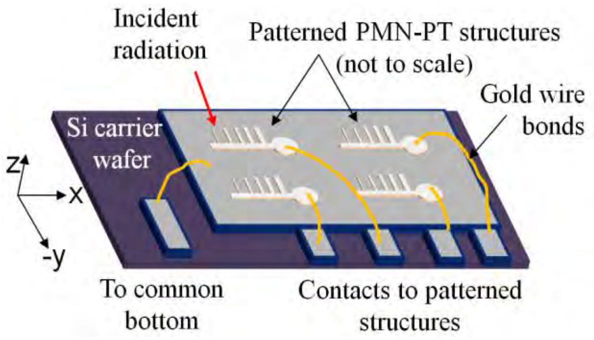

Figure 5-9: Schematic of patterned film with underlying substrate, and wire bonded contact bars which would be electrically accessed with alligator clips. Not drawn to scale.

X-ray diffraction experiments can offer high resolution *in-situ* characterization of DC field-induced lattice displacements, and, with sufficient experimental design, can record such data on a relatively local lateral scale. Beamline 2-ID-D at the APS of Argonne National Laboratory, equipped with a “nanoprobe” X-ray beam (240 nm wide beam at FWHM), was employed for local mapping of electric field induced changes in {002} d-spacing. In these measurements, a beam energy of 10.1 keV and an X-ray wavelength of 1.2276 Å were used. The experimental setup included the incident beam, directed though a zone plate, aperture, and a 2.7 µm pinhole, a 2-D area detector (Mar165 CCD, marXperts GmbH, Norderstedt, Germany) with an 11° window to capture the diffracted beam, cables for electrical contact, and an X-ray fluorescence detector to determine the beam location on the sample and structures. With the X-ray focused beam on a patterned PMN-PT arm, the Ti fluorescence was detected. The sample was scanned in x-, y-, and z-directions to locate known features on the surface and navigate from one arm to another due to known separation distances. The sample was aligned with the length of the arms parallel with the beam path and then rotated 17.6°, near the expected {002} PMN-PT diffraction angle. The experimental set up is shown schematically in Figure 5-10.

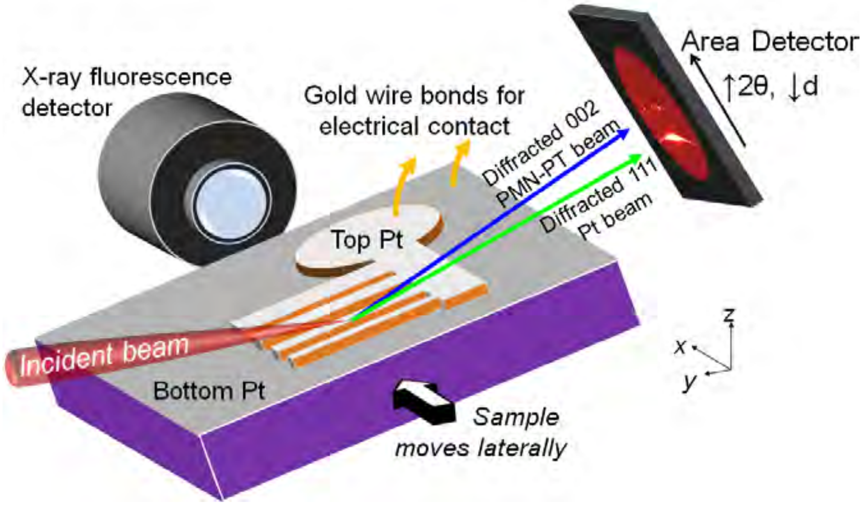

Figure 5-10: Schematic of experimental setup with beam path, optics, and feature geometry. The actual patterned structure was comprised of 0.75 µm 1 µm, 2 µm, 3 µm, …, 9 µm wide arms.

To begin a measurement, electrical connectivity was verified with the HP 4248A precision LCR meter (Agilent Technology, Palo Alto, CA). With the desired DC-voltage applied and the beam on, the sample was moved along “x” in a stepwise manner. For structure widths of 4 µm and below, the step size was 0.4 µm, while wider arm structures were characterized using a 1.25 µm step size. At each step position, a diffraction image was recorded. Once the diffraction pattern was recorded across each of the arm structures, the voltage was changed and the experiment repeated. The voltage steps used in this study were from 0 V, 0.25 V_C, 0.5 V_C, 0.75 V_C, and then in steps of integer increments of the coercive field (V_C) until 300 kV/cm was reached (9 V).

The peak positions of the diffraction patterns were calibrated using diffraction pattern of a National Institute of Standards and Technology standard cerium dioxide powder with known d-spacing. After this, the diffraction images from the PMN-PT diffraction were integrated using DataSqueeze software.[301] The PMN-PT {002} and Pt {111} peaks were fit using a Pseudo-Voigt function. The peak positions across each arm structure and at each voltage step were determined from the center of the peak fits. The piezoelectric coefficient, $d_{33,eff}$, was determined from the linear fit of strain in d-spacing of the PMN-PT {002} peak position vs. electric field at each spatial position on an arm structure.

Increased spatial resolution was achieved via piezoresponse force microscopy (PFM) performed by Linhan Ye and James Bosse at the University of Connecticut in the Huey Group AFM Laboratory. The patterned, wire bonded features were studied in ambient conditions in an Asylum Research Cypher (Asylum Research, Santa Barbara, CA). Operating in contact mode, setpoint forces of 286 nN were applied by a grounded doped diamond conducting probe (Nanosensors CDT-FMR). The patterned top electrode was electrically grounded while the bottom electrode was accessed for ferroelectric poling and/or small signal piezoactuation. An Agilent 33220A function generator was used to induce piezoelectric actuation which was detected by analyzing the cantilever displacements with a lock-in amplifier (Zurich Instruments HF2LI) with an average per image pixel time constant of 600 μs. The signal was calibrated by a quartz crystal specimen.

Due to limits in PFM scan distances, 2 μm, 1 μm and 0.75 μm PMN-PT microfabricated arms were studied. Characterization began with poling at +5 Volts (DC) for 15 minutes, followed by 40 minutes of room temperature aging. Because PMN-PT films on Si exhibit low coercive voltages, domain back-switching during the measurement was avoided with application of a DC bias offset, ranging from 0.4 to 1.5 V, coupled with an AC sinusoidal signal of 0.8 $V_{\text{peak-to-peak}}$ with a frequency near the probe-sample contact resonance of ~500 kHz. Leveraging multi-parametric concepts reported elsewhere,[302] the DC bias was incremented by 100 mV for consecutive image frames of the same imaged area. Total spatial drift during the 12 continuously acquired images was less than 35 nm. This was corrected in post-processing by simple pixel shifts (at most a total of 3 pixels in the x and y directions) necessary to align topographic features in the image sequence according to standard image processing routines (ImageJ, Labview). Ultimately, this provided the image-independent topography and the piezoresponse maps for all three PMN-PT arm widths tested.

5.3 Results and discussion

5.3.1 Crystallinity and microstructure

Figure 5-11 depicts the θ-2θ x-ray diffraction pattern of 70PMN-30PT thin films grown by chemical solution deposition on platinized silicon substrates on the PbO seed layer. The film is highly {001} oriented (Lotgering factors of the $\{h00\}$ orientation exceeding 98%) and perovskite phase pure (within X-ray diffraction detection limits). Figure 5-12 depicts the dense microstructure of the films via a top-down FESEM micrograph.

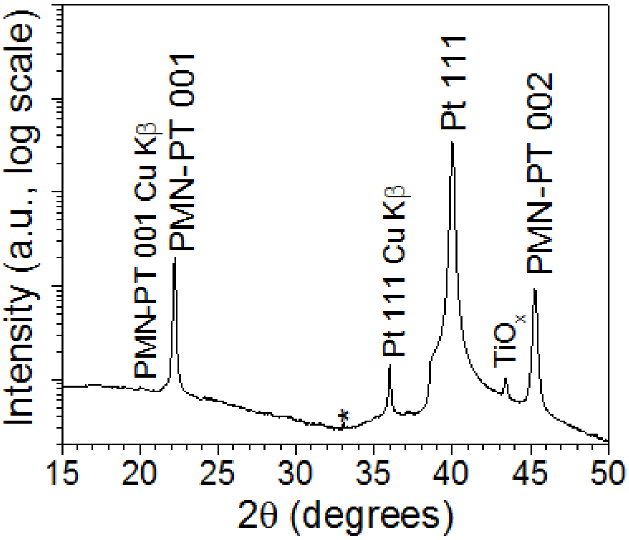

Figure 5-11: X-ray diffraction pattern of chemical solution deposited 70PMN-30PT thin film on Pt-coated Si.

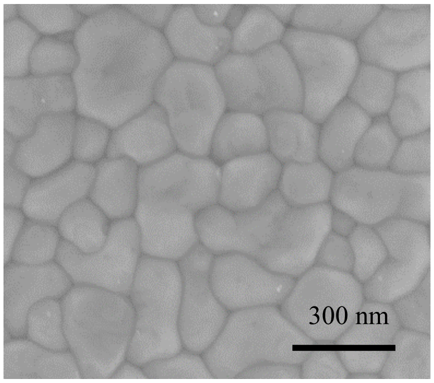

Figure 5-12: Surface morphology of 350 nm thick {001} oriented PMN-PT film.

5.3.2 Electrical characterization of the PMN-PT thin films

The relative permittivity of the blanket PMN-PT film was 1510 ±20 with ~1% loss when measured at 1 kHz with a small signal amplitude of 30 mV$_{ac}$, in good agreement with previously published data on PMN-PT films on Si[199,303] and data presented in previous sections of this dissertation (Chapter 3). Electromechanical properties of the blanket films were measured via double beam interferometry. The piezoelectric coefficient, $d_{33,f}$, was 80-90 pm/V, taken from the slope of the displacement-electric field curve at small fields. The clamped films exhibited a high breakdown strength (>1500 kV/cm) with a maximum strain of nearly 1%, as shown in Figure 3-10.

After patterning, differences in the dielectric properties among the PMN-PT antennae varying in their respective degrees of declamping, were characterized. Figure 5-13a shows the P-E hysteresis behavior for the partially declamped antennae structures with aspect ratios ranging from over 380 (strongly clamped) to less than1. It was found that as the aspect ratio was reduced, the P-E hysteresis loop rotated counterclockwise. The rotation in the loop serves to increase both remanent and maximum polarization observed for a given electric field excursion, depicted in Figure 5-13b. The squarer shape of the highly scaled hysteresis loops is indicative of reduced tensile stresses upon patterning, which otherwise yield slim loops on Si with rapid backswitching and less stable out-of-plane polarizations.[90,165,199]

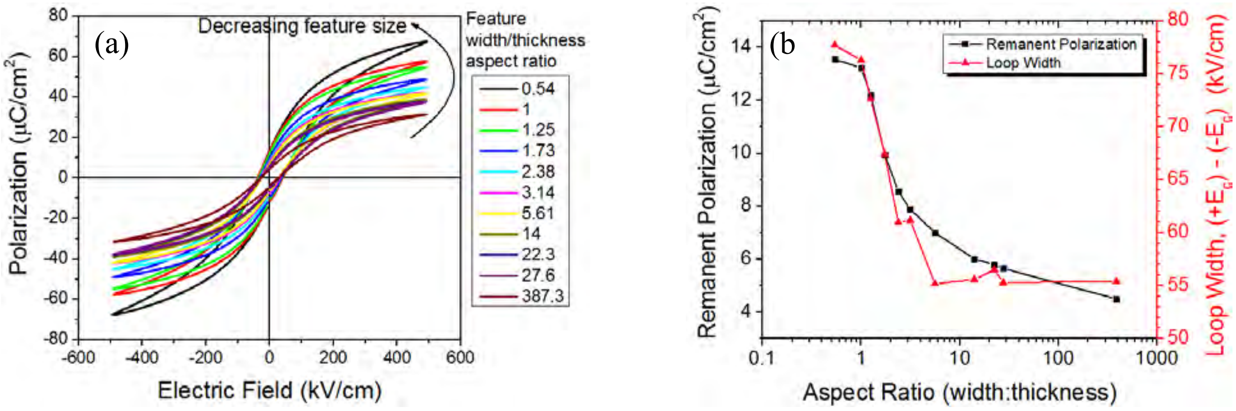

Figure 5-13: (a) The P-E field hysteresis loops measured at 1 kHz on antennae structures with varying degrees of substrate clamping. Counterclockwise rotation in the P-E loops is observed upon patterning. (b) Changes in remanent and maximum polarization upon patterning of the PMN-PT film to laterally finer feature sizes.

The P-E loop rotation can be attributed to the net changes in domain wall motion and an increased intrinsic response. These changes could be a result of some combination of declamping from the underlying substrate, reduction in net in-plane stress, or the change in the aspect ratio of the feature. Supporting this geometry dependence, McQuaid *et al.* reported that switching occurs more readily in unclamped $BaTiO_3$ single crystals patterned in rod-shaped parts rather than plate-shaped.[304] It should also be noted that although the loops widen (that is, E_C increases) on patterning, there is no observable pinching in the loops, suggesting that the etching process did not induce a significant concentration of randomly oriented defect dipoles.[305]

Figure 5-14a shows the reversible and irreversible Rayleigh coefficients for the patterned PMN-PT film as a function of feature aspect ratio. Figure 5-14b shows the total permittivity with the models for laterally scaled PMN-PT films of equivalent thickness near the MPB. Both the reversible and irreversible Rayleigh coefficients increase upon scaling to structures of smaller lateral dimension. The size dependence of the irreversible Rayleigh coefficient is strong evidence for an increase in irreversible domain wall motion. Relative to the clamped state, the antenna structures with a 1:1 aspect ratio show a doubling of the reversible contribution to permittivity. Even more enhancement upon patterning is observed in the irreversible Rayleigh constant which increased ~3.1x from the clamped to the features with 1:1 aspect ratio. The reduction in the Rayleigh coefficients at the 0.7 aspect ratio dimension may have been caused by an increased significance of the sidewall damage and point defects acting as pinning sites for irreversible domain wall motion, as described below. Despite this, the total relative permittivity increases continuously with lateral patterning and nearly doubled from the clamped state upon patterning to sub 1:1 aspect ratios. Figure 5-14 shows the good agreement between the experimentally obtained result of lateral scaling and the finite element modeling. The experimental data begins to stray from the models at small features sizes with aspect ratios less than one. These results indicate that lateral scaling of piezoelectric thin films serves to increase both reversible and irreversible domain wall motion as well as to change in the intrinsic dielectric response of the material. The intrinsic change may be attributed to a reduction of stress in the thin film built up during growth on the Si substrate. More on this matter is discussed later in the chapter.

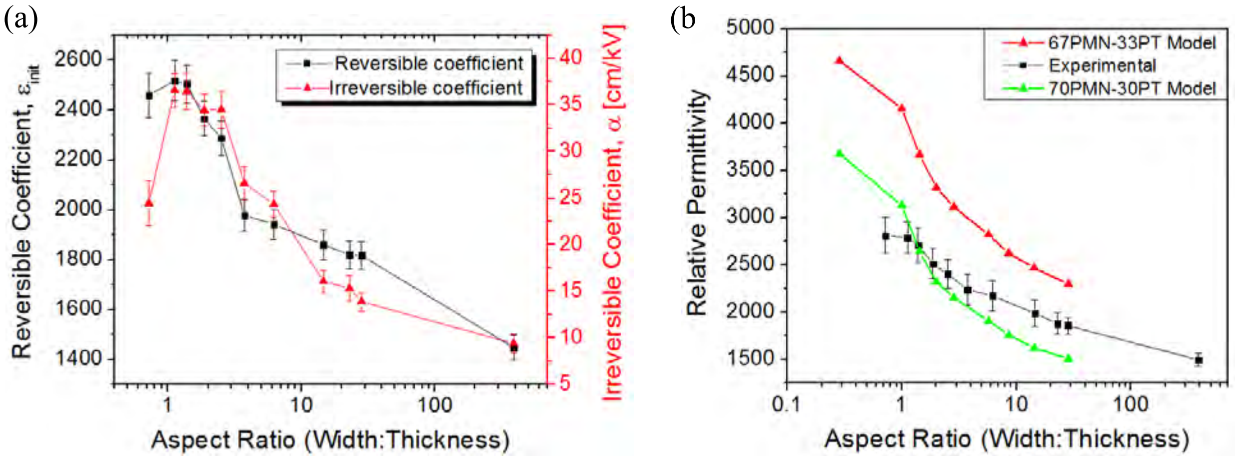

Figure 5-14: (a) Reversible and irreversible Rayleigh coefficients and (b) total permittivity for patterned antennae structures as a function of both aspect ratio compared to finite element modeling obtained from single crystal PMN-PT data.

In order to study changes in dielectric behavior of the patterned structures above the coercive field, first-order reversal curves (FORCs) and the Preisach model were employed.[150] The FORC distributions provide information on domain wall motion and the intrinsic response of the material outside the Rayleigh regime. Figure 5-15 depicts the FORC distribution for clamped features and a patterned feature with an aspect ratio of 3:1. The plots have α and β on the axes with the color gradient showing the relative concentrations of a given hysteron with the corresponding α and β values. Because the P-E loop of the clamped PMN-PT film on a silicon substrate is slim, the concentration of reversible hysterons is high, and the irreversible hysterons are concentrated near the α = β line. It is also apparent that there is a higher concentration of irreversible hysterons in the finely patterned antennae than in the clamped electrode. The highest hysteron concentration is observed at fields near and less than the coercive field of the material. The increased concentration of irreversible hysterons in the patterned film can be attributed to the increased remanent and saturation polarization of the patterned P-E loops shown in Figure 5-13.

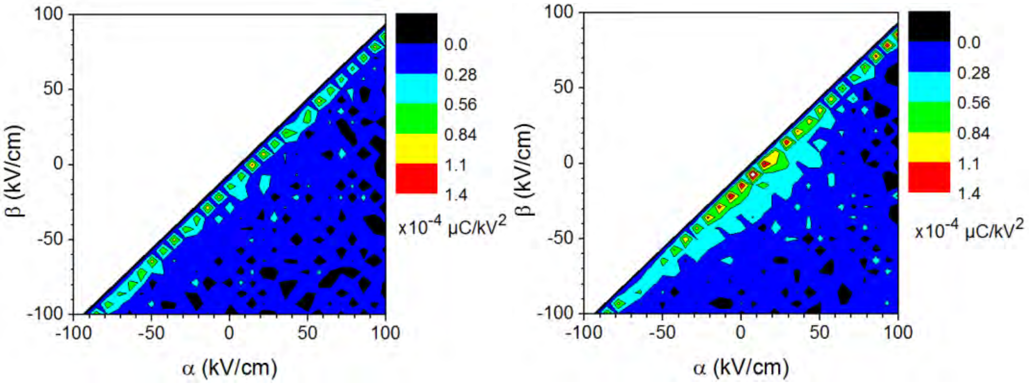

Figure 5-15: (a) Irreversible Preisach behavior for clamped electrode of 0.25 mm^2 area. (b) Irreversible Preisach behavior for a patterned antennae structure comprised of 1 μm arms, a 3:1 width to thickness aspect ratio.

The reversible FORC distributions, as shown in Figure 5-16, also indicate that the ferroelectric response increases for more finely patterned features. For structures with a 3:1 width:thickness aspect ratio, the measured reversible Preisach response is 43% larger than in clamped structures, reaching ~0.10 μC/kV/cm. Note also that there is no significant shift in the peak position of the reversible Preisach response. If etching the PMN-PT film induced a large concentration of defect dipoles which generated an internal bias in the material, the more highly patterned structures would exhibit some finite level of electrical imprint. Likewise, randomly oriented defects would be expected to split the maximum. Because neither of these factors were observed up to aspect ratios of 3:1, it is believed that the etch process combined with the 400 °C anneal step was sufficient to avoid high defect dipole concentrations.

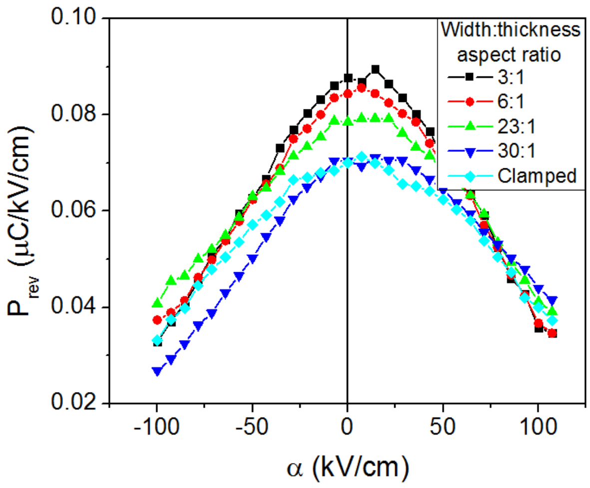

Figure 5-16: Reversible Preisach behavior for various antennae structures and a large circular electrode.

Temperature dependent dielectric characterization revealed that lateral scaling of 70PMN-30PT thin films also served to sharpen the peak shape in permittivity near T_{max} from the clamped response, as depicted in Figure 5-17. The relative permittivity for the structures of varying degrees of declamping does not converge above T_{max}, further indicating an increase in the intrinsic response of the PMN-PT film upon declamping. This behavior is perhaps achieved in part by moving the material closer to the stress-free state by reducing the average stress in the features and by reducing the volume fraction of the probe material affected by substrate clamping. The shift in T_{max} towards higher temperatures, as is measured in bulk ceramics,[63] for more finely patterned structures also corroborates this understanding.

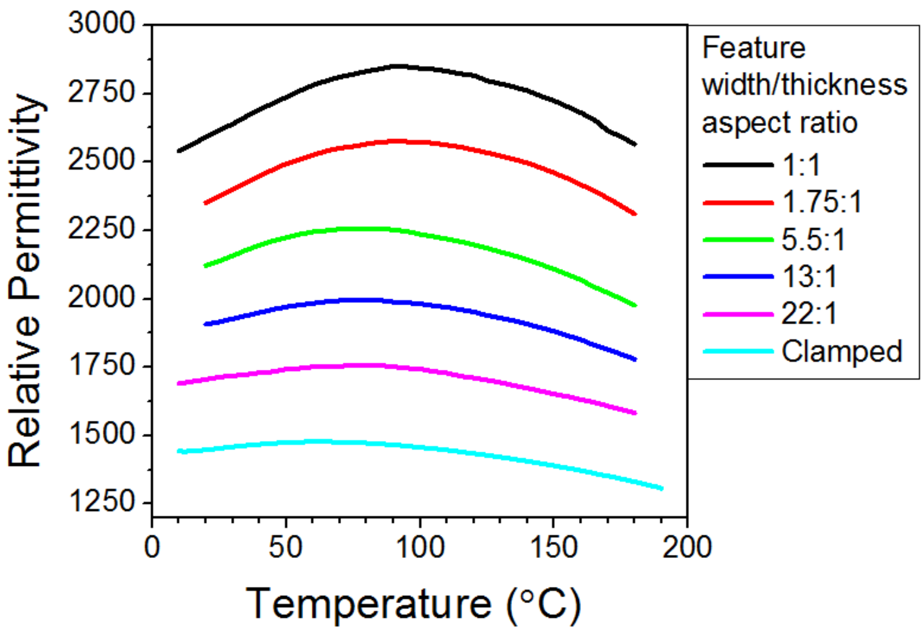

Figure 5-17: Temperature dependence of the relative permittivity for a laterally scaled 70PMN-30PT film

The observed increases in both polarization and dielectric permittivity suggest that significant increases in the piezoelectric response will also be observed upon declamping. $d_{33} = 2\varepsilon_0\varepsilon_r Q P_s$ Equation 5-2 5-2 defines the intrinsic piezoelectric coefficient, d_{33}, in terms of the spontaneous polarization (P_s) the dielectric constant (ε_r), and the electrostrictive constant (Q). In this case, for oriented polycrystalline films, the remanent polarization can be used as a stand-in for P_s. The polarization and permittivity increase substantially upon scaling from large, clamped structures to the partially declamped antennae structures with a 0.7 aspect ratio. The electrostrictive constant should also rise on declamping.[205] Thus, it is anticipated that the d_{33} constant should rise substantially in the laterally patterned structures.

$$d_{33} = 2\varepsilon_0\varepsilon_r Q P_s \qquad \text{Equation 5-2}$$

5.3.3 Piezoelectric properties in patterned films

Figure 5-18 displays the topography (top row) and deflection (second row) of the three arm widths probed via PFM, along with piezoresponse maps for 3 of the 12 DC bias conditions as labelled (remaining rows). The common contrast scale for all PFM images highlights the clear overall voltage dependence of the response. Individual grains are clearly resolved, as well as signal enhancements as the probe falls off the edges of the mesa-like arms due to changes in the contact area and/or applied load. These PFM images clearly demonstrate the reduction in piezoelectric response around grain boundaries, similar to what has been observed in PZT[139,140,142] and $BiFeO_3$.[138]

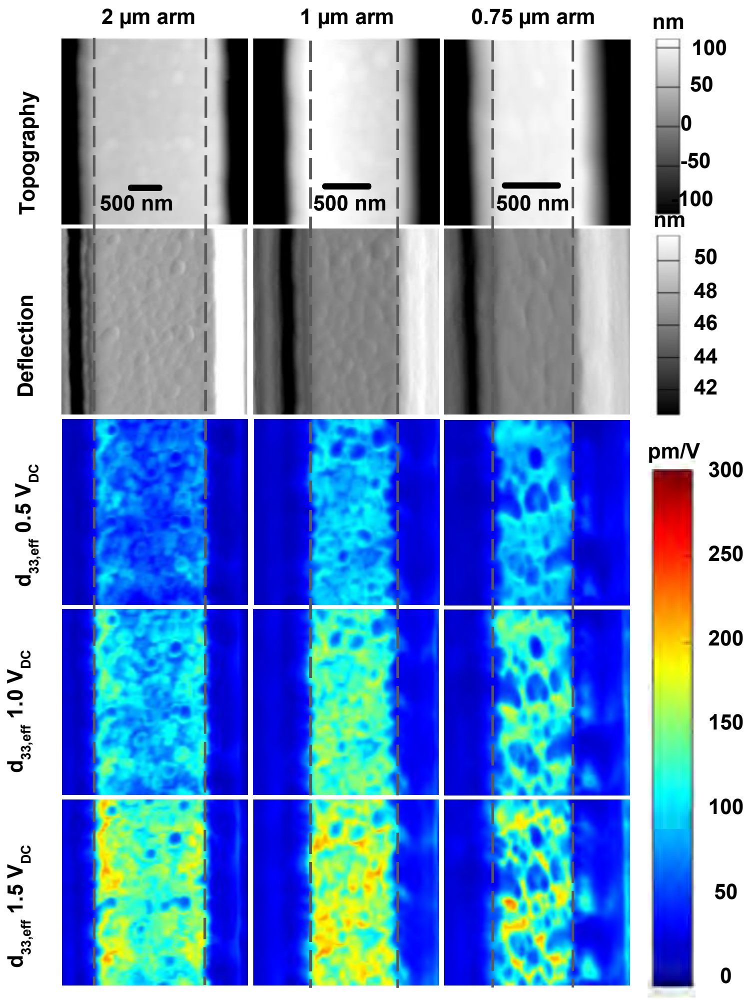

Figure 5-18: Topography, deflection and unipolar piezoresponse (PFM amplitude) maps, with DC biasing of 0.5, 1.0, and 1.5 V.

The PFM displacement data were divided by the AC amplitude (0.4 V) and the remanent $d_{33,\ eff}$ coefficients were calculated pixel by pixel by extrapolating the $d_{33,eff}$ signal as a function of DC offset back to 0 V. Over the DC bias range of 0.4 V to +1.5 V, the response is linear with a mean fitting parameter (R^2) of 0.99. Figure 5-19 depicts the piezoresponse maps taken from ~60,000 data points per microfabricated feature, per voltage step (slightly less than the 256x256 initial image resolution due to drift correction of the original datasets). The top row displays the resolved d_{33} coefficient for 3 arms studied, while standard deviation error maps for d_{33} are presented in the bottom row. All images are again depicted using the same contrast scale. Spatial variation in the piezoelectric properties develops as a function of position on a given arm and from distinct grains within the arms.

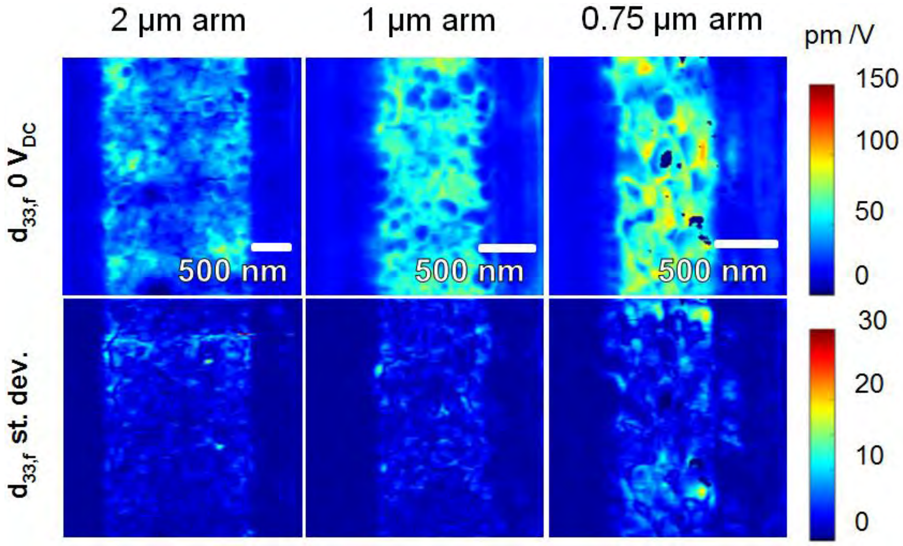

Figure 5-19: Maps of the extracted zero bias $d_{33,f}$ coefficients (top row), and the essentially negligible standard deviation of error for $d_{33,f}$ (displayed with a 5x enhancement in the contrast scale), for microfabricated 2 µm, 1 µm, and 0.75 µm arms.

The spatial variations in Figure 5-19, which couple to grain size, suggest that eventual devices leveraging the declamping effect would benefit from epitaxial films, for greater spatial uniformity and reduced domain wall pinning centers.[230] To assess the performance that might be achieved in such a film, the integrated mean and the peak (optimized) remanent $d_{33,eff}$ coefficients determined along the lateral axis of the images in Figure 5-19 are displayed in Figure 5-20 for all three microstructured arms.

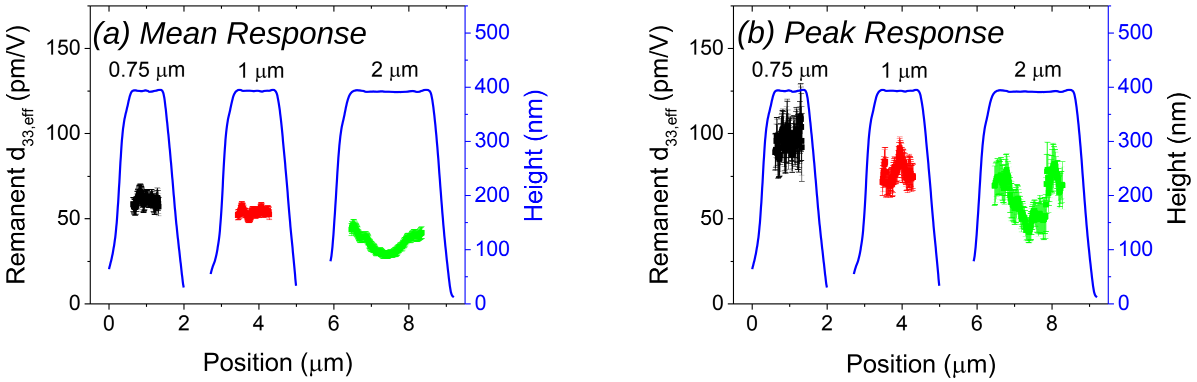

Figure 5-20: (a) Mean and (b) peak intrinsic $d_{33,eff}$ coefficient and topography as a function of position for microfabricated 0.75 μm, 1 μm, and 2 μm arms of 300 nm thick 70PMN-30PT with 100 nm top Pt.

The 2 μm wide arm structure exhibits a remanent $d_{33,eff}$ coefficient of ~35 pm/V in the feature center, in agreement with the small signal clamped response for PMN-PT films of this thickness.[165,306] The piezoelectric response at the sidewalls increases up to values of 80-90 pm/V, consistent with declamping.[35,108] The sidewalls show enhanced response to a width of ~600 nm, suggesting that arms narrower than 1.2 μm should benefit from at least partial declamping throughout their widths. This is confirmed by nearly uniform mean and peak $d_{33,eff}$ values across the 1 μm and especially 0.75 μm arms. Mean peak small signal $d_{33,eff}$ coefficients for these features are approximately 80 pm/V and 90 pm/V, respectively, yielding a 3x increase from the mean clamped response.

Figure 5-21 depicts the recorded field-induced shifts in {002} d-spacing along with the calculated intrinsic $d_{33,eff}$. At zero field, the out-of-plane lattice parameter near the free sidewalls is large as compared to the center of the features, indicating that patterning does relieve local stresses imposed by the substrate, in agreement with Bühlmann *et al.* Using the single crystal compliance of 70PMN-30PT, this relaxation correlates to a reduction in stress of ~50 MPa, about 10% of the total expected thermal stress accumulated during cooling from the PMN-PT crystallization temperature (740 °C) to the Curie temperature (120 °C).[91,92] The high field intrinsic $d_{33,eff}$ coefficient was extracted from the linear fit of strain vs. field for each position of the X-ray beam; an example of this is shown in Figure 5-22. The R^2 values of the linear fits for the strain vs. DC-field data were between 0.84-0.99, which is reflected in the error bars of the data in Figure 5-23.

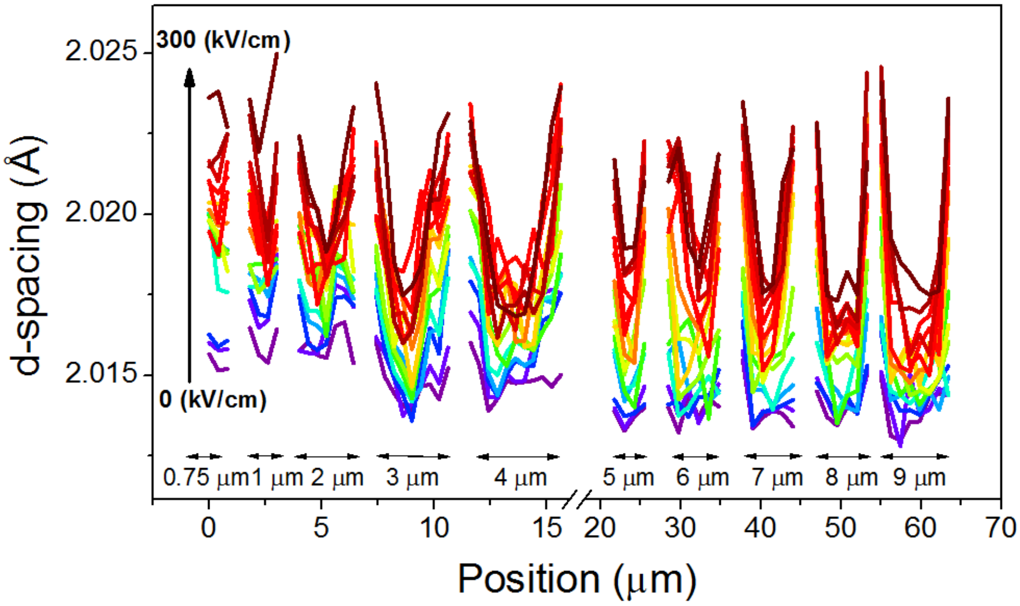

Figure 5-21: 70PMN-30PT $\{002\}_{PC}$ d-spacing under increasing DC-electric field as a function of lateral position across arm structures varying in width/thickness aspect ratio from 2.5 to 30.

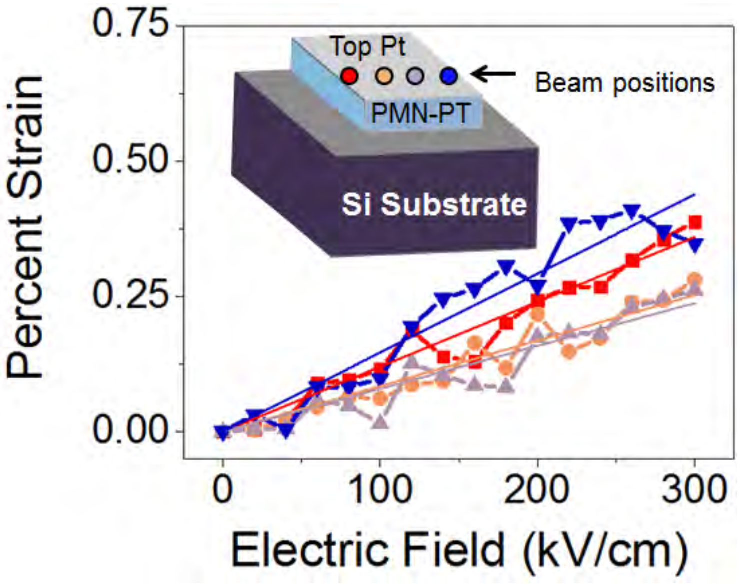

Figure 5-22: Strain as a function of DC electric field across a 5 μm wide feature with an X-ray step size of 1.25 μm. Position of the beam in relation to sidewall is confirmed with Ti fluorescence. Slope of the strain vs. field dependence yields the intrinsic $d_{33,eff}$ piezoelectric coefficient.

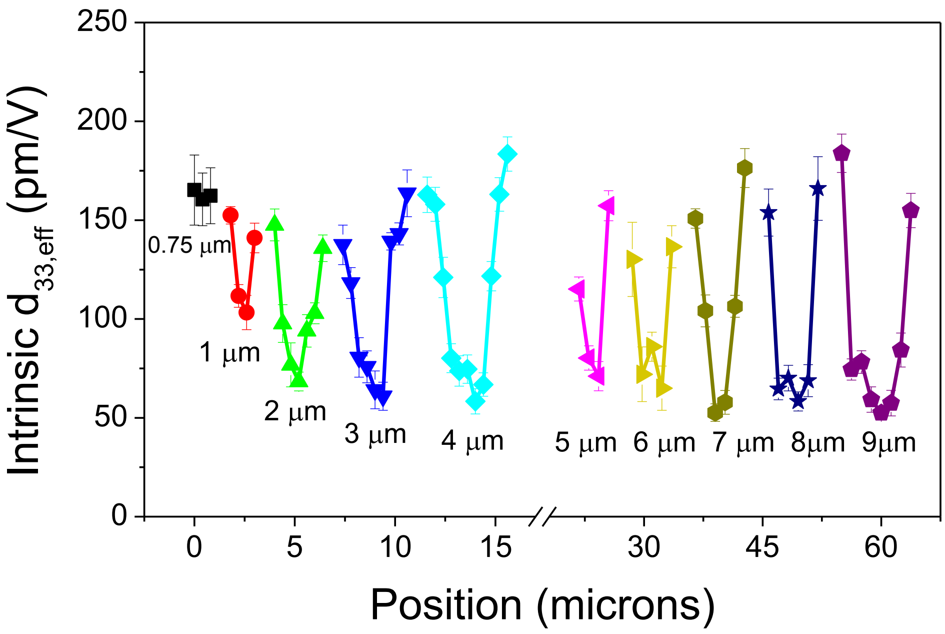

Figure 5-23: Intrinsic $d_{33,eff}$ coefficient of a 300 nm thick 70PMN-30PT film as a function of position across microfabricated arm structures. X-ray probed volumes nearest free sidewalls exhibit piezoelectric enhancement of ~2.7 times the clamped response.

As discussed in section 4.3.3 the presence of in interfacial layer would drop the externally applied voltage by a factor related to the interfacial capacitance. The effects of this layer are approximated in Figure 5-24 assuming similar interfacial properties are present in the 300 nm thick film used in local $d_{33,eff}$ characterization as was present in the thickness series experiments. The effects of the voltage reduction are more pronounced in areas where the $d_{33,eff}$ is relatively higher since voltage and d_{33} are inversely proportional.

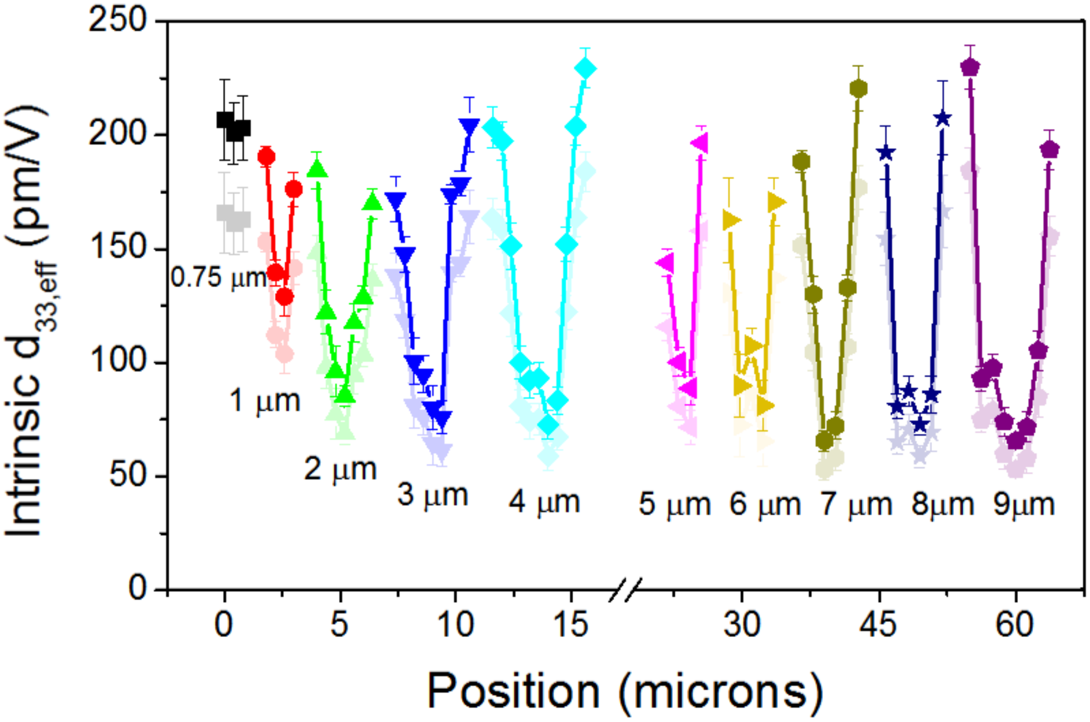

Figure 5-24: Adjusted $d_{33,eff}$ as a function of position across patterned arm structures after adjustment for interfacial layer which reduces the voltage applied across the ferroelectric as discussed in section 4.3.3 The lighter-shade symbols represent the as-measured data, while the color saturated symbols represent the $d_{33,eff}$ after accounting for the interfacial layer.

The data shown in Figure 5-23 correspond to the intrinsic $d_{33,eff}$ coefficient, including polarization rotation enabled by the {001} texture, since the DC biased measurement minimizes contributions from domain wall motion. The data show that the more clamped regions near the middle of a patterned structure exhibit $d_{33,f}$ of ~50-60 pm/V (slightly higher than observed in

PFM due to the higher excitation fields) which increases by ~2.5-3.2 times at the sidewall where the piezoelectric coefficient is 160 ±15 pm/V.

The quantitative difference of the X-ray data and the PFM data is likely a function of the field dependence of the piezoelectric coefficient.[223] The $d_{33,eff}$ as a function of position exhibits more pronounced declamping in the large signal XRD measurement than the mean remanent $d_{33,eff}$ recorded via PFM, suggesting that the changes in domain wall contributions and intrinsic response upon declamping[108] also increase with field. This may also be correlated to pinning sites incurred during etching of the sidewall.

The finite element models predict $d_{33,eff}$ coefficients of ~200 pm/V in clamped films, closer to the maximum saturated piezoresponse of PMN-PT films with thickness $> 1\ \mu m$[165,175] where the significance of any interfacial layers of lower ferroelectric character is reduced.[227] Furthermore, the finite element models were constructed from the single crystal, engineered domain state bulk materials properties of PMN-PT at the MPB composition. In the oriented polycrystalline films on Si substrates, there are additional factors that may also reduce the functional properties. These include reduced domain wall motion from grain boundary pinning,[230] thermally induced stresses,[87,166,237,259] defects near interfaces and grain boundaries,[165,231,307] pores/voids,[193] misoriented material,[308] and strain-induced shifts in the %PT composition of the morphotropic phase boundary.[198] Furthermore, the local piezoelectric response is averaged over the finite probing volumes, potentially leading to an underestimate of declamping at the sidewall. Finally, the non-vertical sidewalls could reduce the voltage applied to the functional piezoelectric volume of the capacitor.

Figure 5-25 depicts the $d_{33,eff}$ piezoelectric coefficient across a 2 μm wide 70PMN-30PT structure normalized to the observed value at the feature center from the three declamping characterization tools employed. Good agreement in the $d_{33,eff}$ curves as a function of position confirms the predicted influence of free sidewalls and the mechanisms which yields increased functional properties with reduced width:thickness aspect ratio. Futhermore, the normalized peak PFM response matches quite well with the FEM data, suggesting that patterned epitaxial films, lacking the property limiting factors present in polycrystalline films, may declamp more strongly than the films studied in this work.

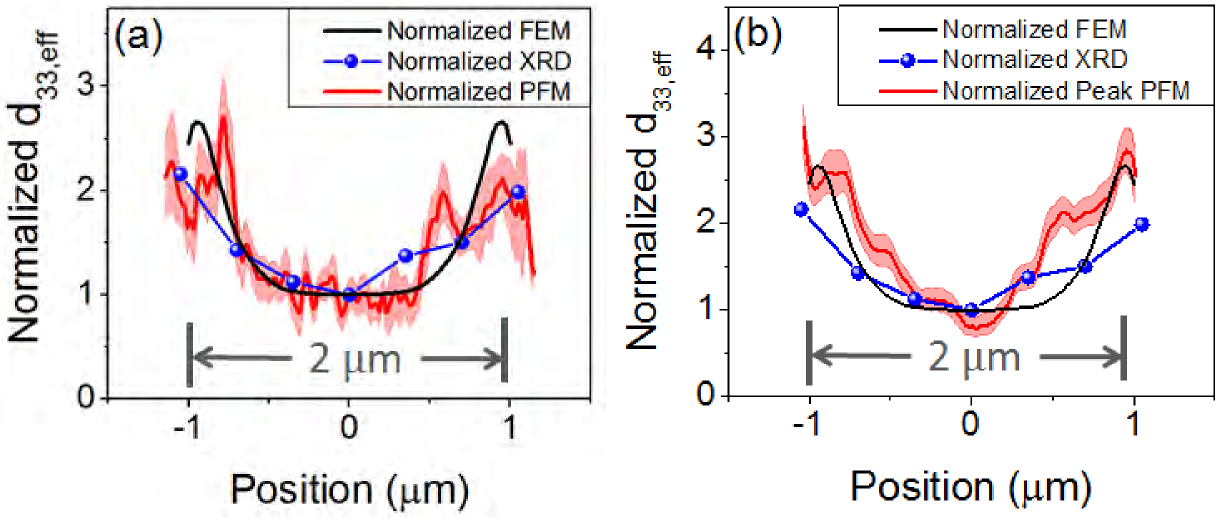

Figure 5-25: Normalized piezoelectric response from finite element modeling, piezoresponse force microscopy, and X-ray diffraction. The mean PFM response is depicted in (a) while the maximum PFM response is depicted in (b).

5.3.4 Sidewall structure

The finite probing volumes of the declamped $d_{33,eff}$ characterization techniques introduce difficulty in resolving small volumes of material which may be damaged from the patterning process. The dielectric data of Figure 5-14b, for example, suggests that such damage may persist following the hot plate annealing procedure. Antennae structures with arm widths less than ~300 nm show decreased Rayleigh coefficients and stronger deviation from the finite element models for relative permittivity as a function of aspect ratio. Since the structures were patterned to have identical areas, finer patterning is linked to increased perimeter/area ratios, thereby increasing the effects of defect-rich sidewalls (if present).

Transmission electron microscopy was employed as a means to characterize the local structure of the patterned features as a function of position to identify any non-crystalline material. Figure 5-26 displays a transmission electron micrograph of the cross-section of a patterned PMN-PT sidewall, etched under the conditions provided above. Crystalline planes are visible in the bulk of the patterned feature and extend up to about 5-10 nm from the sidewall where the PMN-PT turns amorphous. An energy dispersive spectroscopy scan taken parallel to the film surface from the sidewall toward the feature center, shown in Figure 5-27, provides information on the stoichiometry of this amorphous region.

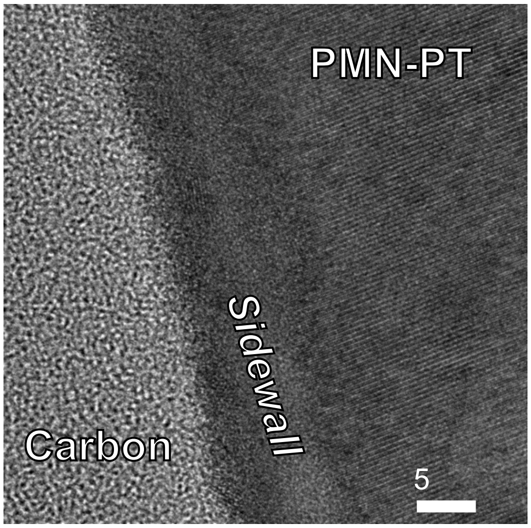

Figure 5-26: Transmission electron micrograph of a patterned PMN-PT sidewall.

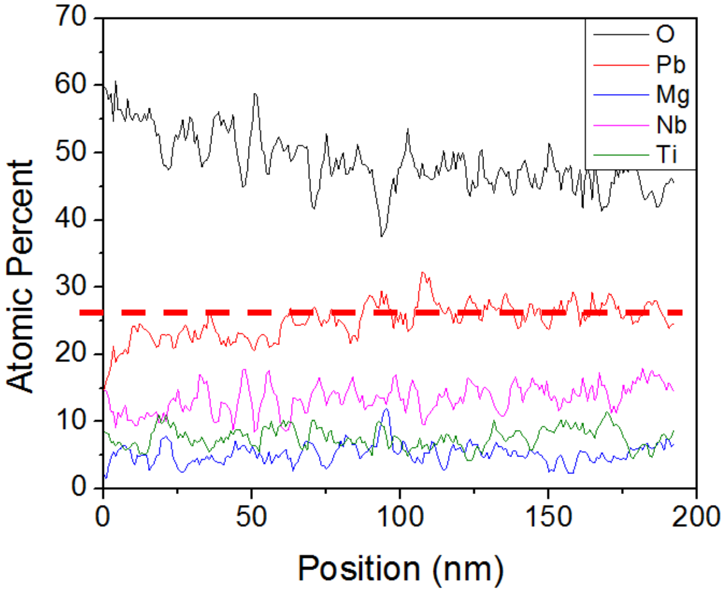

Figure 5-27: Energy dispersive spectroscopy scan recorded in a transmission electron microscope of a patterned arm structure, recorded parallel to the film surface from the sidewall towards the center of a patterned feature.

While the TEM image suggests that the crystallinity of the PMN-PT is maintained up to ~5 nm away from the sidewall, the EDS data shows that the Pb composition reduces ~5-10 atomic percent within 100 nm of the free sidewall. Of the cations in PMN-PT, Pb is typically cited as the most volatile,[179,188,309] and deficiencies of only a few atomic percent can have significant influence on the functional response.[188] These regions may be culpable for the property reductions observed in the features of smallest lateral dimension prepared and studied in this work. Annealing in a PbO atmosphere (discussed in Chapter 6) or improvement to the patterning process may ameliorate these effects.

The three TEM images in Figure 5-28 show that the lateral distance to which the amorphous region extends into an arm structure from a sidewall is a function of film thickness, with the material near the top surface having the thinnest amorphous region. To explain this observation, consider the initial ion bombardment and chemical reaction of the etching process resulting in an amorphous layer of a given thickness, “x”. It is possible that prolonged ion bombardment sputters away this amorphous region, yielding thinner amorphous regions at the top surface, where more time for such sputtering was afforded. At the base of the patterned film structure, the amorphous region thickness would be very close to “x” since the etch process was stopped before significant sputtering of that layer could occur. In this model, thinner films, which were etched for less time, would have larger volume fractions of amorphous material than thicker films, which would limit the rate of declamping as a function of aspect ratio. Figure 5-29 shows the thickness dependence in the rate of declamping which agrees with this model of amorphous layer formation and subsequent removal via continued etching. Other thickness effects, discussed in more detail in Chapter 4, may also contribute to the behavior depicted in Figure 5-29.

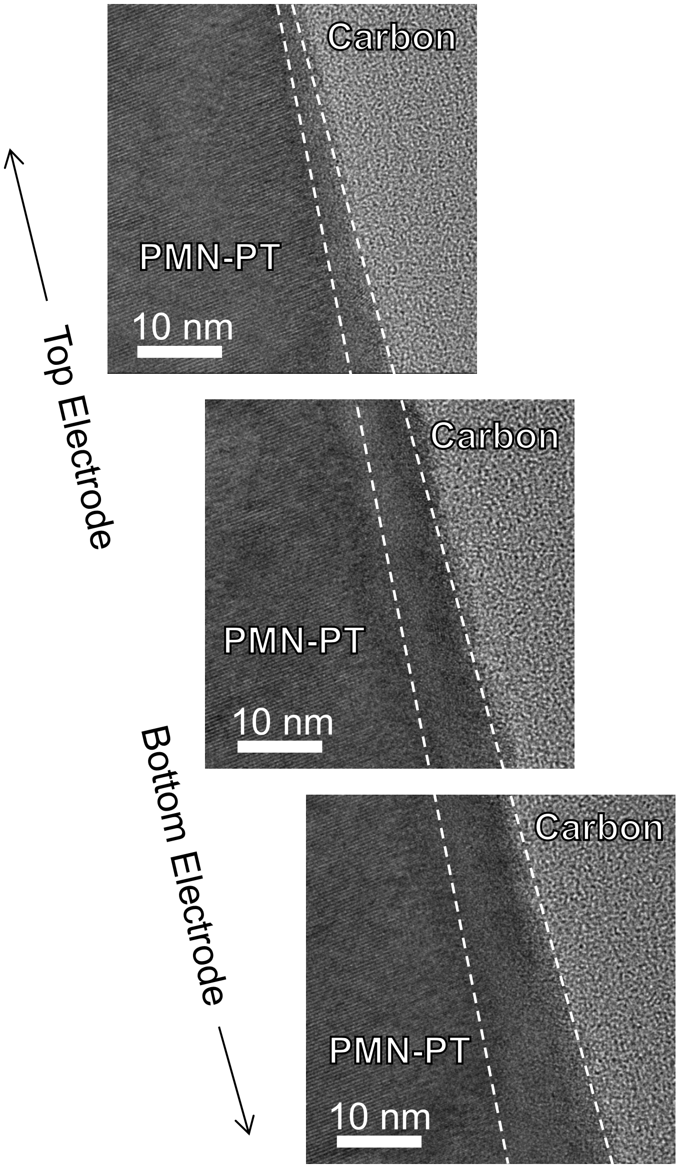

Figure 5-28: Three transmission electron micrographs of a patterned 350 nm thick 70PMN-30PT sidewall showing the change in the depth of the amorphous layer into the arm structure as a function of film thickness. The position in film thickness where the images were recorded was not precisely noted.

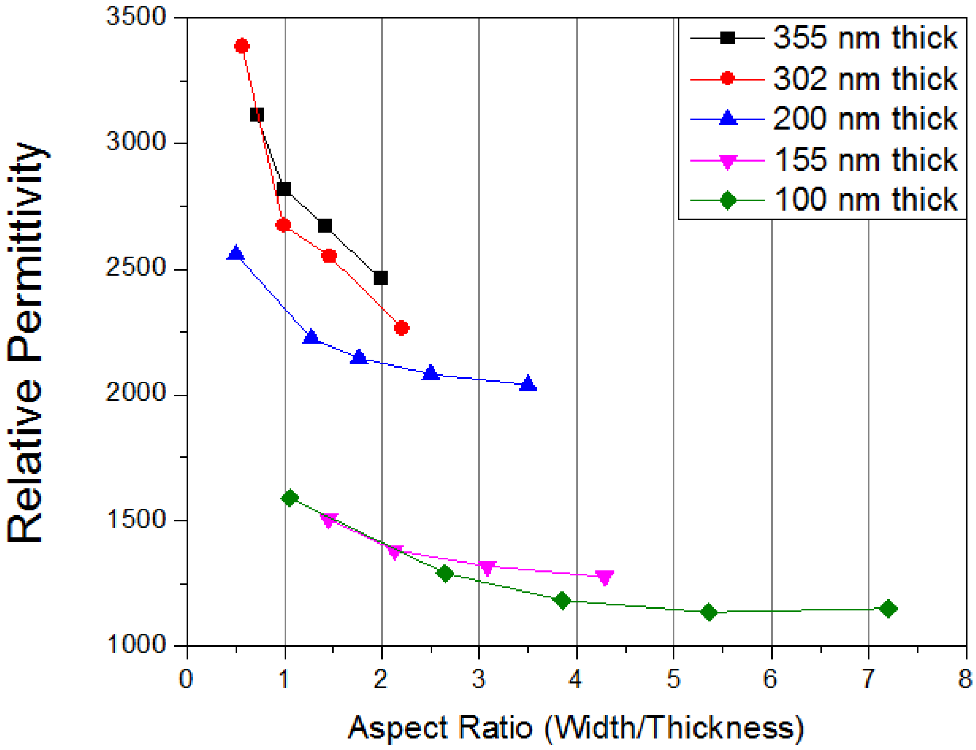

Figure 5-29: Enhancement in the relative permittivity of patterned {001}-oriented, polycrystalline 70PMN-30PT films on Si substrates as a function of film thickness.

5.4 Conclusions

On laterally patterning to reduce substrate clamping of $70Pb(1/3Nb_{2/3})O_3$-$30PbTiO_3$ films with strong{001} orientation, both the reversible and irreversible Rayleigh constants and P_r increased considerably, due to enhanced domain wall motion and increased intrinsic response. The relative permittivity of the 350nm thick 70PMN-30PT films was measured to be nearly 3000, doubled from the clamped state. It is observed that the effects of declamping dominated over etch-induced damage in structures with lateral features sizes of 250 nm (0.7 thickness to width aspect ratio.

Characterization of $d_{33,\,eff}$ as a function of local position across the arms by piezoresponse force microscopy and nanoprobe X-ray diffraction revealed the mechanism of the observed property enhancement. The $d_{33,f}$ increased ~3 times from the clamped value to the free sidewall under 200 kV/cm excitation and the free sidewalls enabled partial declamping 500-600 nm into the patterned structure. The spatial influence of declamping raised the average piezoelectric response significantly for features with lateral dimension less than 1 μm (3:1 width to aspect ratio). Finally, the observed enhancement in $d_{33,f}$ upon patterning to width:thickness aspect ratio features of ~3:1 was in good agreement with the finite element models. These models also predict significantly more declamping upon further lateral reduction, especially below aspect ratios of 1:1.

Chapter 6

Conclusions and Recommended Future Work

This section describes both applied and fundamental studies in PMN-PT films which are motivated by the conclusions of this dissertation, also discussed here. The proposed experiments are framed by both aforementioned results and new results not previously presented in the thesis.

6.1 Conclusions

It was found that rhombohedral 70/30 $Pb(Mg_{1/3}Nb_{2/3})O_3$-$PbTiO_3$ (70PMN-30PT) thin films could be grown on platinized Si substrates via chemical solution deposition with essentially perfect {001}-orientation as detectable by lab source X-ray diffraction without a perovskite orienting layer. The mechanism of the textured growth is proper accommodation for Pb loss to the bottom electrode by deposition of a 2-3 nm thin PbO buffer layer prior to PMN-PT spin casting. It was observed that at least 10% of the local Pb content can diffuse to the bottom electrode, changing the grain morphology and crystallinity of the film significantly. The benefit of employing a Pb reservoir for {001} orientation as opposed to a second perovskite seed layer is to avoid the parasitic capacitance and voltage drop that occurs across seed layers with smaller dielectric permittivities. This method also avoids pyrochlore formation and can allow for reduced excess Pb batching in the PMN-PT film, which would otherwise cause pore and void formation within the perovskite grains and at triple points.

The 300 nm {001}-oriented blanket films had dielectric permittivities of ~1650 with loss tangents < 1%, and high breakdown strengths enabling ~1% strain. The large signal $d_{33,f}$ was

~90 pm/V in clamped films. The P-E characteristics were heavily influenced by the tensile stress imposed by the Si substrate, as expected from elastic constants, and were rotated clockwise and slim in nature. The thickness dependence of these and of compressively stressed epitaxial films on $SrRuO_3/SrTiO_3$ substrates was also studied. Both film types exhibited similar intrinsic dielectric responses. EDS measurement across the interface revealed, however, ~3-6 nm thick regions of graded composition. The functional properties of the epitaxial films suggest that pinning of domain wall motion at the interface is a significant factor in the observed thickness dependence. The Rayleigh behavior demonstrated that irreversible domain wall motion is strongly thickness dependent in the epitaxial films. It is believed that large angle grain boundaries may be responsible for a higher density of pinning sites though the thickness of the polycrystalline films, reducing the thickness dependence.

The thickness dependence of the piezoelectric coefficient mimicked that of the dielectric behavior. However, correcting for the presence of the observed interfacial layers, with dielectric properties fit via the series-capacitor model, largely eliminates the thickness dependence of the piezoelectric properties. In the epitaxial films with {002} FWHM less than ~0.01°, a field-induced rhombohedral to tetragonal phase transition initiated at DC bias fields of ~300 kV/cm. It is anticipated that additional phase switching would be enabled on laterally patterning to finer feature sizes. Thus, highly scaled devices may leverage the phase transition for increased functionality.

The dielectric and piezoelectric properties of blanket {001}-oriented 70PMN-30PT films with only 100 nm thickness were similar to those of $Pb(Zr_{0.52}Ti_{0.48})O_3$ (52/48 PZT) films with thicknesses an order of magnitude higher. This result makes 70PMN-30PT films quite attractive for various ferroelectric microelectromechanical systems. However, there are significant gains to be made in the functional behavior of the films when compared to the ferroelectric and piezoelectric response of free bulk materials of the same composition. An effort to regain this functionality from the substrate-constrained films was done by lateral subdivision of blanket films to partially declamp the response.

On laterally patterning of 300 and 350 nm thick {001}-oriented 70PMN-30PT polycrystalline films, and subsequent annealing to recover etch induced damage, both the reversible and irreversible Rayleigh constants and P_r increased considerably, due to enhanced domain wall motion and increased intrinsic response. The relative permittivity of the 350 nm thick 70PMN-30PT films was nearly 3000, doubled from the clamped state and nearing that of the epitaxial blanket films under compressive stress. It is observed that the effects of declamping dominated over etch-induced damage in structures with lateral features sizes of 250nm (0.7 thickness to width aspect ratio).

Characterization of the longitudinal effective piezoelectric coefficient, $d_{33,f}$, as a function of local position across the patterned arm structures by piezoresponse force microscopy and nanoprobe X-ray diffraction revealed the mechanism of the property enhancement. The $d_{33,f}$ increased ~3 times from the clamped value to the free sidewall under 200 kV/cm excitation and the free sidewalls enabled partial declamping 500-600 nm into the patterned structure. By reducing the width:thickness aspect ratio of patterned structure, the volume fraction of material within the highly declamped regions of the structures increases, thereby increasing the globally measured dielectric and ferroelectric response. The spatial influence of declamping raised the average piezoelectric response significantly for features with lateral dimension less than 1 μm

(1:3 width to aspect ratio). Finally, the smallest width:thickness aspect ratio studied experimentally was only ~3:1 and the observed enhancement in $d_{33,f}$ was in strong agreement with the finite element models which also predict significantly more declamping upon further lateral reduction, especially below aspect ratios of 1:1.

6.2 Continued aspect ratio scaling and characterization

This dissertation studied the enhancement of dielectric and ferroelectric properties upon lateral scaling to width:thickness aspect ratios of ~0.5 and of piezoelectric properties to an aspect ratio of ~2.5. These aspect ratios were a function of several constraints. First, the smallest width of the patterned structures brought to the nanoprobe X-ray beam line was 750 nm so that three diffraction patterns could be collected with the 240 nm wide beam: two near the sidewalls and one at the feature center. The dimension of the features for dielectric and ferroelectric characterization was limited by the geometry of the patterned structure and erosion of Ni hard mask during the patterning process. For example, in the smallest width:thickness aspect ratio structure studied, electron beam lithography defined 2474 arm structures, each 546 µm long and 150 nm in width. This amounts to more than 2.7 meters of perimeter with little tolerance for defects in the lithography which could pinch off electrical contact to significant fractions of the declamped regions of the feature.

Property enhancement from lateral subdivision is predicted to continue with further reduced width:thickness aspect ratio (see Figure 5-2) and to do so at an increasing rate. In order to support the pursuit of truly bulk-like piezoelectric response from thin films for devices such as the piezoelectronic transistor, one aspect of the future work could include the characterization of further scaled structures achievable by the following methods. First, the minimum feature width could be further reduced by reducing the total feature size (i.e. feature perimeter) to reduce the potential for lithography errors. Secondly, the sidewall angle would need to be increased closer to 90° so that the top metal would not be pinched off with basal dimensions below 130 nm (shown schematically in Figure 6-1). This will require optimizing the etch procedure to yield more vertical sidewalls.

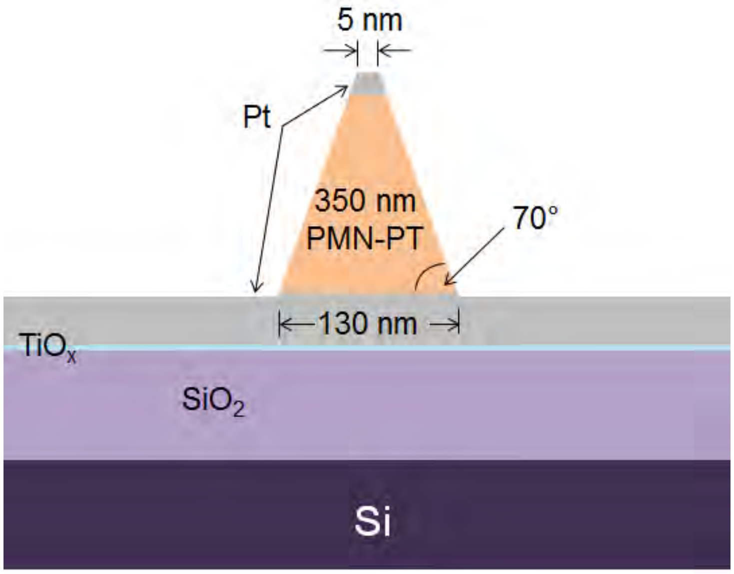

Figure 6-1: Schematic depiction of the geometry limited feature size due to the 70° sidewall angles achieved using the etching procedure developed in this thesis.

A third means of reducing the aspect ratio would be to increase the PMN-PT film thickness. While chemical solution deposition (CSD) of 70PMN-30PT films in this work to thicknesses greater than 350-400 nm on Si results in film cracking, other growth techniques such as sputtering[199,310] and pulsed laser deposition[185] have been employed to grow crack-free PMN-PT to thicknesses exceeding 1 μm on Si.

6.2.1 Declamping of epitaxial PMN-PT films

Figure 6-2 depicts the locally mapped piezoresponse force microscopy images showing significantly smaller responses near grain boundaries. This reduces the mean piezoresponse as compared to both the peak response and to finite element model predictions for enhancement near the sidewalls (see Figure 5-20). Similar reductions in the piezoresponse at the grain boundaries have been observed in PZT[139,140,142] and $BiFeO_3$[138] films.

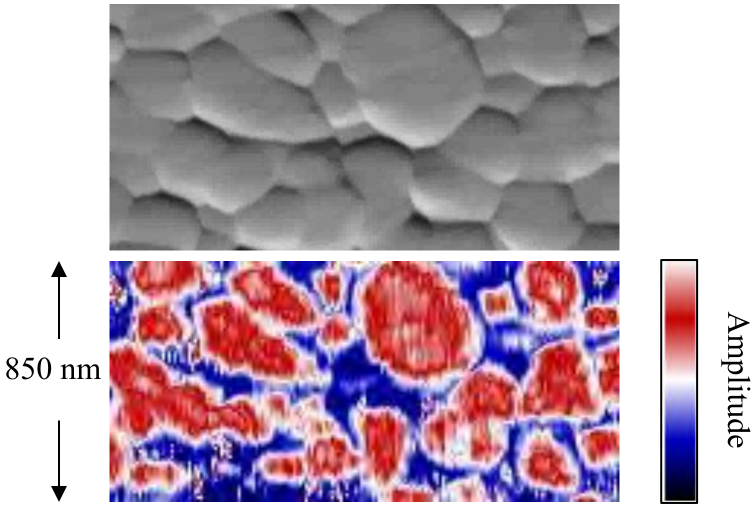

Figure 6-2: Film surface grain morphology (top) and piezoresponse amplitude (bottom) by piezoresponse force microscopy of a 350 nm thick {001}-oriented 70PMN-30PT thin film on $Pt/TiO_x/SiO_2/Si$.

To avoid this, and to better probe the limits of achievable piezoelectric response, it is suggested that lateral patterning of epitaxial films be explored, with concomitant piezoelectric measurements. Epitaxial films were grown by CSD on $SrRuO_3$ bottom electrodes on 1 cm^2 $SrTiO_3$ substrates for thickness dependent measurements. A declamping study on similar films is recommended. In addition, epitaxial films should be grown on $SrTiO_3$ buffered Si wafers and patterned to better assess the limiting properties for future piezoelectronic transistor applications. The relatively small substrate size will limit the number of patterned features to about four per sample, with fewer being preferred in order to avoid edges of the film where reduced crystallinity and thickness variations are more likely. The local piezoelectric response on the patterned epitaxial structures could be studied via band excitation PFM[311] and synchrotron XRD at the nanoprobe beamline, 2-ID-D, at Argonne National Laboratory. Slight modifications to the feature geometry to avoid significant substrate bending effects near an actuated arm would enable characterization by single beam laser interferometry as well, as described by Shetty *et al.*[284]

To minimize challenges associated with spatial uniformity of epitaxial $SrRuO_3$ growth by pulsed laser deposition (PLD) at Penn State University, epitaxial patterning studies are recommended to be performed on $SrTiO_3$ buffered Si wafers with $LaNiO_3$ (LNO) electrodes which can be grown via CSD on larger area substrates.[90]

6.3 Clamping via top electrodes

This dissertation addressed the partial declamping of PMN-PT from the underlying substrate. However, the top electrode may impose some clamping as well. Finite element modeling, performed by Marcelo Kuroda of Auburn University, shows that the rigidity of the top metal layer may reduce the out-of-plane strain of the ferroelectric film. These effects are most pronounced where the strain of the piezoelectric is highest. For example, Figure 5-2 depicts the reduction in $d_{33,f}$ at the edges of the patterned features stemming from the bending rigidity of the Pt electrode. Predicted improvement in the piezoelectronic transistor performance was recently reported by Magdau *et al.* by employing a more compliant Au bottom electrode as compared to the stiffer Ir metal.[163]

To assess the importance of the top electrode stiffness, different top electrodes should be deposited with varying thicknesses on pieces of the same blanket PMN-PT film. Patterning could be conducted using the methodology described in section 5.2.3 to define antennae structures comprised of various arm widths. Then, piezoresponse force microscopy may be employed to record differences in local out-of-plane strain as a function of electrode material and thickness. The patterning should be performed to ensure constant sidewall angles to maintain similar field concentrations across the various samples.

The bending rigidity, D, of a top electrode in plate geometry with thickness *h* can be calculated from the elastic moduli (E) and the Poisson's ratio, ν, as shown in Equation 6-1:

$$D = \frac{Eh^3}{12(1-\nu^2)} \qquad \text{Equation 6-1}$$

Salvadori *et al.* reported ~12% change in the elastic modulus from bulk form in Pt and Au thin films with grain sizes of 35 and 20 nm, respectively, measuring ~69 GPa and ~140 GPa, respectively; it is possible that the lower moduli were due to a reduced density, although densities were not reported.[312] Since the Poisson's ratio of the two metals is similar (around 0.4), it is expected that patterned PMN-PT structures with thinner Au top electrodes will exhibit the most enhancement upon declamping due to lower clamping effects from the bending mechanics of the top electrode.

6.4 Characterization of sidewall defects

Subtractive patterning processes are known to be potentially damaging to the crystallinity and functional response of the material. Using the etching procedures described in section 5.2.3 amorphous regions were observed at the PMN-PT sidewalls with Pb loss extending over 100 nm into the bulk. This could affect the rate of declamping as a function of aspect ratio compared to predicted behavior from finite element modeling. Further investigation of the defects, their relative concentrations, and influence on the lifetime characteristics are thus warranted.

As a means to ameliorate the Pb loss near the sidewalls, patterned films may be annealed in a PbO furnace which has been built at Penn State University.[313,314] The Pb furnace is plumbed with nitrogen gas to dilute and carry a tetraethyl lead (TEL) precursor into a furnace providing the desired Pb partial pressure. Oxygen is introduced into the atmosphere to disassociate the Pb from the ethyl groups and to provide an oxidizing atmosphere. The gas flows through a diffuser into the "hot zone" of the furnace where the crystallization temperature of the desired perovskite phase is maintained. With the increased surface area and short diffusion lengths in patterned structures, this furnace should be an effective means of correcting the A-site stoichiometry. Annealing profiles can vary in time and temperature with subsequent anneals in air or a dip in acetic acid to any remove excess PbO. Improvement in dielectric permittivity would suggest reincorporation of Pb atoms into the lattice, which can be confirmed with EDS in a TEM.

In addition to the Pb furnace anneals, highly accelerated lifetime testing (HALT) may be performed on patterned PMN-PT films before annealing, after annealing (in air and Pb atmosphere), and after sidewall passivation. HALT can be performed by the procedure described by Minford[315] and Polcawich *et al.*[316] with the 30 nm thick HfO_2 sidewall passivation procedure developed by J.-I. Yang *et al.* for patterned PZT films.[282]

6.5 Strain tuning of PMN-PT phase stability

Being a soft piezoelectric, the functional properties of PMN-PT near the MPB are highly dependent on stress state. Cao *et al.* demonstrated that the clamped relative permittivity of 67PMN-33PT crystals increased more than 12x upon removal of a zero strain condition. For comparison, 58PMN-42PT (a tetragonal composition of PMN-PT, further from the MPB) exhibited only a ~2.5x increase under the same conditions.[89] This is one of the factors that leads to PMN-PT properties being highly sensitive to declamping upon patterning of thin films. It must also be considered, however, that this sensitivity to stress state may result in changes in phase stability in the PMN-PT system from film growth on substrates with dissimilar thermal expansion coefficients. Several studies have suggested that stresses and electric fields can induce shifts in the composition of the MPB,[317] including the stresses developed when PZT[318–320] or PMN-PT[321] are grown as thin films. In efforts to maximize the $d_{33,f}$, the free energy landscape and phase stability should be well understood in PMN-PT films grown on Si.

6.5.1 MPB composition in strained PMN-PT films

It is proposed that PMN-PT films varying in PT composition be grown on various substrates which differ in thermal expansion coefficient, thereby imparting different stress states. As discussed in Chapter 2, thermal strain, ξ, is accumulated in a film upon cooling from $T_{crystallization}$ to T_C where domain formation occurs and partially relieves stress in the film. Coefficient of thermal expansion data are shown in Figure 6-3 for PMN-PT [92] and Si, $SrTiO_3$,[91] MgO,[91] and $(LaAlO_3)_{0.3}(Sr_2AlTa_6)_{0.7}$ (LSAT)[322] substrates. Each substrate would put PMN-PT films in a different in-plane strain state due to the CTE mismatch and the thermal excursion of $T_{crystallization}$-T_C. Although the CTE is not a strong function of PT content in PMN-PT films, changes in T_C as a function of PT composition result in different room temperature strain states for different x in (1-x)PMN-xPT films, as shown in Figure 6-4.

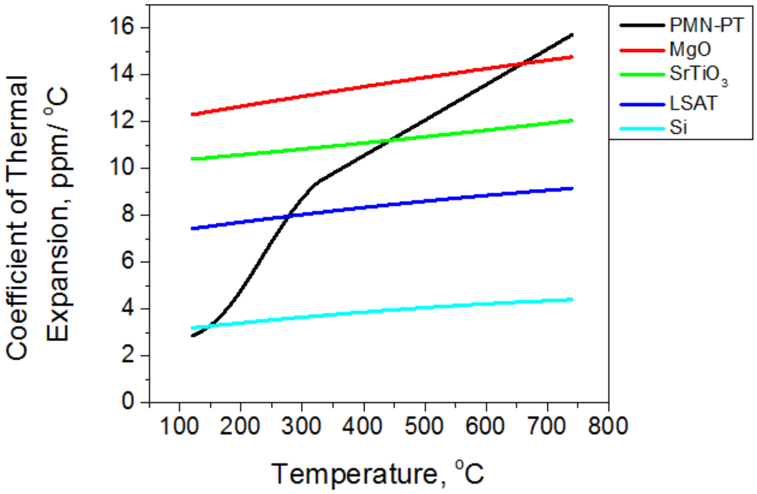

Figure 6-3: Thermal expansion coefficient for PMN-PT films and MgO, Si, LSAT, and $SrTiO_3$ substrates in the temperature range of T_C to $T_{crystallization}$.[91,92,322]

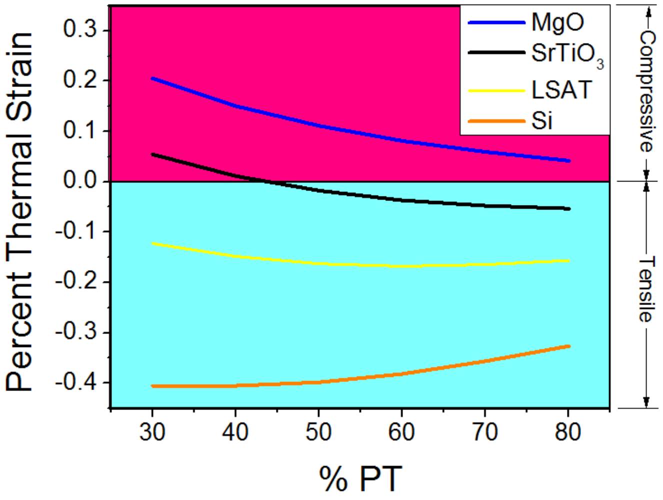

Figure 6-4: Calculated in-plane strain values due to thermal expansion mismatch for PMN-PT grown on various substrates as a function of $PbTiO_3$ content, which vary in T_C and the T regime over which strain is accumulated.

PMN-PT films can be grown over a compositional range of 20-60% PT in 5% PT increments on Si, $SrTiO_3$, MgO, and LSAT substrates while maintaining {001} orientation. The phase and lattice parameters of the films should be characterized via XRD. Top Pt electrodes should be sputtered onto the blanket films for dielectric, ferroelectric, and piezoelectric characterization. The piezoelectric coefficients should be plotted against composition to determine maxima for each substrate-induced strain state. If differences from bulk materials appear, the films can be patterned and measured again in order to determine any MPB shifts upon reduction of in plane stress via lateral scaling. Preliminary results on the composition dependence of PMN-PT thin films on Si are presented in Appendix A.

6.5.2 Stabilization of relaxor character

Since various ferroelectric phases can be strain tuned,[77] it is reasonable to suspect that the stability of relaxor phases may be influenced by the strain state of a system. Additionally, Figure 4-12 shows the 70PMN-30PT films exhibit frequency dispersion in ε_r below T_C, suggesting relaxor characteristics. This behavior differs from the bulk response which has little dispersion in relative permittivity over a 10 °C range near T_C.[189] Furthermore, several curiosities were observed via piezoresponse force microscopy of the epitaxial and polycrystalline films from this thesis. As seen in Figure 6-5, no large, distinct 71°, 109°, or 180° domains were visible as one would expect in a rhombohedral ferroelectric of {001} orientation. Additionally, many grains within the films appeared to be of zero response, potentially linked to grains of slightly differing crystallographic orientation,[308] although no large volume fraction of material was observed to be misoriented by XRD. Additional PFM data on these films are presented in Appendix B.

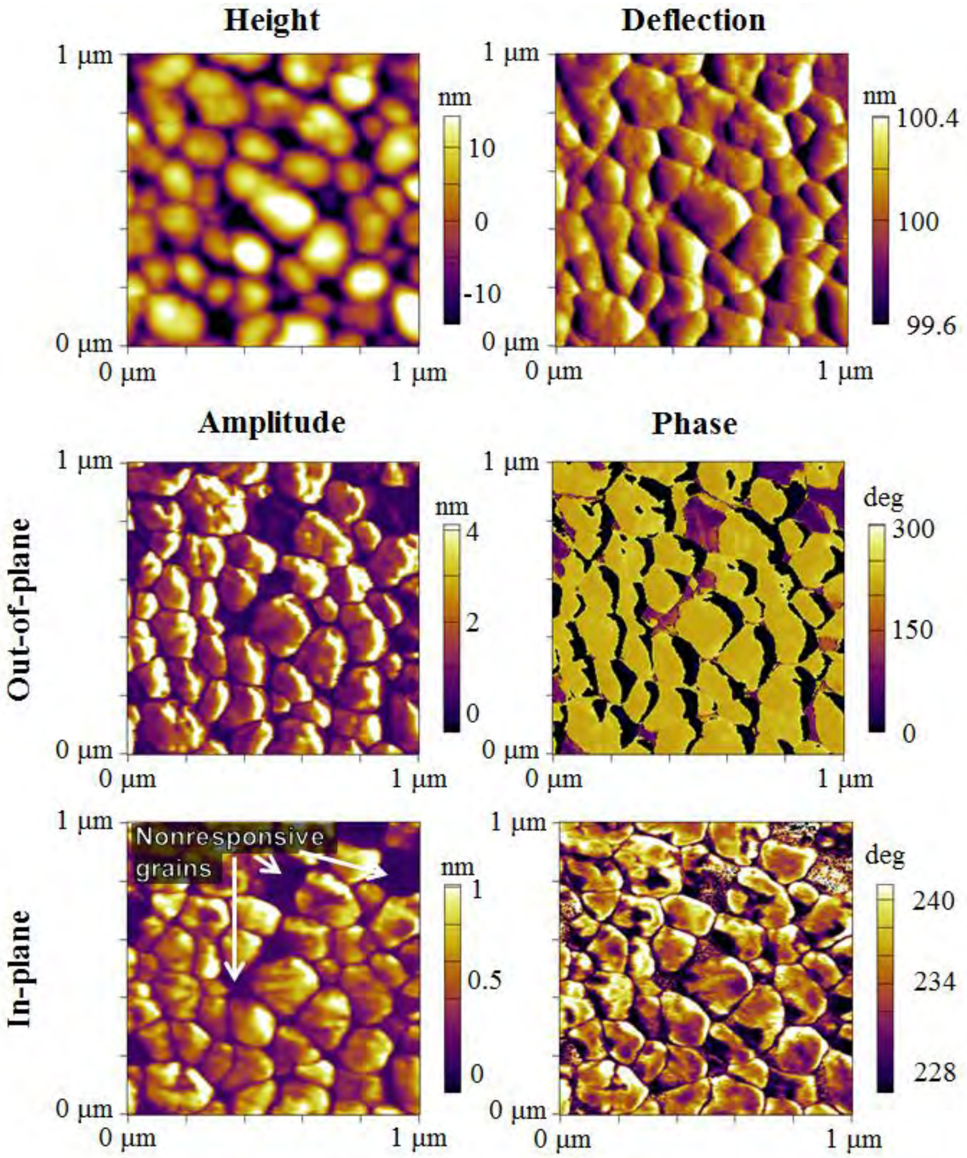

Figure 6-5: Topography and piezoresponse maps of 350 nm thick polycrystalline, {001}-oriented 70PMN-30PT film on platinized Si substrate recorded with 1.5 V_{ac}.

Another data set which suggests interesting phenomena relating to domain size and stability in the PMN-PT films on Si substrates is presented in Figure 6-6 and Figure 6-7. The Rayleigh coefficients of proper ferroelectric films reduce under DC-bias as domain wall motion is suppressed and the intrinsic polarizability decreases as the B-site cation is displaced further from the unit cell center.[223] This is observed in the reversible Rayleigh parameter, ε_{init}, of the

70PMN-30PT films. The irreversible coefficient, α, also decreases under DC-field, but becomes negative in the field range of ~30-75 kV/cm and exhibits a minimum between 50 and 115 kV/cm (depending on film thickness) before converging to zero. The meaning of a negative α coefficient is that the relative permittivity *decreases* with increasing AC signal amplitude. This is an atypical occurence for ferroelectrics. One potential expanation for this is that small, possibly nanometer sized, polar regions are growing to larger, micro, polar regions under electric field, reducing the number of domain walls present in the systen, thereby reducing the irreverisble domain wall contribution. Further investigation is needed to assess this hypothesis. In particular, details on the domain structure in relaxor-based ferroelectric films should be probed as a function of the applied field.

The asymmetric response in field for both Pt/PMN-PT/SRO and Pt/PMN-PT/Pt capacitors (shown in Figure 6-7) may provide insight into the differences of the crystallinity and electronic structure at top and bottom electrode interfaces. This should be further explored as a function of the processing conditions and may be related to a crossover in piezoelectric and electrostrictive dominated strain.

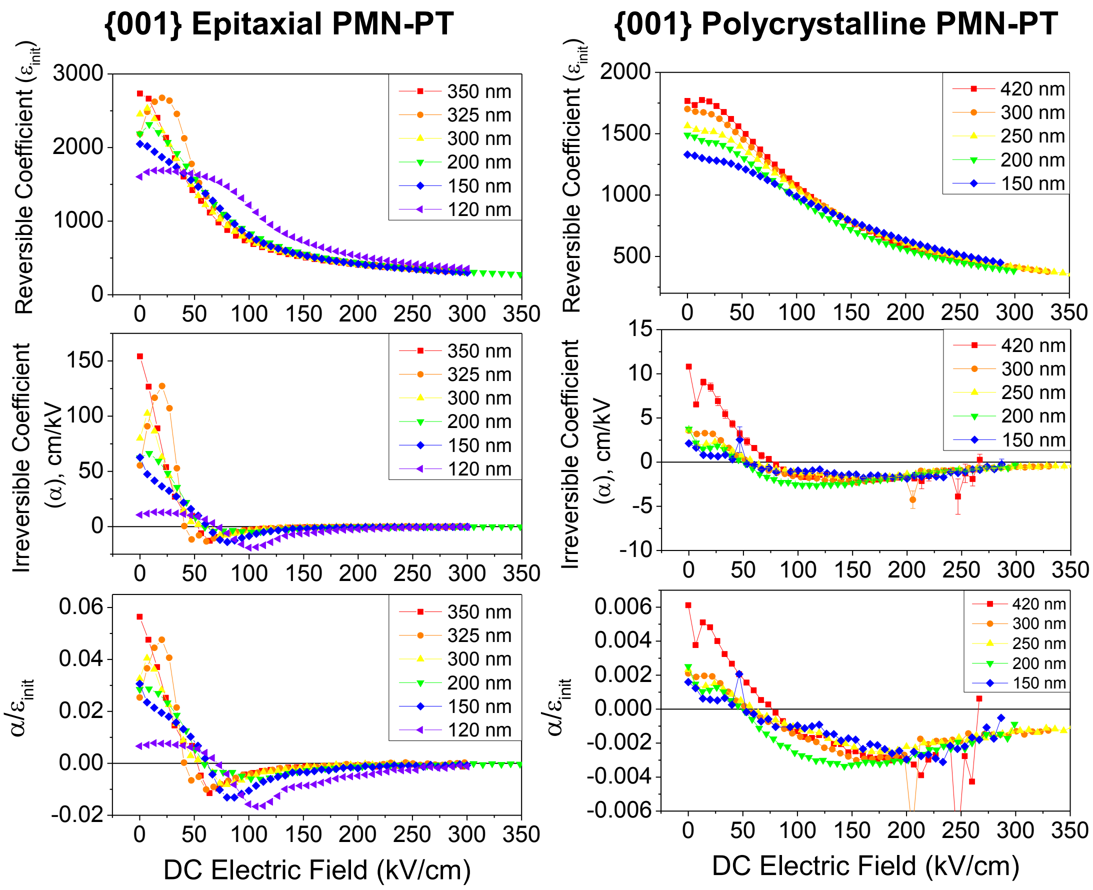

Figure 6-6: Rayleigh parameters for the relative permittivity of epitaxial and polycrystalline {001} oriented 70PMN-30PT films of thicknesses ranging from ~120-420 nm as a function of DC-bias.

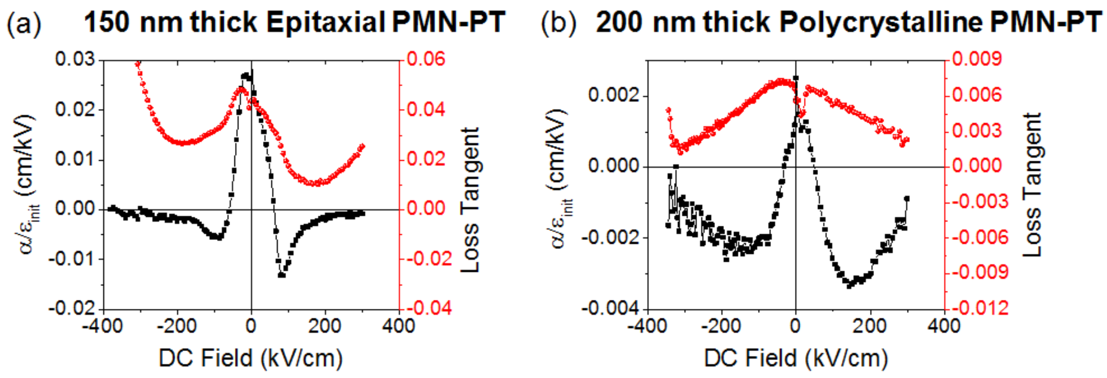

Figure 6-7: The dielectric non-linearity for both polarities of the DC-field applied to the bottom electrodes of epitaxial and polycrystalline 70PMN-30PT films of 150 nm and 200 nm thickness, respectively.

6.6 Fabrication of the piezoelectronic transistor device

The piezoelectronic transistor has been experimentally demonstrated to be a feasible technology;[202] a monolithically integrated device was recently demonstrated.[323] A major goal of the novel device fabrication effort was to demonstrate that the complex processing procedure was achievable while avoiding excessive or catastrophic damage to the functional components of the device. In this thesis, good scaling was shown down to films with lateral dimensions of 150 nm. This is sufficient for RF switch and large area low voltage applications.[163] Ultimately, to reach very-large-scale integration applications, further scaling is required. Thus, to continue the development of the device roadmap, it is essential to further the understanding of the mechanisms influencing the functional aspects of scaled devices, while simplifying the integration.

6.6.1 Piezoresistive switching as a function of $d_{33,f}$

The normally off piezoelectronic transistor device is turned on by the electrical conductivity changing several orders of magnitude with applied pressure from the piezoelectric. With the local piezoelectric response of patterned 70PMN-30PT beam structures characterized (section 5.3.3 it is proposed that a linear array of piezoresistive dots (~100 nm in diameter) be grown on a sapphire plate, spaced 50 nm apart, and changes in electrical resistivity be characterized as a function of $d_{33,f}$ from the patterned piezoelectric beam structure. The experiment shown schematically in Figure 6-8 would provide information on the change in resistivity which may be expected from lateral scaling of piezoelectric films.

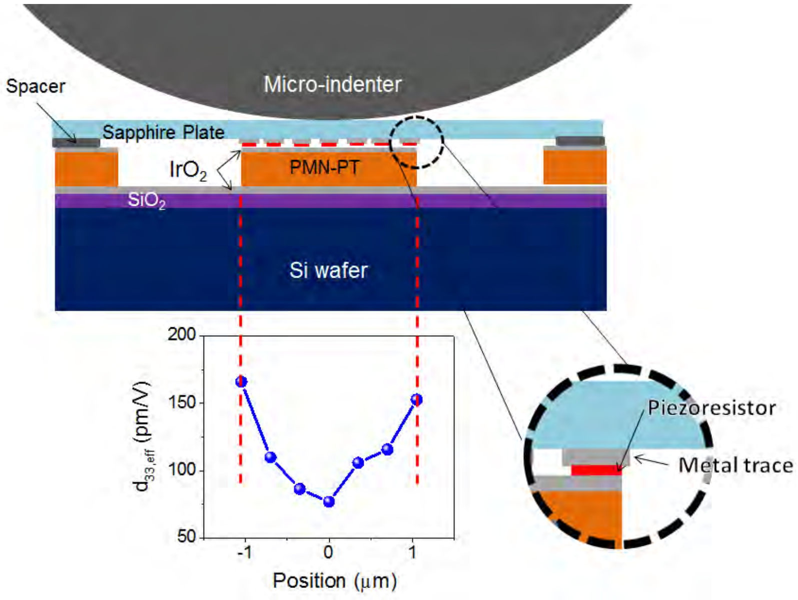

Figure 6-8: Schematic for the proposed experimental setup for measuring the change in electrical resistivity through a piezoresistor nanodot as a function of applied stress from a patterned PMN-PT beam with known local $d_{33,f}$.

The experimental setup for electrical characterization could mimic that of the first piezoelectric switching device described by Solomon *et al.*[202] IrO_2 electrodes, offering increased hardness as compared to Pt, are recommended on all parts of the piezoelectric and piezoresistor which will be exposed to stress to avoid deformation of the electrodes and maximize stress transfer to the PR from the piezoelectric. A sapphire plate can serve as the substrate for the PR dots; electron beam lithography will be required to define the metal traces for the PR. The sapphire plate and micro-indenter ball will serve as the high yield strength yoke material required for stress concentration in the PR.[25]

Piezoelectric PMN-PT for this study can be grown via chemical solution deposition on Si (since local declamping behavior for this film stack is already characterized) and also by PLD on $SrRuO_3/SrTiO_3$ substrates. PLD has been employed to grow crack-free epitaxial 70PMN-30PT films exceeding 1 μm in thickness which exhibit clamped $d_{33,f}$ of ~140 pm/V.[185] These films would offer the highest piezoelectric strain to switch the device.

It should also be noted that with this experimental setup, various PR materials can be tested. While rare-earth monochalcogenides have been selected in the publications on the piezoelectronic transistor to date, other potential insulator-to-metal transition materials could be employed. Potential candidates include semiconductors,[324] conductor-filled polymer composites,[325,326] aromatic organometallics and pressure-sensitive electron tunneling materials.[327] In regard to the monochalcogenide films, however, crystalline growth has been demonstrated via cosputtering,[29] beam epitaxy,[328] and horizontal tube furnaces.[329]

6.6.2 Clamping from rigid boundary conditions

Implementation of patterned piezoelectric films in a piezoelectronic switching device will include passivating sidewall layers (such as HfO_2 or Al_2O_3) and a high yield strength yoke material. The declamping phenomena of PMN-PT films should therefore be studied as a function of sidewall coating thickness and material as well as out-of-plane strain condition.

Patterned PMN-PT films can be coated with atomic layer deposited Al_2O_3 or HfO_2 to varying thicknesses, ranging from 5-20 nm. As an additional parameter in the study, the PMN-PT films may be grown to different thicknesses to change the contact area of the film/ALD coating and effective clamping of the sidewall layers. Following sidewall passivation, band excitation piezoresponse force microscopy can be employed to monitor any changes in resonance frequency and out-of-plane strain as a function of sidewall passivation material and thickness.

The influence of the sapphire plate on the 33-mode materials properties of the patterned PMN-PT can be studied using the experimental setup outlined in Figure 6-8. The study should focus on stress depoling of the ferroelectric state by the rigid out-of-plane boundary constraint and an externally applied load. Changes in the partially declamped functional properties, such as relative permittivity, should be monitored *in situ*.

6.6.3 Dynamics of GHz-range switching in patterned thin films

A final recommendation for the future work of this dissertation is to characterize the high frequency behavior of patterned PMN-PT films. By finite element modeling, the piezoelectronic device can afford ~100x power savings from a CMOS transistor switching at comparable clock speeds in the low GHz. The models, however, assume fairly idealized materials properties which are yet to be thoroughly characterized upon patterning and fabrication in a stiff system. While contributions to permittivity from domain wall motion have been observed to roll-off at frequencies lower than 1 GHz,[330–332] well poled 70PMN-30PT may remain a high ε_r material in higher GHz regimes due to significant contributions from intrinsic effects and polarization rotation. The frequency dispersion observed in the PMN-PT films should be investigated to higher frequencies before and after patterning. Model structures will need to be utilized to make the high frequency measurements on such high permittivity materials.

Appendices

Appendix A

Compositional dependence

Figure 2-7 shows the predicted magnitude and sign of strain within the films as a function of PT content as calculated from the thermal expansion data given by Wongmaneerung *et al.*[92] and Touloukian *et al.*[91] with the strain calculated using Equation 2-2 and elastic properties of PMN-PT at various compositions by Zhang *et al.*[89] The crystallinity (Figure A- 1), microstructure (Figure A- 3), and functional properties (Figure A- 4 through Figure A- 7) of 185 ±5 nm thick (1-x)PMN-xPT films grown on platinized Si wafers (Nova Electronics Materials, Flower Mound, TX) were characterized as a function of PT content by the methods described in Chapter 3. As can be seen from free bulk systems,[89] changing the relative PT content influences the functional properties. In addition to this, variation of the film strain state develops as a function of PT content due to the PT dependence in thermal expansion coefficient[92] which may also influence the properties.[294]

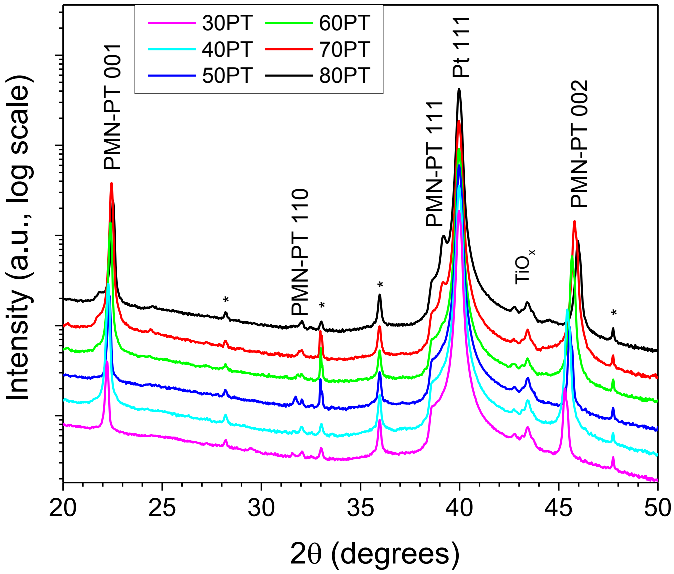

Figure A- 1: Diffraction patterns recorded in the Bragg-Brentano geometry using Cu-K$_\alpha$ radiation of PMN-PT thin films on platinized Si substrates from Nova Electronics (Flower Mound, TX) as a function of PT composition. Strong {001} orientation was achieved in all cases using a thin PbO buffer layer by the methods described in Chapter 3.

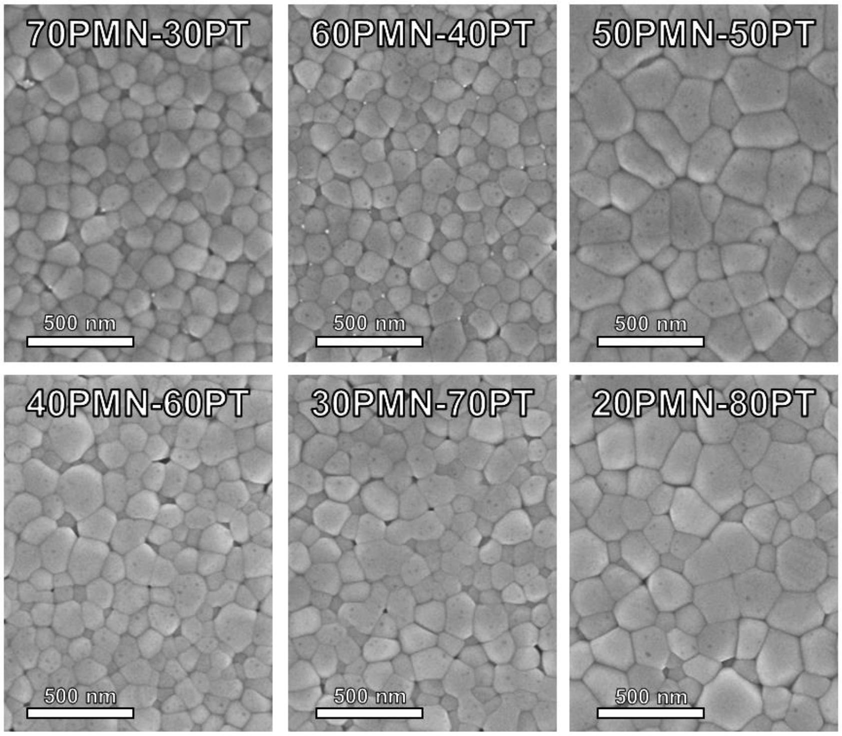

Figure A- 2: Top surface grain morphology of 185 nm thick PMN-PT films grown by chemical solution deposition as a function of PT composition.

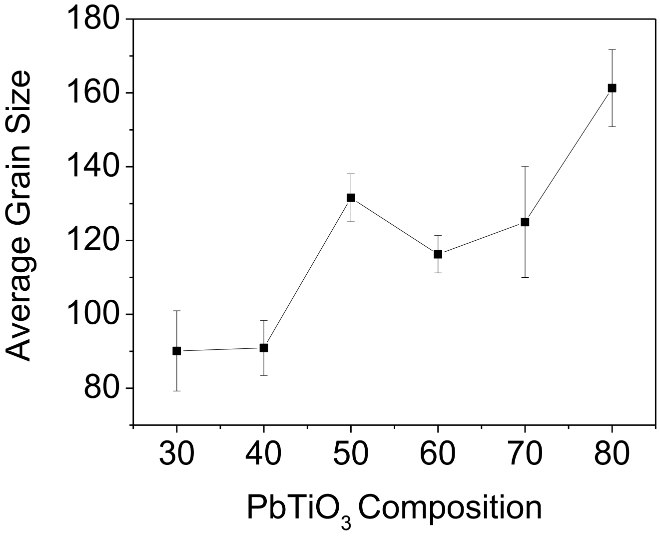

Figure A- 3: Average grain size of (1-x)PMN-xPT thin films on platinized Si substrates as calculated by the linear intercept method.

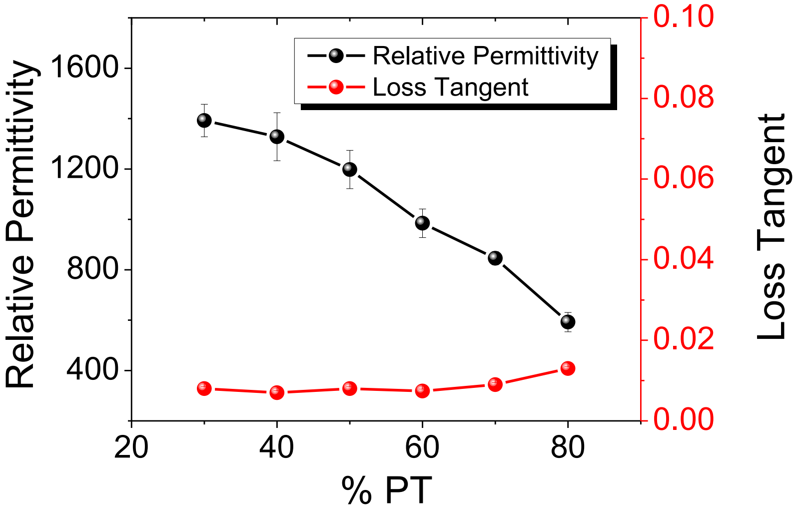

Figure A- 4: Relative permittivity and loss tangent of ~185 nm thick (1-*x*)PMN-*x*PT films for $0.2 \leq x \leq 0.8$ recorded at 1 kHz and 30 mV$_{ac}$.

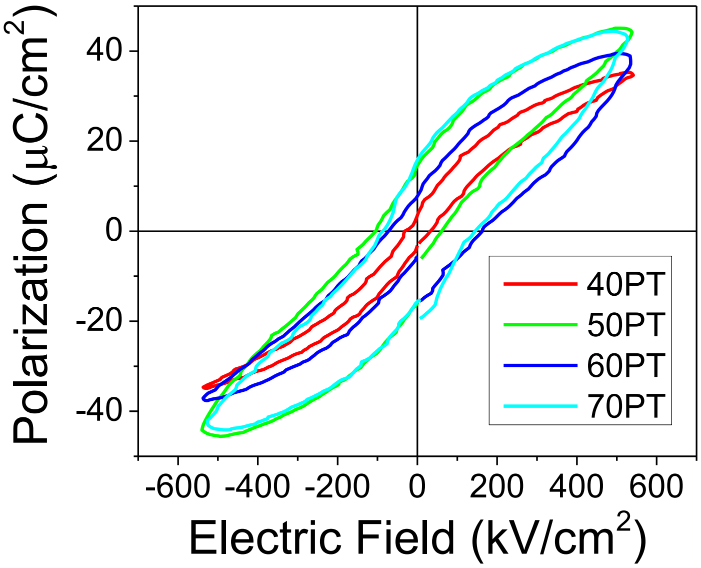

Figure A- 5: Polarization-electric field hysteresis loops recorded at 100 Hz of ~185 nm thick PMN-PT films of varying PT composition.

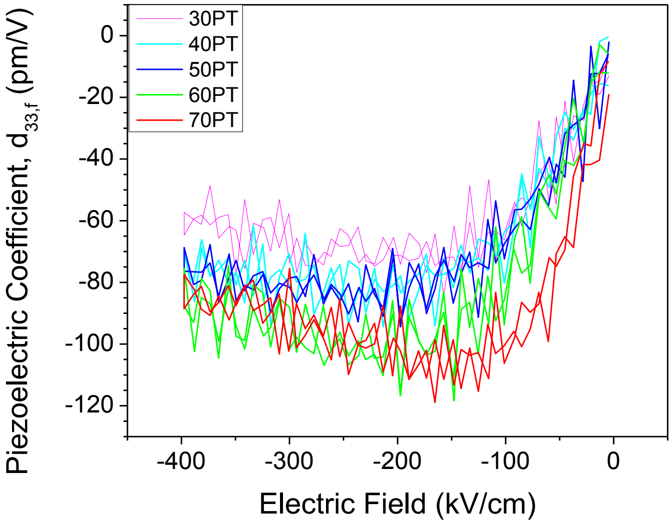

Figure A- 6: The piezoelectric coefficient, $d_{33,f}$, of blanket 185 nm thick PMN-PT films with {001}-orientation on platinized Si substrates. The data were recorded and averaged 10 times on an aixACCT double beam laser interferometer (aixACCT Systems, Aachen, Germany) on 600 µm diameter electrodes after wafer backside polishing to 0.6 µm diamond slurry. The excitation signal was a unipolar triangular function to 400 kV/cm at 0.5 Hz and 1 V_{ac} at 1 kHz after 15 minutes of room temperature poling with 2 times the coercive field.

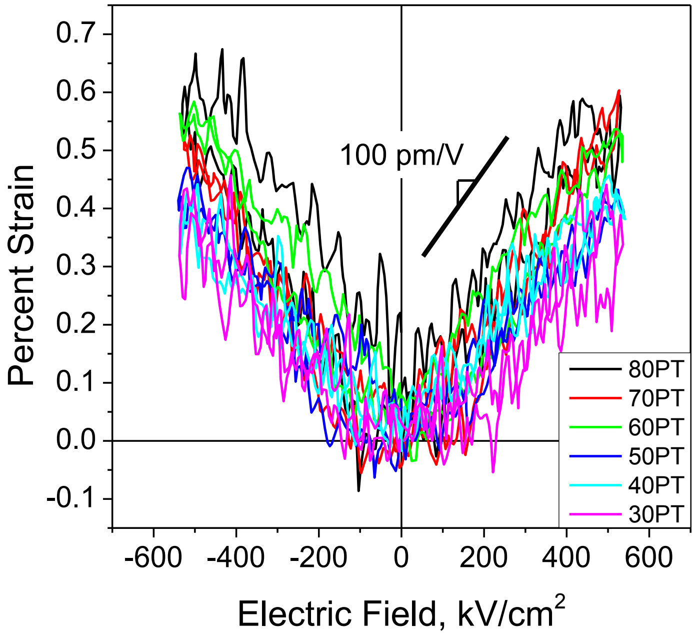

Figure A- 7: The out-of-plane strain (averaged from 10 field excursions) exhibited by blanket 185 nm thick PMN-PT films with {001}-orientation on platinized Si substrates. The data were recorded on an aixACCT double beam laser interferometer (aixACCT Systems, Aachen, Germany) on 600 um wide electrodes after wafer backside polishing to 0.6 μm diamond slurry. The excitation signal was a bipolar triangular function to 550 kV/cm at 1 k Hz.

Appendix B

Piezoresponse force microscopy

The local piezoresponse was recorded in polycrystalline and epitaxial 70PMN-30PT films as a function of thickness at the Center for Nanophase Materials Science at Oak Ridge National Laboratory. The band excitation measurements[333] were recorded on an Asylum Research Cypher with platinum-coated silicon tips (Nanosensors PPP-EFM-50) as described in detail elsewhere.[32] The piezoresponse of the films was excited with an AC voltage applied to the bottom electrode while the top electrode and tip were grounded.

Because of the low remanence of the functional properties, challenges were encountered in imaging domain structures below the coercive field. The study shifted to focus on characterizing the regions of non-responsive grains and regions in the polycrystalline and epitaxial films, respectively. Some groups have attributed similarly observed regions to polarization relaxation due to crystallographic orientation, lattice tilt, and related local strain gradients within thin films.[308] The recorded piezoresponse amplitude, phase, resonant frequency, and deflection for the 70PMN-30PT films are summarized below. Future work could include further characterization of the domain structures or stability of ferroelectricity in the films as a function of PT content.

B.1 Polycrystalline films:

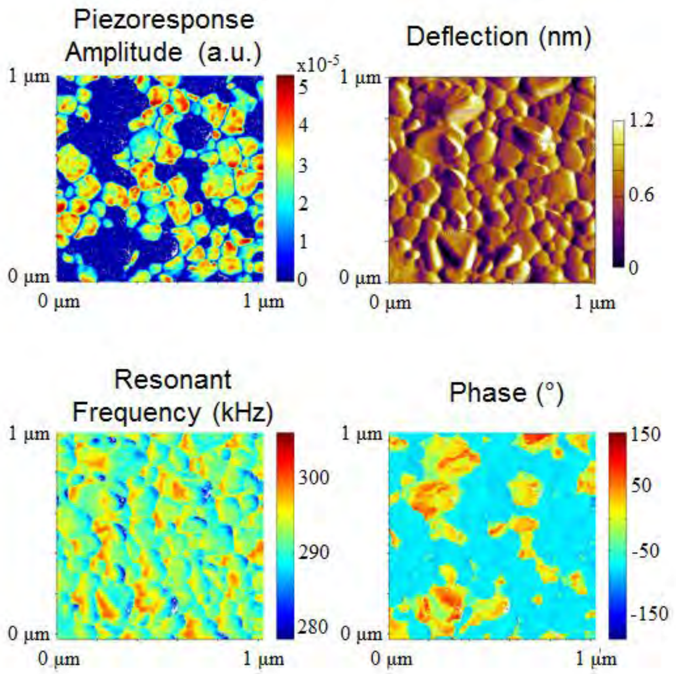

Figure B- 1: 100 nm thick polycrystalline {001}-oriented 70PMN-30PT film, measured with 1.2 V_{ac}.

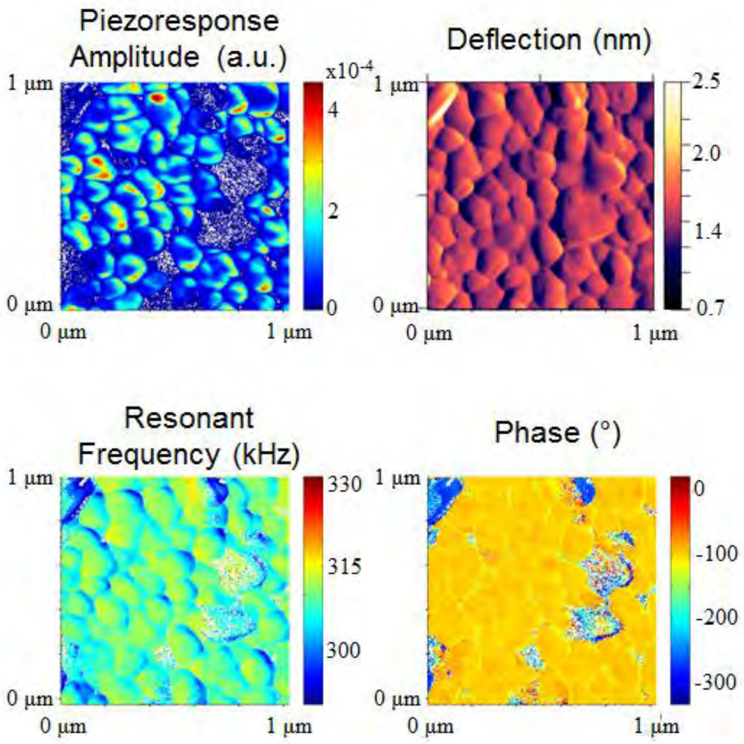

Figure B- 2: 150 nm thick polycrystalline {001}-oriented 70PMN-30PT film, measured with 1.2 V_{ac}.

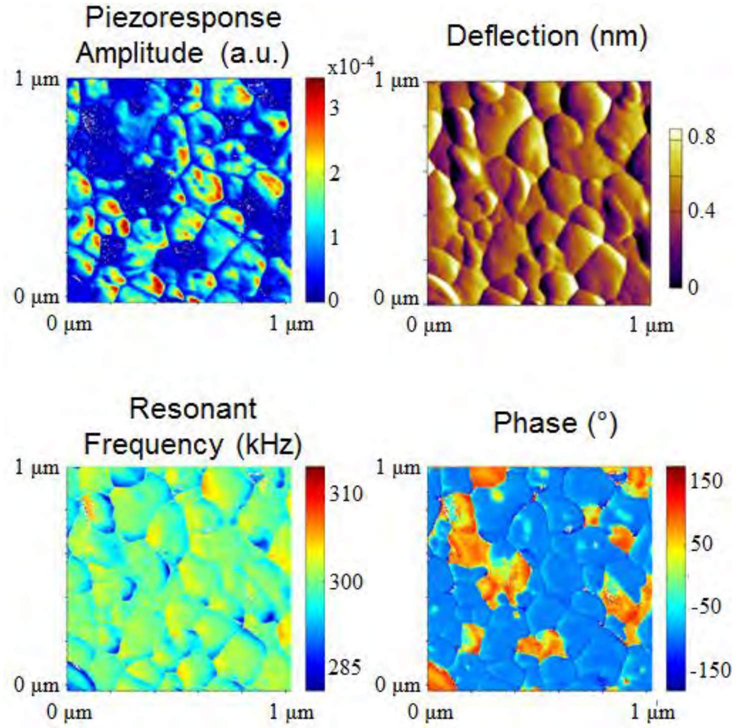

Figure B- 3: 200 nm thick polycrystalline {001}-oriented 70PMN-30PT film, measured with 1.2 V_{ac}.

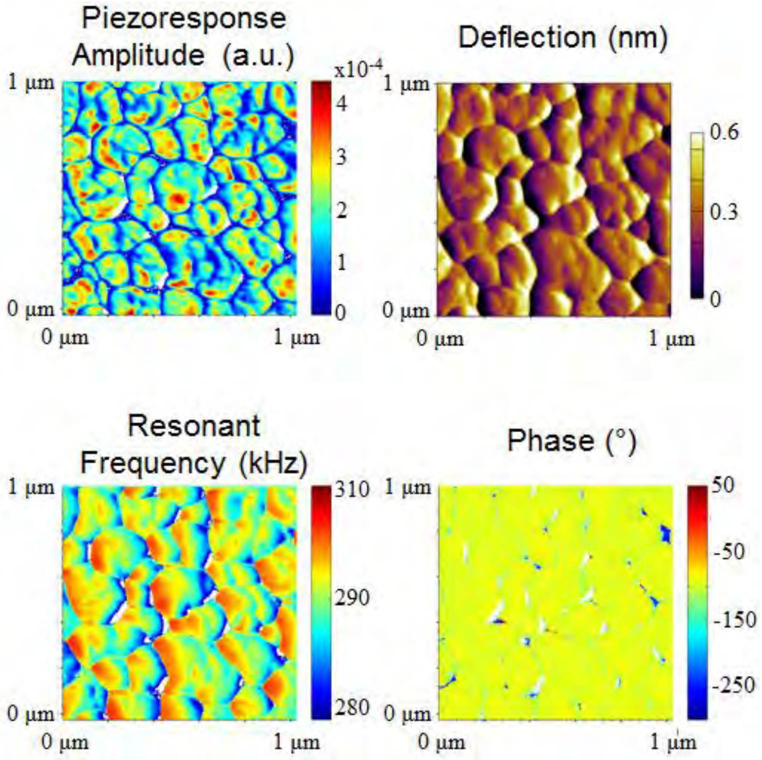

Figure B- 4: 250 nm thick polycrystalline {001}-oriented 70PMN-30PT film, measured with 1.2 V_{ac}.

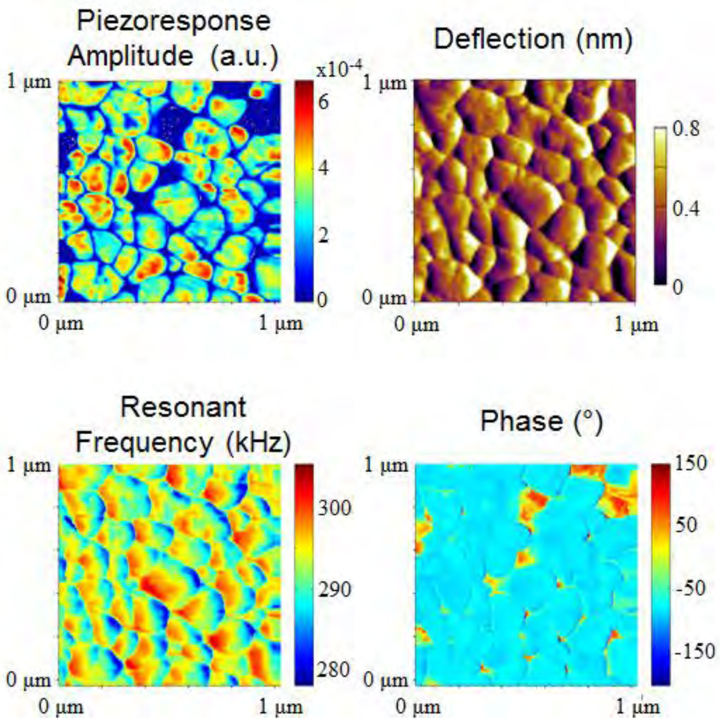

Figure B- 5: 350 nm thick polycrystalline {001}-oriented 70PMN-30PT film, measured with 1.2 V_{ac}.

B.2 Epitaxial films:

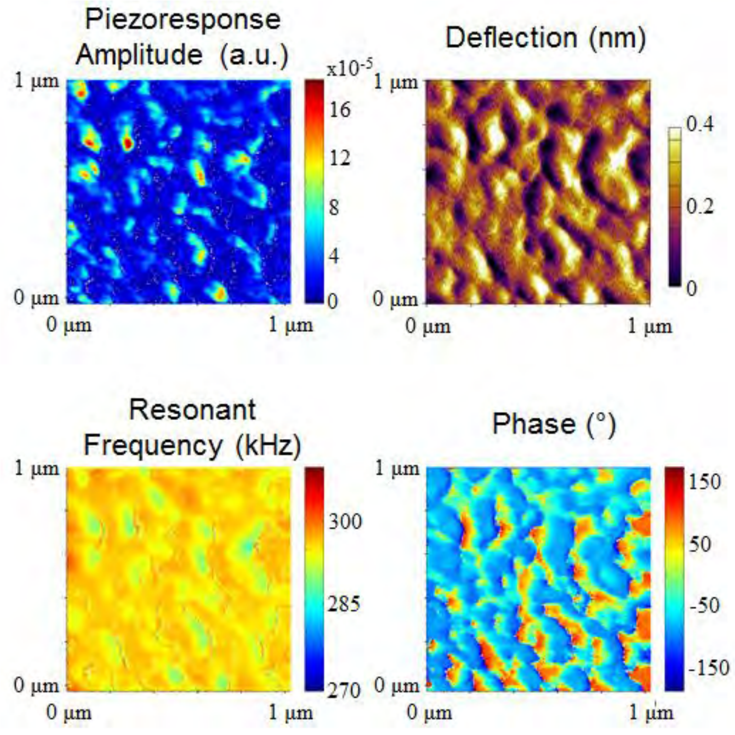

Figure B- 6: 100 nm thick epitaxial {001}-oriented 70PMN-30PT film, measured with 1.6 V_{ac}.

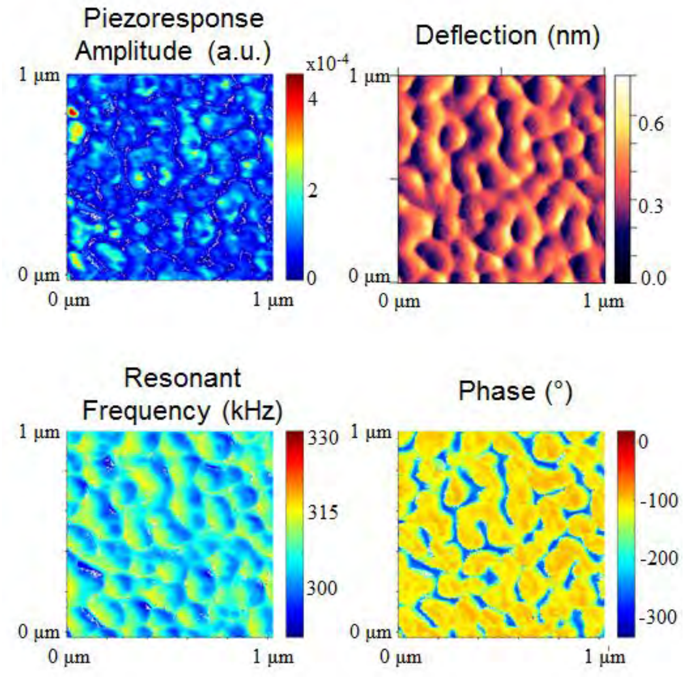

Figure B- 7: 150 nm thick epitaxial {001}-oriented 70PMN-30PT film, measured with 1.6 V_{ac}.

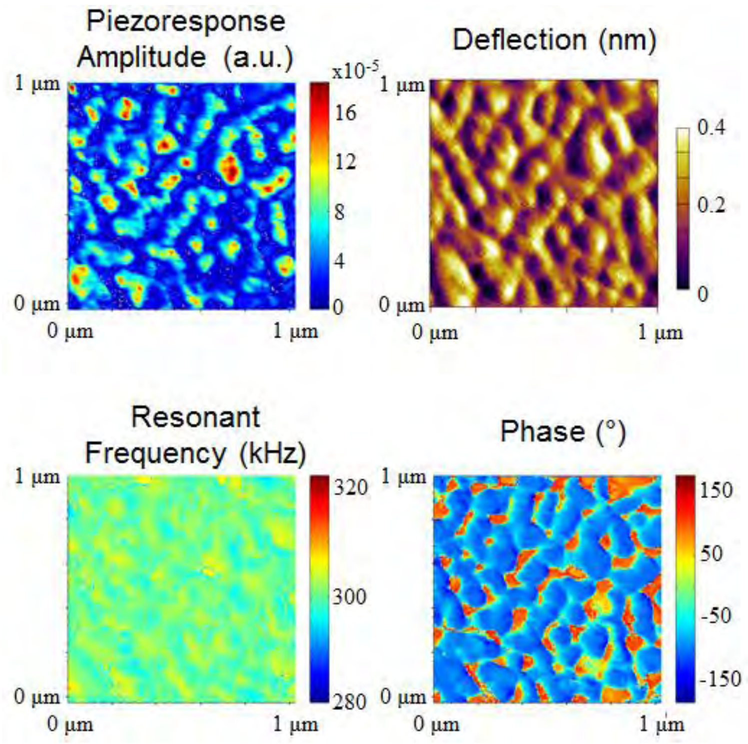

Figure B- 8: 200 nm thick epitaxial {001}-oriented 70PMN-30PT film, measured with 1.6 V_{ac}.

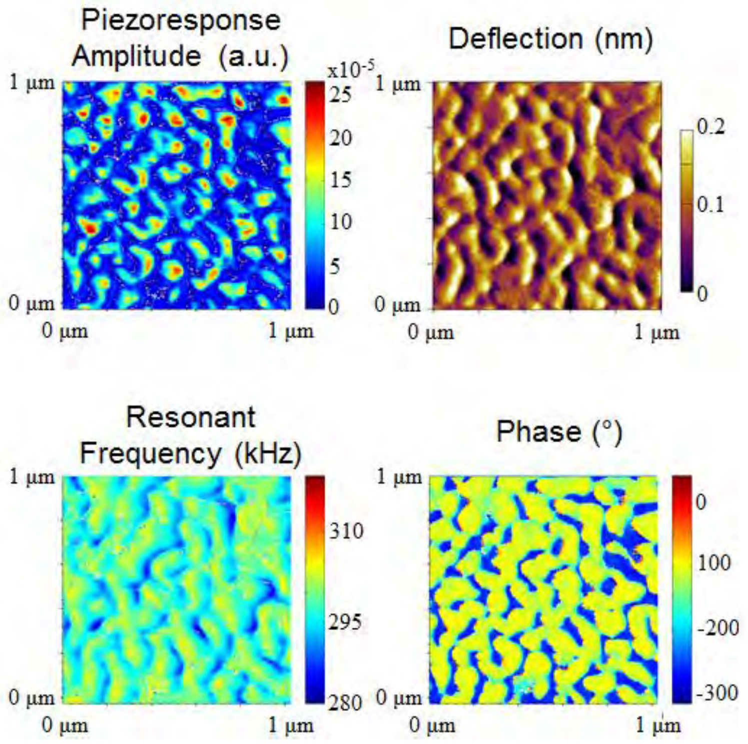

Figure B- 9: 250 nm thick epitaxial {001}-oriented 70PMN-30PT film, measured with 1.6 V_{ac}.

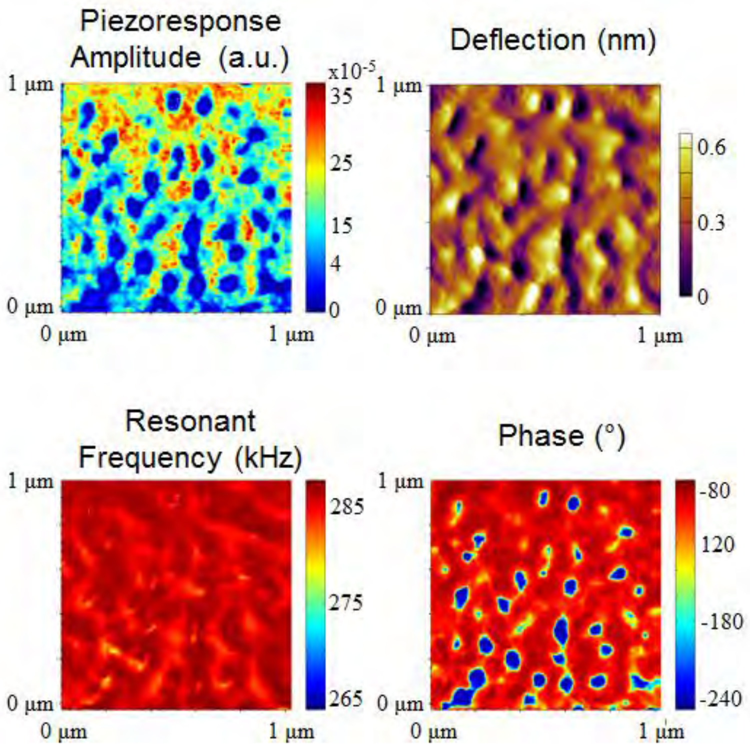

Figure B- 10: 300 nm thick epitaxial {001}-oriented 70PMN-30PT film, measured with 2 V_{ac}.

Appendix C
Peak fitting code

C.1 Mathematica code for peak fitting data from Advanced Photon Source Beamline 11-ID-C

The Mathematica code below was adapted from code written by Tim Fister (APS), Dan Tinberg (PSU), Derek Wilke (PSU) Raegan Johnson-Wilke (PSU), Zach Merritt (Grinnell University), and Margeaux Wallace (PSU) for fitting of diffraction peaks from similar experiments. It was used here to fit the epitaxial {002} PMN-PT Bragg peaks from the 11-ID-C beamline for the characterization of the $d_{33,f}$ coefficient as a function of thickness in epitaxial films. Conversion from the .tiff files obtained at APS to intensity vs. 2θ text files was performed first using Fit2D software (European Radiation Synchrotron Facility, Grenoble, France).

Thickness Dependence
Code used for Epitaxial PMN-PT 002 Peak Fitting

Define Options

```
 Needs["PlotLegends`"]
<<PlotLegends`

Needs["ErrorBarPlots`"]
Needs["HypothesisTesting`"]
(*$TextStyle={FontFamily->"Arial",FontSize26};
<<TXRFtools`*)
 plotoptionsLegend=Sequence[Frame->True,BaseStyle->{FontFamily->" Arial ",FontSize->30},Frame-
>True,FrameTicksStyle->{FontSize->25,FontSize->25},ImageSize->700,FrameTicksStyle-
>Directive[Thick],LegendShadow->None];
 plotoptions=Sequence[Frame->True,BaseStyle->{FontFamily->" Arial ",FontSize->30},Frame-
>True,FrameTicksStyle->{FontSize->25,FontSize->25},ImageSize->500,FrameTicksStyle-
>Directive[Thick]];
```

File Import

Zak’s Importing Method

```
 SetDirectory[NotebookDirectory[]];
files=FileNames[];
Grid[Table[{i,files[[i]]},{i,1,Position[files,Last[files]][[1]][[1]]}],Frame->All]
```

Making steps

```
(*define number of steps dont forget to add 1/2 if successful*)
 tablenum = Position[files,Last[files]][[1]][[1]] -1
 25
 dataD= Table[Drop[Import[NotebookDirectory[]<>files[[i]],"Table"],4], {i,1,tablenum}];
dataD[[1]][[500]];
(*converting to d spacing*)
data=Table[{(0.117978/(2*Sin[((dataD[[i]][[j]][[1]])*(π/180))/2])),dataD[[i]][[j]][[2]]},{i,1,tab
lenum},{j,1,500}];
test=data[[2]];
ListLogPlot[test,PlotMarkers->Automatic,Joined->True,PlotMarkers->{Automatic,10},PlotRange->All]
(*datadone=Table[dataD[[i]][[j]],data[[i]][[j]][[2]]];*)
```

Truncation Method

```
 (*Find the peak position first*)
(*001 peaks
regular-- 60 to 9
cut -- 32 to -5
background subtraction -- 47 to 3*)
 (*note: search parameter is second parameter in Nearest[...]*)
PeakPosition001= Position[data[[1]][[All,1]],Nearest[data[[1]][[All,1]], 4.02][[1]]][[1]][[1]];
PeakPosition002= Position[data[[1]][[All,1]],Nearest[data[[1]][[All,1]], 2.01][[1]]][[1]][[1]];

 Manipulate[ListPlot[ Trunc002 = Table[Take[data[[i]], {PeakPosition002 - range + shift,
PeakPosition002 +range+shift}], {i,1,tablenum }], PlotRange -> Full], {range, 5, 60, 1},
{{shift,-15}, -30, 80,1}]
(*range = 12, shift = -6*)
```

Fitting Functions

```
 pV2=amp1 (mu1*2/π*fwhm1/(4 (x-cen1)^2+fwhm1^2)+(1-mu1) √(4 Log[2]) /(√π fwhm1) Exp[-((4Log[2])/fwhm1^2)
(x-cen1)^2])+amp2 (mu2*2/π*fwhm2/(4 (x-cen2)^2+fwhm2^2)+(1-mu2) √(4 Log[2]) /(√π fwhm2) Exp[-
((4Log[2])/fwhm2^2) (x-cen2)^2])+amp3*x+const;

pV2CON=amp1 (mu1*2/π*fwhm1/(4 (x-cen1)^2+fwhm1^2)+(1-mu1) √(4 Log[2]) /(√π fwhm1) Exp[-
((4Log[2])/fwhm1^2) (x-cen1)^2])+amp2 (mu2*2/π*fwhm1/(4 (x-cen2)^2+fwhm1^2)+(1-mu2) √(4 Log[2]) /(√π fwhm1)
Exp[-((4Log[2])/fwhm1^2) (x-cen2)^2])+amp3*x+const;

pV3CON=amp1 (mu1*2/π*fwhm1/(4 (x-cen1)^2+fwhm1^2)+(1-mu1) √(4 Log[2]) /(√π fwhm1) Exp[-
((4Log[2])/fwhm1^2) (x-cen1)^2])+
   amp2 (mu2*2/π*fwhm1/(4 (x-cen2)^2+fwhm1^2)+(1-mu2) √(4 Log[2]) /(√π fwhm1) Exp[-((4Log[2])/fwhm1^2)
(x-cen2)^2])+amp3 (mu3*2/π*fwhm1/(4 (x-cen3)^2+fwhm1^2)+(1-mu3) √(4 Log[2]) /(√π fwhm1) Exp[-
((4Log[2])/fwhm1^2) (x-cen3)^2])+const;

pV2x=amp1 (mu1*2/π*fwhm1/(4 (x-cen1)^2+fwhm1^2)+(1-mu1) √(4 Log[2]) /(√π fwhm1) Exp[-((4Log[2])/fwhm1^2)
(x-cen1)^2])+amp2 (mu2*2/π*fwhm2/(4 (x-cen2)^2+fwhm2^2)+(1-mu2) √(4 Log[2]) /(√π fwhm2) Exp[-
((4Log[2])/fwhm2^2) (x-cen2)^2])+amp4*x+const;

pV3a=amp1 (mu1*2/π*fwhm1/(4 (x-cen1)^2+fwhm1^2)+(1-mu1) √(4 Log[2]) /(√π fwhm1) Exp[-((4Log[2])/fwhm1^2)
(x-cen1)^2])+amp3*x+const;

pV3b=amp2 (mu2*2/π*fwhm2/(4 (x-cen2)^2+fwhm2^2)+(1-mu2) √(4 Log[2]) /(√π fwhm2) Exp[-((4Log[2])/fwhm2^2)
(x-cen2)^2])+amp3*x+const;

pV3c=amp3 (mu3*2/π*fwhm3/(4 (x-cen3)^2+fwhm3^2)+(1-mu3) √(4 Log[2]) /(√π fwhm3) Exp[-((4Log[2])/fwhm3^2)
(x-cen3)^2])+amp3*x+const;

pV1=amp0 (mu0*2/π*fwhm0/(4 (x-cen0)^2+fwhm0^2)+(1-mu0) √(4 Log[2]) /(√π fwhm0) Exp[-((4Log[2])/fwhm0^2)
(x-cen0)^2])+amp2*x+const;

pV1x=amp1 (mu1*2/π*fwhm1/(4 (x-cen1)^2+fwhm1^2)+(1-mu1) √(4 Log[2]) /(√π fwhm1) Exp[-((4Log[2])/fwhm1^2)
(x-cen1)^2])+amp2*x+const;

pV1a=amp0 (mu0*2/π*fwhm0/(4 (x-cen0)^2+fwhm0^2)+(1-mu0) √(4 Log[2]) /(√π fwhm0) Exp[-((4Log[2])/fwhm0^2)
(x-cen0)^2])+const;
```

```
pV1b=amp1 (mu1*2/π*fwhm1/(4 (x-cen1)^2+fwhm1^2)+(1-mu1) √(4 Log[2]) /(√π fwhm1) Exp[-((4Log[2])/fwhm1^2) (x-cen1)^2])+const;

pvl=amp1 (mu1*2/π*fwhm1/(4 (x-cen1)^2+fwhm1^2)+(1-mu1) √(4 Log[2]) /(√π fwhm1) Exp[-((4Log[2])/fwhm1^2) (x-cen1)^2])+
   amp2 (2/π*fwhm2/(4 (x-cen2)^2+fwhm2^2))+amp3 (mu3*2/π*fwhm3/(4 (x-cen3)^2+fwhm3^2)+(1-mu3) √(4 Log[2]) /(√π fwhm3) Exp[-((4Log[2])/fwhm3^2) (x-cen3)^2])+const;
PearVIIasym2=Piecewise[{{amp1*(1+(x-cen1)^2/fwhm1L^2)^-mu1L,x<cen1},{amp1*(1+(x-cen1)^2/fwhm1R^2)^-mu1R,x>=cen1}}]+Piecewise[{{amp2*(1+(x-cen2)^2/fwhm2L^2)^-mu2L,x<cen2},{amp2*(1+(x-cen2)^2/fwhm2R^2)^-mu2R,x>=cen2}}]+const;
PearVIIasym2a=Piecewise[{{amp1*(1+(x-cen1)^2/fwhm1L^2)^-mu1L,x<cen1},{amp1*(1+(x-cen1)^2/fwhm1R^2)^-mu1R,x>=cen1}}]+const;
PearVIIasym2b=Piecewise[{{amp2*(1+(x-cen2)^2/fwhm2L^2)^-mu2L,x<cen2},{amp2*(1+(x-cen2)^2/fwhm2R^2)^-mu2R,x>=cen2}}]+const;
```

Peak Constraints/Initial Guesses

PZT 002 constraints/initial guesses

PZT 002 - 2 peaks - Pseudo-Voight

```
 amp1minpv3002=0;
amp1guesspv3002=3880;

fwhm1minpv3002=0.008;
fwhm1maxpv3002=0.02;
fwhm1guesspv3002=0.013;

mu1minpv3002=0;
mu1maxpv3002=1;
mu1guesspv3002=.5;

cen1minpv3002=2.035;
cen1maxpv3002=2.05;
cen1guesspv3002=2.04;

amp2minpv3002=0;
amp2guesspv3002=5250;

fwhm2minpv3002=0.008;
fwhm2maxpv3002=0.025;
fwhm2guesspv3002=.014;

mu2minpv3002=0;
mu2maxpv3002=1;
mu2guesspv3002=.4;

cen2minpv3002=2.02;
cen2maxpv3002=2.04;
cen2guesspv3002=2.027;

amp3minpv3002=0;
amp3guesspv3002=-100000;

constminpv3002=0;
constguesspv3002=143550;
```

PZT 002 peaks (2 peaks)

PZT 002 - High Field Test - Fitting - Pseudo-Voigt

(*When changing from 2 peak fit to just one, need to change pv2 to pV3b wherever it is. Also comment out anything having to do with amp1 or any term "1". *)

25 V - Epi {002} peak

```
 epi002PMNT350nm25V=NonlinearModelFit[Trunc002[[25]],{pV2,

{amp1>amp1minpv3002,fwhm1minpv3002<fwhm1<fwhm1maxpv3002,mu1minpv3002<mu1<mu1maxpv3002,cen1minpv3002<cen1<cen1maxpv3002,
```

```
amp2>amp2minpv3002,fwhm2minpv3002<fwhm2<fwhm2maxpv3002,mu2minpv3002<mu2<mu2maxpv3002,cen2minpv300
2<cen2<cen2maxpv3002,
     amp3<amp3minpv3002,const>constminpv3002}},
   {{amp1,amp1guesspv3002},{fwhm1,fwhm1guesspv3002},{mu1,mu1guesspv3002},{cen1,cen1guesspv3002},
    {amp2,amp2guesspv3002},{fwhm2,fwhm2guesspv3002},{mu2,mu2guesspv3002},{cen2,cen2guesspv3002},
    {amp3,amp3guesspv3002},{const,constguesspv3002}},x,Weights->(1/#^0 &),MaxIterations->150];
epi002PMNT350nm25VFitspv=epi002PMNT350nm25V["BestFitParameters"]
epi002PMNT350nm25VErrorpv=epi002PMNT350nm25V["ParameterErrors"]
epi002PMNT350nm25VConfIntpv=epi002PMNT350nm25V["ParameterConfidenceIntervals"]
epi002PMNT350nm25VBICpv=epi002PMNT350nm25V["BIC"]
Show[ListPlot[Trunc002[[25]],PlotRange->All,plotoptions,FrameLabel->{"d-
spacing(Å)","Intensity"},AspectRatio->1,PlotMarkers->{Automatic,8},PlotStyle->Black],
 Plot[pV2/.epi002PMNT350nm25VFitspv,{x,1.96,2.12},PlotRange->All, PlotStyle-
>{Red,Thick}],Plot[pV3a/.{amp1->epi002PMNT350nm25VFitspv[[1,2]],fwhm1-
>epi002PMNT350nm25VFitspv[[2,2]],mu1->epi002PMNT350nm25VFitspv[[3,2]], cen1-
>epi002PMNT350nm25VFitspv[[4,2]] ,amp3-> 0 ,const->0},{x,1.96,2.12},PlotRange->All,PlotStyle-
>{Darker[Cyan],Thick}],Plot[pV3b/.{amp2->epi002PMNT350nm25VFitspv[[5,2]],fwhm2-
>epi002PMNT350nm25VFitspv[[6,2]], mu2->epi002PMNT350nm25VFitspv[[7,2]],cen2-
>epi002PMNT350nm25VFitspv[[8,2]] , amp3-> 0 ,const->0},{x,1.96,2.12},PlotStyle->{Purple,Thick}],
 plotoptions, FrameLabel->{"d-spacing {002} (Å)","Intensity"},LabelStyle->22]
points25V14L=Table[{x,pV2/.epi002PMNT350nm25VFitspv,pV3a/.{amp1-
>epi002PMNT350nm25VFitspv[[1,2]],fwhm1->epi002PMNT350nm25VFitspv[[2,2]],mu1-
>epi002PMNT350nm25VFitspv[[3,2]], cen1->epi002PMNT350nm25VFitspv[[4,2]] ,amp3-> 0 ,const-
>0},pV3b/.{amp2->epi002PMNT350nm25VFitspv[[5,2]],fwhm2->epi002PMNT350nm25VFitspv[[6,2]], mu2-
>epi002PMNT350nm25VFitspv[[7,2]],cen2->epi002PMNT350nm25VFitspv[[8,2]] , amp3-> 0 ,const-
>0}},{x,Range[1.98,2.07, 0.001]}];
Export["points25V14L.dat", points25V14L]
```

0 V - Epi {002} peak - 00232-500 bins

```
 epi002PMNT350nm0V=NonlinearModelFit[Trunc002[[1]],{pV3b,

{(*amp1>amp1minpv3002,fwhm1minpv3002<fwhm1<fwhm1maxpv3002,mu1minpv3002<mu1<mu1maxpv3002,cen1minpv
3002<cen1<cen1maxpv3002,*)

amp2>amp2minpv3002,fwhm2minpv3002<fwhm2<fwhm2maxpv3002,mu2minpv3002<mu2<mu2maxpv3002,cen2minpv300
2<cen2<cen2maxpv3002,
     amp3<amp3minpv3002,const>constminpv3002}},

{(*amp1,amp1guesspv3002},{fwhm1,fwhm1guesspv3002},{mu1,mu1guesspv3002},{cen1,cen1guesspv3002},*)
    {amp2,amp2guesspv3002},{fwhm2,fwhm2guesspv3002},{mu2,mu2guesspv3002},{cen2,cen2guesspv3002},
    {amp3,amp3guesspv3002},{const,constguesspv3002}},x,Weights->(1/#^0 &),MaxIterations->150];
epi002PMNT350nm0VFits=epi002PMNT350nm0V["BestFitParameters"]
epi002PMNT350nm0VErrorpv=epi002PMNT350nm0V["ParameterErrors"]
epi002PMNT350nm0VConfIntpv=epi002PMNT350nm0V["ParameterConfidenceIntervals"]
epi002PMNT350nm0VBICpv=epi002PMNT350nm0V["BIC"]
Show[ListPlot[Trunc002[[1]],PlotRange->All,plotoptions,FrameLabel->{"d-
spacing(Å)","Intensity"},AspectRatio->1,PlotMarkers->{Automatic,8},PlotStyle->Black],
 Plot[pV3b/.epi002PMNT350nm0VFits,{x,1.96,2.12},PlotRange->All, PlotStyle-
>{Red,Thick}],(*Plot[pV3a/.{amp1□epi002PMNT350nm0V[[1,2]],fwhm1□epi002PMNT350nm0V[[2,2]],mu1□epi0
02PMNT350nm0V[[3,2]], cen1□epi002PMNT350nm0V[[4,2]] ,amp3□ epi002PMNT350nm0V[[9,2]] ,
const□0},{x,1.96,2.12},PlotRange□All,PlotStyle□{Darker[Cyan],Thick}],*)Plot[pV3b/.{amp2-
>epi002PMNT350nm0V[[5,2]],fwhm2->epi002PMNT350nm0V[[6,2]], mu2->epi002PMNT350nm0V[[7,2]],cen2-
>epi002PMNT350nm0V[[8,2]] , const->0},{x,1.96,2.12},PlotStyle->{Purple,Thick}],
 plotoptions, FrameLabel->{"d-spacing {002} (Å)","Intensity"},LabelStyle->22]

points0V14L=Table[{x,pV3b/.epi002PMNT350nm0VFits},{x,Range[1.98,2.07, 0.001]}];
Export["points0V14L.dat", points0V14L]

(*make more of the above for each voltage run*)
```

C.2 Process for peak fitting data from Advanced Photon Source Beamline 2-ID-D

The process for peak fitting the diffraction data from beamline 2-ID-D differs from that of 11-ID-C because of the different detector which is used; the detector in this beamline only gathers diffraction data over an 11° window. First, the diffraction .tiff files were sorted into separate folders for each voltage excursion. The “generateCommand” and “OnBeamSorting” Python codes were placed in each folder as well. Secondly, the DataSqueeze software was calibrated with the CeO_2 diffraction pattern. Then, the “generateCommand” Python code was used to generate a “DataSqueezeBatch” that converted the diffraction patterns in .tiff format to intensity vs. 2θ text using the DataSqueeze batch function. Then, the “OnBeamSorting” Python file was run to convert the intensity vs. 2θ files to intensity vs. d-spacing files. Assuming a given lateral scan of the stage at a given voltage at the beamline captured diffraction patterns with the X-ray beam on and off of the PMN-PT features, the “OnBeamSorting” file also sorted the intensity vs. d-spacing files into separate folders based on whether the data contains a statistically significant PMN-PT 002 peak. It is recommended that the data files be sorted into folders for each arm width based on file name/number. In each of these folders, the Mathematica code (with original authors listed in Appendix section C.1) below can be used for fitting and outputting the peak fitting parameters (such as peak center, FWHM, etc.). The Python code “GetFitParameters” can be used to prepare files with those output parameters organized for importing to plotting software.

generateCommand:

```
import os # Written by Chris Fancher and Giovanni Esteves, Department of
Materials Science and Engineering, North Carolina State University, 2014

#import Tkinter

#def main():
        #import tkFileDialog
        #import re
        #ff = tkFileDialog.askopenfilenames()
        #filez = re.findall('{(.*?)}', ff)
        #import tkFileDialog
        #root = Tkinter.Tk()
       # filez = tkFileDialog.askopenfilenames(parent=root,title='Choose a
file')

      #  lst = list(filez)

# Integration Parameters to Edit
Min2T=30
Max2T=38
IntStep2T=0.023
MinCHI=-10.5
MaxCHI=10.5
IntStepCHI=0.338


#Chris

paramaterFile = 'param_S2_Dec_2015.txt' # edit the parameter file name (this
should be in the same directory as the actual data)

outFile = open('DataSqueezeBatch.txt','w')
for name in os.listdir('.'):
    if '.tif' in name:
        outFile.write('>READIN 0 true false "' +  os.getcwd() + '\\' + name +
'" "MAR_CCD" 0 1 -1 \n')
        outFile.write('>DEZING\n>RECALCIMAGE \n')
        outFile.write('>RETRIEVEINSTRUMENTPARAMETERS ' + '"' +  os.getcwd() +
'\\' + paramaterFile + '"\n')
        outFile.write('>PLOT false false false TTHETA ' + str(Min2T) + ' '+
str(Max2T)+ ' ' + str(IntStep2T) + ' CHI ' + str(MinCHI)+ ' ' + str(MaxCHI)+
' ' + str(IntStepCHI) + ' 0\n')
        outFile.write('>EXPORTPLOT "'+ os.getcwd() + '\\' +
name.replace('.tif','.xy') + '" ASCIITAB\n')
      outFile.close()
```

OnBeamSorting:

```
# -*- coding: utf-8 -*-
"""
Created on Mon Dec 07 11:07:04 2015

@author: Jared
"""

import numpy as np # efficient arrays
import glob # getting filenames
import os # making folders

# Make folder if one doesn't exist

if not os.path.exists(os.getcwd()+'\\dsp\\onPMNT'):
    os.makedirs(os.getcwd()+'\\dsp\\onPMNT')

if not os.path.exists(os.getcwd()+'\\dsp\\nothing'):
    os.makedirs(os.getcwd()+'\\dsp\\nothing')

# Grab all .xy files in the folder
rawfiles = glob.glob('.\*.xy')
# Clean up filenames
xyfiles = [x[2:] for x in rawfiles]
wavelength = 1.2276 #Angstroms
for filename in xyfiles:
    # Load data
    data = np.loadtxt(filename)
    # Calculate d spacing
    dsp = wavelength/(2.0*np.sin(data[:,0]*np.pi/360.0))
    # Make a new array with data we want to export
    outdata = np.column_stack((dsp, data[:,1]))
    # Save the file
    if
outdata[233,1]+outdata[235,1]+outdata[237,1]+outdata[239,1]+outdata[241,1]+ou
tdata[243,1]+outdata[244,1]+outdata[246,1]+outdata[249,1]>151:
        np.savetxt(os.getcwd()+'\\dsp\\onPMNT\\{}_dsp.xy'.format(filename[:-
3]),outdata, fmt='%6f', delimiter=' ')
    else:
np.savetxt(os.getcwd()+'\\dsp\\nothing\\{}_dsp.xy'.format(filename[:-
3]),outdata, fmt='%6f', delimiter=' ')
```

GetFitParameters (for PMN-PT 002 peaks):

```
# -*- coding: utf-8 -*-
"""Created on Mon Dec 07 11:07:04 2015    @author: Jared"""
import numpy as np # efficient arrays
import glob # getting filenames
import os # making folders

# Grab all .dat files in the folder
rawfiles = glob.glob('.\*.dat')
# Clean up filenames
xyfiles = [x[2:] for x in rawfiles]

for filename in xyfiles:
    with open(filename) as f:
        amp2 = []
        fwhm2 = []
        mu2 = []
        cen2 = []
        for line in f:
            line.replace("*^", "e")
            splitline = line.split("\t")
            if splitline[0].startswith("amp2"):
                amp2.append(splitline[0][8:])
                fwhm2.append(splitline[1][9:])
                mu2.append(splitline[2][7:])
                cen2.append(splitline[3][8:])

        for i,value in enumerate(mu2):
            try:
                mu2[i] = float(value)
            except ValueError:
                mu2[i] = 0.0

        with open(filename[:-4]+"_pretty.txt","w") as d:
            d.write("amp2\tfwhm2\tmu2\tcen2\n")
            for i in range(len(amp2)):

d.write("{0}\t{1}\t{2}\t{3}\n".format(amp2[i],fwhm2[i],mu2[i],cen2[i]))

# Grab all .dat files in the folder
paramfiles = glob.glob('.\*.txt')
# Clean up filenames
txtfiles = [x[2:] for x in paramfiles]

AllFits = np.array([0,0,0,0])
emptyrow = np.array([np.nan, np.nan, np.nan, np.nan])

for filename2 in txtfiles:
    combine = np.loadtxt(filename2, skiprows = 1)
    AllFits = np.vstack((AllFits, combine))
    AllFits = np.vstack((AllFits, emptyrow))
np.savetxt("AllFits.txt", AllFits, delimiter = "\t", header =
"amp2\tfwhm2\tmu2\tcen2")
```

GetFitParameters-PLAT (for Pt 111 peaks):

```
# -*- coding: utf-8 -*-
"""Created on Mon Dec 07 11:07:04 2015     @author: Jared"""
import numpy as np # efficient arrays
import glob # getting filenames
import os # making folders

# Grab all .dat files in the folder
rawfiles = glob.glob('.\*.dat')
# Clean up filenames
xyfiles = [x[2:] for x in rawfiles]

for filename in xyfiles:
    with open(filename) as f:
        amp2 = []
        fwhm2 = []
        mu2 = []
        cen2 = []
        for line in f:
            line.replace("*^", "e")
            splitline = line.split("\t")
            if splitline[0].startswith("amp2"):
                amp2.append(splitline[0][10:])
                fwhm2.append(splitline[1][11:])
                mu2.append(splitline[2][9:])
                cen2.append(splitline[3][10:])

        for i,value in enumerate(mu2):
            try:
                mu2[i] = float(value)
            except ValueError:
                mu2[i] = 0.0

        with open(filename[:-4]+"_pretty.txt","w") as d:
            d.write("amp2\tfwhm2\tmu2\tcen2\n")
            for i in range(len(amp2)):

d.write("{0}\t{1}\t{2}\t{3}\n".format(amp2[i],fwhm2[i],mu2[i],cen2[i]))

# Grab all .dat files in the folder
paramfiles = glob.glob('.\*.txt')
# Clean up filenames
txtfiles = [x[2:] for x in paramfiles]

AllFits = np.array([0,0,0,0])
emptyrow = np.array([np.nan, np.nan, np.nan, np.nan])

for filename2 in txtfiles:
    combine = np.loadtxt(filename2, skiprows = 1)
    AllFits = np.vstack((AllFits, combine))
    AllFits = np.vstack((AllFits, emptyrow))
np.savetxt("AllFits.txt", AllFits, delimiter = "\t", header =
"amp2\tfwhm2\tmu2\tcen2")
```

Mathematica Code:

2-ID-D Nanobeam line

PMN-PT 002 and Pt 111 Peak Fitting

Define Options

```
Needs["PlotLegends`"]
<<PlotLegends`

Needs["ErrorBarPlots`"]
Needs["HypothesisTesting`"]
(*$TextStyle={FontFamily->"Arial",FontSize→26};
<<TXRFtools`*)
plotoptionsLegend=Sequence[Frame->True,BaseStyle->{FontFamily->" Arial ",FontSize-
>30},Frame->True,FrameTicksStyle->{FontSize->25,FontSize->25},ImageSize-
>700,FrameTicksStyle->Directive[Thick],LegendShadow->None];
plotoptions=Sequence[Frame->True,BaseStyle->{FontFamily->" Arial ",FontSize-
>30},Frame->True,FrameTicksStyle->{FontSize->25,FontSize->25},ImageSize-
>500,FrameTicksStyle->Directive[Thick]];
```

File Import

Importing Method

```
SetDirectory[NotebookDirectory[]];
files=FileNames[];
Grid[Table[{i,files[[i]]},{i,1,Position[files,Last[files]][[1]][[1]]}],Frame->All]
{
 {1, 9_5_um_arms_Vdown_structure2_01012_dsp.xy},
 {2, 9_5_um_arms_Vdown_structure2_01013_dsp.xy},
 {3, 9_5_um_arms_Vdown_structure2_01014_dsp.xy},
 {4, 9_5_um_arms_Vdown_structure2_01015_dsp.xy},
 {5, 9_5_um_arms_Vdown_structure2_01016_dsp.xy},
 {6, 9_5_um_arms_Vdown_structure2_01017_dsp.xy},
 {7, twoIDD_6_um_1_0Vdown.nb}
}
```

Making steps

```
(*define number of steps dont forget to add 1/2 if successful*)
tablenum = Position[files,Last[files]][[1]][[1]] -1
6
data= Table[Drop[Import[NotebookDirectory[]<>files[[i]],"Table"],4], {i,1,tablenum}];
data[[1]][[348]];
test=data[[2]];
ListLogPlot[test,PlotMarkers->Automatic,Joined->True,PlotMarkers-
>{Automatic,10},PlotRange->All]
(*datadone=Table[dataD[[i]][[j]],data[[i]][[j]][[2]]];*)
```

Truncation Method

```
 (*Find the peak position first*)
(*002 peaks
regular-- 60 to 9
cut -- 32 to -5
background subtraction -- 47 to 3*)
(*note: search parameter is second parameter in Nearest[...]*)
PeakPosition002= Position[data[[1]][[All,1]],Nearest[data[[1]][[All,1]],
2.006][[1]]][[1]][[1]];

Manipulate[ListPlot[ Trunc002 = Table[Take[data[[i]], {PeakPosition002 - range +
shift, PeakPosition002 +range+shift}], {i,1,tablenum }], PlotRange -> Full], {{range,
18},11, 20, 1}, {{shift, 1}, -4, 5,1}]
(*range = 24, shift = 3*)
```

Fitting Functions

```
(*defining the various fitting functions*)
```

```
pV2=amp1 (mu1*2/π*fwhm1/(4 (x-cen1)^2+fwhm1^2)+(1-mu1) √(4 Log[2]) /(√π fwhm1) Exp[-((4Log[2])/fwhm1^2) (x-cen1)^2])+amp2 (mu2*2/π*fwhm2/(4 (x-cen2)^2+fwhm2^2)+(1-mu2) √(4 Log[2]) /(√π fwhm2) Exp[-((4Log[2])/fwhm2^2) (x-cen2)^2])+amp3*x+const;
pV2CON=amp1 (mu1*2/π*fwhm1/(4 (x-cen1)^2+fwhm1^2)+(1-mu1) √(4 Log[2]) /(√π fwhm1) Exp[-((4Log[2])/fwhm1^2) (x-cen1)^2])+amp2 (mu2*2/π*fwhm1/(4 (x-cen2)^2+fwhm1^2)+(1-mu2) √(4 Log[2]) /(√π fwhm1) Exp[-((4Log[2])/fwhm1^2) (x-cen2)^2])+amp3*x+const;
pV3CON=amp1 (mu1*2/π*fwhm1/(4 (x-cen1)^2+fwhm1^2)+(1-mu1) √(4 Log[2]) /(√π fwhm1) Exp[-((4Log[2])/fwhm1^2) (x-cen1)^2])+
   amp2 (mu2*2/π*fwhm1/(4 (x-cen2)^2+fwhm1^2)+(1-mu2) √(4 Log[2]) /(√π fwhm1) Exp[-((4Log[2])/fwhm1^2) (x-cen2)^2])+amp3 (mu3*2/π*fwhm1/(4 (x-cen3)^2+fwhm1^2)+(1-mu3) √(4 Log[2]) /(√π fwhm1) Exp[-((4Log[2])/fwhm1^2) (x-cen3)^2])+const;
pV2x=amp1 (mu1*2/π*fwhm1/(4 (x-cen1)^2+fwhm1^2)+(1-mu1) √(4 Log[2]) /(√π fwhm1) Exp[-((4Log[2])/fwhm1^2) (x-cen1)^2])+amp2 (mu2*2/π*fwhm2/(4 (x-cen2)^2+fwhm2^2)+(1-mu2) √(4 Log[2]) /(√π fwhm2) Exp[-((4Log[2])/fwhm2^2) (x-cen2)^2])+amp4*x+const;
pV3a=amp1 (mu1*2/π*fwhm1/(4 (x-cen1)^2+fwhm1^2)+(1-mu1) √(4 Log[2]) /(√π fwhm1) Exp[-((4Log[2])/fwhm1^2) (x-cen1)^2])+amp3*x+const;
pV3b=amp2 (mu2*2/π*fwhm2/(4 (x-cen2)^2+fwhm2^2)+(1-mu2) √(4 Log[2]) /(√π fwhm2) Exp[-((4Log[2])/fwhm2^2) (x-cen2)^2])+amp3*x+const;
pV3c=amp3 (mu3*2/π*fwhm3/(4 (x-cen3)^2+fwhm3^2)+(1-mu3) √(4 Log[2]) /(√π fwhm3) Exp[-((4Log[2])/fwhm3^2) (x-cen3)^2])+amp3*x+const;
pV1=amp0 (mu0*2/π*fwhm0/(4 (x-cen0)^2+fwhm0^2)+(1-mu0) √(4 Log[2]) /(√π fwhm0) Exp[-((4Log[2])/fwhm0^2) (x-cen0)^2])+amp2*x+const;
```

Peak Constraints/Initial Guesses

002 constraints/initial guesses

PMNT 002 - 2 peaks - Pseudo-Voight

```
(*amp1minpv3002=0;
amp1guesspv3002=3880;

fwhm1minpv3002=0.008;
fwhm1maxpv3002=0.02;
fwhm1guesspv3002=0.013;

mu1minpv3002=0;
mu1maxpv3002=1;
mu1guesspv3002=.5;

cen1minpv3002=2.035;
cen1maxpv3002=2.05;
cen1guesspv3002=2.04;*)

amp2minpv3002=0;
amp2guesspv3002=.8;

fwhm2minpv3002=0.001;
fwhm2maxpv3002=0.02;
fwhm2guesspv3002=.006;

mu2minpv3002=0;
mu2maxpv3002=1;
mu2guesspv3002=.7;

cen2minpv3002=2;
cen2maxpv3002=2.01;
```

```
cen2guesspv3002=2.006;

amp3minpv3002=0;
amp3guesspv3002=0;

constminpv3002=0;
constguesspv3002=12;
```

002 - 2 peaks - Pearson VII

```
amp1minpVII3002=0;
amp1guesspVII3002=500;

fwhm1minpVII3002=0.006;
fwhm1maxpVII3002=0.02;
fwhm1guesspVII3002=0.011;

mu1minpVII3002=0;
mu1maxpVII3002=1;
mu1guesspVII3002=.1;

cen1minpVII3002=1.97;
cen1maxpVII3002=2.02;
cen1guesspVII3002=1.98;

amp2minpVII3002=0;
amp2guesspVII3002=200;

fwhm2minpVII3002=0.001;
fwhm2maxpVII3002=0.06;
fwhm2guesspVII3002=.003;

mu2minpVII3002=0;
mu2maxpVII3002=1;
mu2guesspVII3002=.1;

cen2minpVII3002=2.03;
cen2maxpVII3002=2.1;
cen2guesspVII3002=2.33;

amp3minpVII3002=0;
amp3guesspVII3002=100;

constminpVII3002=0;
constguesspVII3002=500;
```

002 peaks (2 peaks)

PMNT 002 - High Field Test - Fitting - Pseudo-Voigt
(*When changing from 2 peak fit to just one, need to change pv2 to pV3b. Also comment out anything having to do with amp1 or any term "1". *)

File 1 - 9 to 5 umwide

```
file1pmntpeak=NonlinearModelFit[Trunc002[[1]],{pV3b,

{(*amp1>amp1minpv3002,fwhm1minpv3002<fwhm1<fwhm1maxpv3002,mu1minpv3002<mu1<mu1maxpv300
2,cen1minpv3002<cen1<cen1maxpv3002,*)

amp2>amp2minpv3002,fwhm2minpv3002<fwhm2<fwhm2maxpv3002,mu2minpv3002<mu2<mu2maxpv3002,c
en2minpv3002<cen2<cen2maxpv3002,
```

```
     amp3<amp3minpv3002,const>constminpv3002}},

{(*amp1,amp1guesspv3002},{fwhm1,fwhm1guesspv3002},{mu1,mu1guesspv3002},{cen1,cen1guess
pv3002},*)

{amp2,amp2guesspv3002},{fwhm2,fwhm2guesspv3002},{mu2,mu2guesspv3002},{cen2,cen2guesspv
3002},
    {amp3,amp3guesspv3002},{const,constguesspv3002}},x,Weights->(1/#^0
&),MaxIterations->150];
file1pmntpeakFits=file1pmntpeak["BestFitParameters"]
file1pmntpeakErrorpv=file1pmntpeak["ParameterErrors"]
file1pmntpeakConfIntpv=file1pmntpeak["ParameterConfidenceIntervals"]
file1pmntpeakBICpv=file1pmntpeak["BIC"]
Show[ListPlot[Trunc002[[1]],PlotRange->All,plotoptions,FrameLabel->{"d-
spacing(Å)","Intensity"},AspectRatio->1,PlotMarkers->{Automatic,8},PlotStyle->Black],
 Plot[pV3b/.file1pmntpeakFits,{x,1.97,2.3},PlotRange->All, PlotStyle-
>{Red,Thick}],(*Plot[pV3a/.{amp1□file1pmntpeak[[1,2]],fwhm1□file1pmntpeak[[2,2]],mu1□f
ile1pmntpeak[[3,2]], cen1□file1pmntpeak[[4,2]] ,amp3□ file1pmntpeak[[9,2]] ,
const□0},{x,1.97,2.33},PlotRange□All,PlotStyle□{Darker[Cyan],Thick}],*)Plot[pV3b/.{amp
2->file1pmntpeak[[5,2]],fwhm2->file1pmntpeak[[6,2]], mu2->file1pmntpeak[[7,2]],cen2-
>file1pmntpeak[[8,2]] , const->0},{x,1.97,2.33},PlotStyle->{Purple,Thick}],
 plotoptions, FrameLabel->{"d-spacing {002} (Å)","Intensity"},LabelStyle->22]

(*Repeat the above fitting script for as many steps as there are
make a new mathematica book in another folder for all voltage steps*)
```

File Outputs

```
points6umfile1=Table[{x,pV3b/.file1pmntpeakFits},{x,Range[1.97,2.05, 0.001]}];
Export["points6umfile1.dat", points6umfile1]



parameterOutputs=List[
   file1pmntpeakFits,file1pmntpeakErrorpv,file1pmntpeakConfIntpv,file1pmntpeakBICpv,
"end",
   ];
Export["parameterOutputs_6um_1.dat",parameterOutputs]
```

Pt Peak Positions

```
(*Find the peak position first*)

(*note: search parameter is second parameter in Nearest[...]*)
PeakPositionPt= Position[data[[1]][[All,1]],Nearest[data[[1]][[All,1]],
2.256][[1]]][[1]][[1]];

Manipulate[ListPlot[ TruncPt = Table[Take[data[[i]], {PeakPositionPt - range + shift,
PeakPositionPt +range+shift}], {i,1,tablenum }], PlotRange -> Full], {{range, 12}, 8,
20, 1}, {{shift, 0}, -10, 10,1}]
(*range = 12, shift = 0*)
pV3bPt=amp2Pt(mu2Pt*2/π*fwhm2Pt/(4(x-cen2Pt)^2+fwhm2Pt^2)+(1-mu2Pt) √4 Log[2] /(√π
fwhm2Pt) Exp[-((4Log[2])/fwhm2Pt^2) (x-cen2Pt)^2])+amp3Pt*x+constPt;


amp2minpv3Pt=0;
amp2guesspv3Pt=12;

fwhm2minpv3Pt=0.001;
fwhm2maxpv3Pt=0.02;
fwhm2guesspv3Pt=.008;
```

```
mu2minpv3Pt=0;
mu2maxpv3Pt=1;
mu2guesspv3Pt=.7;

cen2minpv3Pt=2.22;
cen2maxpv3Pt=2.3;
cen2guesspv3Pt=2.256;

amp3minpv3Pt=0;
amp3guesspv3Pt=0;

constminpv3Pt=0;=
constguesspv3Pt=4;
```

Pt 111 - High Field Test - Fitting - Pseudo-Voigt

```
(*When changing from 2 peak fit to just one, need to change pv2 to
pV3b wherever it is. Also comment out anything having to do with amp1
or any term "1". *)
File 1 - 9 to 5 umwide - Pt
file1Ptpeak=NonlinearModelFit[TruncPt[[1]],{pV3bPt,

{amp2Pt>amp2minpv3Pt,fwhm2minpv3Pt<fwhm2Pt<fwhm2maxpv3Pt,mu2minpv3Pt<mu2Pt<mu2maxpv3Pt
,cen2minpv3Pt<cen2Pt<cen2maxpv3Pt,
     amp3Pt<amp3minpv3Pt,constPt>constminpv3Pt}},

{{amp2Pt,amp2guesspv3Pt},{fwhm2Pt,fwhm2guesspv3Pt},{mu2Pt,mu2guesspv3Pt},{cen2Pt,cen2g
uesspv3Pt},
    {amp3Pt,amp3guesspv3Pt},{constPt,constguesspv3Pt}},x,Weights->(1/#^0
&),MaxIterations->150];
file1PtpeakFits=file1Ptpeak["BestFitParameters"]
file1PtpeakError=file1Ptpeak["ParameterErrors"]
file1PtpeakConfInt=file1Ptpeak["ParameterConfidenceIntervals"]
file1PtpeakBIC=file1Ptpeak["BIC"]
Show[ListPlot[TruncPt[[1]],PlotRange->All,plotoptions,FrameLabel->{"d-
spacing(Å)","Intensity"},AspectRatio->1,PlotMarkers->{Automatic,8},PlotStyle->Black],
 Plot[pV3bPt/.file1PtpeakFits,{x,2.2,2.33},PlotRange->All, PlotStyle-
>{Red,Thick}],Plot[pV3bPt/.{amp2Pt->file1Ptpeak[[5,2]],fwhm2Pt->file1Ptpeak[[6,2]],
mu2Pt->file1Ptpeak[[7,2]],cen2Pt->file1Ptpeak[[8,2]] , constPt-
>0},{x,1.97,2.33},PlotStyle->{Purple,Thick}],
 plotoptions, FrameLabel->{"d-spacing {Pt} (Å)","Intensity"},LabelStyle->22]

(*Repeat the above fitting script for as many steps as there are
make a new mathematica book in another folder for all voltage steps*)
```

References

[1] G.H. Haertling, "Ferroelectric ceramics: History and technology," J. Am. Ceram. Soc., **818**, [82], 797–818, (1999).

[2] J. Chen and R. Panda, "Review: Commercialization of piezoelectric single crystals for medical imaging applications," IEEE Ultrason. Symp., **1**, 235–240, (2005).

[3] S. Lucyszyn, "Review of radio frequency microelectromechanical systems technology," IEEE Proc.-Sci. Meas. Technol, **151**, [2], 93–103, (2005).

[4] J.J. Yao, "RF MEMS from a device perspective," J. Micromechanics Microengineering, **10**, R9–R38, (2000).

[5] D. Damjanovic, "Materials for high temperature piezoelectric transducers," Curr. Opin. Solid State Mater. Sci., **3**, 469–473, (1998).

[6] R.C. Turner, P.A. Fuierer, R.E. Newnham, and T.R. Shrout, "Materials for high temperature acoustic and vibration sensors: A review," Appl. Acoust., **41**, 299–324, (1994).

[7] R.J. Vaccaro, "The past, present, and the future of underwater acoustic signal processing," IEEE Signal Process. Mag., 21–51, (1998).

[8] M.M. Waldrop, "Chips are down for Moore's Law," Nature, **530**, 144–147, (2016).

[9] R. Courtland, "Gordon Moore: The man whose name means progress, the visionary engineer reflects on 50 years of Moore's Law," IEEE Spectr., (2015).

[10] R. Dennard, F. Gaensslen, Y. Hwa-Nien, V.L. Rideout, E. Bassous, and A. Leblanc, "Design of ion-implanted MOSFET's with very small physical dimensions," IEEE, **87**, [5], 256–268, (1974).

[11] W. Haensch, E.J. Nowak, R.H. Dennard, P.M. Solomon, A. Bryant, O.H. Dokumaci, A. Kumar, X. Wang, J.B. Johnson, and M. V. Fischetti, "Silicon CMOS devices beyond scaling," IBM J. Res. Dev., **50**, [4.5], 339–361, (2006).

[12] T. Simonite, "Intel puts the brakes on Moore's Law," MIT Technol. Rev., 2016, (https://www.technologyreview.com/s/601102/intel-puts-the-brakes-on-moores-law/).

[13] A. Seabaugh, "The Tunneling Transistor: Quantum tunneling is a limitation in today's transistors, but it could be the key to future devices," IEEE Spectr., (2013).

[14] T. Simonite, "Moore's Law is dead. Now what?," MIT Technol. Rev., 2016, (https://www.technologyreview.com/s/601441/moores-law-is-dead-now-what/).

[15] W. Hansch, C. Fink, J. Schulze, and I. Eisele, "A vertical MOS-gated Esaki tunneling

transistor in silicon," Thin Solid Films, **369**, 387–389, (2000).

[16] W.Y. Choi, B. Park, J.D. Lee, and T.K. Liu, "Tunneling field-effect transistors (TFETs) with subthreshold swing (SS) less than 60 mV/dec," IEEE Electron Device Lett., **28**, [8], 743–745, (2007).

[17] K.K. Bhuwalka, J. Schulze, and I. Eisele, "Scaling the vertical tunnel FET with tunnel bandgap modulation and gate workfunction engineering," IEEE Trans. Electron Devices, **52**, [5], 909–917, (2005).

[18] P.-F. Wang, K. Hilsenbeck, T. Nirschl, M. Oswald, C. Stepper, M. Weis, D. Schmitt-Landsiedel, and W. Hansch, "Complementary tunneling transistor for low power application," Solid. State. Electron., **48**, 2281–2286, (2004).

[19] D. Hisamoto, W.-C. Lee, J. Kedzierski, E. Anderson, H. Takeuchi, K. Asano, T. King, J. Bokor, and C. Hu, "A folded-channel MOSFET for deep-sub-tenth micron era," Int. Electron Devices Meet., 1032, (1998).

[20] D. Hisamoto, W. Lee, J. Kedzierski, H. Takeuchi, K. Asano, C. Kuo, E. Anderson, T. King, J. Bokor, and C. Hu, "FinFET — A self-aligned double-gate MOSFET scalable to 20 nm," IEEE Trans. Electron Devices, **47**, [12], 2320–2325, (2000).

[21] X. Huang, W.-C. Lee, C. Kuo, D. Hisamoto, L. Chang, J. Kedzierski, E. Anderson, H. Takeuchi, Y.-K. Choi, K. Asano, V. Subramanian, T.-J. King, J. Bokor, and C. Hu, "Sub 50-nm FinFET: PMOS," Int. Electron Devices Meet. 1999. Tech. Dig., 67–70, (1999).

[22] A. Bachtold, P. Hadley, T. Nakanishi, and C. Dekker, "Logic circuits with carbon nanotube transistors," Science, **294**, 1317–20, (2001).

[23] S.J. Tans, A. Verschueren, and C. Dekker, "Room-temperature transistor based on a single carbon nanotube," Nature, **393**, 49–52, (1998).

[24] R. Martel, T. Schmidt, H.R. Shea, T. Hertel, and P. Avouris, "Single- and multi-wall carbon nanotube field-effect transistors," Appl. Phys. Lett., **73**, [17], 2447–2449, (1998).

[25] D.M. Newns, B.G. Elmegreen, X.-H. Liu, and G.J. Martyna, "The piezoelectronic transistor: A nanoactuator-based post-CMOS digital switch with high speed and low power," MRS Bull., **37**, 1071–1076, (2012).

[26] D. Newns, B. Elmegreen, X. Hu Liu, and G. Martyna, "A low-voltage high-speed electronic switch based on piezoelectric transduction," J. Appl. Phys., **111**, 084509, (2012).

[27] D.M. Newns, G.J. Martyna, B.G. Elmegreen, X.-H. Liu, T.N. Theis, and S. Trolier-McKinstry, "Piezoelectronics: a novel, high-performance, low-power computer switching technology," Micro- Nanotechnol. Sensors, Syst. Appl., **8373**, 837304, (2012).

[28] D.M. Newns, B.G. Elmegreen, X.-H. Liu, and G.J. Martyna, "High response piezoelectric and piezoresistive materials for fast, low voltage switching: simulation and theory of transduction physics at the nanometer-scale," Adv. Mater., **24**, 3672–7, (2012).

[29] M. Copel, M.A. Kuroda, M.S. Gordon, X.-H. Liu, S.S. Mahajan, G.J. Martyna, N. Moumen, C. Armstrong, S.M. Rossnagel, T.M. Shaw, P.M. Solomon, T.N. Theis, J.J. Yurkas, Y. Zhu, and D.M. Newns, "Giant Piezoresistive On/Off Ratios in Rare-Earth Chalcogenide Thin Films Enabling Nanomechanical Switching," Nano Lett., **13**, [10], 4650–3, (2013).

[30] M. Wallace, R.L. Johnson-Wilke, G. Esteves, C.M. Fancher, R.H.T. Wilke, J.L. Jones, and S. Trolier-McKinstry, "In situ measurement of increased ferroelectric/ferroelastic domain wall motion in declamped tetragonal lead zirconate titanate thin films," J. Appl. Phys., **117**, [5], 054103, (2015).

[31] G. Esteves, M. Wallace, R. Johnson-Wilke, C.M. Fancher, R.H.T. Wilke, S. Trolier-McKinstry, and J.L. Jones, "Effect of Mechanical Constraint on Domain Reorientation in Predominantly {111}-Textured Lead Zirconate Titanate Films," J. Am. Ceram. Soc., **99**, [5], 1802–1807, (2016).

[32] F. Griggio, S. Jesse, A. Kumar, O. Ovchinnikov, H. Kim, T.N. Jackson, D. Damjanovic, S. V. Kalinin, and S. Trolier-McKinstry, "Substrate clamping effects on irreversible domain wall dynamics in lead zirconate titanate thin films," Phys. Rev. Lett., **108**, 157604, (2012).

[33] Y. Qi, N.T. Jafferis, K. Lyons, C.M. Lee, H. Ahmad, and M.C. McAlpine, "Piezoelectric Ribbons Printed onto Rubber for Flexible Energy Conversion," Nano Lett., **10**, 524–528, (2010).

[34] X. Chen, S. Xu, N. Yao, and Y. Shi, "1.6 V nanogenerator for mechanical energy harvesting using PZT nanofibers," Nano Lett., **10**, 2133–2137, (2010).

[35] V. Nagarajan, A. Roytburd, A. Stanishevsky, S. Prasertchoung, T. Zhao, L. Chen, J. Melngailis, O. Auciello, and R. Ramesh, "Dynamics of ferroelastic domains in ferroelectric thin films," Nat. Mater., **2**, [1], 43–7, (2003).

[36] S. Bühl ann, B. Dwir, J. Baborowski, and P. Muralt, "Size effect in mesoscopic epitaxial ferroelectric structures: Increase of piezoelectric response with decreasing feature size," Appl. Phys. Lett., **80**, [17], 3195–97, (2002).

[37] M. Hambe, S. Wicks, J.M. Gregg, and V. Nagarajan, "Creation of damage-free ferroelectric nanostructures via focused ion beam milling," Nanotechnology, **19**, [17], 175302, (2008).

[38] J.F. Scott, "Nanoferroelectrics: statics and dynamics," J. Phys. Condens. Matter, **18**, [17], R361–86, (2006).

[39] J.F. Scott, "High-dielectric constant thin films for dynamic random access memories (DRAM)," Annu. Rev. Mater. Sci., **28**, 79–100, (1998).

[40] K.-T. Kim, M.-G. Kang, and C.-I. Kim, "Study on the etching damage characteristics of PZT thin films after etching in Cl-based plasma," Microelectron. Eng., **71**, 294–300, (2004).

[41] F. Chu, G. Fox, T. Davenport, Y. Miyaguchi, and K. Suu, "The control of Pb loss for PZT based FRAM," Intergrated Ferroelectr., **48**, [1], 161–169, (2002).

[42] J.F. Scott, "Applications of modern ferroelectrics," Science, **315**, 954–959, (2007).

[43] Y. Arimoto and H. Ishiwara, "Current status of ferroelectric random-access memory," MRS Bull., **11**, 823–28, (2004).

[44] R.A. Cowley, S.N. Gvasaliya, S.G. Lushnikov, B. Roessli, and G.M. Rotaru, "Relaxing with relaxors: a review of relaxor ferroelectrics," Adv. Phys., **60**, [2], 229–327, (2011).

[45] C.A. Randall and A.S. Bhalla, "Nanostructural-property relations in complex lead perovskites," Jpn. J. Appl. Phys., **29**, [2], 327–333, (1990).

[46] K. Hirota, Z.-G. Ye, S. Wakimoto, P. Gehring, and G. Shirane, "Neutron diffuse scattering from polar nanoregions in the relaxor $Pb(Mg_{1/3}Nb_{2/3})O_3$," Phys. Rev. B, **65**, [10], 1–7, (2002).

[47] G. Burns and F.H. Dacol, "Crystalline ferroelectrics with glassy polarization behavior," Phys. Rev. B, **28**, [5], 2527–2530, (1983).

[48] P. Gehring, S. Wakimoto, Z.-G. Ye, and G. Shirane, "Soft mode dynamics above and below the Burns temperature in the relaxor $Pb(Mg_{1/3}Nb_{2/3})O_3$," Phys. Rev. Lett., **87**, [27], 1–4, (2001).

[49] Z. Kighelman, D. Damjanovic, and N. Setter, "Electromechanical properties and self-polarization in relaxor $Pb(Mg_{1/3}Nb_{2/3})O_3$ thin films," J. Appl. Phys., **89**, [2], 1393, (2001).

[50] R.A. Cowley, S.N. Gvasaliya, S.G. Lushnikov, B. Roessli, and G.M. Rotaru, "Relaxing with relaxors: a review of relaxor ferroelectrics," Adv. Phys., **60**, [2], 229–327, (2011).

[51] S. Fishman and A. Aharony, "Random field effects in disordered anisotropic antiferromagnets," J. Phys. C Solid State Phys., **12**, 729–733, (1979).

[52] Z.G. Lu and G. Calvarin, "Frequency dependence of the complex dielectric permittivity of ferroelectric relaxors," Phys. Rev. B, **51**, [5], 2694–2702, (1995).

[53] V. Bovtun, S. Veljko, S. Kamba, J. Petzelt, S. Vakhrushev, Y. Yakymenko, K. Brinkman, and N. Setter, "Broad-band dielectric response of $PbMg_{1/3}Nb_{2/3}O_3$ relaxor ferroelectrics: Single crystals, ceramics and thin films," J. Eur. Ceram. Soc., **26**, [14], 2867–2875, (2006).

[54] P. Bonneau, P. Garnier, E. Husson, and A. Morell, "Structural study of PMN ceramics by X-ray diffraction between 297 and 1023 K," Mat. Res. Bull., **24**, 201–206, (1989).

[55] P. Bonneau, A. Morell, and G. Calvarin, "X-Ray and neutron diffraction studies transition in

$PbMg_{1/3}Nb_{2/3}0_3$ ceramics of the diffuse phase," J. Solid State Chem., **91**, 350–361, (1991).

[56] N. de Mathan, E. Husson, G. Calvarin, J.R. Gavarri, A.W. Hewat, and A. Morell, "A structural model for the relaxor $PbMg_{1/3}Nb_{2/3}0_3$ at 5 K," J. Phys. Condens. Matter, **3**, 8159–8171, (1991).

[57] B. Dkhil, J.M. Kiat, G. Calvarin, G. Baldinozzi, S.B. Vakhrushev, and E. Suard, "Local and long range polar order in the relaxor-ferroelectric compounds $PbMg_{1/3}$ $Nb_{2/3}O_3$ and $PbMg_{0.3}Nb_{0.6}Ti_{0.1}O_3$," Phys. Rev. B, **65**, [2], 024104, (2001).

[58] D. Damjanovic, "Comments on origins of enhanced piezoelectric properties in ferroelectrics," IEEE Trans. Ultrason. Ferroelectr. Freq. Control, **56**, [8], 1574–85, (2009).

[59] V.A. Shuvaeva, A.M. Glazer, and D. Zekria, "The macroscopic symmetry of $Pb(Mg_{1/3}Nb_{2/3})_{1-x}Ti_xO_3$ in the morphotropic phase boundary region (x = 0.25–0.5)," J. Phys. Condens. Matter, **17**, [37], 5709–5723, (2005).

[60] S.-E. Park and T.R. Shrout, "Ultrahigh strain and piezoelectric behavior in relaxor based ferroelectric single crystals," J. Appl. Phys., **82**, [4], 1804–1811, (1997).

[61] Z.-G. Ye, B. Noheda, M. Dong, D. Cox, and G. Shirane, "Monoclinic phase in the relaxor-based piezoelectric/ferroelectric $Pb(Mg_{1/3}Nb_{2/3})O_3$-$PbTiO_3$ system," Phys. Rev. B, **64**, [18], 184114, (2001).

[62] T.R. Shrout, Z.P. Chang, N. Kim, and S. Markgraf, "Dielectric behavior of single crystals near the (1−x) $Pb(Mg_{1/3}Nb_{2/3})O_3$ -(x) $PbTiO_3$ morphotropic phase boundary," Ferroelectr. Lett. Sect., **12**, [3], 63–69, (1990).

[63] S.W. Choi, T.R. Shrout, S.J. Jang, and A.S. Bhalla, "Dielectric and pyroelectric properties in the $Pb(Mg_{1/3}Nb_{2/3})O_3$-$PbTiO_3$ system," Ferroelectrics, **100**, [1], 29–38, (1989).

[64] B. Jaffe, W.R. Cook Jr., and H. Jaffe, *Piezoelectric Ceramics* (Academic Press, New York, NY, 1971).

[65] M.J. Haun, E. Furman, S.J. Jang, H.A. McKinstry, and L.E. Cross, "Thermodynamic Theory of $PbTiO_3$," J. Appl. Phys., **62**, [8], 3331–38, (1987).

[66] F. Li, S. Zhang, Z. Xu, X. Wei, J. Luo, and T.R. Shrout, "Composition and phase dependence of the intrinsic and extrinsic piezoelectric activity of domain engineered (1-x)$Pb(Mg_{1/3}Nb_{2/3})O_3$-x$PbTiO_3$ crystals," J. Appl. Phys., **108**, 034106, (2010).

[67] H. Fu and R. Cohen, "Polarization rotation mechanism for ultrahigh electromechanical response in single-crystal piezoelectrics," Nature, **403**, [6767], 281–3, (2000).

[68] B. Noheda, D.E. Cox, G. Shirane, J. Gao, and Z.-G. Ye, "Phase diagram of the ferroelectric relaxor (1−x)$Pb(Mg_{1/3}Nb_{2/3}O_3$−x$PbTiO_3$," Phys. Rev. B, **66**, [5], 054104, (2002).

[69] J.-K. Lee, J.Y. Yi, K.-S. Hong, S.-E. Park, and J. Millan, "Domain configuration and crystal structure of $Pb(Zn_{1/3}Nb_{2/3})O_3$–5%$PbTiO_3$ crystals as a function of the electric-field direction," J. Appl. Phys., **91**, [7], 4474–4478, (2002).

[70] K. Fujishiro, R. Vlokh, Y. Uesu, Y. Yamada, J.-M. Kiat, B. Dkhil, and Y. Yamashita, "Optical observation of heterophase and domain structures in relaxor ferroelectrics $Pb(Zn_{1/3}Nb_{2/3})O_3$/9%$PbTiO_3$," Jpn. J. Appl. Phys., **37**, 5246–5248, (1998).

[71] M.K. Durbin, J.C. Hicks, S.-E. Park, and T.R. Shrout, "X-ray diffraction and phenomenological studies of the engineered monoclinic crystal domains in single crystal relaxor ferroelectrics," J. Appl. Phys., **87**, [11], 8159–8164, (2000).

[72] K.K. Rajan and L.C. Lim, "Particle size dependent x-ray linewidth of rhombohedral phase in $Pb(Zn_{1/3}Nb_{2/3})O_3$–(6,7)%$PbTiO_3$," Appl. Phys. Lett., **83**, [25], 5277, (2003).

[73] A.G. Khachaturyan, S.M. Shapiro, and S. Semenovskaya, "Adaptive phase formation in martensitic transformation," Phys. Rev. B, **43**, [13], 832–843, (1991).

[74] D. Viehland, "Symmetry-adaptive ferroelectric mesostates in oriented $Pb(BI_{1/3}BII_{2/3})O_3$-$PbTiO_3$ crystals," J. Appl. Phys., **88**, [8], 4794–4806, (2000).

[75] D. Damjanovic, "Contributions to the piezoelectric effect in ferroelectric single crystals and ceramics," J. Am. Ceram. Soc., **88**, [10], 2663–2676, (2005).

[76] R. Ramesh and N.A. Spaldin, "Multiferroics: progress and prospects in thin films," Nat. Mater., **6**, 21–29, (2007).

[77] D.G. Schlom, L.-Q. Chen, C.-B. Eom, K.M. Rabe, S.K. Streiffer, and J.-M. Triscone, "Strain tuning of ferroelectric thin films," Annu. Rev. Mater. Res., **37**, [1], 589–626, (2007).

[78] S. Trolier-McKinstry, J.F. Shepard, J.L. Lacey, T. Su, G. Zavala, and J. Fendler, "Piezoelectricity in ferroelectric thin films: domain and stress issues," Ferroelectrics, **206**, 381–392, (1998).

[79] K. Lefki and G.J.M. Dormans, "Measurement of piezoelectric coefficients of ferroelectric thin films," J. Appl. Phys., **76**, 1764–1767, (1994).

[80] M. Sayer, D.A. Barrow, R. Noteboom, E.M. Griswold, and Z. Wu, in *Sci. Technol. Electroceramic Thin Film. NATO ASI Ser. Ser. E Appl. Sci. Vol. 284*, edited by O. Auciello and R. Waser (Kluwer Academic Publishers, 1995), pp. 399–412.

[81] D.-J. Kim, J.-P. Maria, A.I. Kingon, and S.K. Streiffer, "Evaluation of intrinsic and extrinsic contributions to the piezoelectric properties of $Pb(Zr_{1-X}Ti_X)O_3$ thin films as a function of composition," J. Appl. Phys., **93**, [9], 5568, (2003).

[82] S. Hiboux, P. Muralt, and T. Maeder, "Domain and lattice contributoins to dielectric and

piezoelectric properties of Pb(Zr_x,Ti_{1-x})O_3 thin films as a function of composition," J. Mater. Res., **14**, [11], 4307–4318, (1999).

[83] Q.M. Zhang, H. Wang, N. Kim, and L.E. Cross, "Direct evaluation of domain-wall and intrinsic contributions to the dielectric and piezoelectric response and their temperature dependence on lead zirconate-titanate ceramics," J. Appl. Phys., **75**, [1], 454, (1994).

[84] F. Xu, S. Trolier-McKinstry, W. Ren, B. Xu, Z.-L. Xie, and K.J. Hemker, "Domain wall motion and its contribution to the dielectric and piezoelectric properties of lead zirconate titanate films," J. Appl. Phys., **89**, [2], 1336–1348, (2001).

[85] B.A. Tuttle, T.J. Garino, J.A. Voigt, T.J.Headley, D. Dimos, and M.O. Eatough, in *Sci. Technol. Electroceramic Thin Film. NATO ASI Ser. Ser. E Appl. Sci. Vol. 284*, edited by O. Auciello and R. Waser (Kluwer Academic Publishers, 1995), pp. 117–132.

[86] C.D. Theis and D.G. Schlom, "Epitaxy of $PbTiO_3$ on (100) $SrTiO_3$ and vicinal (100) $SrTiO_3$ by pulsed laser deposition," MRS Proc., **401**, [100], 171–176, (1996).

[87] B.A. Tuttle, J.A. Voigt, T.J. Garino, D.C. Goodnow, R.W. Schwartz, D.L. Lamppa, T.J. Headley, and M.O. Eatough, "Chemically prepared Pb(Zr, Ti)O_3 thin films: the effects of orientation and stress," ISAF ’92. Proc. 8th IEEE Int. Symp. Appl. Ferroelectr., 344–48, (1992).

[88] G.L. Brennecka, W. Huebner, B.A. Tuttle, and P.G. Clem, "Use of stress to produce highly oriented tetragonal lead zirconate titanate (PZT 40/60) thin films and resulting electrical properties," J. Am. Ceram. Soc., **87**, [8], 1459–65, (2004).

[89] H. Cao, V.H. Schmidt, R. Zhang, W. Cao, and H. Luo, "Elastic, piezoelectric, and dielectric properties of $0.58Pb(Mg_{1/3}Nb_{2/3})O_3$-$0.42PbTiO_3$ single crystal," J. Appl. Phys., **96**, [1], 549–554, (2004).

[90] Z. Zhang, J.H. Park, and S. Trolier-McKinstry, "(001)-Oriented $LaNiO_3$ bottom electrodes and (001)-textured ferroelectric thin films on $LaNiO_3$," MRS Bull., **596**, 73–78, (2000).

[91] Y.S. Touloukian, R.K. Kirby, R.E. Taylor, and T.Y.R. Lee, *Thermophysical Properties of Matter* (IFI/Plenum, New York, 1977).

[92] R. Wongmaneerung, R. Guo, A. Bhalla, R. Yimnirun, and S. Ananta, "Thermal expansion properties of PMN–PT ceramics," J. Alloys Compd., **461**, [1-2], 565–569, (2008).

[93] A. Stanishevsky, S. Aggarwal, A.S. Prakash, J. Melngailis, and R. Ramesh, "Focused ion-beam patterning of nanoscale ferroelectric capacitors," J. Vac. Sci. Technol. B, **16**, 3899–3902, (1998).

[94] V. Nagarajan, A. Stanishevsky, L. Chen, T. Zhao, B.-T. Liu, J. Melngailis, A.L. Roytburd, R. Ramesh, J. Finder, Z. Yu, R. Droopad, and K. Eisenbeiser, "Realizing intrinsic piezoresponse in epitaxial submicron lead zirconate titanate capacitors on Si," Appl. Phys. Lett., **81**, [22], 4215,

(2002).

[95] M.J. Madou, *Fundamentals of Microfabrication: The Science of Miniaturization*, 2nd ed. (CRC Press, New York, NY, 2002).

[96] R.J. Shul and S.J. Pearton, editors , *Handbook of Advanced Plasma Processing Techniques*, 1st ed. (Springer-Verlag, Berlin, 2000).

[97] M. Ohring, *Materials Science of Thin Films: Deposition and Structure*, 2nd ed. (Academic Press, San Diego, CA, 2002).

[98] P. May, "Physics of Advanced Semiconductor Materials," Bristol Univ., (1998).

[99] P. Verdonck, "Plasma Etching," Div. Integr. Microstruct. Cid. Univ. Brazil, http://wcam.engr.wisc.edu/Public/Reference/PlasmaEtch/Plasma paper.pdf).

[100] J.L. Cecchi, in *Handb. Plasma Process. Technol.*, edited by R.J. Shyl and S.J. Pearton, 1st ed. (William Andrew Publishing, New York, NY, 1990), pp. 14–69.

[101] D. Lishan, in *Plasma-Therm Workshop*, (University Park, PA, 2013).

[102] J. Mcvittie, in *NNIN Etch Workshop,* (Stanford University, Stanford, CA, 2008), pp. 1–25.

[103] G.S. Oehrlein, in *Handb. Plasma Process. Technol.*, edited by S.J. Shul and S.J. Pearton (William Andrew Publishing, 1990), pp. 196–231.

[104] R. Abdolvand and F. Ayazi, "An advanced reactive ion etching process for very high aspect-ratio sub-micron wide trenches in silicon," Sensors Actuators, A Phys., **144**, [1], 109–116, (2008).

[105] J. Baborowski, "Microfabrication of Piezoelectric MEMS," J. Electroceramics, **12**, 33–51, (2004).

[106] J.W.U. Jang, Y.H. Lee, Y.J. Lee, J. Lee, and G.Y. Yeom, "Etching characteristics of lead magnesium niobate - lead titanate relaxor ferroelectrics," Surf. Coatings Technol., [131], 252–256, (2000).

[107] W.L. Warren, D. Dimos, B. A. Tuttle, R.D. Nasby, and G.E. Pike, "Electronic domain pinning in Pb(Zr,Ti)O_3 thin films and its role in fatigue," Appl. Phys. Lett., **65**, [8], 1018, (1994).

[108] R. Keech, S. Shetty, M.A. Kuroda, X. Hu Liu, G.J. Martyna, D.M. Newns, and S. Trolier-McKinstry, "Lateral scaling of Pb($Mg_{1/3}Nb_{2/3}$)TiO_3-$PbTiO_3$ thin films for piezoelectric logic applications," J. Appl. Phys., **115**, [23], 234106, (2014).

[109] D.D. Fong, G.B. Stephenson, S.K. Streiffer, J.A. Eastman, O. Auciello, P.H. Fuoss, and C. Thompson, "Ferroelectricity in ultrathin perovskite films," Science, **304**, [5677], 856–858,

(2004).

[110] L. Despont, C. Koitzsch, F. Clerc, M.G. Garnier, and P. Aebi, "Direct evidence for ferroelectric polar distortion in ultrathin lead titanate perovskite films," Phys. Rev. B, **73**, 094110, (2006).

[111] C. Lichtensteiger, J. Triscone, J. Junquera, and P. Ghosez, "Ferroelectricity and tetragonality in ultrathin $PbTiO_3$ films," Phys. Rev. Lett., **94**, 047603, (2005).

[112] N. Kim, W. Huebner, S.-J. Jang, and T.R. Shrout, "Dielectric and piezoelectric properties of lanthanum-modified lead magnesium niobium-lead titanate ceramics," Ferroelectrics, **93**, 341–349, (1989).

[113] H. Wang, B. Jang, T.R. Shrout, and W. Cao, "Electromechanical Properties of Fine-Grain, 0.7 $Pb(Mg_{1/3}Nb_{2/3})O_3$-0.3$PbTiO_3$ Ceramics," IEEE Trans. Ultrason. Ferroelectr. Freq. Control, **51**, [7], 907–911, (2004).

[114] P. Papet, J.P. Dougherty, and T.R. Shrout, "Particle and grain size effects on the dielectric behavior of the relaxor ferroelectric $Pb(Mg_{1/3}Nb_{2/3})O_3$," J. Mater. Res., **5**, [12], 2902–2909, (1990).

[115] C.A. Randall, N. Kim, J.-P. Kucera, W. Cao, and T.R. Shrout, "Intrinsic and extrinsic size effects in fine-grained morphotropic-phase-boundary lead zirconate titanate ceramics morphotropic-phase-boundary lead zirconate titanate ceramics," J. Am. Ceram. Soc., **81**, [3], 677–88, (1998).

[116] Y. Bastani, T. Schmitz-Kempen, A. Roelofs, and N. Bassiri-Gharb, "Critical thickness for extrinsic contributions to the dielectric and piezoelectric response in lead zirconate titanate ultrathin films," J. Appl. Phys., **109**, 014115, (2011).

[117] G. Arlt, D. Hennings, and G. de With, "Dielectric properties of fine-grained barium titanate ceramics," J. Appl. Phys., **58**, [4], 1619–25, (1985).

[118] M.H. Frey and D.A. Payne, "Grain-size effect on structure and phase transformations for barium titanate," Phys. Rev. B, **54**, [5], 3158–3168, (1996).

[119] H. Kniekamp and W. Heywang, "Naturwissenschaften," Z. Angew Phys., **6**, 385, (1954).

[120] G.H. Jonker and W. Noorlander, in *Sci. Ceram. Vol. 1* (Academic Press, London, 1962), p. 255.

[121] N.C. Sharma and E.R. McCartney, "Dielectric properties of pure barium titanate as a function of grain size," J. Austr. Ceram. Soc., **10**, 16–22, (1974).

[122] K. Kinoshita and A. Yamaji, "Grain size effects on dielectric properties in barium titanate ceramics," J. Appl. Phys., **47**, [1], 371–373, (1976).

[123] W. Cao and C.A. Randall, "Grain Size and Domain Size Relations in Bulk Ceramic Materials," J. Phys. Chem. Solids, **57**, [10], 1499–1505, (1996).

[124] T. Hoshina, Y. Kigoshi, S. Hatta, H. Takeda, and T. Tsurumi, "Domain Contribution to Dielectric Properties of Fine-Grained $BaTiO_3$ Ceramics," Jpn. J. Appl. Phys., **48**, (2009).

[125] S. Wada, K. Yako, H. Kakemoto, and T. Tsurumi, "Enhanced piezoelectric properties of barium titanate single crystals with different engineered-domain sizes," J. Appl. Phys., **98**, (2005).

[126] M.H. Frey, Z. Xu, P. Han, and D.A. Payne, "The role of interfaces on an apparent grain size effect on the dielectric properties for ferroelectric barium titanate ceramics," Ferroelectrics, **206**, 337–353, (1998).

[127] J.F. Ihlefeld, W.J. Borland, and J. Maria, "Enhanced dielectric and crystalline properties in ferroelectric barium titanate thin films," Adv. Funct. Mater., **17**, 1199–1203, (2007).

[128] J.F. Ihlefeld, A.M. Vodnick, S.P. Baker, W.J. Borland, and J. Maria, "Extrinsic scaling effects on the dielectric response of ferroelectric thin films," J. Appl. Phys., **103**, 074112, (2008).

[129] C.B. Parker, J.-P. Maria, and A.I. Kingon, "Temperature and thickness dependent permittivity of BST thin films," Appl. Phys. Lett., **81**, [2], 340–343, (2002).

[130] R. Waser, "Dielectric analysis of intergrated ceramic thin film capacitors," Integr. Ferroelectr., **15**, [1-4], 39–51, (1997).

[131] D. Ghosh, A. Sakata, J. Carter, P.A. Thomas, H. Han, J.C. Nino, and J.L. Jones, "Domain wall displacement is the origin of superior permittivity and piezoelectricity in $BaTiO_3$ at intermediate grain sizes," Adv. Funct. Mater., **24**, [7], 885–896, (2013).

[132] D. Damjanovic and M. Demartin, "Contribution of the irreversible displacement of domain walls to the piezoelectric effect in barium titanate and lead zirconate titanate ceramics," J. Phys. Condens. Matter, **9**, 4943–53, (1997).

[133] R. Ahluwalia and W. Cao, "Size dependence of domain patterns in a constrained ferroelectric system," J. Appl. Phys., **89**, [12], 8105–09, (2001).

[134] H.-I. Hsiang and F.-S. Yen, "Effect of crystallite size on the ferroelectric domain growth of ultrafine $BaTiO_3$ powders," J. Am. Ceram. Soc., **79**, [4], 1053–60, (1996).

[135] Y. Zhang, J. Li, and D. Fang, "Size dependent domain configuration and electric field driven evolution in ultrathin ferroelectric films: A phase field investigation," J. Appl. Phys., **107**, 034107, (2010).

[136] Z. Zhao, V. Buscaglia, M. Viviani, M.T. Buscaglia, L. Mitoseriu, A. Testino, M. Nygren, M. Johnsson, and P. Nanni, "Grain-size effects on the ferroelectric behavior of dense nanocrystalline

$BaTiO_3$ ceramics," Phys. Rev. B, **70**, 024107, (2004).

[137] M.T. Buscaglia, M. Viviani, V. Buscaglia, L. Mitoseriu, A. Testino, P. Nanni, Z. Zhao, M. Nygren, C. Harnagea, D. Piazza, and C. Galassi, "High dielectric constant and frozen macroscopic polarization in dense nanocrystalline $BaTiO_3$ ceramics," Phys. Rev. B, **73**, 064114, (2006).

[138] B.J. Rodriguez, Y.H. Chu, R. Ramesh, and S. V Kalinin, "Ferroelectric domain wall pinning at a bicrystal grain boundary in bismuth ferrite," Appl. Phys. Lett., **93**, 142901, (2008).

[139] D.M. Marincel, H. Zhang, S. Jesse, A. Belianinov, M.B. Okatan, S. V. Kalinin, W.M. Rainforth, I.M. Reaney, C.A. Randall, and S. Trolier-McKinstry, "Domain wall motion across various grain boundaries in ferroelectric thin films," J. Am. Ceram. Soc., **98**, [6], 1848–1857, (2015).

[140] D.M. Marincel, H.R. Zhang, J. Britson, A. Belianinov, S. Jesse, S. V Kalinin, L.Q. Chen, W.M. Rainforth, I.M. Reaney, C.A. Randall, and S. Trolier-McKinstry, "Domain pinning near a single-grain boundary in tetragonal and rhombohedral lead zirconate titanate films," Phys. Rev. B, **91**, 134113, (2015).

[141] S. Choudhury, Y.L. Li, C.I. Krill, and L.Q. Chen, "Effect of grain orientation and grain size on ferroelectric domain switching and evolution: Phase field simulations," Acta Mater., **55**, 1415–1426, (2007).

[142] B.D. Huey, R.N. Premnath, S. Lee, and N.A. Polomoff, "High speed SPM applied for direct nanoscale mapping of the influence of defects on ferroelectric switching dynamics," J. Am. Ceram. Soc., **95**, [4], 1147–1162, (2012).

[143] J.F. Ihlefeld, D.T. Harris, R. Keech, J.L. Jones, J.-P. Maria, S. Trolier-McKinstry, and D. Damjanovic, "Scaling Effects in Perovskite Ferroelectrics: Fundamental Limits and Process-Structure-Property Relations," J. Am. Ceram. Soc., **21**, 1–21, (2016).

[144] B.A. Strukov, S.T. Avitadze, S.G. Shulman, B.M. Goltzman, and V. V. Lemanov, "Clarification of size effects in polycrystalline $BaTiO_3$ thin films by means of the specific heat measurements: grain size or film thickness?," Ferroelectrics, **301**, 157–162, (2004).

[145] C.T. Shelton, P.G. Kotula, G.L. Brennecka, P.G. Lam, K.E. Meyer, J.P. Maria, B.J. Gibbons, and J.F. Ihlefeld, "Chemically homogeneous complex oxide thin films via improved substrate metallization," Adv. Funct. Mater., **22**, 2295–2302, (2012).

[146] R. Kretschmer and K. Binder, "Surface effects on phase transitions in ferroelectrics and dipolar magnets," Phys. Rev. B, **20**, [3], 1065–1076, (1979).

[147] L.-W. Chang, M. Alexe, J.F. Scott, and J.M. Gregg, "Settling the dead layer debate in nanoscale capacitors," Adv. Mater., **21**, [48], 4911–4914, (2009).

[148] M.M. Saad, P. Baxter, R.M. Bowman, J.M. Gregg, F.D. Morrison, and J.F. Scott, "Intrinsic dielectric response in ferroelectric nano-capacitors," J. Phys. Condens. Matter, **16**, [41], L451–L456, (2004).

[149] M. Stengel and N.A. Spaldin, "Origin of the dielectric dead layer in nanoscale capacitors," Nature, **443**, [7112], 679–82, (2006).

[150] I. Fujii, E. Hong, and S. Trolier-McKinstry, "Thickness dependence of dielectric nonlinearity of lead zirconate titanate films," IEEE Trans. Ultrason. Ferroelectr. Freq. Control, **57**, [8], 1717–1723, (2010).

[151] D.M. Kim, C.B. Eom, V. Nagarajan, J. Ouyang, R. Ramesh, V. Vaithyanathan, and D.G. Schlom, "Thickness dependence of structural and piezoelectric properties of epitaxial $Pb(Zr_{0.52}Ti_{48})O_3$ films on Si and $SrTiO_3$ substrates," Appl. Phys. Lett., **88**, [14], 142904, (2006).

[152] V. Nagarajan, I.G. Jenkins, S.P. Alpay, H. Li, S. Aggarwal, L. Salamanca-Riba, A.L. Roytburd, and R. Ramesh, "Thickness dependence of structural and electrical properties in epitaxial lead zirconate titanate films," J. Appl. Phys., **86**, [1], 595–602, (1999).

[153] T.M. Shaw, S. Trolier-McKinstry, and P.C. McIntyre, "The Properties of Ferroelectric Films at Small Dimensions," Annu. Rev. Mater. Sci., **30**, 263–98, (2000).

[154] S.-E. Park and T.R. Shrout, "Ultrahigh strain and piezoelectric behavior in relaxor based ferroelectric single crystals," J. Appl. Phys., **82**, [4], 1804–11, (1997).

[155] E.M. Sabolsky, A.R. James, S. Kwon, S. Trolier-McKinstry, and G.L. Messing, "Piezoelectric properties of ⟨001⟩ textured $Pb(Mg_{1/3}Nb_{2/3})O_3$–$PbTiO_3$ ceramics," Appl. Phys. Lett., **78**, [17], 2551–53, (2001).

[156] E.M. Sabolsky, S. Trolier-McKinstry, and G.L. Messing, "Dielectric and piezoelectric properties of <001> fiber-textured $0.675Pb(Mg_{1/3}Nb_{2/3})O_3$-$0.325PbTiO_3$ ceramics," J. Appl. Phys., **93**, [7], 4072–4080, (2003).

[157] Y. Yan, Y.U. Wang, and S. Priya, "Electromechanical behavior of [001]-textured $Pb(Mg_{1/3}Nb_{2/3})TiO_3$-$PbTiO_3$ ceramics," Appl. Phys. Lett., **100**, 192905, (2012).

[158] S. Kwon, E.M. Sabolsky, G.L. Messing, and S. Trolier-McKinstry, "High strain, <001> textured $0.675Pb(Mg_{1/3}Nb_{2/3})O_3$-$0.325PbTiO_3$ ceramics: templated grain growth and piezoelectric properties," J. Am. Ceram. Soc., **88**, [2], 312–317, (2005).

[159] S.F. Poterala, S. Trolier-McKinstry, R.J. Meyer, and G.L. Messing, "Processing, texture quality, and piezoelectric properties of $<001>_C$ textured $(1-x)Pb(Mg_{1/3}Nb_{2/3})TiO_3$-$xPbTiO_3$ ceramics," J. Appl. Phys., **110**, 014105, (2011).

[160] V.K. Wadhawan, P. Pandit, and S.M. Gupta, "PMN–PT based relaxor ferroelectrics as very smart materials," Mater. Sci. Eng. B, **120**, [1-3], 199–205, (2005).

[161] J. Kelly, M. Leonard, C. Tantigate, and A. Safari, "Effect of composition on the electromechanical properties of PMN-PT ceramics," J. Am. Ceram. Soc., **64**, 957–964, (1997).

[162] S. Xu, G. Poirier, and N. Yao, "PMN-PT nanowires with a very high piezoelectric constant," Nano Lett., **12**, [5], 2238–42, (2012).

[163] I.-B. Magdău, X.-H. Liu, M.A. Kuroda, T.M. Shaw, J. Crain, P.M. Solomon, D.M. Newns, and G.J. Martyna, "The piezoelectronic stress transduction switch for very large-scale integration, low voltage sensor computation, and radio frequency applications," Appl. Phys. Lett., **107**, [7], 073505, (2015).

[164] Z. Jiwei, S. Bo, Z. Liangying, and Y. Xi, "Preparation and dielectric properties by sol – gel derived PMN-PT powder and ceramic," Mater. Chem. Phys., **64**, 1–4, (2000).

[165] Y. Bastani and N. Bassiri-Gharb, "Processing optimization of lead magnesium niobate-lead titanate thin films for piezoelectric MEMS application," J. Am. Ceram. Soc., **95**, [4], 1269–1275, (2012).

[166] H. Zhu, D.P. Chu, N.A. Fleck, S.E. Rowley, and S.S. Saxena, "Polarization change in ferroelectric thin film capacitors under external stress," J. Appl. Phys., **105**, [6], 061609, (2009).

[167] J.H. Park, F. Xu, and S. Trolier-McKinstry, "Dielectric and piezoelectric properties of sol–gel derived lead magnesium niobium titanate films with different textures," J. Appl. Phys., **89**, [1], 568, (2001).

[168] P. Muralt, "Texture control and seeded nucleation of nanosize structures of ferroelectric thin films," J. Appl. Phys., **100**, [5], 051605, (2006).

[169] K. Ishikawa, K. Sakura, D. Fu, S. Yamada, H. Suzuki, and T. Hayashi, "Effect of $PbTiO_3$ seeding layer on the growth of sol-gel-derived $Pb(Zr_{0.53}Ti_{0.47})O_3$ thin film," Jpn. J. Appl. Phys., **37**, 5128–31, (1998).

[170] E. Cattan, G. Velu, B. Jaber, D. Remiens, and B. Thierry, "Structure control of $Pb(Zr, Ti)O_3$ films using $PbTiO_3$ buffer layers produced by magnetron sputtering," Appl. Phys. Lett., **70**, [13], 1718–1721, (2001).

[171] P. Muralt, T. Maeder, L. Sagalowicz, S. Hiboux, S. Scalese, D. Naumovic, R.G. Agostino, N. Xanthopoulos, H.J. Mathieu, L. Patthey, and E.L. Bullock, "Texture control of $PbTiO_3$ and $Pb(Zr,Ti)O_3$ thin films with TiO_2 seeding," J. Appl. Phys., **83**, [7], 3835, (1998).

[172] C. Zhong, X. Wang, L. Guo, and L. Li, "Characterization of (100)-oriented $0.63BiMg_{1/2}Ti_{1/2}O_3$–$0.37PbTiO_3$ piezoelectric films by a sol–gel process," Thin Solid Films, **580**, 52–55, (2015).

[173] Z. Xie, B. Peng, J. Zhang, X. Zhang, Z. Yue, and L. Li, "Highly (100)-Oriented $Bi(Ni_{1/2} Hf_{1/2})O_3$ -$PbTiO_3$ Relaxor-Ferroelectric Films for Integrated Piezoelectric Energy Harvesting and

Storage System," J. Am. Ceram. Soc., **98**, [10], 2968–2971, (2015).

[174] K.G. Brooks, I.M. Reaney, R. Klissurska, Y. Huang, L. Bursill, and N. Setter, "Orientation of rapid thermally annealed lead zirconate titanate thin films on (111) Pt substrates," J. Mater. Res., **9**, [10], 2540–53, (1994).

[175] J. Ouyang, D.M. Kim, C.B. Eom, R. Ramesh, and A.L. Roytburd, "Orientation dependence of the intrinsic converse longitudinal piezoelectric constant for $0.67Pb(Mg_{1/3}Nb_{2/3})O_3$ $-0.33PbTiO_3$ ferroelectric films with a rhombohedral structure," Smart Mater. Struct., **14**, 524–528, (2005).

[176] X. Du, J. Zheng, U. Belegundu, and K. Uchino, "Crystal orientation dependence of piezoelectric properties of lead zirconate titanate near the morphotropic phase boundary," Appl. Phys. Lett., **72**, [19], 2421–23, (1998).

[177] D. Fu, H. Suzuki, T. Ogawa, and K. Ishikawa, "High-piezoelectric behavior of c-axis-oriented lead zirconate titanate thin films with composition near the morphotropic phase boundary," Appl. Phys. Lett., **80**, [19], 3572–74, (2002).

[178] F. Griggio and S. Trolier-McKinstry, "Grain size dependence of properties in lead nickel niobate-lead zirconate titanate films," J. Appl. Phys., **107**, [2], 024105, (2010).

[179] N. Bassiri-Gharb, Y. Bastani, and A. Bernal, "Chemical solution growth of ferroelectric oxide thin films and nanostructures," Chem. Soc. Rev., **43**, 2125–2140, (2014).

[180] P. Bintachitt, S. Jesse, D. Damjanovic, Y. Han, I.M. Reaney, S. Trolier-McKinstry, and S. V Kalinin, "Collective dynamics underpins Rayleigh behavior in disordered polycrystalline ferroelectrics," Proc. Natl. Acad. Sci., **107**, [16], 7219–7224, (2010).

[181] J. Zhu, X. Zhu, M. Jiang, X. Li, J. Zhu, and D. Xiao, "Enhanced ferroelectric and dielectric properties of highly (100)-oriented $0.67Pb(Mg_{1/3}Nb_{2/3})O_3$-$0.33PbTiO_3$ thin films with a special $Pb(Zr_{0.2},Ti_{0.8})O_3$/ PbO_x bilayered buffer layer," J. Appl. Phys., **104**, 086104, (2008).

[182] G.L. Brennecka, J.F. Ihlefeld, J.-P. Maria, B. A. Tuttle, and P.G. Clem, "Processing technologies for high-permittivity thin films in capacitor applications," J. Am. Ceram. Soc., **93**, [12], 3935–3954, (2010).

[183] J.L. Jones, J.M. Lebeau, J. Nikkel, A.A. Oni, J.H. Dycus, C. Cozzan, F. Lin, A. Chernatynskiy, J.C. Nino, S.B. Sinnott, S. Mhin, G.L. Brennecka, and J. Ihlefeld, "Combined experimental and computational methods reveal the evolution of buried interfaces during synthesis of ferroelectric thin films," Adv. Mater. Interfaces, 1500181, (2015).

[184] R.W. Schwartz, "Chemical Solution Deposition of Perovskite Thin Films," **4756**, [97], 2325–2340, (1997).

[185] C. Morandi and S. Trolier-McKinstry, *Unpublished Work* (2015).

[186] F.K. Lotgering, "Topotactical reactions with ferrimagnetic oxides having hexagonal crystal structures," J. Inorg. Nucl. Chem., **9**, 113–123, (1959).

[187] S. Sivaramakrishnan, P. Mardilovich, A. Mason, A. Roelofs, T. Schmitz-Kempen, and S. Tiedke, "Electrode size dependence of piezoelectric response of lead zirconate titanate thin films measured by double beam laser interferometry," Appl. Phys. Lett., **103**, 132904, (2013).

[188] G.L. Brennecka, C.M. Parish, B.A. Tuttle, L.N. Brewer, and M.A. Rodriguez, "Reversibility of the perovskite-to-fluorite phase transformation in lead-based thin and ultrathin films," Adv. Mater., **20**, [8], 1407–1411, (2008).

[189] C.-S. Tu, C.-L. Tsai, V.H. Schmidt, H. Luo, and Z. Yin, "Dielectric, hypersonic, and domain anomalies of $(PbMg_{1/3}Nb_{2/3}O_3)_{(1-x)}(PbTiO_3)_x$ single crystals," J. Appl. Phys., **89**, [12], 7908–16, (2001).

[190] H.J. Lee, S. Zhang, and T.R. Shrout, "Scaling effects of relaxor-$PbTiO_3$ crystals and composites for high frequency ultrasound," J. Appl. Phys., **107**, [12], 124107, (2010).

[191] F. Chu, I.M. Reaney, and N. Setter, "Role of Defects in the Ferroelectric Relaxor Lead Scandium Tantalate," J. Am. Ceram. Soc., **78**, [7], 1947–1952, (1995).

[192] J.P. Maria, W. Hackenberger, and S. Trolier-McKinstry, "Phase development and electrical property analysis of pulsed laser deposited PMN-PT 70/30 epitaxial thin films," J. Appl. Phys., **84**, [9], 5147–5154, (1998).

[193] K. Okazaki and K. Nagata, "Effects of grain size and porosity on electrical and optical properties of PLZT ceramics," J. Am. Ceram. Soc., **56**, [12], 82–86, (1973).

[194] M. Villegas, A.C. Caballero, M. Kosec, C. Moure, P. Duran, and J.F. Fernandez, "Effects of PbO excess in $Pb(Mg_{1/3}Nb_{2/3})O_3$–$PbTiO_3$ ceramics: Part I. Sintering and dielectric properties," J. Mater. Res., **14**, [3], 891–897, (1999).

[195] H.J. Lee, S. Zhang, J. Luo, F. Li, and T.R. Shrout, "Thickness dependent properties of relaxor-$PbTiO_3$ ferroelectrics for ultrasonic transducers," Adv. Funct. Mater., **20**, [18], 3154–3162, (2010).

[196] F. Calame and P. Muralt, "Growth and properties of gradient free sol-gel lead zirconate titanate thin films," Appl. Phys. Lett., **90**, [6], 062907, (2007).

[197] S. Zhang and F. Li, "High performance ferroelectric relaxor-$PbTiO_3$ single crystals: Status and perspective," J. Appl. Phys., **111**, 031301, (2012).

[198] S. Yokoyama, S. Okamoto, S. Okamoto, H. Funakubo, H. Matsuda, T. Iijima, K. Saito, H. Okino, and T. Yamamoto, "$PbTiO_3$ content dependence of crystal structure and electrical properties of (100)-/(001)-oriented epitaxial $Pb(Mg_{1/3}Nb_{2/3})O_3$-$PbTiO_3$ films grown by metalorganic chemical vapor deposition," J. Appl. Phys., **98**, [8], 086112, (2005).

[199] S.H. Baek, J. Park, D.M. Kim, V.A. Aksyuk, R.R. Das, S.D. Bu, D.A. Felker, J. Lettieri, V. Vaithyanathan, S.S.N. Bharadwaja, N. Bassiri-Gharb, Y.B. Chen, H.P. Sun, C.M. Folkman, H.W. Jang, D.J. Kreft, S.K. Streiffer, R. Ramesh, X.Q. Pan, S. Trolier-McKinstry, D.G. Schlom, M.S. Rzchowski, R.H. Blick, and C.B. Eom, "Giant piezoelectricity on Si for hyperactive MEMS," Science, **334**, 958–961, (2011).

[200] N.H. Fletcher, A.D. Hilton, and B.W. Ricketts, "Optimization of energy storage density in ceramic capacitors," J. Phys. D. Appl. Phys., **29**, 253–258, (1996).

[201] E.K. Michael and S. Trolier-McKinstry, "Cubic pyrochlore bismuth zinc niobate thin films for high-temperature dielectric energy storage," J. Am. Ceram. Soc., **98**, [4], 1223–1229, (2015).

[202] P.M. Solomon, B.A. Bryce, M.A. Kuroda, R. Keech, S. Shetty, T.M. Shaw, M. Copel, L.-W. Hung, A.G. Schrott, C. Armstrong, M.S. Gordon, K.B. Reuter, T.N. Theis, W. Haensch, S.M. Rossnagel, H. Miyazoe, B.G. Elmegreen, X.-H. Liu, S. Trolier-McKinstry, G.J. Martyna, and D.M. Newns, "Pathway to the piezoelectronic transduction logic device," Nano Lett., **15**, [4], 2391–5, (2015).

[203] J. Zhao, Q. Zhang, N. Kim, and T. Shrout, "Electromechanical properties of relaxor ferroelectric lead magnesium niobate-lead titanate ceramics," Japanese J. Appl., **34**, 5658–5663, (1995).

[204] A.F. Devonshire, "Theory of ferroelectrics," Philos. Mag., **3**, [10], 85–130, (1954).

[205] A.L. Kholkin, E.K. Akdogan, A. Safari, P.-F. Chauvy, and N. Setter, "Characterization of the effective electrostriction coefficients in ferroelectric thin films," J. Appl. Phys., **89**, [12], 8066, (2001).

[206] F. Li, L. Jin, Z. Xu, D. Wang, and S. Zhang, "Electrostrictive effect in $Pb(Mg_{1/3}Nb_{2/3})O_3$-$xPbTiO_3$ crystals," Appl. Phys. Lett., **102**, 152910, (2013).

[207] X. Zhao, B. Fang, H. Cao, Y. Guo, and H. Luo, "Dielectric and piezoelectric performance of PMN-PT single crystals with compositions around the MPB: influence of composition, poling field and crystal orientation," Mater. Sci. Eng. B, **96**, 254–262, (2002).

[208] S.-E. Park and T.R. Shrout, "Relaxor based ferroelectric single crystals for electro-mechanical actuators," Mater. Res. Innov., **1**, 20–25, (1997).

[209] R. Zhang, B. Jiang, and W. Cao, "Orientation dependence of piezoelectric properties of single domain $0.67Pb(Mn_{1/3}Nb_{2/3})O_3$–$0.33PbTiO_3$ crystals," Appl. Phys. Lett., **82**, [21], 3737, (2003).

[210] S. Saitoh, T. Kobayashi, K. Harada, S. Shimanuki, and Y. Yamashita, "A 20 MHz single-element ultrasonic probe using $0.91Pb(Zn_{1/3}Nb_{2/3})O_3$-$0.09PbTiO_3$ single crystal," IEEE Trans. Ultrason. Ferroelectr. Freq. Control, **45**, [4], 1071–76, (1998).

[211] J. Chen, R. Panda, and B. Savord, *Realizing Dramatic Improvements in the Efficiency,*

Sensitivity and Bandwidth of Ultrasound Transducers - Philips PureWave Crystal Technology (2006).

[212] S.-E.E. Park and W. Hackenberger, "High performance single crystal piezoelectrics: applications and issues," Solid State Mater. Sci., **6**, 11–18, (2002).

[213] Y. Sakashita, T. Fujii, and Y. Hishinuma, Patent No. US7845767 (2010).

[214] H. Kohlstedt, Y. Mustafa, A. Gerber, A. Petraru, M. Fitsilis, R. Meyer, U. Böttger, and R. Waser, "Current status and challenges of ferroelectric memory devices," Microelectron. Eng., **80**, 296–304, (2005).

[215] V. Bornand, S. Trolier-McKinstry, K. Takemura, and C.A. Randall, "Orientation dependence of fatigue behavior in relaxor ferroelectric–$PbTiO_3$ thin films," J. Appl. Phys., **87**, [8], 3965–72, (2000).

[216] K. Takemura, M. Ozgul, V. Bornand, S. Trolier-McKinstry, and C.A. Randall, "Fatigue anisotropy in single crystal $Pb(Zn_{1/3}Nb_{2/3})O_3$-$PbTiO_3$," J. Appl. Phys., **88**, [12], 1–6, (2000).

[217] T.P. Ma and J. Han, "Why is Nonvolatile Ferroelectric Memory Field-Effect Transistor Still Elusive?," IEEE Elelectron Device Lett., **23**, [7], 386–388, (2002).

[218] N. Setter, D. Damjanovic, L. Eng, G. Fox, S. Gevorgian, S. Hong, A. Kingon, H. Kohlstedt, N.Y. Park, G.B. Stephenson, I. Stolitchnov, A.K. Taganstev, D. V. Taylor, T. Yamada, and S. Streiffer, "Ferroelectric thin films: Review of materials, properties, and applications," J. Appl. Phys., **100**, [5], 051606, (2006).

[219] H. Funakubo, T. Hioki, M. Otsu, K. Shinozaki, and N. Mizutani, "Film Thickness Dependence of Dielectric Property and Crystal Structure of $PbTiO_3$ Film Prepared on Pt / SiO_2 / Si Substrate by Metal Organic Chemical Vapor Deposition," Jpn. J. Appl. Phys., **32**, 4175–4178, (1993).

[220] C. Zhong, X. Wang, J. Fang, and L. Li, "Investigation of Thickness Dependence of Structure and Electric Properties of Sol–Gel-Derived $BiScO_3$ –$PbTiO_3$ Thin Films," J. Am. Ceram. Soc., **93**, [10], 3305–3311, (2010).

[221] C.S. Hwang, B.T. Lee, C.S. Kang, K.H. Lee, H.-J. Cho, H. Hideki, W.D. Kim, S.I. Lee, and M.Y. Lee, "Depletion layer thickness and Schottky type carrier injection at the interface between Pt electrodes and (Ba, Sr)TiO_3 thin films," J. Appl. Phys., **85**, [1], 287, (1999).

[222] N. Sama, C. Soyer, D. Remiens, C. Verrue, and R. Bouregba, "Bottom and top electrodes nature and PZT film thickness influence on electrical properties," Sensors Actuators A Phys., **158**, [1], 99–105, (2010).

[223] N. Bassiri-Gharb, I. Fujii, E. Hong, S. Trolier-McKinstry, D. V. Taylor, and D. Damjanovic, "Domain wall contributions to the properties of piezoelectric thin films," J. Electroceramics, **19**,

47–65, (2007).

[224] L. Pintilie, I. Vrejoiu, D. Hesse, G. LeRhun, and M. Alexe, "Extrinsic contributions to the apparent thickness dependence of the dielectric constant in epitaxial Pb (Zr, Ti)O_3 thin films," Phys. Rev. B, **75**, 224113, (2007).

[225] A.J. Welsh, R.H.T. Wilke, M.A. Hickner, and S. Trolier-McKinstry, "Low-Cost , Damage-Free Patterning of Lead Zirconate Titanate Films," J. Am. Ceram. Soc., **96**, [9], 2799–2806, (2013).

[226] T. Tybell, C.H. Ahn, and J.-M. Triscone, "Ferroelectricity in thin perovskite films," Appl. Phys. Lett., **75**, [6], 856–858, (1999).

[227] C. Zhou and D.M. Newns, "Intrinsic dead layer effect and the performance of ferroelectric thin film capacitors," J. Appl. Phys., **82**, [6], 3081, (1997).

[228] B. Meyer and D. Vanderbilt, "Ab initio study of $BaTiO_3$ and $PbTiO_3$ surfaces in external electric fields," Phys. Rev. B. Condens. Matter, **63**, 205426, (2008).

[229] M. Demartin and D. Damjanovic, "Dependence of the direct piezoelectric effect in coarse and fine grain barium titanate ceramics on dynamic and static pressure," Appl. Phys. Lett., **68**, [21], 3046–3049, (1996).

[230] D.M. Marincel, H. Zhang, A. Kumar, S. Jesse, S. V. Kalinin, W.M. Rainforth, I.M. Reaney, C.A. Randall, and S. Trolier-McKinstry, "Influence of a single grain boundary on domain wall motion in ferroelectrics," Adv. Funct. Mater., **24**, [10], 1409–1417, (2014).

[231] L.J. Sinnamon, M.M. Saad, R.M. Bowman, and J.M. Gregg, "Exploring grain size as a cause for “dead-layer” effects in thin film capacitors," Appl. Phys. Lett., **81**, [4], 703–705, (2002).

[232] L. Pintilie and M. Alexe, "Metal-ferroelectric-metal heterostructures with Schottky contacts . I . Influence of the ferroelectric properties," J. Appl. Phys., **98**, 124103, (2005).

[233] I. Stolichnov, A. Tagantsev, and N. Setter, "Control of leakage conduction of high-fatigue-endurance (Pb,La)(Zr,Ti)O_3 film ferroelectric capacitors with Pt/$SrRuO_3$ electrodes," Appl. Phys. Lett., **75**, [12], 1790–1793, (1999).

[234] L.W. Chang, M. McMillen, F.D. Morrison, J.F. Scott, and J.M. Gregg, "Size effects on thin film ferroelectrics: Experiments on isolated single crystal sheets," Appl. Phys. Lett., **93**, [13], 132904, (2008).

[235] M.-G. Han, M.S.J. Marshall, L. Wu, M.A. Schofield, T. Aoki, R. Twesten, J. Hoffman, F.J. Walker, C.H. Ahn, and Y. Zhu, "Interface-induced nonswitchable domains in ferroelectric thin films," Nat. Commun., **5**, 4693, (2014).

[236] J.H. Park and S. Trolier-McKinstry, "Dependence of dielectric and piezoelectric properties on

film thickness for highly {100} -oriented lead magnesium niobate – lead titanate (70/30) thin films," J. Mater. Res., **16**, [1], 268–275, (2001).

[237] V. Nagarajan, S.P. Alpay, C.S. Ganpule, B.K. Nagaraj, S. Aggarwal, E.D. Williams, A.L. Roytburd, and R. Ramesh, "Role of substrate on the dielectric and piezoelectric behavior of epitaxial lead magnesium niobate-lead titanate relaxor thin films," Appl. Phys. Lett., **77**, [3], 438, (2000).

[238] A. Ferri, M. Detalle, J.-F. Blach, M. Warenghem, D. Rémiens, and R. Desfeux, "Thickness effect on nanoscale electromechanical activity in $Pb(Mg_{1/3}Nb_{2/3})O_3$-$PbTiO_3$ thin films studied by piezoresponse force microscopy," J. Appl. Phys., **110**, [10], 104101, (2011).

[239] D.S. Tinberg, R.L. Johnson-Wilke, D.D. Fong, T.T. Fister, S.K. Streiffer, Y. Han, I.M. Reaney, and S. Trolier-McKinstry, "Octahedral tilt transitions in relaxed epitaxial $Pb(Zr_{1-X}Ti_X)O_3$ films," J. Appl. Phys., **109**, 094104, (2011).

[240] D. Tinberg, Pulsed Laser Deposition of $xBiScO_3$-$(1-x)BaTiO_3$ Thin Films for Pb-Free Dielectric Applications, The Pennsylvania State University, 2006.

[241] R.L. Johnson-Wilke, R.H.T. Wilke, M. Wallace, A. Rajashekhar, G. Esteves, Z. Merritt, J.L. Jones, and S. Trolier-McKinstry, "Ferroelectric/Ferroelastic Domain Wall Motion in Dense and Porous Tetragonal Lead Zirconate Titanate Films," IEEE Trans. Ultrason. Ferroelectr. Freq. Control, **62**, [1], 46–55, (2015).

[242] P. Muralt, "Recent Progress in Materials Issues for Piezoelectric MEMS," J. Am. Ceram. Soc., **91**, [5], 1385–1396, (2008).

[243] Y. Sakashita, H. Segawa, K. Tominaga, and M. Okada, "Dependence of electrical properties on film thickness in $Pb(Zr_xTi_{1-x})O_3$ thin films produced by metalorganic chemical vapor deposition," J. Appl. Phys., **73**, [11], 7857, (1993).

[244] R. Bouregba, G. Le Rhun, G. Poullain, and G. Leclerc, "Investigation of thickness dependence of the ferroelectric properties of $Pb(Zr_{0.6}Ti_{0.4})O_3$ thin-film capacitors," J. Appl. Phys., **99**, [3], 034102, (2006).

[245] A. Gruverman, H. Tokumoto, A.S. Prakash, S. Aggarwal, B. Yang, M. Wuttig, R. Ramesh, O. Auciello, and T. Venkatesan, "Nanoscale imaging of domain dynamics and retention in ferroelectric thin films," Appl. Phys. Lett., **71**, [24], 3492–3494, (1997).

[246] L.J. Sinnamon, R.M. Bowman, and J.M. Gregg, "Investigation of dead-layer thickness in $SrRuO_3/Ba_{0.5}Sr_{0.5}TiO_3/Au$ thin-film capacitors," Appl. Phys. Lett., **78**, [12], 1724, (2001).

[247] D. Damjanovic and M. Demartin, "The Rayleigh law in piezoelectric ceramics," J. Phys. D. Appl. Phys., **29**, 2057–2060, (1996).

[248] J.W.L. Rayleigh, "On the behavior of iron and steel under the operation of feeble magnetic

force," Philos. Mag., **5**, [23], 225–45, (1887).

[249] Y. Bastani and N. Bassiri-Gharb, "Enhanced dielectric and piezoelectric response in PZT superlattice-like films by leveraging spontaneous Zr/Ti gradient formation," Acta Mater., **60**, [3], 1346–1352, (2012).

[250] P. Muralt, R.G. Polcawich, and S. Trolier-McKinstry, "Piezoelectric thin films for sensors, actuators, and energy harvesting," MRS Bull., **34**, [September], 658–664, (2009).

[251] L.M. Garten, P. Lam, D. Harris, J. Maria, and S. Trolier-McKinstry, "Residual ferroelectricity in barium strontium titanate thin film tunable dielectrics," J. Appl. Phys., **116**, 044104, (2014).

[252] P. Finkel, K. Benjamin, and A. Amin, "Large strain transduction utilizing phase transition in relaxor-ferroelectric $Pb(In_{1/2}Nb_{1/2})O_3$–$Pb(Mg_{1/3}Nb_{2/3})O_3$–$PbTiO_3$ single crystals," Appl. Phys. Lett., **98**, [19], 192902, (2011).

[253] P. Finkel, R. Pérez Moyet, M. Wun-Fogle, J. Restorff, J. Kosior, M. Staruch, J. Stace, and A. Amin, "Non-resonant magnetoelectric energy harvesting utilizing phase transformation in relaxor ferroelectric single crystals," Actuators, **5**, [2], (2015).

[254] G. Schwarz, "Estimating the dimension of a model," Ann. Stat., **6**, [2], 461–464, (1978).

[255] V. Kovacova, N. Vaxelaire, G. Le Rhun, P. Gergaud, T. Schmitz-Kempen, and E. Defay, "Correlation between electric-field-induced phase transition and piezoelectricity in lead zirconate titanate films," Phys. Rev. B, **90**, [14], 140101, (2014).

[256] S.-E. Park and T.R. Shrout, "Characteristics of relaxor-based piezoelectric single crystals for ultrasonic transducers," IEEE Trans. Ultrason. Ferroelectr. Freq. Control, **44**, [5], 1140–1147, (1997).

[257] F. Xu, F. Chu, and S. Trolier-McKinstry, "Longitudinal piezoelectric coefficient measurement for bulk ceramics and thin films using pneumatic pressure rig," J. Appl. Phys., **86**, [1], 588–594, (1999).

[258] A. Kholkin, "Non-linear piezoelectric response in lead zirconate-titanate (PZT) films," Ferroelectrics, **238**, 235–243, (2000).

[259] R.A. Wolf and S. Trolier-McKinstry, "Temperature dependence of the piezoelectric response in lead zirconate titanate films," J. Appl. Phys., **95**, [3], 1397–1406, (2004).

[260] R. Zhang, B. Jiang, and W. Cao, "Elastic, piezoelectric, and dielectric properties of multidomain $0.67Pb(Mg_{1/3}Nb_{2/3})O_3$-$0.33PbTiO_3$ single crystals," J. Appl. Phys., **90**, [7], 3471–3475, (2001).

[261] K.A. Cook-Chennault, N. Thambi, and A.M. Sastry, "Powering MEMS portable devices — a review of non-regenerative and regenerative power supply systems with special emphasis on

piezoelectric energy," Smart Mater. Struct., **17**, 043001, (2008).

[262] S.R. Anton and H.A. Sodano, "A review of power harvesting using piezoelectric materials (2003–2006)," Smart Mater. Struct., **1**, [16], 1–21, (2006).

[263] K.S. Hwang, H. Lee, J. Park, S. Yoon, and H. Park, "In-situ quantitative analysis of a prostate-specific antigen (PSA) using a nanomechanical PZT cantilever," Lab Chip, **4**, 547–552, (2004).

[264] J. Hoon, K. Hyun, K. Seon, J. Park, S. Ahn, and T. Song, "Label free novel electrical detection using micromachined PZT monolithic thin film cantilever for the detection of C-reactive protein," Biosens. Bioelectron., **20**, 269–275, (2004).

[265] J. Xie, M. Hu, S.-F. Ling, and H. Du, "Fabrication and characterization of piezoelectric cantilever for micro transducers," Sensors Actuators A Phys., **126**, [1], 182–186, (2006).

[266] F. Griggio, H. Kim, S.O. Ural, T.N. Jackson, K. Choi, R.L. Tutwiler, and S. Trolier-McKinstry, "Medical Applications of Piezoelectric Microelectromechanical Systems," Integr. Ferroelectr., **141**, [1], 169–186, (2013).

[267] C.S. Ganpule, A. Stanishevsky, Q. Su, S. Aggarwal, J. Melngailis, and E. Williams, "Scaling of ferroelectric properties in thin films," Appl. Phys. Lett., **75**, [3], 409–11, (1999).

[268] A. Roytburd, S. Alpay, V. Nagarajan, C. Ganpule, S. Aggarwal, E. Williams, and R. Ramesh, "Measurement of internal stresses via the polarization in epitaxial ferroelectric films," Phys. Rev. Lett., **85**, [1], 190–3, (2000).

[269] L. Chen, J.-H. Li, J. Slutsker, J. Ouyang, and A.L. Roytburd, "Contribution of substrate to converse piezoelectric response of constrained thin films," J. Mater. Res., **19**, [10], 2853–2858, (2004).

[270] H. Han, Y. Kim, M. Alexe, D. Hesse, and W. Lee, "Nanostructured ferroelectrics: fabrication and structure-property relations," Adv. Mater., **23**, [40], 4599–613, (2011).

[271] M. Hiratani, C. Okazaki, H. Hasegawa, N. Sugh, Y. Tarutanti, and K. Takagi, "Fabrication of Pb(Zr,Ti)O_3 Microscopic Capacitors by Electron Beam Lithography," Jpn. J. Appl. Phys., **36**, 5219–5220, (1997).

[272] A. Cofer, P. Rajora, S. Deornellas, and D. Keil, "Plasma etch processing of advanced ferroelectric devices," Integr. Ferroelectr., **16**, 53–61, (1997).

[273] M. Kang, K. Kim, D. Kim, and C. Kim, "Reduction of dry etching damage to PZT films etched with a Cl-based plasma and the recovery behavior," J. Korean Phys. Soc., **41**, [4], 445–450, (2002).

[274] E.G. Lee, D.J. Wouters, G. Willems, and H.E. Maes, "Voltage shift and deformation in the

hysteresis loop of Pb(Zr,Ti)O_3 thin film by defects," Appl. Phys. Lett., **69**, [9], 1223–25, (1996).

[275] R.H. Liang, D. Rémiens, C. Soyer, N. Sama, X.L. Dong, and G.S. Wang, "Etching characteristics and absence of electrical properties damage of PZT thin films etched before crystallization," Microelectron. Eng., **85**, 670–674, (2008).

[276] M. Dawber, D.J. Jung, and J.F. Scott, "Perimeter effect in very small ferroelectrics," Appl. Phys. Lett., **82**, [3], 436–438, (2003).

[277] A. Pramanick, D. Damjanovic, J.C. Nino, and J.L. Jones, "Subcoercive cyclic electrical loading of lead zirconate titanate ceramics I: nonlinearities and losses in the converse piezoelectric effect," J. Am. Ceram. Soc., **92**, [10], 2291–2299, (2009).

[278] J.K. Lee, T.-Y. Kim, I. Chung, and S.B. Desu, "Characterization and elimination of dry etching damaged layer in Pt/Pb($Zr_{0.53}Ti_{0.47}$)O_3/Pt ferroelectric capacitor," Appl. Phys. Lett., **75**, [3], 334–336, (1999).

[279] G.E. Menk, S.B. Desu, W. Pan, and D.P. Vijay, "Dry etching issues in the integration of ferroelectric thin film capacitors," Mat. Res. Soc. Symp. Proc., **433**, 189–200, (1996).

[280] W. Pan, C.L. Thio, and S.B. Desu, "Reactive ion etching damage to the electrical properties of ferroelectric thin films," J. Mater. Res., **13**, [02], 362–367, (2011).

[281] M.-G. Kang, K.-T. Kim, and C.-I. Kim, "Plasma-induced damage in PZT thin films etched by inductively coupled plasma," Thin Solid Films, **435**, 222–226, (2003).

[282] J.-I. Yang, Ph.D. Thesis in Materials Science and Engineering, The Pennsylvania State University, 2016.

[283] L.-H. Wang, Y. Dai, and Z. Deng, "Etch damage evaluation in integrated ferroelectric capacitor side wall by piezoresponse force microscopy," Chinese Phys. Lett., **25**, [9], 3489, (2008).

[284] S. Shetty, J.I. Yang, J. Stitt, and S. Trolier-McKinstry, "Quantitative and high spatial resolution d_{33} measurement of piezoelectric bulk and thin films," J. Appl. Phys., **118**, [17], 174104, (2015).

[285] T. Jungk, A. Hoffmann, and E. Soergel, "Quantitative analysis of ferroelectric domain imaging with piezoresponse force microscopy," Appl. Phys. Lett., **89**, [16], 163507, (2006).

[286] S. V Kalinin, A. Rar, and S. Jesse, "A Decade of Piezoresponse Force Microscopy : Progress , Challenges , and Opportunities," IEEE Trans. Ultrason. Ferroelectr. Freq. Control, **53**, [12], 2226–2252, (2006).

[287] G. Zavala, J.H. Fendler, and S. Trolier-McKinstry, "Characterization of ferroelectric lead zirconate titanate films by scanning force microscopy," J. Appl. Phys., **81**, [11], 7480–91,

(1997).

[288] E. Soergel, "Piezoresponse force microscopy (PFM)," J. Phys. D. Appl. Phys., **44**, [46], 464003, (2011).

[289] S. Jesse, A.P. Baddorf, and S. V Kalinin, "Dynamic behaviour in piezoresponse force microscopy," Nanotechnology, **17**, [6], 1615–28, (2006).

[290] T. Jungk, A. Hoffmann, and E. Soergel, "Challenges for the determination of piezoelectric constants with piezoresponse force microscopy," Appl. Phys. Lett., **91**, [25], 253511, (2007).

[291] D. V Taylor, N. Setter, A.L. Kholkin, and C. Wu, "Interferometric measurements of electric field-induced displacements in piezoelectric thin films," Rev. Sci. Instrum., **67**, [5], 1935–1942, (1996).

[292] R. Steinhausen, T. Hauke, W. Seifert, V. Mueller, H. Beige, S. Seifert, and P. Lobmann, "Clamping of piezoelectric thin films on metallic substrates: influence on the effective piezoelectric modulus d_{33}," Proc. Elev. IEEE Int. Symp. Appl. Ferroelectr., 93–96, (1998).

[293] P.G. Evans and R.J. Sichel-Tissot, "In situ X-ray characterization of piezoelectric ceramic thin films," J. Am. Ceram. Soc., **92**, [1], 18–23, (2013).

[294] Q.M. Zhang and J. Zhao, "Electromechanical properties of lead zirconate titanate piezoceramics under the influence of mechanical stresses," IEEE Trans. Ultrason. Ferroelectr. Freq. Control, **46**, [6], 1518–26, (1999).

[295] R. Keech, S. Shetty, K. Wang, and S. Trolier-McKinstry, "Management of Lead Content for Growth of {001}-Oriented Lead Magnesium Niobate-Lead Titanate Thin Films," J. Am. Ceram. Soc., **99**, [4], 1144–1146, (2016).

[296] D. V. Taylor and D. Damjanovic, "Evidence of domain wall contribution to the dielectric permittivity in PZT thin films at sub-switching fields," J. Appl. Phys., **82**, [4], 1973–1975, (1997).

[297] A. Stancu, C. Pike, L. Stoleriu, P. Postolache, and D. Cimpoesu, "Micromagnetic and Preisach analysis of the First Order Reversal Curves (FORC) diagram," J. Appl. Phys., **93**, [10], 6620–6622, (2003).

[298] I. Fujii, Dielectric Nonlinearity of Ferroelectrics, Ph.D. Thesis in Materials Science and Engineering, The Pennsylvania State Univeristy, 2010.

[299] G. Robert, D. Damjanovic, N. Setter, and A. V. Turik, "Preisach modeling of piezoelectric nonlinearity in ferroelectric ceramics," J. Appl. Phys., **89**, [9], 5067, (2001).

[300] P. Hejda and T. Zelinka, "Modelling of hysteresis processes in magnetic rock samples using the Preisach diagram," Phys. Earth Planet. Inter., **63**, 32–40, (1990).

[301] P. Heiney, "Datasqueeze Software," (2002).

[302] J.L. Bosse, I. Grishin, O. V. Kolosov, and B.D. Huey, "Multidimensional SPM applied for nanoscale conductance mapping," J. Mater. Res., **28**, [24], 3311–3321, (2013).

[303] V. Nagarajan, C.S. Ganpule, B. Nagaraj, S. Aggarwal, S.P. Alpay, and A.L. Roytburd, "Effect of mechanical constraint on the dielectric and piezoelectric behavior," Appl. Phys. Lett., **75**, [26], 4183–4185, (1999).

[304] R.G.P. McQuaid, M. McMillen, L.-W. Chang, A. Gruverman, and J.M. Gregg, "Domain wall propagation in meso- and nanoscale ferroelectrics," J. Phys. Condens. Matter, **24**, [2], 024204, (2012).

[305] M.E. Lines and A.M. Glass, *Principles and Applications of Ferroelectric and Related Materials* (Oxford University Press Inc., New York, 1977).

[306] M. Detalle, A. Ferri, A. Da Costa, R. Desfeux, C. Soyer, and D. Rémiens, "Nanoscale study by piezoresponse force microscopy of relaxor 0.7Pb($Mg_{1/3}Nb_{2/3}$)O_3–0.3PbTiO_3 and 0.9Pb($Mg_{1/3}Nb_{2/3}$)O_3–0.1PbTiO_3 thin films grown on platinum and LaNiO_3 electrodes," Thin Solid Films, **518**, [16], 4670–4674, (2010).

[307] H. Fujisawa, S. Nakashima, K. Kaibara, M. Shimizu, and H. Niu, "Size effects of epitaxial and polycrystalline Pb(Zr, Ti)O_3 thin films grown by metalorganic chemical vapor deposition," Jpn. J. Appl. Phys., **38**, 5392–5396, (1999).

[308] V. Nagarajan, S. Aggarwal, A. Gruverman, R. Ramesh, and R. Waser, "Nanoscale polarization relaxation in a polycrystalline ferroelectric thin film: Role of local environments," Appl. Phys. Lett., **86**, [26], 1–3, (2005).

[309] D. Dimos, R.W. Schwartz, and S.J. Lockwood, "Control of Leakage Resistance in Pb(Zr,Ti)O_3 Thin Films," J. Am. Ceram. Soc., **77**, [11], 3000–3005, (1994).

[310] R. Herdier, M. Detalle, D. Jenkins, C. Soyer, and D. Remiens, "Piezoelectric thin films for MEMS applications—A comparative study of PZT, 0.7PMN–0.3PT and 0.9PMN–0.1PT thin films grown on Si by r.f. magnetron sputtering," Sensors Actuators A Phys., **148**, [1], 122–128, (2008).

[311] S. Jesse, P. Maksymovych, and S. V. Kalinin, "Rapid multidimensional data acquisition in scanning probe microscopy applied to local polarization dynamics and voltage dependent contact mechanics," Appl. Phys. Lett., **93**, [11], (2008).

[312] M.C. Salvadori, I.G. Brown, A.R. Vaz, L.L. Melo, and M. Cattani, "Measurement of the elastic modulus of nanostructured gold and platinum thin films," Phys. Rev. B, **67**, [15], 153404, (2003).

[313] D. Marincel, The Influence of Crystal Defects on Domain Wall Motion in Thin Film

$Pb(Zr,Ti)O_3$, PhD Thesis in Materials Science and Engineering, The Pennsylvania State University, 2014.

[314] D.M. Marincel, S. Jesse, A. Belianinov, M.B. Okatan, S. V Kalinin, T.N. Jackson, C.A. Randall, and S. Trolier-McKinstry, "A-site stoichiometry and piezoelectric response in thin film $PbZr_{(1-x)}Ti_xO_3$," J. Appl. Phys., **117**, 204104, (2015).

[315] W.J. Minford, "Accelerated Life Testing and Reliability of High K Multilayer Ceramic Capacitors," IEEE Trans. Components, Hybrids, Manuf. Technol., **5**, [3], 297–300, (1982).

[316] R.G. Polcawich, C. Feng, P. Vanatta, R. Piekarz, S. Trolier-McKinstry, M. Dubey, and M. Ervin, "Highly accelerated lifetime testing (HALT) of lead zirconate titanate (PZT) thin films," Proc. 2000 12th IEEE Int. Symp. Appl. Ferroelectr., 357–360, (2000).

[317] S. Stotz, "Shift of the morphotropic phase boundary in the PZT system under the influence of electric fields and uniaxial stresses," Ferroelectrics, **76**, 123–132, (1987).

[318] Z.-X. Zhu, J.-F. Li, Y. Liu, and J. Li, "Shifting of the morphotropic phase boundary and superior piezoelectric response in Nb-doped $Pb(Zr,Ti)O_3$ epitaxial thin films," Acta Mater., **57**, [14], 4288–4295, (2009).

[319] S.Q. Zhang, L.D. Wang, W.L. Li, C.Q. Liu, J.N. Wang, N. Li, A.R. Darvishi, and W.D. Fei, "Stress-induced shifting of the morphotropic phase boundary in sol–gel derived $Pb(Zr_{0.5}Ti_{0.5})O_3$ thin films," Mater. Res. Bull., **46**, [8], 1237–1242, (2011).

[320] Q. Yu, J.-F. Li, Z.-X. Zhu, Y. Xu, and Q.-M. Wang, "Shift of morphotropic phase boundary in high-performance [111]-oriented epitaxial $Pb(Zr,Ti)O_3$ thin films," J. Appl. Phys., **112**, [1], 014102, (2012).

[321] S. Yokoyama, S. Okamoto, H. Funakubo, T. Iijima, K. Saito, H. Okino, T. Yamamoto, K. Nishida, T. Katoda, and J. Sakai, "Crystal structure, electrical properties, and mechanical response of (100)-/(001)-oriented epitaxial $Pb(Mg_{1/3}Nb_{2/3})O_3$–$PbTiO_3$ films grown on (100)c $SrRuO_3$‖(100)$SrTiO_3$ substrates," J. Appl. Phys., **100**, [5], 054110, (2006).

[322] B.C. Chakoumakos, D.G. Schlom, M. Urbanik, and J. Luine, "Thermal expansion of $LaAlO_3$ and $(La,Sr)(Al,Ta)O_3$, substrate materials for superconducting thin-film device applications," J. Appl. Phys., **83**, [4], 1979–1982, (1998).

[323] J.B. Chang, H. Miyazoe, M. Copel, P.M. Solomon, X.-H. Liu, T.M. Shaw, A.G. Schrott, L.M. Gignac, G.J. Martyna, and D.M. Newns, "First realization of the piezoelectronic stress-based transduction device," Nanotechnology, **26**, [37], 375201, (2015).

[324] J.S. Shor, D. Goldstein, and A.D. Kurtz, "Characterization of n-type beta-SiC as a piezoresistor," IEEE Trans. Electron Devices, **40**, [6], 1093–1099, (1993).

[325] X.W. Zhang, Y. Pan, Q. Zheng, and X.S. Yi, "Time dependence of piezoresistance for the

conductor-filled polymer composites," J. Polym. Sci. Part B Polym. Phys., **38**, [21], 2739–2749, (2000).

[326] K.T. Chung, A. Sabo, and A.P. Pica, "Electrical permittivity and conductivity of carbon black-polyvinyl chloride composites," J. Appl. Phys., **53**, [10], 6867–6879, (1982).

[327] T.S. Sreeprasad, A.A. Rodriguez, J. Colston, A. Graham, E. Shishkin, V. Pallem, and V. Berry, "Electron-tunneling modulation in percolating network of graphene quantum dots: Fabrication, phenomenological understanding, and humidity/pressure sensing applications," Nano Lett., **13**, [4], 1757–1763, (2013).

[328] A.A. Taskin, F. Yang, S. Sasaki, K. Segawa, and Y. Ando, "Topological surface transport in epitaxial SnTe thin films grown on Bi_2Te_3," Phys. Rev. B, **89**, 121302, (2014).

[329] J. Shen, Y. Jung, A.S. Disa, F.J. Walker, C.H. Ahn, and J.J. Cha, "Synthesis of SnTe nanoplates with {100} and {111} surfaces," Nano Lett., **14**, [7], 4183–4188, (2014).

[330] R. Gerson, J.M. Peterson, and D.R. Rote, "Dielectric constant of lead titanate zirconate ceramics at high frequency," J. Appl. Phys., **34**, [11], 3242–3245, (1963).

[331] W. Williamson III, C.H. Daniel, E.L. Cross, and B.K. Gilbert, "High frequency dielectric properties of PLZT thin films," Integr. Ferroelectr., **17**, [1-4], 197–203, (1997).

[332] D. Dimos and C.H. Mueller, "Perovskite thin films for high-frequency capacitor applications," Annu. Rev. Mater. Sci., **28**, 397–419, (1998).

[333] V. Anbusathaiah, S. Jesse, M.A. Arredondo, F.C. Kartawidjaja, O.S. Ovchinnikov, J. Wang, S.V. Kalinin, and V. Nagarajan, "Ferroelastic domain wall dynamics in ferroelectric bilayers," Acta Mater., **58**, [16], 5316–5325, (2010).

Vita

Ryan Robert Keech was born on March 8th, 1989, in Boston, Massachusetts to Eileen and Robert Keech. Ryan lived in Stoughton, MA, Lee, NH, and Sanford, ME for about seven years each growing up with his younger brother, Adam, and sister, Emily. Starting in 2007, he attended the University of Connecticut majoring in Materials Science and Engineering with a minor in Mathematics. In 2009, Ryan was named UConn's "Fan of the Year" for painting his entire body blue and white in support of the UConn football team. Ryan's research experience began at EigenLight Corporation where he held a summer internships during his undergraduate years. He also worked in Prof. C. Barry Carter's and Prof. Bryan Huey's laboratories at UConn as an undergraduate. After graduating *magna cum laude* from UConn, Ryan joined Professor Susan Trolier-McKinstry's group at The Pennsylvania State University in 2011 in pursuit of his doctorate degree in Materials Science and Engineering.

Ryan feeling at home in a crystal structure exhibit at the Smithsonian Natural History Museum.